Peculiar Transients as Probes of Stellar Evolution and Mass Loss

Citation

Drout, Maria R. 2016. Peculiar Transients as Probes of Stellar Evolution and Mass Loss. Doctoral dissertation, Harvard University, Graduate School of Arts & Sciences.

Peculiar Transients as Probes of Stellar Evolution and Mass Loss

A dissertation presented

by

Maria R. Drout

to

The Department of Astronomy

in partial fulfillment of the requirements

for the degree of

Doctor of Philosophy

in the subject of

Astronomy and Astrophysics

Harvard University

Cambridge, Massachusetts

April 2016

Dissertation Advisor: Professor Edo Berger Maria R. Drout

Peculiar Transients as Probes of Stellar Evolution and Mass Loss

Abstract

Multi-wavelength observations of supernovae (SN) not only probe the explosion mechanism, but also carry information about the configuration of the star at the moment of collapse and the mass-loss history of the progenitor system in the years immediately preceding its death. The study of supernovae therefore offers a rare observational view of the final stages of stellar evolution. As a result, the recent advent of wide-field SN searches—which are discovering new classes of astronomical transients at an ever-increasing rate—has both expanded the types of stellar systems that we can directly probe and challenged theoretical models of the late-stages of stellar evolution. This thesis explores several new regimes of transient space that have been opened by these modern, wide-field, time domain surveys. We present a series of observational studies which constrain the explosion properties, progenitor systems, and intrinsic rates for several classes of peculiar astronomical transients.

First, we investigate the properties of transients that reach SN luminosities but evolve on rapid timescales. We present a detailed study of the rapidly-declining hydrogen-poor SN 2005ek, showing that it could be produced by the core-collapse of a stripped massive star with a very small ejecta mass. We then describe results from the first *systematic* search for rapidly-evolving and luminous transients in a wide-field survey with a rapid cadence. Using data from the PanSTARRS1 Medium-Deep Survey (PS1-

MDS), we both identified a new class of rapidly-evolving transients and calculated their intrinsic rates—demonstrating that these explosions are *not* intrinsically rare. Second, we utilize very early UV/spectroscopic observations and detailed multi-wavelength follow-up of the stripped-envelope core-collapse SN 2013ge to place constraints on the final configuration of the progenitor system. Finally, we investigate the progenitor stars and mass-loss mechanism that operates in a class of luminous SN that explode within a dense circumstellar medium (Type IIn SN). This is accomplished through a joint analysis of the explosion properties and host galaxy environments for a large number of events, including the full sample of Type IIn SN discovered by the PS1-MDS. We find that luminous Type IIn SN explode in a wide range of galaxies which are are robustly distinguished from the host galaxies of hydrogen-poor super-luminous SN in being more luminous, massive, and metal-rich. Furthermore, we show that a significant fraction of luminous Type IIn SN explode in the bright central regions of their host galaxies, indicating that the physical conditions for star formation in these environments are conducive for the formation of luminous Type IIn progenitors.

Contents

Acknowledgments

Where to begin...

As I sit back and reflect on the path that has brought me to where I am today, it is hard not be overwhelmed by the sheer amount of time, effort, and support that so many people have invested in me over the years. I can only hope (and work) to ensure that I will do justice to all of you in my future endeavors.

First, I would like to thank Edo Berger—who graciously took on the task of advising my PhD—for providing me with countless opportunities, pushing me when necessary, and allowing me a tremendous amount freedom to develop and pursue my own research interests. I am continually in awe of the way he is able to both support and challenge the members of his group, and am grateful to have such an example to learn from.

In addition, I cannot express enough gratitude to Alicia Soderberg, Phil Massey, and Cornelia Lang all of whom have acted as advisors and mentors to me, dating back to my time as an undergraduate. I am keenly aware of all that they did not only to help me develop as a researcher, but also to ensure that I was quickly integrated into the broader scientific community. I firmly believe that this was pivotal to my success.

I also acknowledge some of the faculty and staff who have been influential throughout my time at Harvard. To the members of my thesis committee: Bob Kirshner, Ramesh Narayan, Charlie Conroy, and Rosanne Di Stefano for taking the time to provide feedback and guidance. To Enrico Ramirez-Ruiz, for allowing me to crash your very stimulating group meetings and writing me letters of support. To Avi Loeb and John Johnson for providing me with words of advice and being strong advocates for graduate student issues in general. To Peg Herlihy, Robb Scholten, Nina Zonnevylle, and Lisa Catella for *everything*.

Research—especially in time-domain astronomy—does not happen in a vacuum, and I am fortunate to have landed in the midst of a phenomenal set of collaborators. The sheer knowledge, talent, dedication, and grit displayed by this group is humbling. In particular, I thank Dan Milisavljevic and Raffaella Margutti for all they taught me and everything they did behind the scenes. Special thanks to Dan for many highly entertaining nights observing. I also thank Jerod Parrent, Ryan Chornock, Ryan Foley, Armin Rest, Atish Kamble, Nathan Sanders, Ragnhild Lunnan, and Wen-fai Fong for all of their help and advice. I am grateful for all of the other past and present members of the Harvard time-domain groups, who have made research a blast, as well as numerous members of the PanSTARRS1 consortium, without whose work the results presented in this thesis would not have been possible.

One of the reasons I chose to do my Ph.D. at Harvard was a sense that there was a strong graduate student community—and I was not disappointed. Throughout the past five years my fellow graduate students have been a constant source of support, inspiration, motivation, and entertainment, and there is no way I can either list them all or thank them enough. Special thanks to my officemate, Luke Kelly, for being a friend, a sounding board, and for putting up with me over the past year of job and thesis related stress. Similar thanks to Sarah Wellons, Chris Faesi, Katie Auchettl, my entire cohort, and everyone with whom I've shared conversations, coffees, and beers with over the years. I am particularly grateful for everyone involved in both Astrobites and ComSciCon—you demonstrated to me what even a small number of very motivated people can accomplish.

To the Churchill Foundation, for a year in England that was challenging and formative for me as a person, where I also met a group of friends who might be the finest set of dining companions an astronomer can ask for.

To other friends who supported me, near and far.

To my family, who made me the person I am, and always encouraged me to pursue my dreams—no matter how crazy.

Finally, to Mark. For everything.

Chapter 1

Introduction

An understanding of the lifecycle of massive stars is necessary for every subfield in astrophysics. Through their ionizing radiation, powerful stellar winds, nucleosynthesis, and explosive deaths as supernova (SN), massive stars give birth to black holes and neutron stars, and play a large role in the dynamical and chemical evolution of the universe. Although the study of massive stars is one of the oldest subfields in astronomy, the recent advent of wide-field SN searches has launched an upheaval in the field of stellar evolution. These new surveys are uncovering new types of astronomical transients that challenge not only existing models for SN explosions, but also our understanding of the physical processes that occur during the final years of massive stars' lives.

This thesis presents a series of observational studies that constrain the explosion properties, progenitor systems, and intrinsic rates for several classes of peculiar astronomical transients. These studies explore new regimes of transient space that have been opened by modern, wide-field, time-domain surveys. By probing new regimes of the transient sky, we have increased the variety of explosions that we can directly probe, challenged our views of what mass-loss can occur in the final years before core-collapse, and expanded our knowledge of what final states are possible in the evolution of massive stars.

In this Chapter, we provide a brief introduction to modern time-domain studies (Section 1.1), the rapidly expanding landscape of known SN types and theoretical explosion mechanisms (Section 1.2), several ways transients can be used as probes of stellar evolution (Section 1.3), and, finally, a summary of the specific topics and contributions presented in this thesis (Section 1.4).

1.1 Transient Astronomy in the Era of Wide-Field Time-Domain Surveys

Every time-domain survey must make decisions and compromises about its operating procedures (e.g. cadence, depth, area, observing bands) based on its technological capabilities and scientific goals. These decisions, in turn, fundamentally influence both the *quantity* and *types* of transients that the survey is capable of detecting. As a result, the field of time domain astronomy has been marked by several significant revolutions that can be directly tied to advances in technology. For example, the shift from photographic plates to CCD detectors in the 1990s significantly improved image quality and facilitated the development of the first image subtraction and automatic transient detection pipelines. Dedicated SN searches initiated during this time period (e.g. the Calan/Tololo survey, Hamuy 2003; the Lick Observatory SN Search, Filippenko et al. 2001a) increased the number of SN identified per year from tens in the late-1980s to hundreds by the early-2000s[1].

Now, in the past decade, the development of large giga-pixel-class CCD cameras, the availability of smaller science-grade CCDs at “off-the-shelf” prices, and significant increases in computational power have combined to usher in a new era in the study of transient phenomena. Surveys such as the Panoramic Survey Telescope and Rapid Response System (Pan-STARRS; Kaiser et al. 2010), the Palomar Transient Factory (PTF; Law et al. 2009), and the All-Sky Automated Survey for Supernova (ASAS-SN; Shappee et al. 2014) are now capable of imaging significant portions of the sky on a nightly basis. These wide-field surveys have significantly influenced the field of time-domain astronomy.

Due to the sheer volume surveyed, the transients detected each year now number in the *thousands*. This has facilitated large statistical studies of the explosion properties and host galaxy environments SN populations as well as the discovery of new, intrinsically rare, classes of transient phenomena. Just as importantly, these technological advances have provided more flexibly in survey design and have therefore opened up entirely new *regimes* of the transient sky. For example, shorter survey cadences now allow us to characterize transients at rapid timescales and probe known types of SN at very early phases. Untargeted surveys and better image subtraction algorithms now allow us to discover transients in a wide array of host environments, reducing potential biases in statistical studies that are introduced when surveys only target a list of pre-selected galaxies. Deeper images allow us to push to higher redshifts, where transients can act as probes of the star formation history and chemical evolution of the universe. At the

---

[1] http://www.rochesterastronomy.org/snimages/

same time, advances in the sensitivity and availability of instruments and surveys in other wavelength regimes (γ-ray, X-ray, UV, infrared, radio) allow us to probe transient phenomena produced by a wide array of physical emission processes.

1.2 The Expanding Landscape of Astronomical Transients

As both the quantity and quality of SN data has increased, the establishment and refinement of a consistent classification scheme for astronomical transients has proven to be a useful tool in their study. By gathering together similar astronomical events, we can use the aggregated observational data from statistically significant samples to place constraints on the nature of the explosions and their progenitor systems. Traditionally, supernovae are classified based on the elements present in their optical spectra (see, e.g., Filippenko 1997). The main distinction is between events which show conspicuous hydrogen in their spectra (Type II) and those that do not (Type I). Type I events are then further separated into Type Ia SN, which display a strong Si II absorption trough near maximum light, and Type Ib/c SN which lack this feature. The latter are sometimes subdivided into Type Ib SN, which possess prominent helium lines, and Type Ic SN, which do not.

Through decades of observational and theoretical studies of these explosions, their host galaxies, and their progenitor stars, a conventional interpretation linking the largest observational classes SN to distinct progenitor systems/explosion mechanisms has emerged. The two main models that are invoked to explain a majority of SN explosions are the thermonuclear explosion of a white dwarf which undergoes runaway nuclear burning (Hoyle & Fowler 1960) and the gravitational collapse of a massive star ($\gtrsim 8$ $M_\odot$) which has progressed through a series of advanced nuclear burning stages in its core (Baade & Zwicky 1934).

In particular, the light curves and spectra of normal Type Ia SN are remarkably consistent, and it is generally accepted that they are produced by the thermonuclear explosion of an carbon-oxygen white dwarf (WD) in a binary system (see, e.g., reviews by Woosley 1986; Hillebrandt & Niemeyer 2000; Wang & Han 2012). If the WD reaches a critical mass/density—either through accretion or a merger—a runaway nuclear reaction will be triggered in the highly degenerate stellar core. This can lead to an explosion in which a substantial fraction of the available mass is burned to nuclear statistical equilibrium, and the entire star is disrupted. The total energy budget of this explosion is $\sim 10^{51}$ erg (the binding energy of a WD) and the radioactive decay of ^{56}Ni synthesized in the explosion powers optical emission (see., e.g., Woosley 1986). Lines of evidence which support this progenitor scenario for Type Ia SN include the energetics and elements present in the spectra of the explosions, the lack of observed neutron stars in galactic Type Ia SN remnants, and the discovery of Type Ia SN in a wide variety of host environments (including elliptical galaxies with old stellar populations) (see Hillebrandt & Niemeyer 2000; Wang & Han 2012, and references therein). However, several large open questions remain, with the most glaring being the nature of the binary system (e.g. single degenerate or double-degenerate) and thus the sequence of events which triggers the explosion.

In contrast, both Type II and Type Ib/c SN are generally understood to be core-collapse explosions. The physical process that triggers the gravitational collapse can vary for stars in different initial mass ranges[2], but the most commonly invoked is the collapse of an iron core which can no longer support itself via electron degeneracy pressure. The total energy budget of a typical core-collapse is $\sim 10^{53}$ ergs, of which ∼99% is carried away by neutrinos (see, e.g., Woosley 1986). Intriguingly, simulations have found that the initial shock wave produced by the 'bounce' of infalling material off the nuclear density proto-neutron star does not have enough energy to fully explode the star (see Janka et al. 2007, and references therein). As a result, the physical mechanism which revitalizes the shock wave, leading to an explosion with $\sim 10^{51}$ erg of kinetic energy is still debated and is the topic of *considerable* theoretical/computational work. However, the basic picture of core-collapse was confirmed by the detection of neutrinos from the nearby Type II SN 1987A (Hirata et al. 1987).

The various spectroscopic subclasses of core-collapse SN can be then be linked to massive stars with different evolutionary histories. In particular, normal Type II SN are the core-collapse of massive stars which retain a large fraction of their hydrogen envelopes until the ends of their lives, and have been directly identified as Red Supergiants (RSGs) in pre-explosion images (Smartt 2009). In contrast, Type Ib/c SN represent the explosion of stars which had their hydrogen envelopes removed prior to core-collapse, either via massive star winds (e.g. Woosley & Weaver 1995) or binary interactions (e.g. Podsiadlowski et al. 1992).

While this standard picture still remains, the advances in time-domain surveys described in Section 1.1 have expanded and enriched the landscape of astronomical

---

[2] e.g. electron capture in degenerate O+Ne+Mg cores of 8−10 $M_\odot$ stars, pair production in the cores of stars >130−250 $M_\odot$

transients. Multiwavelength observations have revealed diverse properties amongst SN of the same spectroscopic subclass, with a notable example being the association of ∼1% of Type Ib/c SN with long-duration Gamma-Ray Bursts (see, e.g., Woosley & Bloom 2006). Detailed spectroscopic coverage at a wide range of epochs have revealed a variety of core-collapse SN which transition from one spectroscopic sub-class to another (e.g. Filippenko 1988; Milisavljevic et al. 2013; Margutti et al. 2016), pointing to a wide range of progenitor properties and evolutionary histories. Many additional subtypes of SN and other classes of transients that fall entirely outside of the traditional classification scheme have also been identified (e.g. calcium-rich transients, Type Iax SN, luminous red novae, rapidly-evolving transients, super-luminous supernovae). The properties of these new phenomena are diverse and theoretical models have provided a wide range of potential explosive origins (e.g. WD deflagrations, helium-shell detonations, stellar mergers, stellar eruptions, tidal disruption events, pair-instability SN). Thus, on-going research in the field of transient astronomy seeks to define and refine observational classes of events in order to reveal the underlying physical processes which drive these explosions.

1.3 Transients as Probes of Stellar Evolution and Mass-loss

This diversity of astronomical transients not only informs our knowledge of the physics of stellar explosions, but also influences our broader understanding of stellar evolution. First and foremost, by studying supernovae we learn about the final state in the evolution of many stellar systems. The electromagnetic radiation that we observe from a given supernovae is influenced by the mass, radius, composition, and density structure of the progenitor envelope at the time of collapse, as well as the kinetic energy and quantity of radioactive material produced by the explosion itself. This final configuration is the direct byproduct of the initial conditions (mass, metallicity, rotation, binarity) and subsequent evolution (mass-loss, mixing, binary interaction) of the the progenitor system.

As a result, the physical properties of SN progenitors that can be inferred from observations, their intrinsic rates, and how these vary with host environment (e.g. metallicity, star-formation rate, stellar density) provide critical benchmarks for our theoretical understanding of star formation, stellar evolution, and SN feedback. These observational constraints are vital because relatively small changes to adopted prescriptions for effects such as rotationally induced mixing, convectional overshoot, and RSG mass-loss—not to mention the treatment (or lack thereof) of more uncertain evolutionary states such as common-envelope evolution in close binaries and eruptive mass-loss—can drastically change theoretical predictions for the end points in models of stellar evolution (see, e.g., Hirschi et al. 2004; Eldridge & Tout 2004; Heger et al. 2003; Georgy 2012).

In addition, through the study of transients we have the ability to constrain the *physical behavior* of SN progenitors in the decades and centuries before they explode. When a SN blastwave expands, it collides with material located in its immediate vicinity. The density of this circumstellar medium (CSM) is shaped by the mass-loss history of the progenitor system. Electromagnetic signatures of this interaction therefore provide us with another indirect means to link SN of various subtypes to known classes of stellar systems as well as offering us one of our only observational views of the final stages of stellar evolution. For relatively low density environments, the shock-CSM interaction is observed primarily in the radio and X-ray bands as synchrotron and inverse Compton emission, respectively (Chevalier & Fransson 2006). However, for progressively denser ambient media, the shock-CSM interaction will begin to contribute to—and eventually dominate—the optical emission from a given transient (e.g. Chevalier & Fransson 1994; Chugai & Danziger 1994).

1.4 Summary of Thesis Topics and Results

The sections above provide broad context for this thesis, which presents series of observational studies which constrain the explosion properties, progenitor systems, and intrinsic rates for several classes of peculiar astronomical transients. These studies explores several new regimes of transient space that have been opened by modern wide-field time-domain surveys (timescale, wavelength, host environment) in order to probe the uncertain final stages of stellar evolution and the physics of stellar explosions. In particular, we examine the properties of transients which evolve on very rapid timescales (Section 1.4.1), utilize very early observations of hydrogen-poor SN to constrain their progenitor structure (Section 1.4.2), and investigate the progenitors and mass-loss mechanism that operates in a class of luminous SN which explode in a very dense CSM (Section 1.4.3). The following subsections introduce each of these topics in more detail, and summarize the results of our investigations.

The work presented in this thesis combines detailed multi-wavelength observations of nearby SN with data from the PanSTARRS1 Medium Deep Survey (PS1-MDS). The PS1-MDS was a wide-field, untargeted, survey with a daily cadence that operated from

2010−2014, over which time we identified thousands of transients.

1.4.1 Rapidly-Evolving Transients

Rapidly-evolving transients are sources that reach SN luminosities but have timescales an order of magnitude faster. While typical Type I SN spends ∼20−40 days above have of their peak luminosity, rapidly-evolving transients have characteristic timescales $\lesssim$10 days. To date, only a small number of these events have been identified (Kasliwal et al. 2010; Poznanski et al. 2010; Ofek et al. 2010; Drout et al. 2013, 2014). Prior to the work presented in this thesis, the scarcity of rapidly-evolving transients was due to an *unknown* combination of their intrinsic rates and the (in)efficiency with which many optical transient surveys can identify transients at very short timescales.

Rapidly-evolving transients probe the extremes of both the configuration of the progenitor star (e.g. mass, radius) and the explosion parameters themselves (e.g. ejected mass, kinetic energy). As a result, they offer a unique means to study uncertain channels for stellar death, with leading theoretical models including black hole formation (Kashiyama & Quataert 2015), the formation of binary neutron star systems (Tauris et al. 2013), and a range of explosive processes in binary WD systems (Shen et al. 2010). Understanding the demographics of transients on short timescales, the true nature of the explosions, and their intrinsic rates will therefore influence our understanding of stellar evolution. Progress in this area requires not only detailed modeling of individual objects but also the identification of large samples of events—a task which is now possible as wide-field surveys such as the PanSTARRS1 Medium-Deep Survey (PS1-MDS) push to shorter (∼1 day) cadences.

In Chapters 2 and 3 we present a pair of studies which investigate the explosion properties, progenitors, and intrinsic rates of rapidly-evolving transients. Chapter 2 presents extensive multi-wavelength observations of the extremely rapidly declining Type Ic SN 2005ek. Spectroscopic modeling reveals an ejecta mass of $\sim$0.3 $M_\odot$ that is dominated by oxygen ($\sim$80%). Although previous rapidly-evolving Type I events were hypothesized to be result from the detonation of a helium shell on a white dwarf, oxygen-dominated ejecta are difficult to reconcile with this proposed mechanism. We find that the properties of SN 2005ek are consistent with either the edge-lit double detonation of a low-mass white dwarf, or the iron-core collapse of a massive star that is stripped by binary interaction. However, if we assume that the strong spectroscopic similarity of SN 2005ek to other Type Ic SN is an indication of a similar progenitor channel, then a white-dwarf progenitor becomes very improbable. SN 2005ek may be one of the lowest mass stripped-envelope core-collapse explosions ever observed.

Chapter 3 describes the first *systematic* search for rapidly-evolving transients, and the resulting identification of 10 new transients with in the PS1-MDS. This work tripled the number of known rapidly-evolving transients, and identified a new class of events with high peak luminosities and very blue colors. We find it difficult to reconcile the short timescale, high peak luminosity, and lack of UV line-blanketing observed in many of these transients with an explosion powered mainly by the radioactive decay of ^{56}Ni. Rather, we find that many are consistent with either (1) cooling envelope emission from the explosion of a star with a low-mass extended envelope that ejected very little radioactive material, or (2) a shock breakout within a dense, optically thick, wind surrounding the progenitor star. After calculating the detection efficiency for objects with rapid timescales in the PS1-MDS we find a volumetric rate of 4800$-$8000 events yr^{-1} Gpc^{-3} (4%−7% of the core-collapse SN rate at z=0.2). This demonstrates that rapid transients are *not* intrinsically rare. *Few have been detected simply because the previous generation of time-domain surveys were not designed to be efficient at the shortest timescales.* Instead, rapidly-evolving transients represent a significant channel that we must understand to have a complete picture of stellar death.

1.4.2 Early Observations of Hydrogen-Poor Core-Collapse SN

The optical light curves of stripped-envelope core-collapse SN (Type Ib/c) are powered predominately by the radioactive decay of ^{56}Ni synthesized during the explosion (e.g. Arnett 1982). However, at very early phases ($\lesssim$5 days post-explosion) a number of other emission sources could potentially contribute. These include cooling envelope emission (sensitive to both the radius and envelope structure of the progenitor star Nakar & Sari 2010; Rabinak & Waxman 2011), emission from a shock collision with a binary companion (Kasen 2010), and emission from asymmetric outflows/ejections (e.g. Bersten et al. 2013). As a result, very early phase observations offer a unique means to probe both the physical state of the progenitor system at the time of the explosion as well as the explosion mechanism itself. Rapid survey cadences now facilitate the discovery of SN at earlier and earlier phases (Gal-Yam et al. 2014; Cao et al. 2015; Marion et al. 2016), offering a new means to study these events.

In Chapter 4 we use very early phase and multi-wavelength observations to place constraints on the final configuration of the progenitor system for a stripped-envelope CCSN. We present extensive multi-wavelength observations of the Type Ib/c SN 2013ge, which was discovered within ∼2 days of explosion. These observations reveal an excess component of blue/UV emission at early times with a timescale/luminosity never previously observed. We are left with two distinct progenitor scenarios for SN 2013ge, depending on our interpretation of this early emission. If the first component is cooling envelope emission, then the progenitor of SN 2013ge either possessed an extended envelope—which is inconsistent with any hydrostatic envelope structure computed by stellar models to date—or ejected a portion of its envelope in the final year before core-collapse. Alternatively, if the first component is due to outwardly mixed ^{56}Ni, then our observations may be consistent with the asymmetric ejection of a clump of nickel-rich material at high velocities.

1.4.3 Luminous Interacting Transients

Approximately 10% of core-collapse SN (dubbed Type IIn; Schlegel 1990) exhibit narrow hydrogen emission lines in their spectra, indicative of the SN blast wave interacting with a *dense* CSM (Smith et al. 2011; Chevalier & Fransson 1994; Chugai & Danziger 1994). The light curves and spectra of Type IIn SN can be used to estimate pre-SN mass-loss rates and, in many cases, the derived values of 10^{-4} to 10^{-2} $M_\odot$ yr^{-1} are orders of magnitude higher than steady winds observed in evolved massive stars (Vink et al. 2001; Crowther 2007). The origin of this dense CSM poses a challenge for models of stellar evolution, as it implies that a subset of massive stars undergo intense (possibly violent/eruptive) mass-loss in the years immediately preceding core-collapse. While Luminous Blue Variables (LBVs) also undergo episodic/eruptive mass-loss these stars are *not* predicted to explode as SN.

Type IIn SN span a wide range of observed properties (luminosities, timescales) and are likely produced by multiple progenitor channels. Particularly puzzling has been the recent discovery that some Type IIn SN reach luminosities 10−100 times that of normal core-collapse SN, with total radiated energies $\gtrsim 10^{51}$ erg (e.g. Smith et al. 2007, 2008; Rest et al. 2011). If powered primarily by shock heating due to ejecta-CSM interaction, these super-luminous SN require intense mass-loss episodes of up to a $\mathrm{M}_{\odot}\ \mathrm{yr}^{-1}$ and dense CSM shells of $\gtrsim$10 $\mathrm{M}_{\odot}$ (e.g. Smith & McCray 2008; van Marle et al. 2010; Chatzopoulos et al. 2013). Both the progenitor stars for these luminous explosions and the mechanism by which the expel such large quantities of mass are debated. Theoretical mass-loss mechanisms include LBV-like eruptions (Smith et al. 2007), instabilities or wave-driven mass-loss during late nuclear burning stages (Smith & Arnett 2014; Shiode & Quataert 2014), common-envelope evolution (Chevalier 2012), pulsational-pair instability (Woosley et al. 2007), or the presence of a relic protoplanetary disk (Metzger 2010).

Progress in our understanding of the progenitors and mass-loss mechanism that operate in luminous interacting transients can be made both by (a) using the explosions themselves to constrain the full physical scale and density profile of the CSM and (b) investigating the physical conditions which are required to produce the explosions by studying their host galaxies and sub-galactic environments. Both of these endeavors require large and unbiased samples of events. Luminous Type IIn SN are intrinsically rare (Quimby et al. 2013), and hence, it is only in recent years that wide-field surveys have made such studies possible.

These are the topics addressed in Chapters 5, 6 7, and 8, which contain preliminary results from a large observational campaign to constrain the progenitors and mass-loss mechanisms that operate in luminous interacting transients through a joint analysis of their explosion properties and host galaxy environments.

After brief background and motivation given in Chapter 5, Chapter 6 presents the light curves and spectra for the full sample of 25 Type IIn SN discovered in the PS1-MDS. These SN span a wide range in peak luminosity (-16 mag $>$ M > -21 mag) and timescale (12 days $< \mathrm{t}_{\mathrm{char}} <$ 200 days), and include 10 events with peak luminosities above 6×10^{43} erg s^{-1} and total radiated energies in excess of $(0.3 - 1.0) \times 10^{51}$ erg. This represents a significant increase in the number of luminous interacting transients with well-sampled, multi-band light curves available.

In Chapter 7 we report preliminary results from a comprehensive examination of the global host galaxy properties of luminous interacting transients. Using optical photometry and spectroscopy, we calculate luminosities, masses, and metallicities for the host galaxies of a large sample of luminous and "standard-luminosity" interacting transients from the PS1-MDS as well as other untargeted surveys. The host galaxies of luminous interacting transients span a wide range in luminosity, mass, and metallicity, and are robustly distinguished from those of hydrogen-poor super-luminous SN (SLSN-I), in being more luminous, massive, and metal-rich. While a fraction of luminous Type IIn SN do occur in dwarf galaxies with sub-solar metallicities, we observe that the physical conditions present in these galaxies are not required to produce all luminous interacting transients.

Finally, Chapter 8 presents results from the first statistical study of the sub-galactic environments of luminous interacting transients. We determine that a significant fraction of luminous Type IIn SN explode in the central regions of their host galaxies, with a median normalized offset of $\langle \mathrm{R}/\mathrm{R}_{\mathrm{gal},50} \rangle = 0.42$. This central concentration is in excess of that predicted by an exponential disk profile and is in stark contrast to standard-luminosity Type IIn SN for which a central *deficit* is observed. We conclude that the physical conditions of star formation in the bright inner regions of galaxies (including Milky Way-like and S0 galaxies) are conducive for the formation of luminous Type IIn SN progenitors. Relevant factors may include stellar interactions or IMF variations in dense nuclear star clusters or circumnuclear rings.

Chapter 2

The Fast and Furious Decay of the Peculiar Type Ic Supernova 2005ek

M. R. Drout, A. M. Soderberg, P. A. Mazzali, J. T. Parrent, R. Margutti, D. Milisavljevic, N. E. Sanders, R. Chornock, R. J. Foley, R. P. Kirshner, A. V. Filippenko, W. Li, P. J. Brown, S. B. Cenko, S. Chakraborti, P. Challis, A. Friedman, M. Ganeshalingam, M. Hicken, C. Jensen, M. Modjaz, H. B. Perets, J. M. Silverman, D. S. Wong

The Astrophysical Journal, Vol. 774, No. 58, 2013

Abstract

We present extensive multi-wavelength observations of the extremely rapidly declining Type Ic supernova, SN 2005ek. Reaching a peak magnitude of $M_R = -17.3$ and decaying by ~ 3 mag in the first 15 days post-maximum, SN 2005ek is among the fastest Type I supernovae observed to date. The spectra of SN 2005ek closely resemble those of normal SN Ic, but with an accelerated evolution. There is evidence for the onset of nebular features at only nine days post-maximum. Spectroscopic modeling reveals an ejecta mass of ~ 0.3 $M_\odot$ that is dominated by oxygen ($\sim 80\%$), while the pseudo-bolometric light curve is consistent with an explosion powered by ~ 0.03 $M_\odot$ of radioactive ^{56}Ni. Although previous rapidly evolving events (e.g., SN 1885A, SN 1939B, SN 2002bj, SN 2010X) were hypothesized to be produced by the detonation of a helium shell on a white dwarf, oxygen-dominated ejecta are difficult to reconcile with this proposed mechanism. We find that the properties of SN 2005ek are consistent with either the edge-lit double detonation of a low-mass white dwarf or the iron-core collapse of a massive star, stripped by binary interaction. However, if we assume that the strong spectroscopic similarity of SN 2005ek to other SN Ic is an indication of a similar progenitor channel, then a white-dwarf progenitor becomes very improbable. SN 2005ek may be one of the lowest mass stripped-envelope core-collapse explosions ever observed. We find that the rate of such rapidly declining Type I events is at least 1–3% of the normal SN Ia rate.

2.1 Introduction

The advent of dedicated supernova (SN) searches has dramatically increased the rate at which unusual transients are discovered. In particular, high-cadence surveys have uncovered a diverse set of rapidly evolving events which reach SN luminosities (absolute magnitude between -20 and -15) but have observed properties that challenge the parameter space easily explained by traditional SN models (e.g., the collapse of the core of a massive star, or the thermonuclear disruption of a white dwarf).

The plethora of objects that have been referred to as "rapidly evolving" include both Type I (hydrogen poor) and Type II (hydrogen rich) events (see Filippenko 1997 for a review of traditional SN classifications). Although the main physical process leading to optical emission varies among supernovae, in all cases the characteristic timescale offers insight into the amount of participating material. Rapid evolution typically implies lower masses. For supernovae powered by hydrogen recombination (e.g., Types IIP, IIL) and radioactive decay (e.g., Types Ia, Ib, Ic), rapid timescales indicate a low hydrogen envelope mass and a short photon diffusion timescale, respectively. For supernovae powered by interaction with external gas (e.g., Type IIn), a rapid decline implies a steep decrease in circumstellar medium (CSM) density, and a short overall timescale implies a small radius over which this material is located.

Among the Type I events labeled as rapidly evolving are the SN 1991bg-like SN Ia (Filippenko et al. 1992; Leibundgut et al. 1993), the "calcium-rich" transients for which SN 2005E is the prototype (Perets et al. 2010; Kasliwal et al. 2012; Valenti et al. 2014), and some members of the recently defined Type Iax supernovae (Foley et al. 2013). They earn the title "rapidly evolving" because they decay by 1–2 mag in the first 15 days post-maximum. Many of these objects possess peak luminosities lower than those of normal SN I ($\gtrsim -15$ mag) and are thought to be powered by radioactive decay. Although their host galaxies are diverse, members of the first two classes above have exploded in elliptical galaxies. In addition, several luminous (M $\lesssim -19$ mag) transients have been observed that decay on similar timescales, but show narrow hydrogen and/or helium emission lines in their spectra, indicating that they are at least partially powered by interaction with a dense CSM. These include the Type IIn SN PTF09uj (Ofek et al. 2010) and the Type Ibn SN 1999cq (Matheson et al. 2000).

However, the record for the most rapidly declining SN observed thus far does not belong to any of these objects. SN 2002bj (Poznanski et al. 2010) and SN 2010X (Kasliwal et al. 2010) easily outstrip them, declining by $\gtrsim 3$ mag in the first 15 days post-maximum. The ejecta masses inferred for these two events are very small ($\lesssim 0.3$ $M_{\odot}$), but their peak luminosities are within the typical range for SN Ib/Ic ($-19 \lesssim M \lesssim -17$; Drout et al. 2011). These two facts, coupled with the lack of hydrogen in their spectra (SN 2002bj is a SN Ib, SN 2010X a SN Ic), have led several authors to hypothesize that they were produced by the detonation of a helium shell on a white dwarf (a ".Ia" supernova; Woosley et al. 1986; Chevalier & Plait 1988; Bildsten et al. 2007; Shen et al. 2010; Waldman et al. 2011; Sim et al. 2012).

Two potential other members of this class include SN 1885A and SN 1939B (see, e.g., Perets et al. 2011; Chevalier & Plait 1988; de Vaucouleurs & Corwin 1985; Leibundgut et al. 1991). While both SN 2002bj and SN 2010X were found in star-forming galaxies, SN 1939B exploded in an elliptical, a fact suggestive of an old progenitor system. However, while the post-maximum decline rates of these objects are similar, even the well-studied events show differences in their other properties. SN 2002bj was ~ 1.5 mag brighter, significantly bluer, and exhibited lower expansion velocities than SN 2010X. It has not yet been established whether all (or any) of these extremely rapidly declining objects belong to the same class of events.

Here we present the discovery and panchromatic follow-up observations of SN 2005ek, another very rapidly declining and hydrogen-free event that closely resembles SN 2010X. In Section 2.2 we present our extensive multi-wavelength observations, while in Sections 2.3–2.6 we describe the photometric and spectroscopic properties, explosion parameters, and host-galaxy environment of SN 2005ek, respectively. Section 2.7 examines the rates of such transients. Finally, in Section 2.8, we discuss progenitor channels that could lead to such a rapidly evolving explosion.

2.2 Observations

2.2.1 Discovery

SN 2005ek was discovered by the Lick Observatory Supernova Search (LOSS) using the Katzman Automatic Imaging Telescope (KAIT; Filippenko et al. 2001b) on 2005 Sep. 24.53 (UT dates are used throughout this paper) with an unfiltered (clear) $m \approx 17.5$ mag. The object was not detected in previous KAIT images on Sep. 18.51 to a limit of $m \approx 19$ mag, while subsequent imaging on Sep. 25.37 revealed that the transient had brightened to $m \approx 17.3$ mag (Khandrika & Li 2005). SN 2005ek is located in the outskirts of its host galaxy, UGC 2526, with distance $D = 66.6 \pm 4.7$ Mpc[1] and morphology Sb.

---

[1] We adopt the NED distance after correction for Virgo, Great Attractor, and Shapley Supercluster Infall and assuming $H_0 = 73$ km s^{-1} Mpc^{-1} (Mould et al. 2000).

Wong et al. (2005) obtained a spectrum of SN 2005ek on Sep. 26 with the Shane 3-m reflector (plus Kast spectrograph) at Lick Observatory and reported that SN 2005ek was a "young supernova, probably of Type Ic." After this spectroscopic identification, we promptly initiated a panchromatic follow-up program spanning the radio, infrared (IR), optical, ultraviolet (UV), and X-ray bands.

2.2.2 Palomar 60-inch Imaging

We obtained nightly multi-band images of SN 2005ek with the robotic Palomar 60-inch telescope (P60; Cenko et al. 2006) beginning on Sep. 26.3 and spanning through Oct. 15.2. Each epoch consisted of 4–10 120 s frames in filters B, V, R, and I. All P60 images were reduced with IRAF[2] using a custom real-time reduction pipeline (Cenko et al. 2006). Nightly images were combined using standard IRAF tools. Images of the transient and host galaxy constructed from P60 data are shown in Figure 2.1.

For the P60 V and R bands we obtained template images of the region surrounding SN 2005ek on 2007 Aug. 16 (bottom panel of Fig. 2.1), after the SN had faded from view. We subtracted the host-galaxy emission present in the template image using a common point-spread function (PSF) method and then performed aperture photometry on the resulting difference images. For the B and I bands, no suitable template images were obtained, and we therefore performed PSF photometry on our stacked images directly. A comparison of these two methods with our V- and R-band data revealed that the

---

[2] IRAF is distributed by the National Optical Astronomy Observatory, which is operated by the Association for Research in Astronomy, Inc. under cooperative agreement with the National Science Foundation.

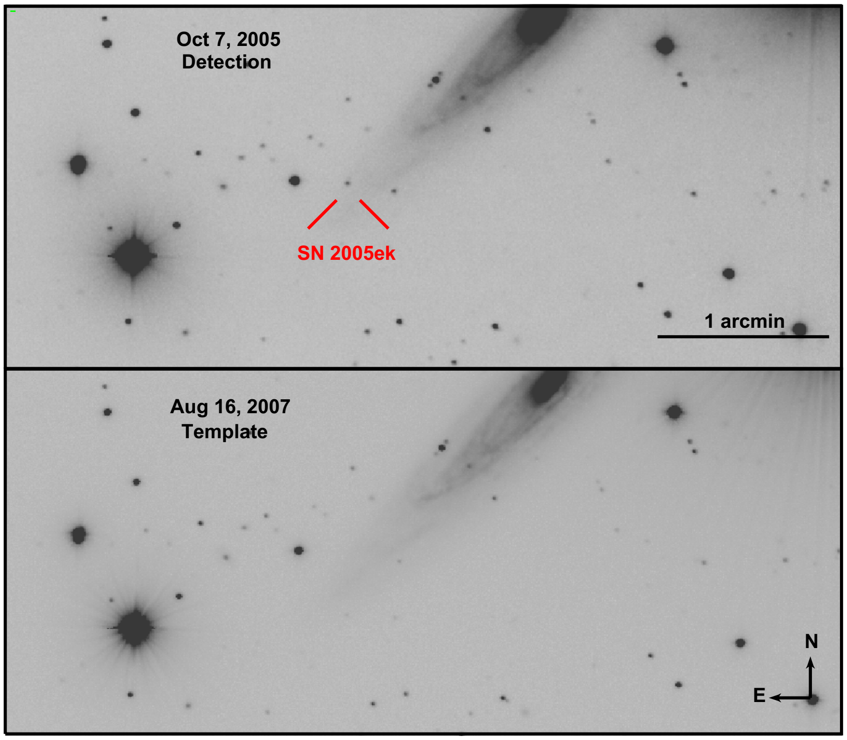

Figure 2.1.—: *Top:* R-band Palomar 60-inch (P60) image of SN 2005ek, on the outskirts of UGC 2526. The SN location is marked by red crosshairs. *Bottom:* P60 template image of the region around SN 2005ek, taken on 2007 Aug. 26.

resulting photometry was consistent within the measured uncertainties.

In all cases, we measured the relative magnitude of the SN with respect to five field stars within the full $13' \times 13'$ P60 field of view. Absolute calibration was performed based on Sloan Digital Sky Survey (SDSS) photometry of the field stars (Ahn et al. 2012), converted to the *BVRI* system using the relations from Smith et al. (2002). Our resulting P60 photometry is listed in Table 2.1 and shown as filled circles in the main panel of Figure 2.2. These data reveal that the light curve reaches maximum at $m_R \approx 17.4$ mag only ~ 9 days after the KAIT nondetection and subsequently decays very rapidly in all bands.

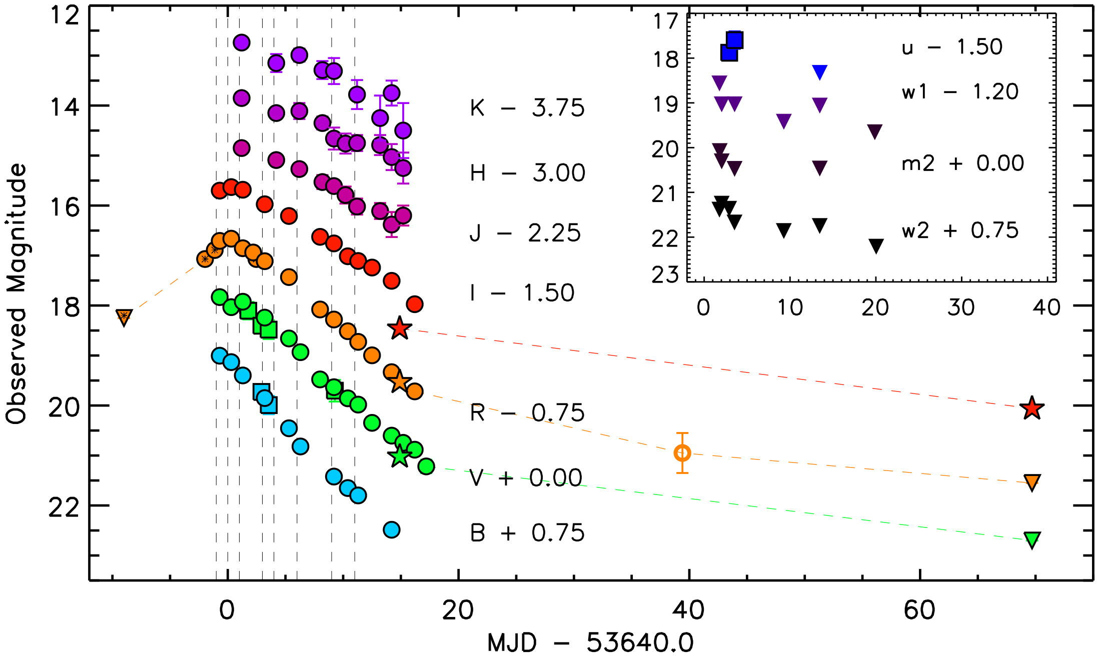

Figure 2.2.—: Photometry of SN 2005ek. P60 *BVRI*- and PAIRITEL *JHK*-band data (circles) are respectively shown as cyan, green, orange, red, and three shades of violet. Lick Observatory discovery observations and the pre-discovery nondetection are shown as orange circles and a triangle with an asterisk inside. P200 *gri*-band data are shown as green, orange, and red stars; triangles denote upper limits. A late-time FLWO *r*-band detection is shown as an open orange circle. UVOT *b*- and *v*-band detections are shown as blue and green squares in the main panel. UVOT *u*-, *w*1-, *m*2-, and *w*2 detections (squares) and upper limits (triangles) are shown in the inset. Vertical lines in the main panel indicate epochs on which spectroscopy was obtained.

2.2.3 Palomar 200-inch Imaging

On 2005 Oct. 11 and Dec. 5 we imaged SN 2005ek with the Large Format Camera (LFC) mounted on the Palomar 200-inch (5 m) telescope in the g', r', and i' bands (120 s expsoures). Image processing and PSF photometry were performed using standard packages within IRAF. We performed our absolute calibration using SDSS photometry of field stars, in the same manner as described above. Our resulting photometry is listed in Table 2.2 and supplements the P60 data in the main panel of Figure 2.2. On our final epoch, the transient was only detected in the i' band at ~ 21.5 mag.

2.2.4 Lick Observatory Imaging

The LOSS unfiltered images of SN 2005ek were reanalyzed for this work in the manner described by Li et al. (2003). These include the discovery images (Sep. 24.5 and 25.4) as well as an additional detection on Sep. 29.5 (orange circles with asterisks in Fig. 2.2; also see Table 2.2). These detections indicate that SN 2005ek was discovered on the rise, while our P60 observations, beginning on Sep. 26.3, show a continued rise for at most one day before a very rapid decline.

2.2.5 FLWO Imaging

We supplement our photometry with the JHK data presented by Modjaz (2007; violet circles in Fig. 2.2). These data were obtained on the PAIRITEL telescope at the Fred Lawrence Whipple Observatory (FLWO) and are well sampled over the same time period as the P60 observations described above. In addition, Modjaz (2007) obtained an r'-band detection with the FLWO 1.2 m telescope on 2005 Nov. 5 (open orange circle; Fig. 2.2).

2.2.6 Swift UVOT Imaging

Swift-UVOT (Roming et al. 2005) observations of SN 2005ek were triggered beginning on 2005 Sep. 29. Seven epochs were obtained in the $uvw2$, $uvm2$, $uvw1$, u, b, and/or v filters over a time period of 20 days. The data were analyzed following the prescriptions of Brown et al. (2009) and photometry is based on the UVOT photometric system of Poole et al. (2008) with the sensitivity corrections and revised UV zeropoints of Breeveld et al. (2011). All data are listed in Table 2.3. The $uvw2$-, $uvm2$-, $uvw1$-, and u-band data are shown in the inset of Figure 2.2, while the b- and v-band data are plotted as squares in the main panel. The flux from SN 2005ek appears to fall off in the blue, with only upper limits obtained in the UV bands. The spectral energy distribution (SED) of SN 2005ek will be examined in more detail in Section 2.3.5.

2.2.7 Optical Spectroscopy

Between 2005 Sep. 17 and 2005 Oct. 8, we obtained eight low-resolution spectra of SN 2005ek from the FAST spectrograph (Fabricant et al. 1998) on the FLWO 60-inch Tillinghast telescope, the Kast double spectrograph (Miller & Stone 1993) on the 3-m Shane reflector at Lick Observatory, the DEIMOS spectrograph (Faber et al. 2003) mounted on the Keck-II 10-m telescope, and the 9.2-m Hobby-Eberly Telescope (HET) at McDonald Observatory. Technical details for all of our spectroscopic observations are summarized in Table 2.4, and the epochs on which they were obtained are marked by dashed vertical lines in Figure 2.2.

Table 2.1. P60 Photometry

UT Date	MJD	B (err) mag	V (err) mag	R (err) mag	I (err) mag
2005 Sep. 26	53639.3	18.25 (0.02)	17.83 (0.02)	17.46 (0.01)	17.20 (0.02)
2005 Sep. 27	53640.3	18.38 (0.03)	18.03 (0.03)	17.41 (0.02)	17.13 (0.04)
2005 Sep. 28	53641.3	18.65 (0.02)	17.92 (0.01)	17.60 (0.01)	17.18 (0.02)
2005 Sep. 29	53642.2	···	···	17.69 (0.02)	···
2005 Sep. 30	53643.2	19.10 (0.05)	18.24 (0.02)	17.86 (0.01)	17.47 (0.03)
2005 Oct. 02	53645.3	19.71 (0.07)	18.66 (0.02)	18.18 (0.01)	17.71 (0.02)
2005 Oct. 03	53646.5	20.07 (0.07)	18.93 (0.02)	···	···
2005 Oct. 05	53648.0	···	19.48 (0.06)	18.83 (0.03)	18.13 (0.06)
2005 Oct. 06	53649.2	20.67 (0.04)	19.63 (0.03)	19.03 (0.02)	18.26 (0.02)
2005 Oct. 07	53650.4	20.90 (0.04)	19.86 (0.03)	19.26 (0.02)	18.51 (0.02)
2005 Oct. 08	53651.3	21.05 (0.04)	19.98 (0.04)	19.48 (0.02)	18.61 (0.02)
2005 Oct. 09	53652.5	···	20.35 (0.05)	19.75 (0.04)	18.74 (0.03)
2005 Oct. 11	53654.2	21.74 (0.12)	20.60 (0.08)	20.08 (0.05)	19.01 (0.05)
2005 Oct. 12	53655.2	···	20.74 (0.10)	···	···
2005 Oct. 13	52656.2	···	20.88 (0.08)	20.47 (0.08)	19.47 (0.06)
2005 Oct. 14	53657.2	···	21.22 (0.13)	···	···

Table 2.2. KAIT/P200 Photometry

UT Date	MJD	Telescope	Filter	mag (err)
2005 Sep. 18	53631.5	KAIT	clear	$\lesssim 19$
2005 Sep. 24	53637.5	KAIT	clear	17.82 (0.08)
2005 Sep. 25	53638.4	KAIT	clear	17.64 (0.09)
2005 Sep. 29	53642.5	KAIT	clear	17.82 (0.07)
2005 Oct. 11	53654.9	P200	g'	21.02 (0.01)
2005 Oct. 11	53654.9	P200	r'	20.28 (0.01)
2005 Oct. 11	53654.9	P200	i'	19.96 (0.01)
2005 Dec. 05	53709.5	P200	g'	<22.7
2005 Dec. 05	53709.5	P200	r'	<22.3
2005 Dec. 05	53709.5	P200	i'	21.56 (0.03)

Table 2.3. UVOT Photometry

UT Date	MJD	*uvw*2 (err) mag	*uvm*2 (err) mag	*uvw*1 (err) mag	*u* (err) mag	*b* (err) mag	*v* (err) mag
2005 Sep. 28	53641.8	<20.6	<20.1	<19.8	···	···	18.10 (0.17)
2005 Sep. 29	53642.0	<20.5	<20.3	<20.2	···	···	···
2005 Sep. 29	53642.9	<20.6	···	···	19.28 (0.15)	18.97 (0.10)	18.40 (0.11)
2005 Sep. 30	53643.5	<20.9	<20.5	<20.2	19.10 (0.19)	19.24 (0.18)	18.48 (0.19)
2005 Oct. 06	53649.3	<21.1		<20.6	···	···	19.70 (0.22)
2005 Oct. 10	53653.5	<21.0	<20.5	<20.3	<19.8	< 19.8	<19.6
2005 Oct. 16	53659.9	<21.5	<19.7	···	···	···	<19.9

Table 2.4. Optical Spectroscopy

UT Date	MJD	Phase (d)[a]	Target	Telescope	Instrument
2005 Sep. 26	53639	-1	SN 2005ek	Shane 3-m	Kast
2005 Sep. 27	53640	0	SN 2005ek	Tillinghast 60-in	FAST
2005 Sep. 28	53641	+1	SN 2005ek	Tillinghast 60-in	FAST
2005 Sep. 30	53643	+3	SN 2005ek	Tillinghast 60-in	FAST
2005 Oct. 01	53644	+4	SN 2005ek	Tillinghast 60-in	FAST
2005 Oct. 03	53646	+6	SN 2005ek	Tillinghast 60-in	FAST
2005 Oct. 06	53649	+9	SN 2005ek	Keck-II	DEIMOS
2005 Oct. 08	53651	+11	SN 2005ek	HET	LRS
2011 Feb. 22	55614	···	UGC 2526	MMT	Blue Channel
2011 Feb. 23	55615	···	UGC 2526	MMT	Blue Channel

[a] With respect to *R*-band maximum light.

The spectra were reduced in the manner described by Matheson et al. (2008), Blondin et al. (2012), and Silverman et al. (2012). Standard IRAF routines were used to subtract the overscan region and flatfield the two-dimensional CCD frames using a combined and normalized flatfield image. One-dimensional spectra were extracted and wavelength calibrated using comparison lamps obtained immediately following each exposure. The FAST, Kast and DEIMOS spectra were flux calibrated utilizing a set of custom IDL routines which fit spectrophotometric standards to the data. In addition, these routines apply a small shift to the wavelength calibration after cross-correlating night-sky lines with a template night-sky spectrum, apply a heliocentric correction, and use the spectrophotometric standards to remove telluric absorption features from the SN spectra (see, e.g., Matheson et al. 2000). The HET spectrum was flux calibrated in IRAF and no telluric correction was made.

All eight spectra are displayed in the top panel of Figure 2.3, where the FAST and Kast spectra have been smoothed with windows of 11 Å and 7 Å, respectively. A thorough analysis of the spectroscopic features and evolution of SN 2005ek will be performed in Section 2.4. The spectra closely resemble those of the rapidly declining SN 2010X (bottom-left panel of Fig. 2.3).

We obtained two spectra of the host galaxy, UGC 2526, with the Blue Channel Spectrograph (Schmidt et al. 1989) on the 6.5-m MMT on 2011 Feb. 22 and 23. The first observation was positioned on the explosion site, while the second was on the galactic nucleus and aligned along the major axis of the galaxy. No strong nebular emission lines were detected in the explosion-site spectrum. Reduction, extraction, flux calibration, and telluric correction were performed in the manner described above, and the final spectrum centered on the galaxy nucleus is shown in the bottom-right panel of Figure 2.3. Weak,

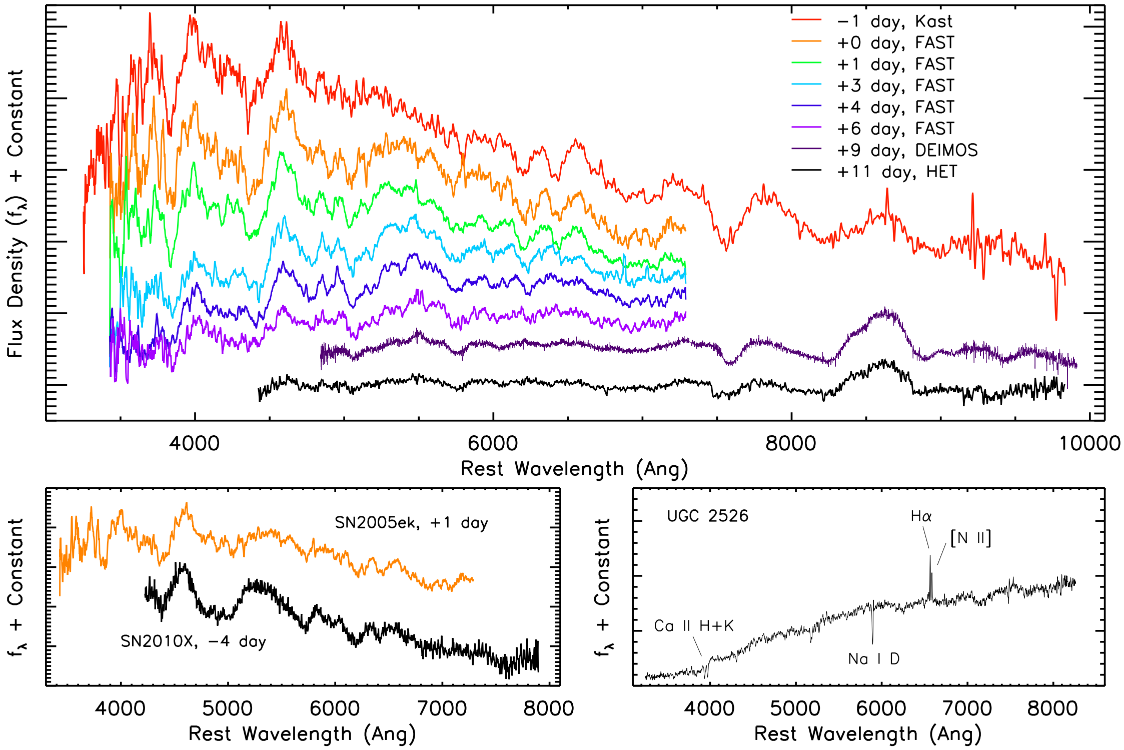

Figure 2.3.—: *Top*: Optical spectra of SN 2005ek (see text for details). FAST and Kast spectra have been smoothed with windows of 11 Å and 7 Å, respectively. *Lower left*: Comparison of the +1 day spectrum of SN 2005ek with the −4 day spectrum of SN 2010X (Kasliwal et al. 2010). *Lower right:* Spectrum of the host galaxy, UGC 2526. Major features are labeled.

narrow Hα and [N II] emission lines are evident, along with a red continuum.

2.2.8 Radio Observations

We observed SN 2005ek with the Very Large Array (VLA) on 2005 Sep. 29 under our Target-of-Opportunity program to study the nonthermal properties of local Type Ib/Ic supernovae[3] . At 8.46 GHz we did not detect a coincident radio source, and we place an

---

[3] VLA Intensive Survey of Naked Supernovae; VISiONS (Soderberg 2007).

upper limit of $F_\nu \lesssim 128$ μJy (2σ) on the flux density. At a distance of ~ 67 Mpc, this corresponds to a radio luminosity of $L_\nu \lesssim 7 \times 10^{26}$ ergs s^{-1} Hz^{-1}. This value is a factor of ~ 7 above the peak radio luminosity observed for the subluminous radio supernova SN 2007gr (Soderberg et al. 2010).

2.2.9 X-ray Observations

SN 2005ek was also observed with the X-ray Telescope (XRT; Burrows et al. 2005)) onboard *Swift* (Gehrels et al. 2004a) beginning on 2005 Sep. 28. The data were analyzed using the latest version of the HEASOFT package available at the time of writing (v. 6.13) and corresponding calibration files. Standard filtering and screening criteria were applied. All XRT data were coadded, resulting in a final 13 ks map spanning 19 days (median time of arrival = 7.44 days). No X-ray source is detected coincident with SN 2005ek with a 3σ upper limit of $F_x < 1.3 \times 10^{13}$ ergs s^{-1} cm^{-2} (unabsorbed, 0.3–10 keV energy band). The Galactic neutral hydrogen column density in the direction of the SN is 1.0×10^{21} cm^{-2} (Kalberla et al. 2005). At $D \approx 67$ Mpc this yields a 3σ limit on the luminosity of $L_\nu \lesssim 6.9 \times 10^{40}$ ergs s^{-1} Hz^{-1}. This value lies above the peak luminosity level for all but the most X-ray loud SN I at a similar time after explosion (e.g., SN 1998bw; Pian et al. 2000) .

2.3 Light-Curve Properties

2.3.1 Reddening

Reddening due to the Milky Way in the direction of UGC 2526 has a value of $E(B-V) = 0.210$ mag, according to the infrared dust maps of Schlegel et al. (1998). In order to estimate the host-galaxy contribution to the total reddening, we examine our spectra for evidence of narrow Na I D lines, which have been shown to correlate with extinction due to dust (Turatto et al. 2003; Poznanski et al. 2012). It is only in our highest signal-to-noise ratio (S/N) spectra (DEIMOS, +9 days) that we see weak Na I D absorption at the redshift of UGC 2526 with an equivalent width $\mathrm{EW}_{\mathrm{Na\ I\ D}} \sim 0.31$ Å. Using the empirical relation of Poznanski et al. (2012), this implies $E(B-V)_{\mathrm{host}} \approx 0.03$ mag. Given the low level of this inferred effect, combined with the uncertainties in the Na I D relation (e.g., Poznanski et al. 2011), we incorporate this value into our error budget for $E(B-V)_{\mathrm{tot}}$. Throughout this paper we adopt an $R_V = A_V/E(B-V) = 3.1$ Milky Way extinction curve with a total reddening value of $E(B-V) = 0.210^{+0.036}_{-0.006}$ mag.

2.3.2 Optical Light-Curve Evolution

In the left four panels of Figure 2.4 we display our *BVRI* light curves, normalized to peak magnitude and epoch along with the *BVRI* light curves for other SN I which have previously been referred to as fast or rapidly evolving (black circles). These include the rapid Type Ic SN 1994I (Richmond et al. 1996), the "calcium-rich" Type Ib SN 2005E (Perets et al. 2010), the SN 1991bg-like Type Ia SN 1998de (Modjaz et al. 2001), and the extremely low-luminosity SN 2008ha (Foley et al. 2009, 2010; Valenti et al. 2009). Also

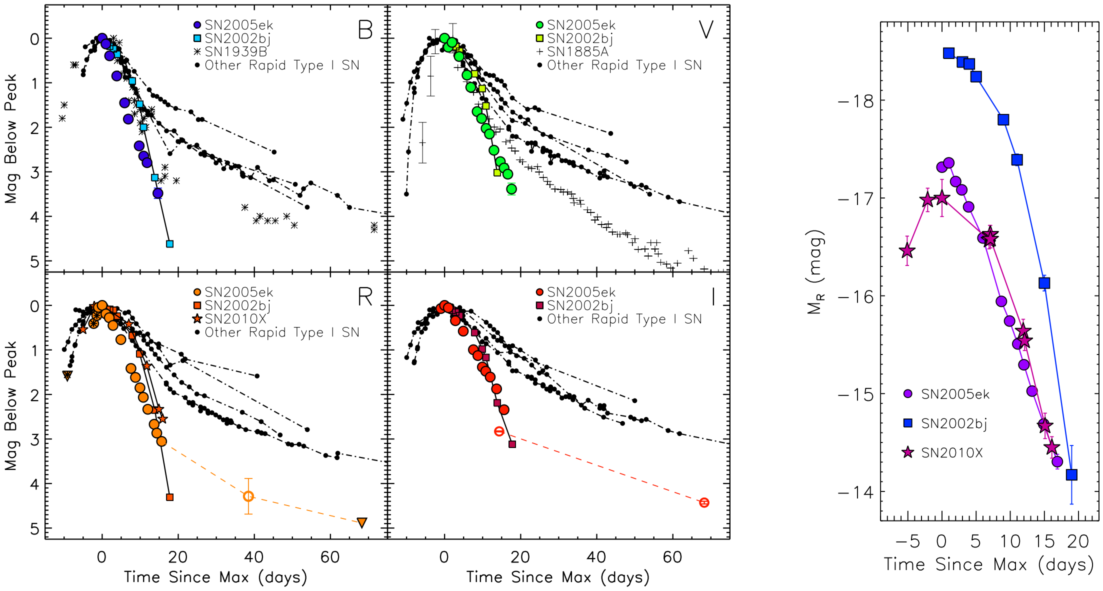

Figure 2.4.—: *Left:* Light curve of SN 2005ek (colored circles), normalized to peak magnitude/epoch and compared to other rapidly evolving supernovae of Type I. The other events are SN 1994I, SN 2008ha, SN 1998de, SN 2005E (black circles), SN 2002bj (colored squares), and SN 2010X (colored stars; *R*-band panel only). *Right:* *R*-band absolute magnitude light curves of SN 2005ek (purple circles), SN 2002bj (blue squares), and SN 2010X (magenta stars). When error bars are not visible they are smaller than the plotted points.

shown are SN 2010X (Kasliwal et al. 2010; colored stars), SN 2002bj (Poznanski et al. 2010; colored squares), SN 1885A (de Vaucouleurs & Corwin 1985; Perets et al. 2011; plus signs), and SN 1939B (Leibundgut et al. 1991; Perets et al. 2011; asterisks).

From Figure 2.4 it is clear that SN 2005ek is an outlier even among rapid Type I supernovae, decaying by $\gtrsim 3$ mag in 15 days and showing an unusually linear decline immediately post-maximum. However, our final r' and i' detections do show evidence for a change in slope around 20–30 days post-maximum. We can place an upper limit of ~ 0.029 mag day^{-1} on the late-time i'-band slope of SN 2005ek by comparing the two P200 i' detections. Both the timing of this transition and the late-time slope are comparable to those of the other rapid SN I plotted in Figure 2.4, although SN 2005ek decays by 1–2 mag more before settling onto this late-time tail.

Basic properties for the $BVRIJHK$ bands are given in Table 2.5. We find the R-band peak epoch by fitting a low-order polynomial to the P60 R-band light curve supplemented with the Lick unfiltered photometry (which most closely mimics and is calibrated to the R band; Li et al. 2003). This yields a peak epoch (MJD) of 53639.9 ± 0.3 day. Unless otherwise noted, all phases throughout this paper are in reference to R-band maximum. After correcting for distance and reddening we derive peak absolute $BVRI$ magnitudes ranging from -16.72 ± 0.15 (B band) to -17.38 ± 0.15 (I band). This places SN 2005ek at a peak optical magnitude very similar to SN 2010X and ~ 1.5 mag below SN 2002bj, SN 1885A, and SN 1939B. In the right panel of Figure 2.4 we compare the absolute R-band light curves of SN 2005ek, SN 2010X, and SN 2002bj.

In order to quantify the rapid decline of SN 2005ek we calculate the time over which the magnitude declines by a factor of e^{-1} (τ_e), the number of magnitudes the light curve declines in the first 15 days past maximum (Δm_{15}), and the linear decline rate in magnitudes per day. The first two quantities are calculated by linearly interpolating our data, and are measured with respect to the observed peak magnitude/date. The decline rates are estimated from linear least-square fits to the data between +2 and +16 days. Uncertainties for all properties listed in Table 2.5 were estimated using a Monte Carlo technique to produce and analyze 1000 realizations of our data[4].

Our best constraint on the rise time of SN 2005ek comes from the nondetection in

---

[4] Each data point in each realization is a random variable chosen from a normal distribution with a mean and variance determined by its counterpart in our initial data set.

Table 2.5. Basic Photometric Properties

Band	$m_{\mathrm{obs,max}}$[a] (mag)	$M_{\mathrm{abs,max}}$[b] (mag)	Δm_{15} (mag)	Decline Rate[c] (mag day^{-1})	τ_e[d] (day)
B	18.25 (0.02)	-16.72 (0.15)	3.51 (0.13)	0.24 (0.01)	4.7 (0.1)
V	17.83 (0.02)	-16.96 (0.15)	2.79 (0.07)	0.22 (0.01)	6.9 (0.1)
R	17.41 (0.02)	-17.26 (0.15)	2.88 (0.05)	0.21 (0.01)	6.3 (0.1)
I	17.13 (0.04)	-17.38 (0.15)	2.13 (0.06)	0.15 (0.01)	8.5 (0.2)
J	17.10 (0.09)	-17.26 (0.17)	1.17 (0.50)	0.11 (0.01)	9.6 (0.5)
H	16.85 (0.10)	-17.45 (0.18)	1.62 (0.77)	0.09 (0.01)	12.6 (0.7)
K	16.49 (0.10)	-17.78 (0.18)	2.51 (1.12)	0.09 (0.02)	10.2 (0.9)

[a] Not corrected for Milky Way extinction.

[b] Corrected for Milky Way extinction and assuming no host-galaxy extinction.

[c] As measured by a linear fit between +2 and +18 days (from *R*-band maximum).

[d] Time for light-curve to decline by a factor of $1/e$.

a LOSS search image obtained on Sep. 18.5 (only $\sim$ 9 days before the observed R-band maximum). Despite this relatively short time frame, the upper limit of $\sim$ 19 mag only moderately constrains the explosion epoch (Figure 2.2). We can infer that SN 2005ek rose slightly faster than its initial decline.

One of the most distinctive features of SN Ia is the tight correlation between light-curve peak magnitude and decay rate. This is in stark contrast to SN Ib/Ic, which have been shown to fill a large portion of this parameter space (Drout et al. 2011). In Figure 2.5 we plot peak absolute magnitude versus Δm_{15} for SN 2005ek and other supernovae of Type I.

The left panel of Figure 2.5 displays these values as measured in the B band, which allows for a comparison with the well-studied Phillips (1993) relation for normal SN Ia (Phillips et al. 1999; grey shaded region and solid black line) and the steeper relation found by Taubenberger et al. (2008) (dark blue points and dashed black line) for "fast" SN Ia, as well as SN 1939B. Also shown in this panel are the literature sample of SN Ib/Ic from Drout et al. (2011) (red points), the SN Iax sample from Foley et al. (2013) (light blue points), and several other peculiar Type I events. The right panel, measured in the R band, allows for a comparison to the full sample of SN Ib/Ic from Drout et al. (2011) as well as SN 2010X (for which r was the only well-sampled band obtained). We also include SN 1885A which was observed in a photographic band which most closely resembles modern day V-band. SN 2005ek falls well outside the phase space covered by normal SN Ib/Ic and is inconsistent with a simple extrapolation of either of the two SN Ia scaling relations.

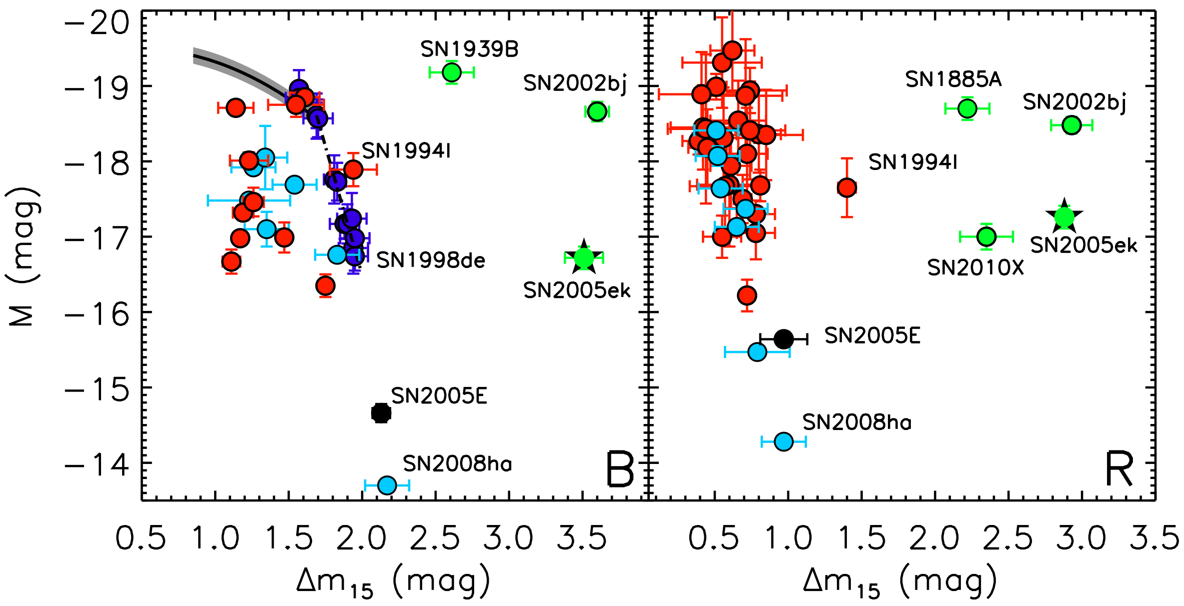

Figure 2.5.—: Absolute magnitude versus Δm_{15} for a variety of SN in the *B* band (left panel) and *R* band (right panel). Normal SN Ia are represented by a black line and shaded region. SN 1991bg-like SN Ia are shown in dark blue, SN Iax are shown in light blue, SN Ib/Ic are shown in red, SN 2005E is shown in black, and SN 2002bj, SN 2010X, SN 1885A, SN 1939B and SN 2005ek are shown in green. SN 2005ek is highlighted by a star. Note the observations obtained for SN 1885A are actually closer to modern day V-band. Objects plotted in Figure 2.4 are labeled.

2.3.3 Color Evolution

In Figure 2.6 we plot the $B-V$, $V-R$, and $R-I$ colors for SN 2005ek, along with the color evolution for other rapidly evolving events. Also displayed is the Lira relation (Phillips et al. 1999) which describes the remarkably similar $B-V$ color evolution for SN Ia between 30 and 90 days past *V*-band maximum (dashed line; top panel). In the middle panel we also show the SN Ib/Ic template color curve from Drout et al. (2011) (grey shaded region). Drout et al. (2011) demonstrated that dereddened SN Ib/Ic show a very similar $V-R$ color evolution with a minimum dispersion at $\sim$ 10 days post-maximum.

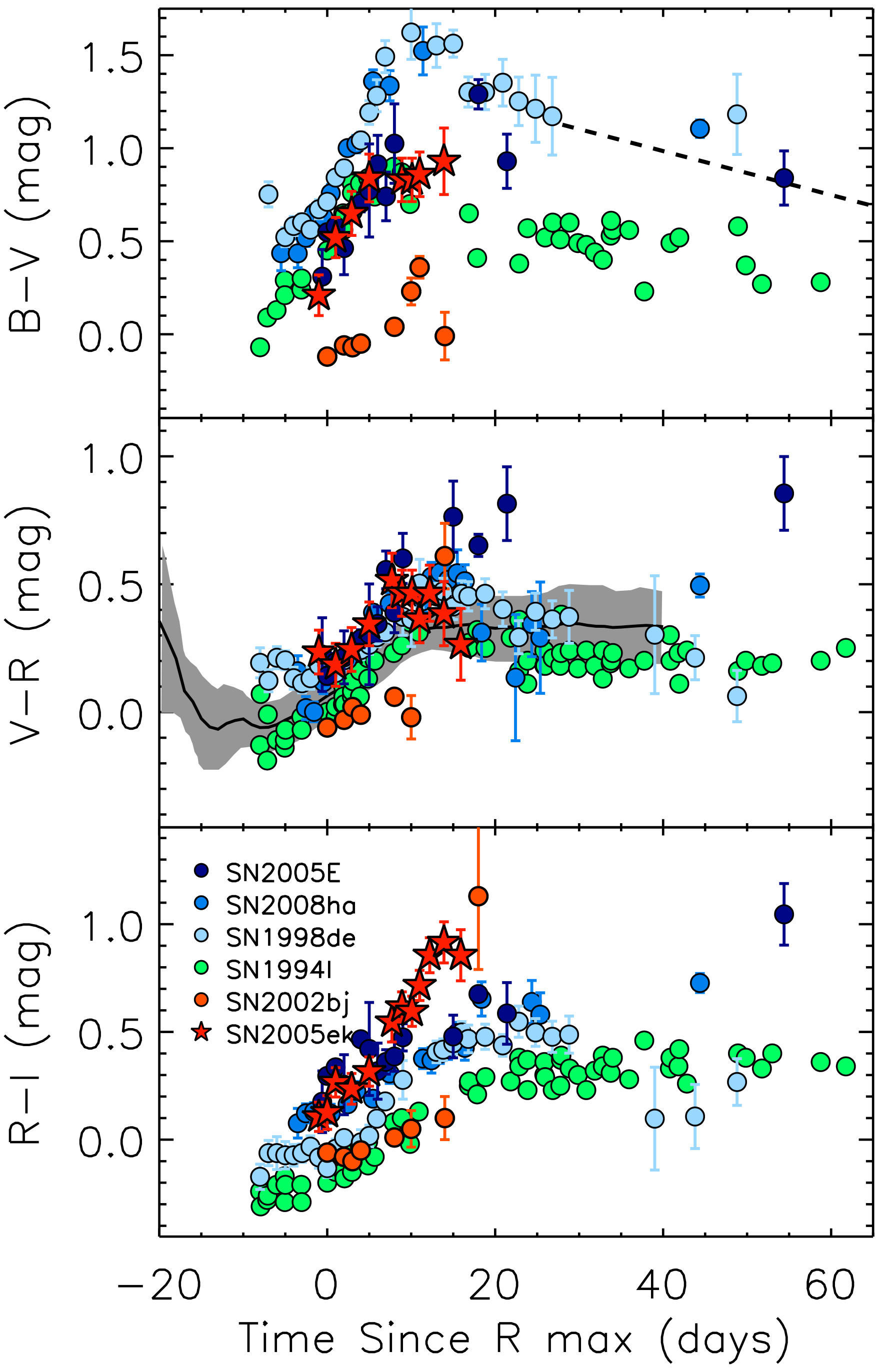

Figure 2.6.—: $B-V$, $V-R$, and $R-I$ color evolution for SN 2005ek (stars) and other rapidly evolving SN (circles). See text for details.

In the first ~ 20 days post-maximum, the $B - V$ and $V - R$ colors of SN 2005ek appear consistent with those of other rapidly evolving SN I: they exhibit a steady reddening with time and tentative evidence for the onset of a plateau between ~ 10 and 15 days. Although the $R - I$ colors of SN 2005ek also show a steady reddening, they do so at a much steeper rate than the other events displayed in Figure 2.6. Because this unusual evolution is present only in $R - I$, it cannot be fully explained by a rapid cooling of the SN ejecta, but must be caused, in part, by a strong spectroscopic feature. Indeed, from Figure 2.3 we see that by +9 days the emission component of the Ca II near-IR triplet (which falls solidly inside the I band) has grown substantially.

Although the colors of SN 2005ek are broadly consistent with those of other SN I, they vary substantially from those of SN 2002bj. SN 2002bj appears much bluer than any other object in $B - V$ and actually shows very little color evolution in either $V - R$ or $R - I$ until the final epoch, when it drastically reddens.

2.3.4 Spectral Energy Distribution

In Figure 2.7 we plot the UV-optical-IR spectral energy distribution (SED) of SN 2005ek from Sep. 30 (3 days post-maximum). Like many SN I near maximum brightness, the SED of SN 2005ek peaks in the optical. Blackbody fits to various portions of the SED yield temperatures clustered around 7000 K (Fig. 2.7, red curve). This likely represents a lower limit on the true temperature due to the strong UV line blanketing produced by iron-peak elements in the spectra of SN I (see, e.g., Mazzali & Lucy 1993; Bongard et al. 2008). Detailed modeling of the photospheric spectra reveals an ionization temperature of 9000–10,000 K near maximum brightness (Section 2.4).

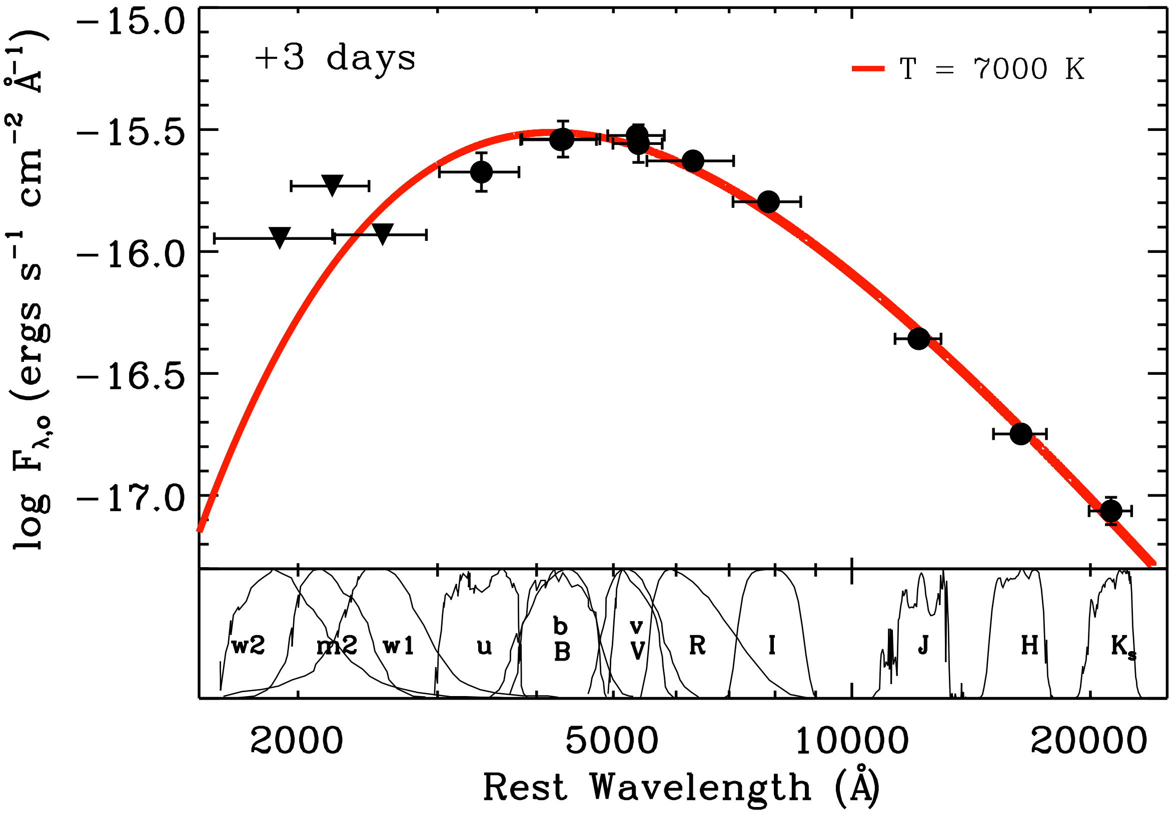

Figure 2.7.—: UV through IR spectral energy distribution of SN 2005ek at three days post-maximum. Upper limits are indicated as triangles and bandpass shapes are shown in the lower panel. The best-fitting 7000 K blackbody is shown as a red line.

2.3.5 Pseudo-Bolometric Light Curve

To construct a pseudo-bolometric light curve we sum our observed $BVRIJHK$ data by means of a trapezoidal interpolation and attach a blackbody tail with a temperature and radius found by fitting a Planck function to the data. For epochs where we do not possess JHK data we add a factor to our summed $BVRI$ data such that the total IR contribution ranges from $\sim 20\%$ near maximum to $\sim 40\%$ at the end of our observations (Valenti et al. 2007). We do not include a UV correction as our *Swift* UV observations contain only upper limits. Using this method, we find a peak bolometric luminosity of

$(1.2 \pm 0.2) \times 10^{42}$ ergs s^{-1} and a total radiated energy between -1 and $+16$ days of $(8.2 \pm 0.3) \times 10^{47}$ ergs.

We also use the r'-band detection at +38 days and the i'-band detection at +68 days to place constraints on the late-time pseudo-bolometric evolution of SN 2005ek. First, we sum the observed flux at each epoch over the width of the appropriate filter to yield estimates for the minimum bolometric luminosity at +38 and +68 days. Second, by comparing the luminosity contained in our P200 $r'i'$-band observations at +15 days to our inferred bolometric luminosity at that epoch, we find that at +15 days the r' and i' bands contained $\sim 15\%$ and $\sim 14\%$ of the bolometric luminosity, respectively. We use this fact to estimate a maximum pseudo-bolometric luminosity at +38 and +68 days under the assumption that the r' and i' contributions to the total luminosity will continue to increase. The true bolometric luminosity likely lies closer to the higher of these two constraints.

In Figure 2.8 we plot our pseudo-bolometric light curve of SN 2005ek (red stars) along with the pseudo-bolometric light curves of SN 1994I (Richmond et al. 1996), SN 2008ha (Moriya et al. 2010), SN 2002bj (Poznanski et al. 2010), SN 2010X (Kasliwal et al. 2010), SN 2005E, and SN 1998de. These last two were constructed in the manner described above from the photometry of Perets et al. (2010) and Modjaz et al. (2001). The bolometric curve of SN 2010X was constructed by computing νF_ν in the r band. A similar analysis of SN 2005ek yields a pseudo-bolometric curve which is broadly consistent with our analysis above, but declines slightly more rapidly. The hatched region in Figure 2.8 represents our constraints on the late-time pseudo-bolometric evolution of SN 2005ek.

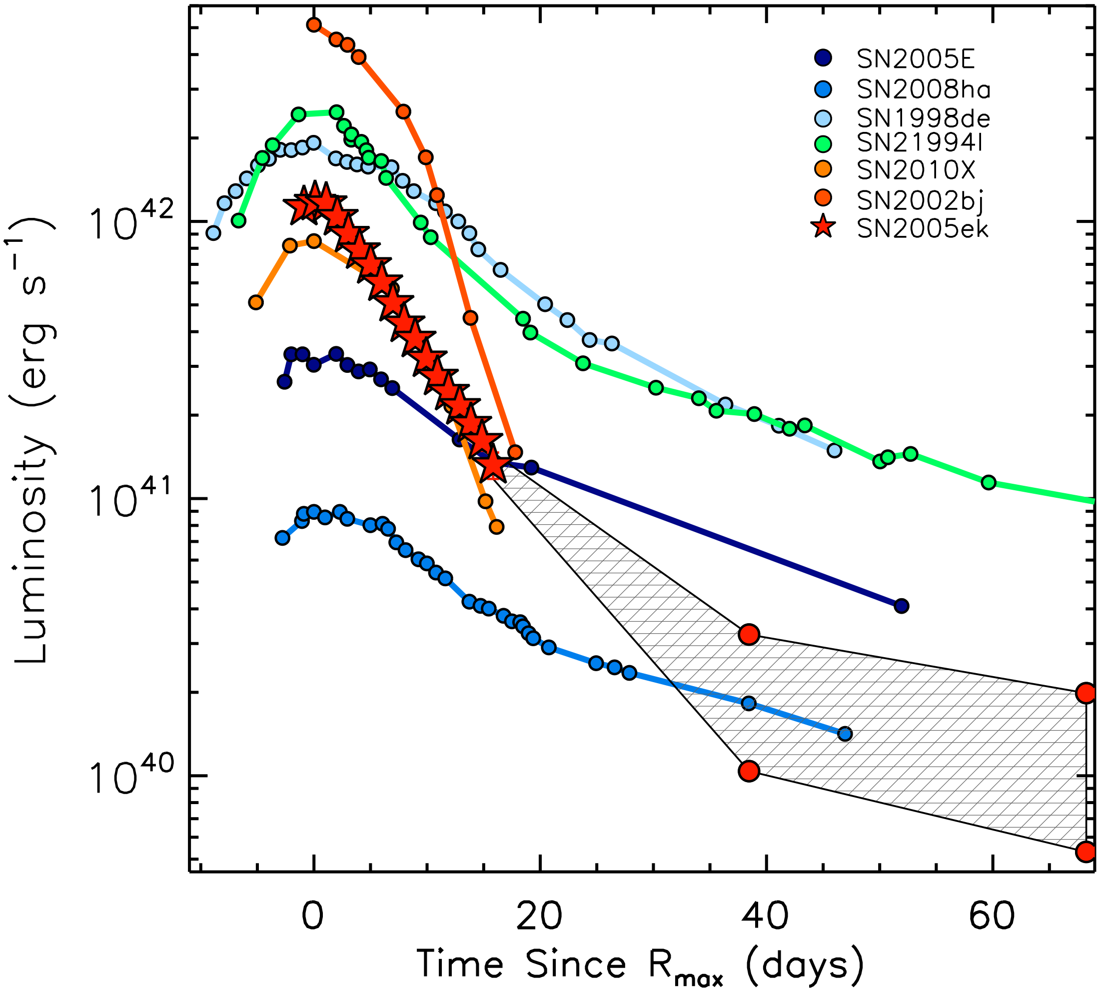

Figure 2.8.—: Pseudo-bolometric light curve for SN 2005ek (red stars) along with those of several other rapidly evolving supernovae (circles). The red circles show our constraints on the late-time pseudo-bolometric luminosity of SN 2005ek based on single-band detections. The hatched region is meant to guide the eye.

2.4 Spectroscopic Properties

The spectra of SN 2005ek shown in Figure 2.3 show considerable evolution over a short time period, and most closely resemble those of normal SN Ic. In Figure 2.9 we compare the maximum-light and transitional[5] spectra of SN 2005ek to a set of SN Ic (SN 2010X, SN 1994I, SN 2007gr, and SN 2004aw). SN 2005ek reaches the transitional phase much faster than the other events but the spectroscopic similarities at both epochs are clear. Of the events displayed in Figure 2.9, only SN 2010X decays on a timescale similar to that of SN 2005ek. The others possess $\Delta m_{15,R}$ values ranging from ~ 1.4 (SN 1994I) to ~ 0.4 (SN 2004aw).

In this section, we examine the spectroscopic properties and evolution of SN 2005ek utilizing two modeling techniques. Initial line identifications and estimates of photospheric velocities were made with the spectral synthesis code SYN++ (Thomas et al. 2011)[6]. This analysis offers information about the ions present in a particular ionization state and spectral range, allowing one to cover a large parameter space with minimal time and computational resources. In addition, we model a subset of the spectra using a one-dimensional Monte Carlo radiative transport code developed for SN outflows (Mazzali & Lucy 1993; Lucy 1999; Mazzali 2000), which allows quantitative assessments of ion abundances to be made. Using the results of both techniques, we compare several distinctive spectroscopic features of SN 2005ek to those of other SN I and comment on the consequences for explosive nucleosynthesis.

---

[5] “Transitional” refers to the transition from optically thick to thin, which, in this case, we characterize by an increased prominence of the emission component of the Ca II near-IR triplet)

[6] This is an updated version of SYNOW; https://c3.lbl.gov/es/ .

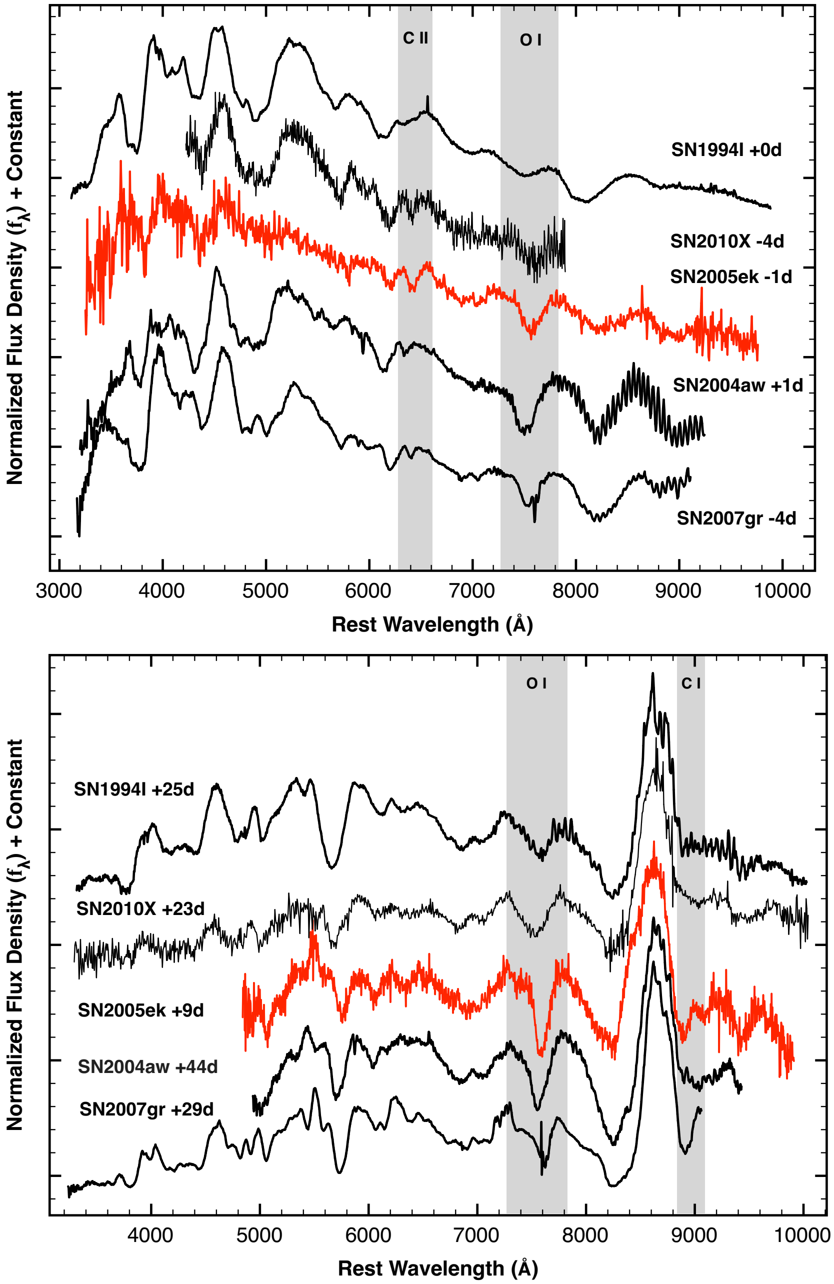

Figure 2.9.—: Comparison of SN 2005ek (red) and other well-studied SN Ic (black; SN 1994I, SN 2004aw, SN 2007gr, and SN 2010X). Strong similarities are seen. *top:* Near maximum light. The regions around C II λ6582 and O I λ7774 are shaded. *bottom:* Transitional spectra. The region around O I λ7774 and C I λ9095 are shaded.

2.4.1 SYN++ Evolution and Photospheric Velocities

SYN++ is a parameterized spectral synthesis code which allows empirical fitting of SN spectra without *a priori* assumptions of the ejecta's density and composition structure. It operates under the assumption of spherical symmetry, homologous expansion (radius proportional to velocity), a sharp photosphere, and a pseudo-blackbody continuum level. Line formation is due to pure resonant scattering (treated using the Sobolev approximation) and Boltzmann statistics are utilized to determine the relative line strengths for a given ion. For more details, see Branch et al. (2002), and Thomas et al. (2011).

In Figure 2.10 we show three representative SYN++ fits, covering the evolution of SN 2005ek between −1 and +9 days. Major spectroscopic features are labeled. In all cases, the excitation temperature was set to 10,000 K and we chose an exponential form for the optical depth profile. The photospheric velocity used in these fits ranges from ~ 9000 km s^{-1} (day −1) to ~ 7000 km s^{-1} (day +9).

The near-maximum-light spectra of SN 2005ek can be modeled with a combination of O I, C II, Mg II, Si II, Ca II, Ti II, and some Fe II at 8000–9000 km s^{-1}. S II is also included, although evidence for it is very weak. Between the −1 day and maximum-light models Na I was added to describe the feature near 5700 Å. In Figure 2.11 we present the individual ion components of the maximum-light model. Also displayed (blue, lower panel) is a model constructed from the same set of ions for the −4 day spectrum of SN 2010X. This highlights the similarities between the spectra of SN 2005ek and SN 2010X and demonstrates that our fitting scheme is equally applicable to both events.

Despite growth in the emission component of the Ca II near-IR triplet, the +9

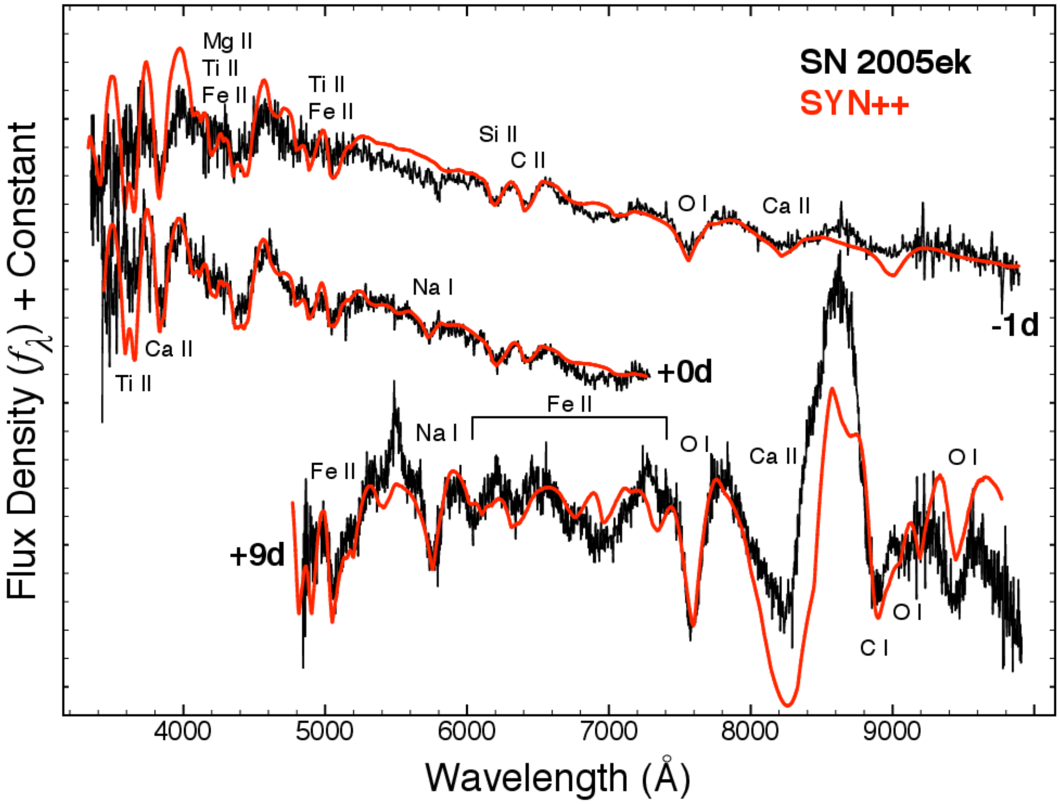

Figure 2.10.—: SYN++ model fits to the −1 day, maximum-light, and +9 day spectra of SN 2005ek (red lines). Observed spectra are shown in black. Major spectroscopic features are labeled.

day spectrum of SN 2005ek still shows a partial environment of resonant-line scattering, indicating it can be approximately modeled with SYN++. By this epoch, the Si II and C II features found near maximum light have already faded. A majority of the features can be attributed to Fe II and O I, along with Na I, Ca II, and a decent fit to C I λ9095 (consistent with the presence of C II at earlier epochs) at $\sim$ 7000 km s^{-1}. SYN++ fits to the intermediate epochs are consistent with the decrease in velocity, increase in prominence of Fe II and Ti II features, and decrease in prominence of the C II and Si II features between the maximum-light and +9 day spectra.

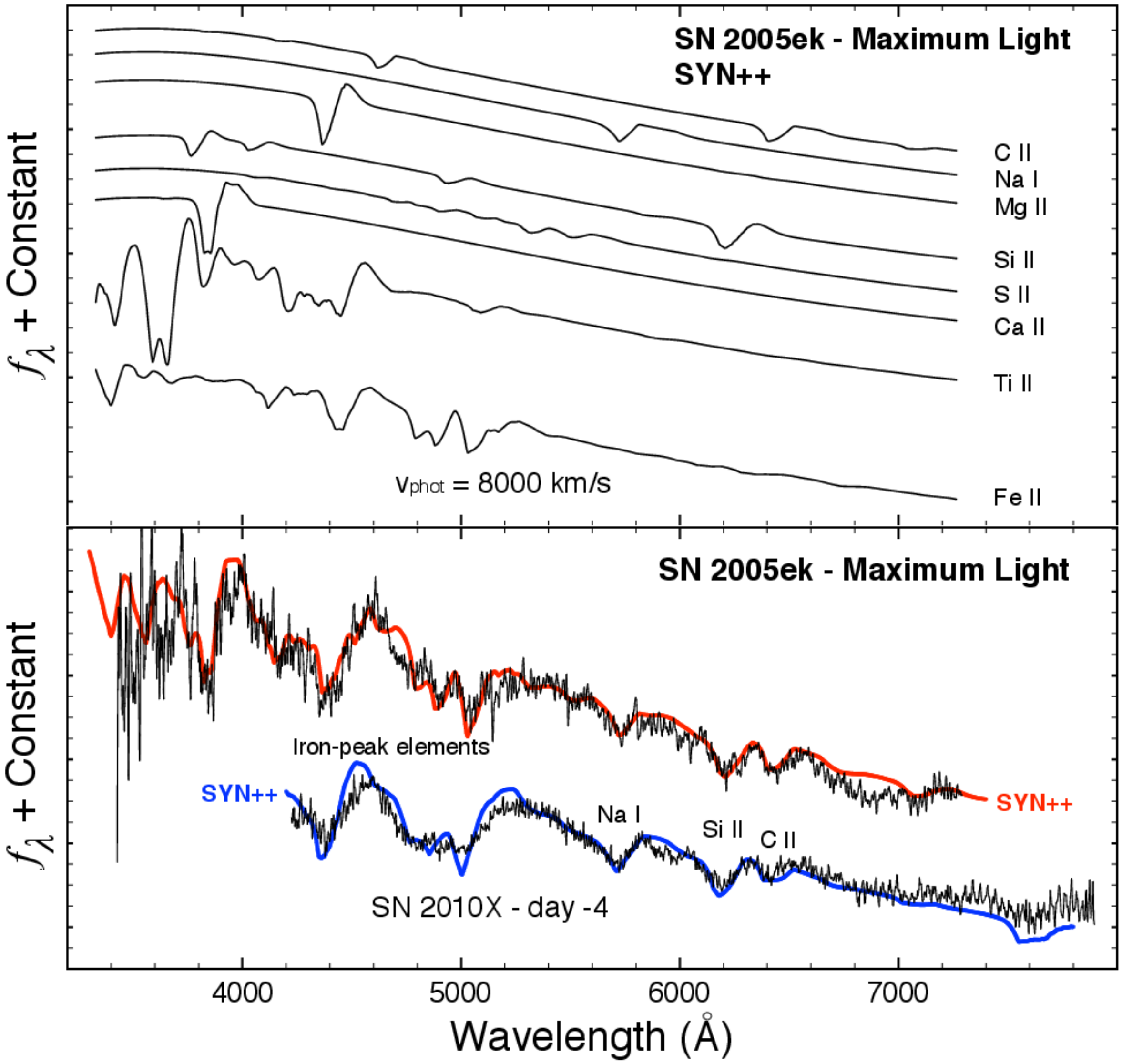

Figure 2.11.—: *top:* SYN++ model for the maximum-light spectrum of SN 2005ek, separated by ion. *bottom:* Full model (red) along with a similar model constructed for the −4 day spectrum of SN 2010X (blue). Observed spectra are shown in black.

2.4.2 Abundance Modeling

To obtain quantitative estimates of the elemental abundances present in the ejecta of SN 2005ek, we also model the −1 day, maximum-light, and +9 day spectra with the one-dimensional Monte Carlo radiation transport code described by Mazzali & Lucy (1993), Lucy (1999), and Mazzali (2000). The code assumes spherical symmetry and that radiation is emitted as a blackbody at a lower boundary (a pseudo-photosphere). The SN ejecta are defined by a run of density vs. velocity (an "explosion model") and a depth-dependent set of abundances. Energy packets are allowed to interact with the ejecta gas via excitation processes and electron scattering. The state of the gas is computed according to that of the radiation using a lambda iteration and adopting the modified nebular approximation (Mazzali & Lucy 1993), while the emerging spectrum is computed by formally solving the transfer equation in a final step (Lucy 1999; Mazzali 2000). This method has been successfully applied to both SN Ia (e.g., Mazzali et al. 2008) and SN Ib/Ic (e.g., Sauer et al. 2006).

In order to model the rapidly evolving spectra of SN 2005ek we first had to establish a reasonable explosion model. The fast light curve and moderate velocities indicate a small ejecta mass. We experimented with different possibilities, and found that a model with mass ~ 0.3 $M_\odot$ and $E_K \approx 2.5 \times 10^{50}$ ergs provides a reasonable match to the evolution of the spectra. The distribution of density with velocity resembles a scaled-down W7 model (Nomoto et al. 1984).

Using this model, and assuming a rise time of 14 days, we were able to reproduce the spectroscopic evolution of SN 2005ek (Fig. 2.12). As the photosphere recedes inward, each model epoch constrains a larger amount of the ejected material. With spectral

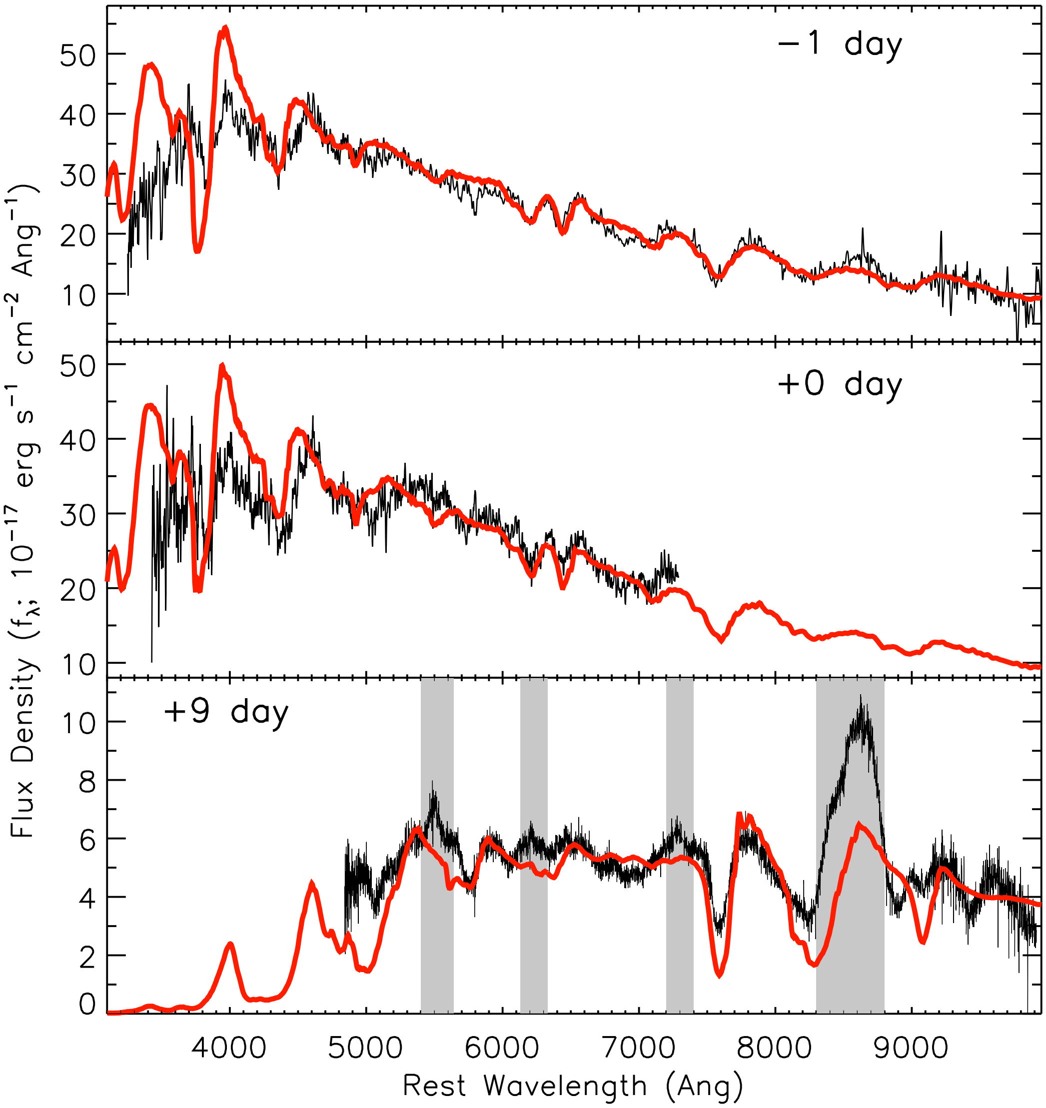

Figure 2.12.—: One-dimensional Monte Carlo radiation transport models for the −1 day (top panel), maximum-light (middle panel), and +9 day (lower panel) spectra of SN 2005ek. Observed spectra are shown in black, models in red. Regions showing excess with respect to the +9 day model, which may represent the onset of nebular features, are shaded (grey).

coverage out to +9 days we are able to probe the outer ~ 0.2 $M_\odot$ ($\sim 66\%$) of the ejecta.

The results are qualitatively consistent with the SYN++ line identifications given above. However, abundances do not necessarily correlate with line strength. Notably, the strength of the O I λ7774 line requires a high oxygen abundance, so that the composition is dominated by oxygen ($\sim$ 80%). Fe is present and is responsible for the absorption near 5000 Å, while Ti and Cr are also important for shaping the spectrum near 4000 Å, but small abundances are sufficient for this as well as for Ca, despite the strength of the near-IR triplet absorption. Smaller fractions of Mg, C, and Si are also present; Mg II lines leave a strong imprint in the earlier spectra, especially in the red (features at 8900 Å and 7600 Å, the latter in a blend with the stronger O I line), but also in the blue (4481 Å, which is the stronger contributor to the absorption near 4000 Å).

The composition shows little or no variation between the three epochs. The ejecta are dominated by oxygen ($\sim$ 86%), with intermediate mass elements such as C, Mg, Si, and limited amounts of S and Ca contributing $\sim$ 13.5% and iron-peak elements (Fe, Ni, Cr, Co, Ti) contributing only $\sim$ 0.5%.

2.4.3 Notable Spectroscopic Features

The ions utilized in the models above are typical of SN I. However, several features warrant further discussion in the context of SN 2005ek.

Carbon Features

The C II λ6582 feature near 6400 Å is noticeably prominent in the near-maximum-light spectra of SN 2005ek. Its strength is comparable to the Si II λ6355 feature. This is due in part to the relative weakness of the Si II feature, which, in the one-dimensional Monte

Carlo models presented above, is caused by a combination of the low overall Si abundance ($\sim 2\%$) and the relatively low-density environment. However, the strength of the C II feature is unusual in its own right, and it is still present several days post-maximum (Fig. 2.3).

In SN Ia, carbon features trace the distribution of unburned material from the carbon-oxygen (C-O) white dwarf. C II features are observed in ~30% of SN Ia although they are rarely either this strong or after maximum light (Howell et al. 2006; Thomas et al. 2007; Parrent et al. 2011; Silverman & Filippenko 2012; Folatelli et al. 2012). In general, the detection of carbon is also considered to be unusual in SN Ic. However, all the spectra shown in Figure 2.9 also show evidence for a notch in this region (highlighted in grey), exemplifying the spectroscopic similarity of these objects. This feature was specifically identified as C II in SN 2007gr (Valenti et al. 2008) and SN 2004aw (Taubenberger et al. 2006), while it is more debated in SN 1994I (Wheeler et al. 1994) where features are broader and, hence, more blended. In the bottom panel of Figure 2.9, we also highlight the region around the feature we identify as C I λ9095. A similar notch is seen in SN 2007gr. Note that despite the strength of the C II feature, the inferred carbon to oxygen abundance ratio is still small (~0.02).

Iron-Peak Features

In the −1 day spectrum of SN 2005ek the broad feature between 4600 Å and 5200 Å, attributed mainly to Fe II, is noticeably weaker than in the pre-maximum-light spectra of other SN Ic (top panel of Fig. 2.9). The depth of the feature does increase in later epochs (Fig. 2.3 and Fig. 2.13). Attempting to replicate this feature with other iron-peak elements produces less satisfactory model spectra.

The presence of a strong Ti II feature around 4400 Å is one of the distinctive spectroscopic features of the rapidly-declining SN 1991bg-like SN Ia. Although Ti II is also identified in the models above, the lack of a strong Si II absorption line (another distinctive feature of SN 1991bg-like SN) distinguishes SN 2005ek from these events.

Helium Features

None of the models presented above include helium. However, although its presence is not required, our data do not completely rule out its presence. Due to the similarity in wavelength of He I (λ5875, λ6678) to Na I λ5890 and C II λ6582, some ambiguity between ions can result (e.g., Kasliwal et al. 2010). In our case, the lack of features between 5200 Å and 5800 Å in the -1 day spectrum (see Fig. 2.9) would require any such helium features to have increased in strength after maximum light. This would not be inconsistent with our abundance models, where we required an increase in sodium abundance to model the Na I feature in the +9 day spectrum. However, He I is difficult to excite (Mazzali & Lucy 1998; Dessart et al. 2012), especially in relatively cool radiation fields like those of SN 2005ek, and we have no direct evidence for helium emission. We find that the lack of helium in our fits does not require the presence of aluminum as implied by Kasliwal et al. (2010). Rather, a majority of the SN features can be reproduced with a combination of Fe II and Na I.

Nebular Features

The +9 day spectrum of SN 2005ek appears to be transitional between the photospheric and nebular phases, with the Ca II near-IR feature significantly influenced by net emission. In addition, there are slight excesses with respect to both the SYN++ and Monte Carlo models near 5500 Å, 6300 Å, and 7300 Å (shaded regions, bottom panel, Fig. 2.12) which may be due to the emergence of [O I] $\lambda5577$, [O I] $\lambda\lambda6300, 6364$, and [Ca II] $\lambda\lambda7291, 7324$ in emission. This may represent the earliest onset of nebular features in a SN I observed to date.

2.4.4 Comparison to SN 2002bj

The decline rate of SN 2005ek is most closely matched by SN 2002bj and SN 2010X and in Figure 2.13 we compare the spectra of these three objects. While SN 2010X possesses very similar spectroscopic features at both early and late times (with moderately higher photospheric velocities), the spectroscopic similarities between SN 2005ek and SN 2002bj are less clear.

Poznanski et al. (2010) model SN 2002bj with SYNOW, finding that a majority of features can be fit with intermediate-mass elements (C, Si, S) and helium at the relatively low velocity of ~ 4000 km s^{-1}. Notably absent from their fit were any iron-peak elements. This is in stark contrast to the maximum-light spectra of SN 2005ek where both iron and titanium play a significant role, and sulfur is not required. Indeed, the first spectrum of SN 2002bj (top, Fig. 2.13) shows a significantly bluer continuum than any of the spectra obtained for either SN 2005ek or SN 2010X. This spectrum was obtained seven days post-maximum. By +11 days (when a second, lower quality, spectrum was

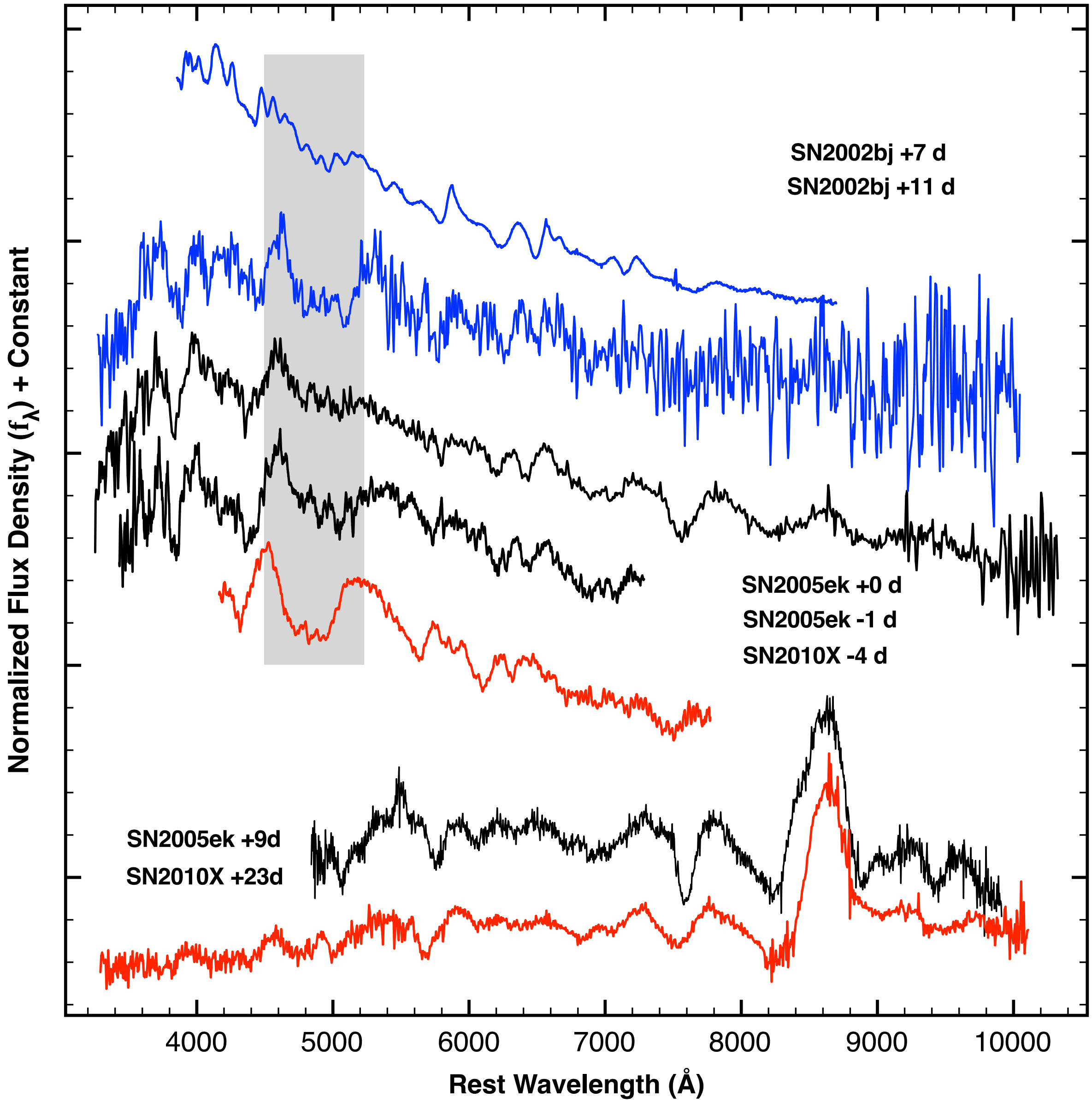

Figure 2.13.—: Comparison of SN 2005ek, SN 2010X, and SN 2002bj spectra. *top:* "Early"-time spectra. *bottom:* "Late"-time spectra. No spectra from a similar phase are available for SN 2002bj.

obtained), SN 2002bj appears to show a distinctly different morphology in the blue (Fig. 2.13). The continuum is more depressed in the region between 3000 Å and 5500 Å, with features that appear similar to those attributed to iron-peak elements in SN 2005ek. This spectroscopic evolution is clearly distinct from that of SN 2005ek and SN 2010X.

2.4.5 Consequences for Nucleosynthesis

The ejecta of SN 2005ek are dominated by oxygen. Unlike the "calcium-rich" objects, such as SN 2005E whose ejecta was $\sim 50\%$ calcium (Perets et al. 2010), this does not necessarily imply an unusual nucleosynthetic channel. Oxygen-dominated ejecta are common in models of SN Ic which are due to core collapse in a stripped C-O star. In that situation, the large oxygen abundance is due to a combination of the initial composition along with partial carbon burning. In contrast, producing oxygen-dominated ejecta via primarily helium burning (the mechanism invoked in the ".Ia" scenario) is not straightforward. Perets et al. (2010) use a one-zone model to examine the explosive nucleosynthetic outputs of He, C, and O mixtures at several temperatures. None of their helium-dominated trials yield oxygen-dominated ejecta.

2.5 Power Source and Explosion Parameters

The optical light curves of normal SN Ia and SN Ib/Ic are powered mainly by the radioactive decay of ^{56}Ni. For SN 2005ek, the change in light-curve slope between +20 and +40 days (Figure 2.8) points to radioactive decay as a possible power source. However, the initial decay timescale as well as the almost linear post-maximum decline are unusual. In this section we examine whether a ^{56}Ni power source is consistent with the observations of SN 2005ek described above.

For the purposes of simplified analytic models, the bolometric light curves of SN Ib/Ic are usually divided into two regimes as follows. (a) The *photospheric phase*, when the optical depth is high and the shape of the light curve is dependent both on the rate of energy deposition and the photon diffusion time scale (Arnett 1982). In normal SN Ib/Ic, the effects of radiative transfer result in an initial post-maximum decline rate which is *slower* than $^{56}\mathrm{Ni} \rightarrow {}^{56}\mathrm{Co}$ decay (Drout et al. 2011). (b) The *nebular phase*, when the optical depth has decreased and the SN luminosity is determined by the instantaneous rate of energy deposition. Normal SN Ib/Ic enter this stage at a late epoch ($\gtrsim$ 60 days;Valenti et al. 2007) when the dominant energy source is expected to be $^{56}\mathrm{Co} \rightarrow {}^{56}\mathrm{Fe}$ decay. The late-time slope of SN Ib/Ic light curves are well matched by this decay rate when the effects of incomplete gamma-ray trapping are included (Clocchiatti & Wheeler 1997; Valenti et al. 2007).

The time when a SN will transition to the second of these two phases is determined in large part by the total ejecta mass and kinetic energy of the explosion. In SN 2005ek, both the small inferred ejecta mass ($\sim 0.3\ \mathrm{M}_\odot$) and the early onset of nebular spectroscopic features indicate that the assumption of optically thick ejecta may break down within a few days of maximum light, making the models of Arnett (1982) inapplicable. Further, we note that the early portion of the pseudo-bolometric light curve appears linear, and decays at a rate of 0.15 mag day^{-1}, comparable to the 0.12 mag day^{-1} given by $^{56}\mathrm{Ni} \rightarrow {}^{56}\mathrm{Co}$ decay. In Figure 2.14 we again plot the pseudo-bolometric light curve of SN 2005ek. Also shown are lines which describe the decay rate of $^{56}\mathrm{Ni} \rightarrow {}^{56}\mathrm{Co}$ and $^{56}\mathrm{Co} \rightarrow {}^{56}\mathrm{Fe}$.

With this early decay rate as motivation, we construct a model for the entire post-maximum pseudo-bolometric light curve of SN 2005ek based on the instantaneous rate of energy deposition from the $^{56}\mathrm{Ni} \rightarrow {}^{56}\mathrm{Co} \rightarrow {}^{56}\mathrm{Fe}$ decay chain. The model is similar to the nebular phase model of Valenti et al. (2007), although we allow for incomplete trapping of the gamma-rays produced from $^{56}\mathrm{Ni} \rightarrow {}^{56}\mathrm{Co}$ decay. One effect of incomplete trapping at this early phase is that the light curve should decay by a larger number of magnitudes before settling onto the ^{56}Co tail. This prediction is in good agreement with our comparison of SN 2005ek to other SN I in Section 2.3.2 (see Fig. 2.4).

Under these assumptions, the luminosity of the SN can be modeled as (Valenti et al. 2007, Sutherland & Wheeler 1984, Cappellaro et al. 1997; we use the notation of Valenti et al. 2007)

$$L(t) = S^{\mathrm{Ni}}(\gamma) + S^{\mathrm{Co}}(\gamma) + S^{\mathrm{Co}}_{e^+}(\gamma) + S^{\mathrm{Co}}_{e^+}(\mathrm{KE}),$$

where the four terms describe the energy due to gamma-rays from nickel decay, gamma-rays from cobalt decay, gamma-rays from the annihilation of positrons created in cobalt decay, and the kinetic energy of positrons created in cobalt decay, respectively. These are given by

$$S^{\mathrm{Ni}}(\gamma) = \mathrm{M}_{\mathrm{Ni}}\epsilon_{\mathrm{Ni}}e^{-t/\tau_{\mathrm{Ni}}}(1 - e^{-F/t^2})$$
$$S^{\mathrm{Co}}(\gamma) = 0.81 \times \mathcal{E}_{\mathrm{Co}}(1 - e^{-(F/t)^2})$$
$$S^{\mathrm{Co}}_{e^+}(\gamma) = 0.164 \times \mathcal{E}_{\mathrm{Co}}(1 - e^{-(F/t)^2})(1 - e^{-(G/t)^2})$$
$$S^{\mathrm{Co}}_{e^+}(\mathrm{KE}) = 0.036 \times \mathcal{E}_{\mathrm{Co}}(1 - e^{-(G/t)^2}),$$

where

$$\mathcal{E}_{\mathrm{Co}} = \mathrm{M}_{\mathrm{Ni}}\epsilon_{\mathrm{Co}}(e^{-t/\tau_{\mathrm{Co}}} - e^{-t/\tau_{\mathrm{Ni}}}).$$

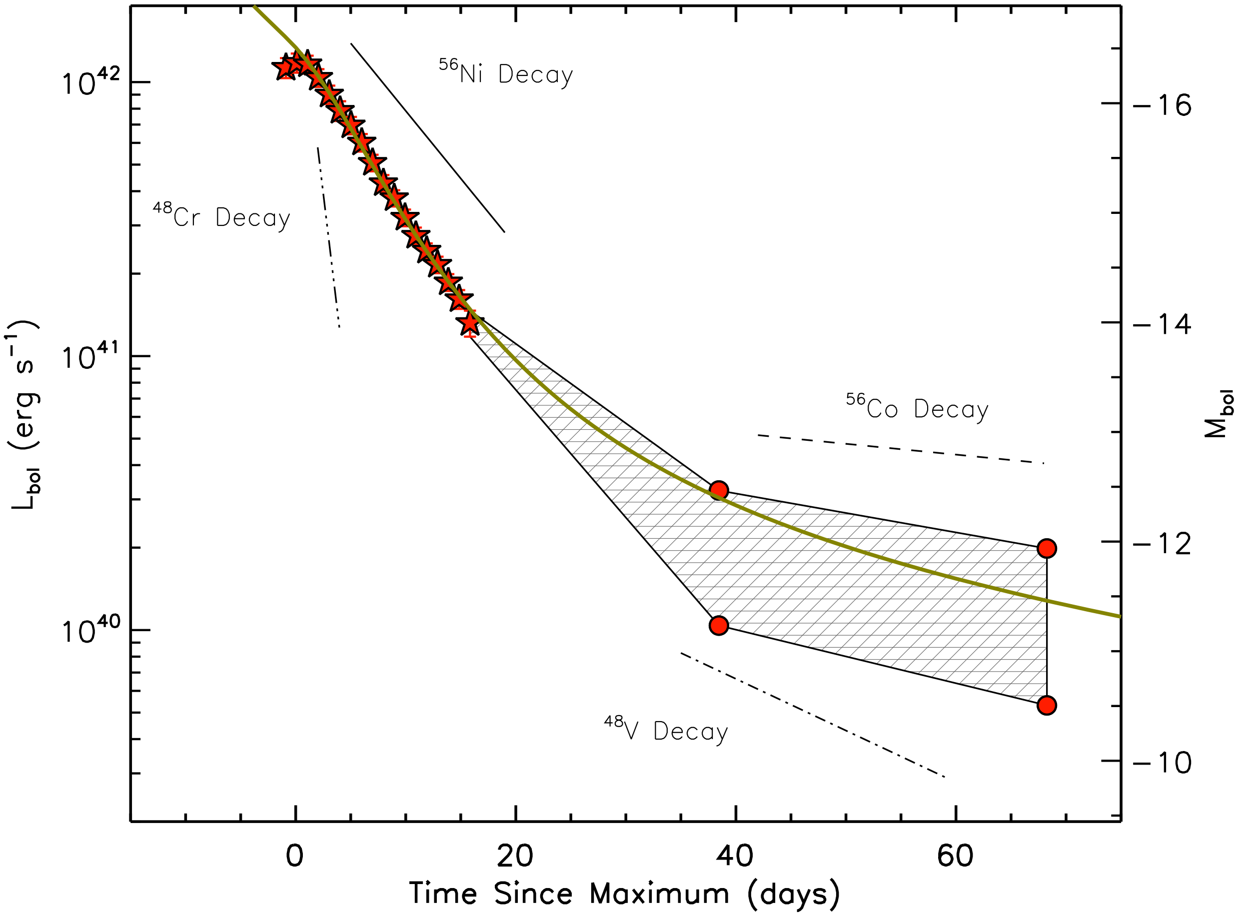

Figure 2.14.—: Radioactive models for the pseudo-bolometric light curve of SN 2005ek. Black lines show the decay rates for ^{56}Ni, ^{56}Co, ^{48}Cr, and ^{48}V, assuming full trapping of gamma-rays. The gold curve shows the best-fit model described in the text, assuming $\sim 0.03\ M_\odot$ of ^{56}Ni, a luminosity which tracks the instantaneous energy input, and incomplete gamma-ray trapping.

Table 2.6. Derived Explosion Parameters

Parameter	Unit	Value
$L_{\rm bol,peak}$	10^{42} ergs s^{-1}	1.2 ± 0.2
$E_{\rm rad}$[a]	10^{47} ergs	8.2 ± 0.3
$M_{\rm ej}$	$M_{\odot}$	0.3–0.7
E_K	10^{51} erg	0.25–0.52
M_{Ni}	$M_{\odot}$	0.02–0.03
$v_{\rm phot,max}$	km s^{-1}	8500 ± 500

[a] Emitted between −1 and +16 days.

The incomplete trapping of gamma-rays and positrons is incorporated with the terms $(1 - e^{-(F/t)^2})$ and $(1 - e^{-(G/t)^2})$. F and G are constants such that the gamma-ray and positron optical depths decrease by a factor proportional to t^{-2} as expected for an explosion in homologous expansion (Clocchiatti & Wheeler 1997) and are functions of the total ejecta mass, kinetic energy, and density distribution of the ejecta (Clocchiatti & Wheeler 1997). Using this model with $M_{\rm Ni} = 0.03$ M$_\odot$, $F = 12.8$ days, and G $\approx 16.1F$ (Valenti et al. 2007), we find the gold curve shown in Figure 2.14 which matches the early decay rate of SN 2005ek and is also consistent with our late-time constraints. Adopting the parameterization of Valenti et al. (2007) where $F \approx 32\ M_{\rm ej,\odot}/\sqrt{E_{K,51}}$, this value of F implies a $M_{\rm ej,\odot}/\sqrt{E_{K,51}} \approx 0.4$. Using the observed photospheric velocity near maximum (~ 8500 km s^{-1}), we can break the degeneracy between $M_{\rm ej}$ and E_K to yield explosion parameters of $M_{\rm ej} \approx 0.7$ M$_\odot$ and $E_K \approx 5.2 \times 10^{50}$ ergs. These values are a factor of two larger than those used in our spectroscopic modeling ($M_{\rm ej} = 0.3$ M$_\odot$ and $E_K = 2.5 \times 10^{50}$ ergs; Section 2.4.2), but given the number of assumptions required to extract explosion parameters from this simplified analytic model the two are relatively consistent. We adopt conservative estimates of the explosion parameters to be $M_{\rm ej} = 0.3$–0.7 M$_\odot$ and $E_K = 2.5$–$5.2\ \times 10^{50}$ ergs.

It has been suggested (e.g. Shen et al. 2010) that other radioactive decay chains such as ^{48}Cr $\rightarrow$ ^{48}V $\rightarrow$ ^{48}Ti, which possess shorter decay times than ^{56}Ni $\rightarrow$ ^{56}Co $\rightarrow$ ^{56}Fe, may contribute to the luminosity of rapidly evolving events. In Figure 2.14 we also include lines that represent the decay rates of ^{48}Cr $\rightarrow$ ^{48}V and ^{48}V $\rightarrow$ ^{48}Ti. The rapid ^{48}Cr decay time ($\tau_{\rm Cr} = 1.3$ days) implies that by a few days post-explosion the power input should already be dominated by ^{48}V $\rightarrow$ ^{48}Ti decay. Although photon diffusion likely plays a role at very early times, it is difficult to reconcile this power source with the change in light-curve slope observed between +20 and +40 days. In addition, in order to fit both of our late-time luminosity constraints with ^{48}V decay, we would require nearly full gamma-ray trapping (~ 0.05 mag day^{-1}, five times steeper than ^{56}Co), which is inconsistent with our low derived ejecta mass. Thus, although we cannot completely rule out some (especially early) contributions from other radioactive decay chains, we find that our observations are consistent with SN 2005ek being powered by the radioactive decay of ~ 0.03 M$_\odot$ of ^{56}Ni. We summarize this and our other inferred explosion parameters in Table 2.6.

2.6 Host Galaxy: UGC 2526

2.6.1 Global Properties

SN 2005ek exploded in the outskirts of UGC 2526, an edge-on spiral galaxy of morphology Sb. In Figure 2.15 we show the SED of UGC 2526, which was compiled from the SDSS (Ahn et al. 2012) and IRAS (Miville-Deschênes & Lagache 2005) catalogs and supplemented with upper limits from our radio observations described in Section 2.2. Also shown is an Sb model template from the SWIRE database (Silva et al. 1998). Using this template, we derive a star-formation rate (SFR) of $\sim$ 2–5 M$_\odot$ yr^{-1} (Yun & Carilli 2002; Kennicutt 1998). SN 2010X, SN 2002bj and SN 1885A also exploded in star-forming galaxies.

UGC 2526 has a low radio luminosity when compared to the Sb template which provides a best fit at other wavelengths. According to Chakraborti et al. (2012) this can be explained if electrons responsible for producing the radio synchrotron emission

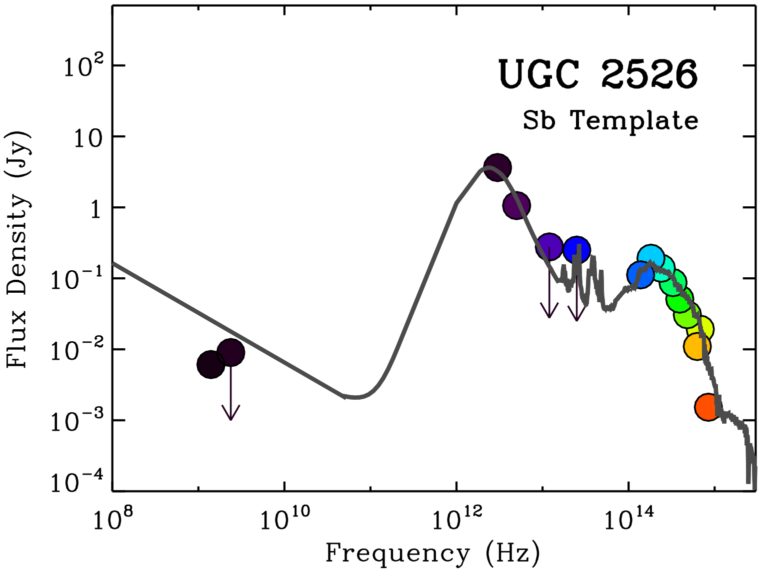

Figure 2.15.—: SED for UGC 2526 (circles) and the best-fit Sb galaxy model (grey line).

undergo significant inverse-Compton losses. Synchrotron and inverse-Compton losses are proportional to the energy density in magnetic fields and seed photons, respectively. The energy density of a characteristic Milky-Way-like magnetic field of $\sim 5\ \mu$G is $\sim 10^{-12}$ ergs cm^{-3}. We estimate that the bolometric luminosity of the host galaxy contributes an energy density of $\sim 3 \times 10^{-12}$ ergs cm^{-3} which could lead to significant inverse-Compton losses.

We measure the metallicity of UGC 2526 using our host-galaxy spectrum centered on the galaxy nucleus (Section 2.2). Hα and [N II] line fluxes were measured using the Markov Chain Monte Carlo (MCMC) technique described by Sanders et al. (2012) and, using the relations of Pettini & Pagel (2004), we find the metallicity of the UGC 2526 to be $12 + \log(\mathrm{O/H})_{\mathrm{PP04N2}} = 8.79 \pm 0.06$. This value is approximately solar[7].

---

[7] $12 + \log(\mathrm{O/H})_{\mathrm{solar}} = 8.69$ on the PP04N2 scale

This metallicity measurement may be affected by absorption from the underlying stellar population, although Hα should be relatively less affected than Hβ, resulting in a slight overestimation of the actual metallicity. For typical SN host galaxies the correction factor is on the order of 0.05 dex and in extreme cases ~ 0.2 dex. Additionally, the relatively high [N II] contribution suggests that the galaxy may be weakly active (probably a LINER; e.g., Ho et al. 1997).

2.6.2 Explosion-Site Properties

The explosion site of SN 2005ek is offset nearly 30 kpc ($1.5'$) in projection from the center of UGC 2526, which possesses a major diameter of $D_{25} \approx 69$ kpc. This places SN 2005ek at the extreme high end of the distribution of offsets seen for all SN subtypes (Prieto et al. 2008; Kelly & Kirshner 2012a), which is especially notable because SN Ib/Ic typically exhibit smaller offsets than SN II and SN Ia. This large offset, coupled with the observation of metallicity gradients in many spiral galaxies (Zaritsky et al. 1994), implies that the explosion-site metallicity is likely lower than the value we measured in the galaxy nucleus. In contrast, SN 2010X, SN 2002bj, and SN 1885A all exploded with low projected offsets (Kasliwal et al. 2010; Poznanski et al. 2010; Perets et al. 2011).

The lack of nebular emission lines in the explosion-site spectrum allows us to place a strict limit on the amount of star formation within the $1''$ slit (~ 0.3 kpc at the distance of UGC 2526). We measure a 3σ upper limit on the Hα line flux of 3.3×10^{37} ergs s^{-1}, which corresponds to an upper limit on the local SFR of 2.6×10^{-4} M$_{\odot}$ yr^{-1} (Eq. 2, Kennicutt 1998). While this value is an order of magnitude below the mean Hα flux measured for H II regions associated with core-collapse supernovae in the sample of

Crowther (2012), negligible Hα flux at the explosion site of a core-collapse supernova is not unprecedented. Only 21 of 39 supernovae in the Crowther (2012) sample show evidence for an associated H II region.

However, a much higher fraction of SN Ib/Ic are associated with H II regions compared to SN II ($70 \pm 26\%$ versus $38 \pm 11\%$; Crowther 2012). This trend may reflect the fact that massive stars with $M \lesssim 12$ M$_\odot$ (which are expected to explode as SN II) have lifetimes longer than the roughly 20 Myr lifetimes of giant H II regions. Thus, the lack of observed H II emission makes the explosion site of SN 2005ek more comparable to those of SN II and is consistent with a progenitor older than ~ 20 Myr.

2.7 Rates

SN 2005ek was discovered as part of the LOSS survey, which achieved a high level of completeness. From the LOSS data, Li et al. (2011) constructed volume-limited samples of Type Ia and core-collapse supernovae out to distances of 80 Mpc and 60 Mpc, respectively, which were used to derive relative rates for various SN subtypes. Although SN 2005ek was not included in this original analysis[8], we can use the LOSS data to obtain a rough estimate for the relative rate of SN 2005ek-like transients. SN 2002bj was also discovered by the LOSS survey, and we derive two sets of rates below, one of which assumes SN 2002bj and SN 2005ek are members of the same class of objects.

The LOSS volume-limited SN Ia sample contains 74 objects and is 99% complete to

---

[8] Its distance of 66 Mpc and classification as a SN Ic placed it just slightly outside the relevant sample volume (60 Mpc for core-collapse SN).

a distance of 80 Mpc. In order to estimate the incompleteness correction for SN 2005ek, we examine the correction factors for SN 2002dk and SN 2002jm, two SN 1991bg-like objects with peak magnitudes similar to that of SN 2005ek. Li et al. (2011) find that both objects are $\sim 97\%$ complete to a distance of 80 Mpc. This correction factor is based on a combination of peak magnitude and light-curve shape, and should therefore be taken as an upper limit for the completeness factor of the rapidly declining SN 2005ek. If the completeness factor of SN 2005ek lies between 50% and 100%, we may estimate that the rate of such transients is $\sim$ 1–2% of the SN Ia rate. If we include SN 2002bj in the same category of objects as SN 2005ek, this rate rises to $\sim$ 2–3% of the SN Ia rate. These rates should be taken as lower limits, and are consistent with those estimated by Poznanski et al. (2010) and Perets et al. (2011). It should also be noted that Poisson errors in this small number regime are large.

2.8 Possible Progenitor Channels

The observations and analysis presented above allow us to examine several possible progenitor models for SN 2005ek. SN 2005ek shows a very rapid post-maximum decline, a peak luminosity of $\sim 10^{42}$ ergs s^{-1}, colors which redden with time, and photospheric velocities which evolve from ~ 9000 km s^{-1} near maximum to ~ 7000 km s^{-1} at +9 days. Spectroscopic modeling reveals a small ejecta mass (0.3–0.7 M$_\odot$) which is predominantly oxygen ($\sim 85\%$), with smaller amounts of other intermediate-mass elements (Mg, C, Si) and an explosion kinetic energy of (2.5–5.0) $\times 10^{50}$ ergs. The pseudo-bolometric light curve is consistent with an explosion powered by ~ 0.03 M$_\odot$ of ^{56}Ni, assuming a non-negligible fraction of the gamma-rays escape at early times. This assumption is consistent with our low inferred ejecta mass and the emergence of nebular features at only 9 days post maximum light. Finally, both the large offset and low level of Hα emission from the explosion site of SN 2005ek are consistent with a progenitor older than ~ 20 Myr.

A robust progenitor model should be able to reproduce all of the above properties. In addition, if one accepts that the spectroscopic and compositional similarities between SN 2005ek and other normal SN Ic imply that they should have a common class of progenitors, the model should be capable of producing a variety of observed decline rates and ejecta masses. Possible progenitor channels can be divided into two classes: those involving a white dwarf (WD) or neutron star (NS) and those involving a massive star. We examine both below.

2.8.1 Degenerate Objects

Explosion models involving degenerate objects make attractive models for faint, rapidly evolving transients, as they naturally predict small ejecta masses. In addition, the old stellar environment of SN 2005ek is consistent with a progenitor system containing at least one degenerate object. Here we discuss several specific scenarios in the context of SN 2005ek: the accretion-induced collapse of a WD, a WD-NS or NS-NS merger, and the detonation of a helium shell on a low-mass WD.

Accretion-Induced Collapse (AIC)

Under certain circumstances, when an accreting WD nears the Chandrasekhar mass, electron capture may occur in its core, causing it to collapse to a NS rather than undergo a thermonuclear explosion (Nomoto & Kondo 1991). Modern simulations suggest that the subsequent bounce and neutrino-driven wind can lead to the ejection of a small amount of material, producing a weak, rapidly evolving transient powered by radioactive decay (e.g., Metzger et al. 2009; Darbha et al. 2010; Fryer 1999; Fryer et al. 2009). The observational properties of these AIC transients should vary if the AIC is caused by the merger of two WDs rather than the collapse of a single degenerate object.

The single-degenerate case is unlikely to produce a transient similar to SN 2005ek. The simulations of Dessart et al. (2006) predict ejecta masses and explosion energies of $\sim 10^{-2}$ $M_{\odot}$ and $\sim 10^{49}$ ergs, respectively, an order of magnitude below those inferred for SN 2005ek. This is evident in the far-left panel of Figure 2.16, where the theoretical light curves of Darbha et al. (2010; black lines) are significantly faster and fainter than those of SN 2005ek (red stars). In addition, the predicted velocities are on the order of $0.1c$, and a majority of the ejecta is likely processed to nuclear statistical equilibrium, implying a dearth of intermediate-mass elements (Darbha et al. 2010; Metzger et al. 2009; Fryer 1999).

An AIC due to the merger of two WDs may be "enshrouded" (Metzger et al. 2009) by ~ 0.1 $M_{\odot}$ of unburned material left in a remnant disk (Yoon et al. 2007). This material will be shock heated by the ensuing explosion, potentially synthesizing intermediate-mass elements, as well as slowing the initially rapid ejecta velocity. However, models of Fryer et al. (2009) suggest that this heating may lead to a transient which peaks in the UV bands, inconsistent with our observations of SN 2005ek.

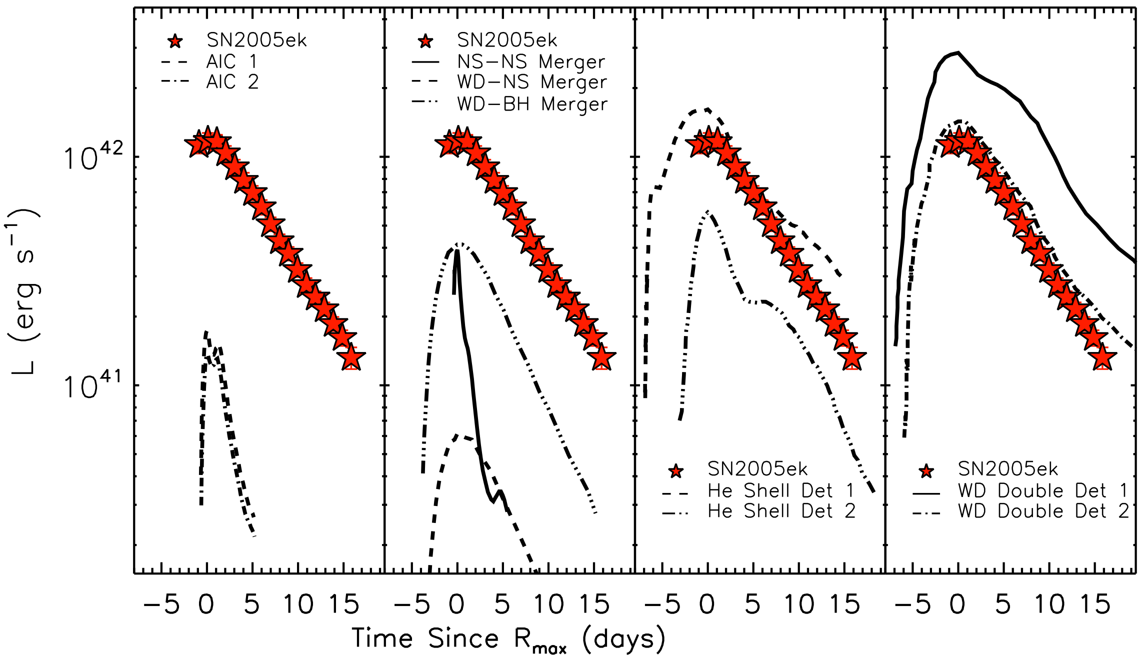

Figure 2.16.—: Comparison of the pseudo-bolometric light curve of SN 2005ek (red stars) to theoretical light curves. *far left:* Two AIC models from Darbha et al. (2010). Both models are calculated for $M_{\rm ej} = 10^{-2}$ M$_\odot$. *middle left:* The NS-NS merger from (Metzger et al. 2010), the WD-BH merger from (Metzger 2012), and the WD-NS merger from (Metzger 2012). *middle right:* Two ".Ia" models from (Shen et al. 2010). Models 1 and 2 represent the detonation of a 0.1 M$_\odot$ He shell on a 1.0 M$_\odot$ WD and a 0.05 M$_\odot$ He shell on a 1.2 M$_\odot$ WD, respectively. *far right:* Two edge-lit double-detonation models from Sim et al. (2012). Models 1 and 2 represent a 0.21 M$_\odot$ He shell on a 0.58 M$_\odot$ and 0.45 M$_\odot$ WD, respectively.

WD-NS/NS-NS Merger

Both NS-NS and NS-WD mergers have also been theorized to produce faint optical transients. In the former case, r-process nucleosynthesis is thought to occur during the ejection of neutron-rich tidal tails, yielding a rapidly evolving transient with peak luminosities between 10^{41} and 10^{42} ergs s^{-1} (Metzger et al. 2010; Roberts et al. 2011; solid line, center left panel of Figure 2.16). However, similar to the single-degenerate AIC scenario described above, the ejecta masses are lower ($\sim 10^{-2}$ M$_\odot$), ejecta velocities are higher ($\sim 0.1c$) and the nucleosynthetic yields are inconsistent (mainly r-process elements) with our observations of SN 2005ek. In addition, using improved r-process opacities Barnes & Kasen (2013) find that these transients may be fainter, longer lived, and significantly redder than previously hypothesized.

In contrast, the tidal disruption of a WD by a NS or BH yields a set of explosion parameters at least broadly consistent with those observed for SN 2005ek. By examining the evolution of and nucleosynthesis within the accretion disk formed during the disruption Metzger (2012) produce a set of models with ejecta masses between 0.3 and 1.0 $M_{\odot}$, ejecta velocities between 1000 and 5000 km s^{-1}, synthesized Nickel masses between 10^{-3} and 10^{-2} $M_{\odot}$, and peak luminosity between 10^{39} and $10^{41.5}$ ergs s^{-1}. The disruption of a larger WD yields a transient with a larger ejecta mass, expansion velocity, and nickel mass. Two example light curves are shown as dashed lines in the middle-left panel of Figure 2.16. Although the curves fall slightly below our observations (a consequence of the slightly lower inferred nickel mass) the shape is reproduced. In addition, because the outer layers of the disk do not burn to nuclear statistical equilibrium, the final ejecta composition is at least qualitatively consistent with our results for SN 2005ek (mainly O, C, Si, Mg, Fe, and S), although the exact compositional fractions may not be reproduced. In particular, in order to synthesize enough ^{56}Ni to power SN 2005ek, the current models would require a total ejecta mass greater than 1.0 $M_{\odot}$.

Helium-Shell Detonation

Finally, we examine the detonation of a helium shell on the surface of a WD, a model for which numerous theoretical light curves and spectra have been produced (e.g., Woosley et al. 1986; Shen et al. 2010; Fryer et al. 2009; Waldman et al. 2011; Sim et al. 2012) and which has been invoked to explain a number of unusual recent transients (e.g., SN 2005E, Perets et al. 2010; SN 2002bj, Poznanski et al. 2010; SN 2010X, Kasliwal et al. 2010; SN 1885A Chevalier & Plait 1988). The term ".Ia," which is often associated with this explosion mechanism, was used by Bildsten et al. (2007) to describe the specific case where the detonation occurs after mass transfer within an AM CVn binary system. In this case, the predicted helium-shell mass at the time of detonation is relatively small ($\lesssim 0.1$ $M_\odot$), which leads to a faint ($-15 > M_R > -18$ mag) and rapidly evolving transient. In the center-right panel of Figure 2.16, we show two ".Ia" model light curves from Shen et al. (2010). SN 2005ek falls comfortably between the two.

However, despite the similarity in light-curve morphology, the ".Ia" model in its basic form fails to reproduce the inferred abundances of SN 2005ek. The detonation of a predominately helium shell should yield ejecta dominated by calcium, iron-peak elements (especially titanium), and unburned helium, with a notable absence of other intermediate-mass elements (Shen et al. 2010; Perets et al. 2010). As discussed in Section 2.4.5, it is not straightforward to produce a high oxygen abundance from helium burning, and although calcium and titanium features are present in the spectra of both SN 2005ek and SN 2010X, these do not correspond to high abundances.

One possible reconciliation of these issues is if the helium-shell detonation triggers a second detonation within the C-O WD. Such "double-detonation" scenarios in solar-mass

WDs have been thoroughly investigated as a possible explosion mechanism for normal SN Ia. However, Sim et al. (2012) extend this analysis to low-mass WDs, considering both core-compression and edge-lit secondary detonations. In the former case significant amounts of iron-peak elements are synthesized and a much more slowly evolving light curve is produced. However, in the latter case the main modification to the observable parameters is the production of additional intermediate-mass elements. Depending on the precise abundances synthesized and amount of unburned C-O material ejected, it is possible that this scenario can explain most of the observational properties of SN 2005ek. In the far-right panel of Figure 2.16 we show two edge-lit models from Sim et al. (2012), demonstrating that they are capable of reproducing the morphology of SN 2005ek.

2.8.2 Massive Stars

In our above discussion, we found that both the edge-lit double detonation of a low mass WD and the tidal disruption of a WD by a NS could potentially explain the observed properties of SN 2005ek. However, as discussed in Section 2.4, SN 2005ek shows remarkable spectroscopic similarity to a number of normal SN Ic. If one assumes a single set of progenitors for these objects, and accepts their inferred ejecta masses (between 1 and 10 $M_{\odot}$; Mazzali et al. 2009, 2013), it is difficult to reconcile the data with a WD progenitor. We therefore now examine the possibility that the progenitor of SN 2005ek was a massive star.

The inferred ejecta mass and abundances provide some constraints on the pre-explosion mass and envelope density structure of any massive-star progenitor for SN 2005ek. With typical core-collapse SN producing a compact remnant having a mass

$\gtrsim 1.3$ M$_\odot$ (Fryer & Kalogera 2001), the ejecta of SN 2005ek would have only constituted a small fraction of the pre-explosion progenitor mass. At the same time, the presence of a small but non-negligible amount of Ni, Si, and Mg implies that a portion of the ejecta was nuclearly processed during the explosion. In this context, we discuss three potential massive-star explosion mechanisms for SN 2005ek: an iron core-collapse SN, an electron-capture SN, and a fallback SN.

Iron Core-Collapse SN

Stars with masses $\gtrsim 11$ M$_\odot$ are expected to proceed through silicon burning before undergoing an iron-core collapse at the ends of their lives. While some amount of fallback is expected in all core-collapse SN (Fryer 1999; Woosley & Heger 2002), for stars with initial masses $\lesssim 20$ M$_\odot$ the final remnant mass will be dominated by the mass of the iron core at the time of collapse (i.e., approximately the Chandrasekhar mass; we will examine the case of more significant fallback in Section 2.8.2). In this case, we would infer a pre-explosion mass for SN 2005ek of ~ 2 M$_\odot$. This may additionally apply for stars with initial masses around ~ 50 M$_\odot$ in the case of strong Wolf-Rayet winds (Woosley & Heger 2002; see their Fig. 16).

The environment of SN 2005ek makes the latter situation (a high-mass progenitor with exceptionally strong Wolf-Rayet winds) less likely. With a large offset from the center of its host (see Section 2.6) and the metallicity gradients common in spiral galaxies (Zaritsky et al. 1994), it is likely that SN 2005ek exploded in a low-metallicity environment. In this case, mass loss from massive stars should be reduced rather than enhanced (Vink et al. 2001). In addition, such a high-mass progenitor would necessarily be short lived, and the lack of Hα flux at the explosion site is more consistent with a lower-mass progenitor ($\lesssim$ 12 $M_\odot$; Section 2.6).

For a lower-mass progenitor, it would likely be necessary to invoke binary stripping as stars of this initial mass are not expected to strip their hydrogen envelopes via winds. This situation would be similar to that described by Nomoto et al. (1994) for SN 1994I. In that model, a star having an initial mass of $\sim$ 15 $M_\odot$ was stripped via binary interaction, yielding a C-O star of $\sim$ 2 $M_\odot$ which underwent core collapse. Recall that the spectra of SN 1994I closely resembled those of SN 2005ek (Fig. 2.9) and its decline rate was intermediate between SN 2005ek and the bulk of other SN Ib/Ic (Fig. 2.5). The ejecta mass Nomoto et al. (1994) derived for SN 1994I was 0.88 $M_\odot$, slightly larger than that inferred for SN 2005ek. Taken at face value, it would be necessary to invoke either a star having a smaller initial mass (only slightly above the lower limit for iron-core collapse, consistent with the host environment described above) or more extreme stripping to reproduce SN 2005ek.

In either case, we would expect the amount of radioactive material produced to be on the low side for SN Ib/Ic (due to the small amount of material at sufficient densities) and the composition to be dominated by oxygen, along with carbon and neon. Both predictions are well matched by our observations of SN 2005ek. The ejecta abundances we derive for SN 2005ek are very similar to those found for SN 2007gr (Mazzali et al. 2010) and SN 1994I (Sauer et al. 2006). If SN 2005ek is due to the iron-core collapse of a massive star, it exhibits one of the lowest kinetic energies (2.5–5.2 $\times 10^{50}$ ergs) and most extreme ratios of ejecta mass to remnant mass ($M_{\rm ej}/M_{\rm remnant} < 1.0$) ever observed. However, the inferred ratio of kinetic energy to ejecta mass is similar to that of other SN Ic ($E_{K,51}/M_{{\rm ej},\odot} \approx 1$).

Detailed modeling would be necessary to determine if the low kinetic energy inferred for SN 2005ek is consistent with what one would expect from the iron-core collapse of a stripped low-mass progenitor. Fryer & Kalogera (2001) argue that although stripping the hydrogen envelope from a massive star should not significantly impact the resulting explosion energy, the same may not be true if the stripping extends into the C-O core (as is the case for SN Ic). In deriving the distribution of remnant masses, Fryer & Kalogera (2001) assume an explosion energy which is proportional to the C-O core mass, an assumption which is qualitatively consistent with the low kinetic energy inferred for SN 2005ek.

Electron-Capture SN

If the progenitor of SN 2005ek was a relatively low-mass star, it is possible that the ensuing explosion was due to a (stripped) electron-capture SN rather than a traditional iron-core-collapse event. Stars within a narrow mass range ($\sim$ 8–10 $M_{\odot}$; Nomoto 1987; Woosley & Weaver 1980; Iben et al. 1997; Kitaura et al. 2006) are expected to undergo electron capture in their O-Ne-Mg core, decreasing pressure support, and causing the core to collapse to a NS (Nomoto 1987). Kitaura et al. (2006) have shown that the explosion proceeds in a similar manner to that of an iron-core-collapse SN (e.g., a delayed explosion driven by neutrinos), although a lower-energy explosion is produced and the density structure of the overlying material differs. The explosion energy found in the models of Kitaura et al. (2006) is $\sim 10^{50}$ ergs, comparable to the kinetic energy inferred for SN 2005ek. However, the envelopes surrounding O-Ne-Mg cores are expected to be relatively diffuse. This leads to an explosion which synthesizes only very small amounts of ^{56}Ni ($\sim 10^{-3}$; Kitaura et al. 2006; Bethe & Wilson 1985) and ejecta which show few signs of nuclear processing. On both these points, our observations of SN 2005ek are more consistent with a low-mass iron-core-collapse event than with an electron-capture SN.

Fallback SN

Alternatively, it is possible that the low ejecta mass of SN 2005ek is not caused by a low pre-explosion mass, but by a significant amount of fallback onto the proto-NS. Qualitatively, this is expected to occur when the binding energy of the outer envelope is high, although the actual fallback criteria are complex, depending on the evolution of the shock velocity within the envelope as well as parameters such as metallicity and rotation. It has been theorized that significant fallback should occur for stars with masses $\gtrsim 30$ $M_{\odot}$ (Fryer & Kalogera 2001; MacFadyen et al. 2001). Although the successful ejecta in such explosions can possess low kinetic energies (MacFadyen et al. 2001), events of this sort lacking a hydrogen envelope are expected to be quite faint, as a majority of the radioactive ^{56}Ni is synthesized in the inner portions of the ejecta (which fall back onto the proto-NS). The peak luminosity of SN 2005ek would likely require a non-negligible amount of mixing prior to fallback. Additionally, the environment-based arguments against a very massive progenitor for SN 2005ek (Section 2.8.2) still hold.

2.8.3 Applicability of Conclusions to Other Rapidly Declining Events

In the discussion above we found that SN 2005ek could potentially be explained by either the edge-lit double detonation of a low mass white dwarf, the tidal disruption of a WD by a NS, or the iron core-collapse of stripped massive star, with the latter option preferred if one takes the strong spectroscopic similarity of SN 2005ek to normal SN Ic to be an indication of a similar progenitor channel. However, we note that these conclusions may not broadly apply to all of the rapidly declining SN I in the literature to date. While SN2005ek, SN 2010X, SN 2002bj, SN 1885A, and SN 1939B all exhibit similar post-maximum decline rates and have low inferred ejecta masses ($\lesssim 0.3$ M$_\odot$), only SN 2010X possess a similar peak luminosity and spectroscopic evolution to SN 2005ek. SN 2002bj, SN 1939B, SN 1885 are all significantly ($\gtrsim 1.3$ mag) more luminous. Coupled with their fast decline rate it is unclear whether a similar modeling scheme evoked in Section 2.5 would produce a self-consistent solution for these events. SN 2002bj also shows significantly bluer colors, slower expansion velocities, and a distinct spectroscopic evolution near maximum. In addition while we argue that the explosion site of SN 2005ek does not rule out the possibility of a massive star progenitor (by analogy with with explosion sites of many SN IIP), SN 1939B exploded in an elliptical galaxy and SN 1885A (which exploded in the bulge of M31) shows no signs of a NS in its remnant (see, Perets et al. 2011). In short, while the conclusions above likely also apply to the rapidly-evolving SN 2010X, their validity with respect to SN 2002bj, SN 1885A, and SN 1939B is less clear. More detailed modeling will be required to distinguish various possibilities. Such modeling is currently underway for SN 2010X (Kleiser et al. *in prep.*).

2.9 Summary and Conclusions

We have presented the discovery and extensive multi-wavelength observations of the rapidly evolving Type I SN 2005ek. Here we summarize our main conclusions.

- Reaching a peak of $M_R = -17.3$ mag and declining by ~ 3 mag in the first 15 days post-maximum, SN 2005ek is one of the fastest declining SN I known thus far.

- Late-time photometric detections show a shallower decay timescale which is similar to the late-time evolution of other SN I.

- The spectra of SN 2005ek closely resemble those of other SN Ic in both morphology and velocity. However, SN 2005ek enters the optically thin phase at a much earlier epoch. We present evidence for the onset of nebular spectroscopic features at only 9 days post-maximum.

- The bolometric light curve of SN 2005ek peaks at $\sim 10^{41}$ ergs s^{-1}. Its evolution is consistent with an explosion powered by ~ 0.03 M$_\odot$ of ^{56}Ni, with incomplete gamma-ray trapping at early times.

- We estimate the ejecta mass and kinetic energy of SN 2005ek to be 0.3–0.7 M$_\odot$ and 2.5–5.2 $\times$ 10^{50} ergs, respectively.

- SN 2005ek exploded in a star forming galaxy, but with a large projected offset in an area lacking strong Hα emission.

- The ejecta of SN 2005ek are dominated by oxygen ($\sim$ 86%). Other intermediate-mass elements (C, Mg, Si, S, Ca) account for $\sim$ 13.5% of the ejecta, while iron-peak elements make up only 0.5%. These oxygen-dominated ejecta are inconsistent with the helium-shell detonation model (".Ia") which has previously been invoked to explain such rapidly declining events.

- Many of the observed properties of SN 2005ek could be explained by either the edge-lit double detonation of a low-mass WD or the tidal disruption of a WD by a NS. However, if we assume that the strong spectroscopic similarities between SN 2005ek and other normal SN Ic (with a wide range of decline timescales and inferred ejecta masses) to be an indication of a similar progenitor channel, a WD progenitor becomes very unlikely.

- Our observations and modeling of SN 2005ek are also consistent with the iron-core collapse of a low-mass star (12–15 $M_\odot$), stripped by binary interaction. In particular, the abundances derived are very similar to those found for other SN Ic. In this case, SN 2005ek may possess the most extreme ratio of ejecta mass to remnant mass observed for a core-collapse SN to date. The ratio of kinetic energy to ejecta mass is similar to that of other SN Ic.
- The rate of such rapidly declining SN I is at least 1–3% of the normal SN Ia rate.
- Based on their strong photometric and spectroscopic similarities, our conclusions likely also apply to the rapidly evolving Type I SN 2010X. However, despite their similar decline rates, there are several important observational differences between SN 2005ek and SN 2002bj, SN 1939B, and SN 1885A. More-detailed analysis will be required to determine if these three (more luminous) objects belong to the same class of explosions.

We thank L. Bildsten, K. Shen, and T. Janka for helpful discussions. We are grateful to the staffs at the numerous observatories where we gathered data. We kindly acknowledge Sung Park, Katsuki Shimasaki, and Tom Matheson for assisting in the acquisition of some of the observations presented here. We acknowledge useful conversations at a Sky House workshop.

MRD is supported in part by the NSF through a Graduate Research Fellowship. Support for this work was provided by the David and Lucile Packard Foundation Fellowship for Science and Engineering awarded to AMS. JMS is supported by an NSF Astronomy and Astrophysics Postdoctoral Fellowship under award AST-1302771. ASF acknowledges support from the US National Science Foundation (NSF) under grant SES 1056580.

This work was supported in part by the National Science Foundation under Grant No. PHYS-1066293 and the hospitality of the Aspen Center for Physics. We also acknowledge the hospitality of the Kavli Institute for Theoretical Physics and partial support by the National Science Foundation under Grant No. NSF PHY11-25915.

The W. M. Keck Observatory, which is operated as a scientific partnership among the California Institute of Technology, the University of California, and NASA; the observatory was made possible by the generous financial support of the W. M. Keck Foundation. Observations reported here were obtained at the MMT Observatory, a joint facility of the Smithsonian Institution and the University of Arizona. The Hobby-Eberly Telescope (HET), is a joint project of the University of Texas at Austin, the Pennsylvania State University, Stanford University, Ludwig-Maximilians-Universität München, and Georg-August-Universität Göttingen. The HET is named in honor of its principal benefactors, William P. Hobby and Robert E. Eberly. The Very Large Array is a facility of the National Science Foundation operated under cooperative agreement by Associated Universities, Inc. PAIRITEL is operated by the Smithsonian Astrophysical Observatory (SAO) and was made possible by a grant from the Harvard University Milton Fund, the camera loan from the University of Virginia, and the continued support of the SAO and UC Berkeley. We thank M. Skrutskie for his continued support of the PAIRITEL project.

The supernova research of A.V.F.'s group at U.C. Berkeley is supported by Gary & Cynthia Bengier, the Richard & Rhoda Goldman Fund, the Christopher R. Redlich Fund, the TABASGO Foundation, and NSF grant AST-1211916. KAIT and its ongoing work were made possible by donations from Sun Microsystems, Inc., the Hewlett-Packard Company, AutoScope Corporation, Lick Observatory, the NSF, the University of California, the Sylvia & Jim Katzman Foundation, and the TABASGO Foundation.

Chapter 3

Rapidly-Evolving and Luminous Transients from Pan-STARRS1

M. R. Drout, R. Chornock, A. M. Soderberg, N. E. Sanders, R. McKinnon, A. Rest, R. J. Foley, D. Milisavljevic, R. Margutti, E. Berger, M. Calkins, W. Fong, S. Gezari, M. E. Huber, E. Kankare, R. P. Kirshner, C. Leibler, R. Lunnan, S. Mattila, G. H. Marion, G. Narayan, A. G. Riess, K. C. Roth, D. Scolnic, S. J. Smartt, J. L. Tonry, W. S. Burgett, K. C. Chambers, K. W. Hodapp, R. Jedicke, N. Kaiser, E. A. Magnier, N. Metcalfe, J. S. Morgan, P. A. Price, C. Waters

The Astrophysical Journal, Vol. 794, No. 23, 2014

Abstract

In the past decade, several rapidly-evolving transients have been discovered whose timescales and luminosities are not easily explained by traditional supernovae (SN) models. The sample size of these objects has remained small due, at least in part, to the challenges of detecting short timescale transients with traditional survey cadences. Here we present the results from a search within the Pan-STARRS1 Medium Deep Survey (PS1-MDS) for rapidly-evolving and luminous transients. We identify 10 new transients with a time above half-maximum ($t_{1/2}$) of less than 12 days and $-16.5 > M > -20$ mag. This increases the number of known events in this region of SN phase space by roughly a factor of three. The median redshift of the PS1-MDS sample is z=0.275 and they all exploded in star forming galaxies. In general, the transients possess faster rise than decline timescale and blue colors at maximum light ($g_{P1} - r_{P1} \lesssim -0.2$). Best fit blackbodies reveal photospheric temperatures/radii that expand/cool with time and explosion spectra taken near maximum light are dominated by a blue continuum, consistent with a hot, optically thick, ejecta. We find it difficult to reconcile the short timescale, high peak luminosity ($L > 10^{43}$ erg s^{-1}), and lack of UV line blanketing observed in many of these transients with an explosion powered mainly by the radioactive decay of ^{56}Ni. Rather, we find that many are consistent with either (1) cooling envelope emission from the explosion of a star with a low-mass extended envelope which ejected very little (<0.03 $M_{\odot}$) radioactive material, or (2) a shock breakout within a dense, optically thick, wind surrounding the progenitor star. After calculating the detection efficiency for objects with rapid timescales in the PS1-MDS we find a volumetric rate of $4800 - 8000$ events yr^{-1} Gpc^{-3} ($4 - 7\%$ of the core-collapse SN rate at z=0.2).

3.1 Introduction

Modern supernova (SN) searches are expanding our knowledge of the phase space occupied by cosmic explosions (e.g., peak luminosity, timescale). High cadence surveys have led to the discovery of a variety of rapidly-evolving ($t_{1/2} \lesssim 12$ days) and luminous ($-15 > M > -20$) transients. These include the type Ic SNe 2005ek (Drout et al. 2013) and 2010X (Kasliwal et al. 2010), the type Ib SN 2002bj (Poznanski et al. 2010), the type IIn SN PTF09uj (Ofek et al. 2010), and the type Ibn SN 1999cq (Matheson et al. 2000), with the latter two showing signs of circumstellar interaction (see Filippenko 1997 for a review of traditional SN classifications).

The properties of these events are varied, and individual events have been hypothesized to be due to a wide number of explosion mechanisms/progenitors, including the explosion of a stripped massive star (Drout et al. 2013; Kleiser & Kasen 2014; Tauris et al. 2013), the detonation of a helium shell on a white dwarf (e.g. Shen et al. 2010; Perets et al. 2010), the shock breakout from a dense circumstellar shell (Ofek et al. 2010), and a super-Eddington tidal disruption flare (Cenko et al. 2012; Strubbe & Quataert 2009).

Since their discovery, the overall number of these rapidly-evolving transients has remained small. This is due to a relatively unknown combination of the true rate of such events and the inefficiency with which optical SN searches detect transients with very short timescales. Despite some success discovering transients at early times, many searches are still optimized for the detection of type Ia SN ($t_{1/2} \sim 20 - 30$ days). As a result, many rapidly-evolving transients are discovered around maximum light, and decay timescales are used as a proxy for overall timescale or rise time in explosion models.

Since rapidly-evolving transients probe the extremes of both explosion parameters and progenitor configurations, such assumptions can have an effect on the theoretical interpretation of these transients.

As such, obtaining a larger sample of rapidly-evolving events with well constrained rise and decline timescales would be beneficial for two reasons. First, the assumptions which go into many simplified analytic models for SN (e.g. Arnett 1982) break down at such short timescales. More detailed modeling of a larger number of transients is necessary to determine whether these events are extreme cases of progenitors/explosions we already know, or if they represent entirely new classes of transients. Second, the true rate at which these rapidly-evolving transients occur will influence our understanding of various stages of stellar evolution. Although rates have been estimated by several previous works (Drout et al. 2013; Perets et al. 2011; Poznanski et al. 2010), they are difficult to constrain when the sample size of known objects from any given survey is typically ~ 1.

The Pan-STARRS1 Medium Deep Survey (PS1-MDS) is well suited for this task because of its rapid cadence and multiple band coverage to a significant depth (~ 24 mag). In this paper we present the results from a search within the PS1-MDS survey data for rapidly-evolving and luminous transients with well constrained rise times. The search was designed to identify transients which persist for multiple rest-frame days, but have $t_{1/2} \lesssim 12$ days. We have identified 10 such objects in the duration of the survey (Oct 2009 - March 2014). This represents a significant increase ($\times$ 3) in the total number of transients that have been found in this portion of SN phase space.

The paper is structured as follows: In Section 3.2 we give a brief overview of the

PS1-MDS, describe the process by which we selected transients, and summarize our observations. In Sections 3.3, 3.4 and 3.5 we give an overview of our selected sample and describe their photometric and spectroscopic properties. In Section 3.6 we examine the host galaxies of the entire sample. In Section 3.7 we calculate volumetric and relative rates for these objects based on four years of the PS1-MDS and, finally, in Section 3.8 we discuss likely explosion mechanisms and progenitor systems for these events.

3.2 Observations and Sample Selection

3.2.1 PS1-MDS Overview

PS1 is a wide-field imaging system dedicated to survey observations. Located on Haleakala, Hawaii, it possesses a 1.8-m diameter primary mirror and a $3^\circ.3$ diameter field of view (Kaiser et al. 2010). The imager consists of an array of sixty 4800 × 4800 pixel detectors with a pixel scale of $0.''258$, providing an instantaneous field of view of 7.1 deg^2 (Tonry & Onaka 2009). Observations are obtained with a set of five broadband filters ($g_{P1}r_{P1}i_{P1}z_{P1}y_{P1}$, hereafter grizy$_{\rm P1}$) which are similar, although not identical, to those used by the Sloan Digital Sky Survey (SDSS; Ahn et al. 2012). Details of the filters and photometry system are given in Tonry et al. (2012) and Stubbs et al. (2010).

The PS1-MDS consists of 10 fields, each a single PS1 imager footprint, distributed throughout the sky. Approximately 25% of PS1 observing time is dedicated to revisiting the PS1-MDS fields on a nightly basis in griz$_{P1}$ to a 5-σ depth of $\sim$ 23.3 mag with a nominal cadence of 3 days in any given filter. In optimal observing conditions, $g_{\rm P1}$ and $r_{\rm P1}$ are observed on the same night with $i_{\rm P1}$ and $z_{\rm P1}$ observations following on consecutive evenings. y_{P1} is observed during times of full moon to a depth of $\sim$ 21.7 mag.

Initial reduction and processing of all PS1-MDS images are carried out with the PS1 Image Processing Pipeline (IPP; Magnier 2006; Magnier et al. 2008). This includes standard reductions, astrometric solution, and stacking of nightly images as well as source detection and photometry. The nightly PS1-MDS stacks are then transferred to the Harvard FAS Research Computing cluster where difference images are produced and potential transients identified by the `photpipe` pipeline (Rest et al. 2005, 2014). Potential transients are visually inspected for possible promotion to status of transient alert. This visual inspection acts to filter out false positives due to time varying trails from saturated sources and poorly subtracted galaxy cores (with obvious large-scale dipole patterns). Once a transient reaches alert status it is flagged for potential spectroscopic follow-up. Spectra are acquired for $\sim$10% of PS1-MDS alerts, with final selections left to the spectroscopic observers.

3.2.2 Rapid Transient Selection Criteria

As part of the normal operation of the PS1-MDS described above, we identified a number of transients that evolved on rapid timescales and reached peak luminosities associated with SN ($-16 > \mathrm{M} > -21$ mag). Objects identified in this way (i.e. flagged by a human operating the pipeline) are certainly useful for determining the properties of rapidly-evolving transients. However, calculating volumetric rates based on the number of transients identified in a survey requires a *well defined* set of selection criteria. To systematically identify objects that lie in this portion of transient phase space, we initiated a search within the $\sim$5000 transient sources discovered with the `photpipe` pipeline during the duration of the PS1-MDS. As a first cut, we required that the transient satisfy the following three criteria in a minimum of two photometric bands (all times are observer frame)[1].

1. The transient must rise by $\gtrsim 1.5$ mag in the 9 days immediately prior to observed maximum light.
2. The transient must decline by $\gtrsim 1.5$ mag in ~ 25 days post observed maximum.
3. The transient must be present ($> 3\ \sigma$) in at least three sequential observations. This criteria selects a unique population of transients than those discussed in Berger et al. (2013) (which possess timescales shorter than 1 day).

These criteria are motivated by the observed timescales of known SN and are intended to exclude the bulk of type Ia, type Ib/c and type II SN. In V-band, typical type Ia and type Ib/c SN will rise by $0.6 - 0.75$ mag in the 10 days immediately prior to maximum light and decline by $1.0 - 1.2$ mag in the 25 days post-maximum (Riess et al. 1999; Drout et al. 2011; Li et al. 2011). At higher redshifts PS1 will probe bluer wavelengths (which typically evolve more rapidly) but this will compete with the effects of time dilation. Many type II SN would easily pass the rise time requirement, but they decline by $\lesssim$0.5 mag in the 25 days post maximum (Li et al. 2011; Hamuy 2003). The most rapid type Ic SN (e.g. SN 1994I; Richmond et al. 1996) and most rapid SN1991bg-like type Ia SN (Taubenberger et al. 2008) would barely pass all three of our requirements if caught at maximum light. However, any given PS1 band is only observed

---

[1] A given photometric band must satisfy all three criteria in order to count towards the two required bands.

every three days and we require the same band to pass both our rise and decline cuts. We therefore expect our selected objects to evolve more rapidly than these events[2].

A number of known low-luminosity transients (nova, CVs, M dwarf flares, etc.) could pass these selection criteria if located within the Milky Way or a nearby galaxy. Thus, all objects that passed these initial criteria were then examined by eye in order to select objects that were likely of extragalactic origin. Objects were removed from consideration if their was a clear stellar source at the location of the transient. In several cases, spectra were obtained of rapidly-evolving transients which revealed Balmer lines in emission at zero redshift, indicating the transient was likely galactic. Our search identified a handful (∼10) of these low luminosity events. If a transient was either host-less, or exploded near a low signal to noise, unresolved, source (such that the stellar versus galactic nature of the host could not be robustly determined) it was kept in the sample and is discussed below.

In the end, by combining the results from this systematic search with results from the normal operation of the PS1-MDS pipeline, we identify 14 transients of interest. For ten of these transients we have obtained spectra of their underlying hosts, confirming their extragalactic origin. In Section 3.3 we provide an overview of the selected objects and divide them into three groups based on the quality of their light curves and constraints available for their distance. In the rest of this section we describe the observations obtained for all 14 transients.

---

[2] Consider a transient that barely passes our selection criteria (i.e. rises 1.5 mag in the 9 days prior to maximum light and declines 1.5 mag in the 25 days post maximum). If instead of observing exactly at maximum light we observe at +1 day then the transient will appear to rise slightly *less* than 1.5 mag in the 10 days prior to *observed* maximum. As a result, it will no longer pass our rise time selection criteria.

Table 3.1. Basic Observational Information

Event	Disc. Date	R.A.	Dec.	Redshift	d_{lum}	Effective Pivot Wavelength (Å)				$E(B-V)_{\mathrm{MW}}$
	(UT)	(2000)	(2000)		(Mpc)	g_{P1}	r_{P1}	i_{P1}	z_{P1}	
Gold Sample										
PS1-10ah	2010 Feb. 21	10:48:15.784	+57:24:19.48	0.074	330.5	4540.7	5772.9	7001.9	8068.3	0.008
PS1-10bjp	2010 Oct. 24	23:26:21.402	−01:31:23.11	0.113	518.6	4381.6	5570.6	6756.5	7785.5	0.049
PS1-11qr	2011 April 2	09:56:41.767	+01:53:38.25	0.324	1685.3	3683.3	4682.9	5679.8	6544.8	0.017
PS1-12bb	2012 Jan. 20	09:57:23.866	+03:11:04.47	0.101	459.7	4429.3	5631.3	6830.2	7870.4	0.026
PS1-12bv	2012 Jan. 20	12:25:34.602	+46:41:26.97	0.405	2192.2	3471.0	4412.9	5352.3	6167.5	0.010
PS1-12brf	2012 Oct. 10	22:16:06.892	−00:58:09.81	0.275	1393.6	3824.9	4862.8	5898.0	6796.3	0.084
Silver Sample										
PS1-11bbq	2011 Dec. 1	08:42:34.733	+42:55:49.61	0.646	3857.8	2962.8	3766.8	4568.7	5264.5	0.026
PS1-13duy	2013 Nov. 1	22:21:47.929	−00:14:34.94	0.270	1364.5	3839.9	4882.0	5921.9	6823.1	0.053
PS1-13dwm	2013 Nov. 5	22:20:12.081	+00:56:22.35	0.245	1220.8	3917.0	4980.0	6040.8	5960.1	0.054
PS1-13ess	2013 Dec. 26	02:22:09.428	−03:03:00.51	0.296	1517.2	3762.9	4784.0	5803.1	6686.2	0.025
Bronze Sample										
PS1-10iu	2010 June 6	16:11:34.886	+55:08:47.91	···	···	···	···	···	···	0.006
PS1-13aea	2013 April 7	12:18:14.320	+47:20:12.60	···	···	···	···	···	···	0.014
PS1-13bit	2013 May 12	16:12:00.765	+54:16:08.16	···	···	···	···	···	···	0.008
PS1-13cgt	2013 July 17	16:18:56.245	+54:19:33.71	···	···	···	···	···	···	0.010

3.2.3 PS1 Transient Photometry

The 14 objects in our sample were discovered in the PS1-MDS imaging spanning 2010 − 2013. Discovery dates, coordinates, and other basic information are listed in Table 3.1. Detailed information on the production of final PSF, template subtracted, griz$_{P1}$ photometry is given in Rest et al. (2014) and Scolnic et al. (2014). For transients discovered before Oct. 2011, object specific deep templates were constructed from pre-explosion images. For transients discovered after this time, template subtraction was performed using the PS1 "deep stacks" constructed from high quality PS1 images obtained between 2010 and 2011.

In Figures 3.1, 3.2 and 3.3 we plot the griz$_{P1}$ light curves for all 14 transients. This includes 3σ pre- and post-explosion limits. To give perspective on the rapid timescale of these events, we have also plotted the type Ibc template light curve (grey area; normalized to the PS1 transient peak magnitude) from Drout et al. (2011). Photometry is listed in Table 3.2.

3.2.4 Other Transient Photometry

In addition to the PS1 photometry, we also obtained one epoch of $r-$band imaging for PS1-11bbq with Gemini GMOS (Hook et al. 2004), one epoch of $ri-$band imaging for PS1-12brf with Magellan IMACS (Dressler et al. 2006) and one epoch of $r-$band imaging for PS1-13ess with Magellan IMACS. This additional photometry was obtained at +2, +45 and +12 rest-frame days for the three objects, respectively. The images were processed using standard tasks in IRAF[3] and calibrated using PS1 magnitudes of field stars. We subtracted contributions from the host galaxies using PS1 template images and the ISIS software package as described in Chornock et al. (2013). These points are also shown (squares) in Figures 3.1 and 3.2, and listed in Table 3.2.

3.2.5 Galaxy Photometry

For our entire sample we compile griz-band photometry for any underlying galaxy/source. When possible, we utilize the SDSS DR9 Petrosian magnitudes which account for galaxy morphology. For cases where the underlying galaxy/source was too faint for a high signal-to-noise SDSS detection, we perform aperture photometry on the PS1 deep template images, choosing an aperture to encompass all of the visible light. Cross-checks show the PS1 and SDSS magnitudes are consistent. In Figures 3.4 and 3.6 we show the environments immediately surrounding the transients.

---

[3] IRAF is distributed by the National Optical Astronomy Observatory, which is operated by the Association for Research in Astronomy, Inc. under cooperative agreement with the National Science Foundation.

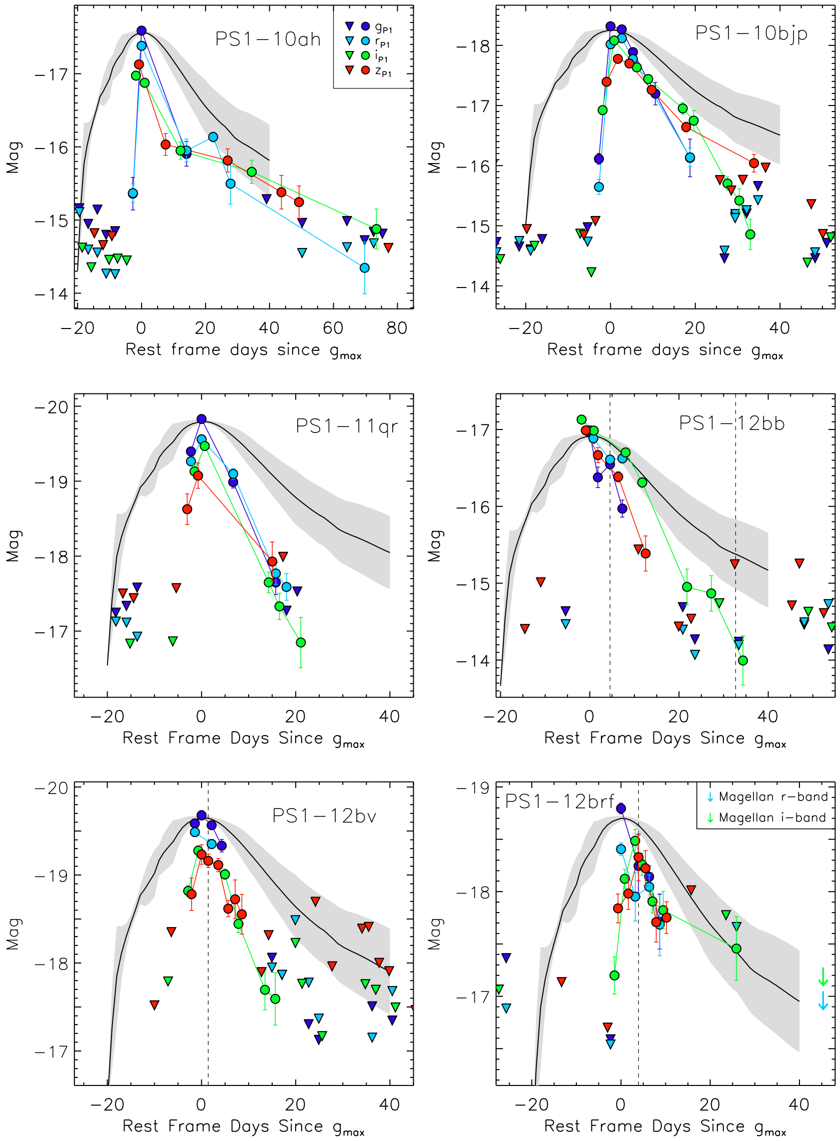

Figure 3.1.—: PS1 absolute magnitude, rest-frame, light curves for gold sample transients. Circles represent griz$_{P1}$ detections and triangles represent 3σ upper limits. Vertical dashed lines indicate epochs when spectroscopic observations were acquired. The grey shaded region is the R−band type Ibc template from Drout et al. (2011), normalized to the peak magnitude of the PS1-MDS transient.

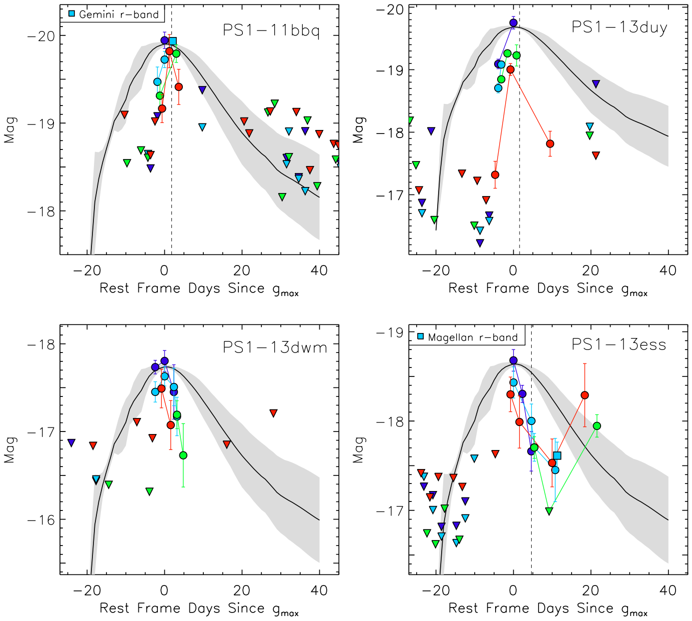

Figure 3.2.—: Same as Figure 3.1 for silver sample objects.

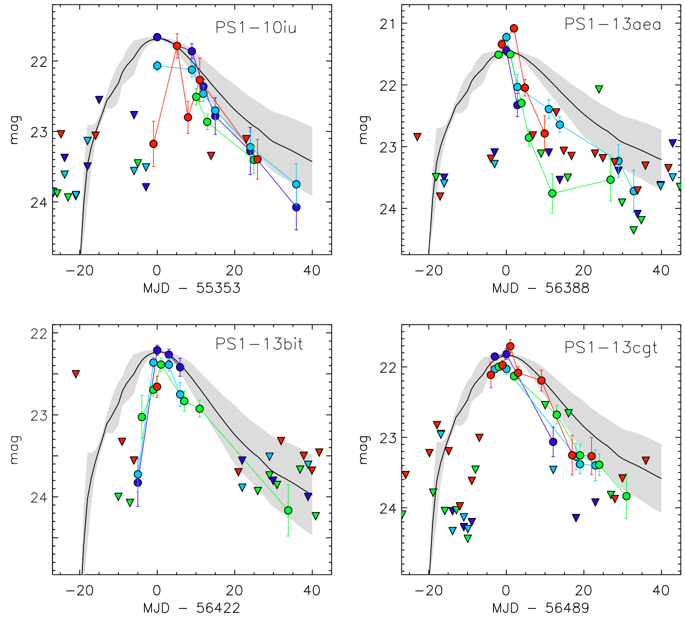

Figure 3.3.—: PS1 apparent magnitude, observer-frame, light curves for our bronze (non-spectroscopic) sample. Symbols have the same meaning as Figure 3.1.

Table 3.2. Optical Photometry

Event	filter	MJD	Phase[a]	AB mag[b]	Error	Instrument
PS1-10ah	g_{P1}	55230.5	-19.5	>22.38	···	PS1
PS1-10ah	g_{P1}	55233.5	-16.7	>22.60	···	PS1
PS1-10ah	g_{P1}	55236.6	-13.8	>22.40	···	PS1
PS1-10ah	g_{P1}	55239.5	-11.1	>22.75	···	PS1
PS1-10ah	g_{P1}	55242.5	-8.3	>22.70	···	PS1
PS1-10ah	g_{P1}	55248.5	-2.7	22.18	0.22	PS1
PS1-10ah	g_{P1}	55251.4	0.0	19.95	0.05	PS1
PS1-10ah	g_{P1}	55266.5	14.1	21.64	0.17	PS1
PS1-10ah	g_{P1}	55281.3	27.8	>22.02	···	PS1
PS1-10ah	g_{P1}	55293.4	39.1	>22.26	···	PS1

[a] Rest-frame days since observed $g-$band maximum.

[b] Upper limits presented are 3σ.

Note. — Table 3.2 is published in its entirety in the electronic edition. A portion is shown here for guidance regarding its form and content.

3.2.6 Optical Spectroscopy

Spectroscopic follow-up for the PS1-MDS is carried out on a number of telescopes, with the MMT, Magellan and Gemini bearing most of the load. Spectra are acquired for roughly 10% of the transients identified by the `photpipe` pipeline, with final selections left to the observer. We obtained spectra of five transients while they were active, including two observations of PS1-12bb. The epochs on which these spectra were taken are indicated by a dashed vertical line in the appropriate panels of Figures 3.1 and 3.2. Host galaxy spectra were also obtained for six transients. A summary of our spectroscopic data is given in Table 3.3.

Initial reduction (overscan correction, flat fielding, extraction, wavelength calibration) of all long slit spectra was carried out using the standard packages in IRAF. Flux calibration and telluric correction were performed using a set of custom idl scripts (see, e.g., Matheson et al. 2008; Blondin et al. 2012) and standard star observations obtained the same night as the science exposures. Spectra obtained with the Hectospec multi-fiber spectrograph (Fabricant et al. 2005) were reduced using the IRAF package "hectospec" and the CfA pipeline designed for this instrument.

Table 3.3. Optical Spectroscopy

UT Date	MJD	Event	Target	Phase[a]	Telescope	Instrument[b]
2010 Mar. 08	55263	PS1-10ah	Host	···	NOT	ALFOSC
2011 Apr. 06	55657	PS1-10ah	Host	···	MMT	Hectospec
2011 Jun. 08	55720	PS1-10ah	Host	···	MMT	Hectospec
2012 Jan. 17	55943	PS1-10ah	Host	···	MMT	Blue Channel
2010 Nov. 28	55528	PS1-10bjp	Host	···	MMT	Hectospec
2011 Sep. 25	55829	PS1-10bjp	Host	···	MMT	Hectospec
2011 Jun. 26	55738	PS1-11qr	Host	···	Magellan-Clay	LDSS3
2011 Dec. 04	55899	PS1-11bbq	Transient	+2	Gemini-N	GMOS
2012 Jan. 27	55953	PS1-12bb	Transient	+5	MMT	Blue Channel
2012 Feb. 27	55984	PS1-12bb	Transient	+33	Gemini-S	GMOS
2012 Jan. 27	55953	PS1-12bv	Transient	+2	MMT	Blue Channel
2012 Oct. 14	56214	PS1-12brf	Transient	+4	MMT	Blue Channel
2013 Nov. 07	56603	PS1-13duy	Transient	+2	MMT	Blue Channel
2013 Nov. 10	56606	PS1-13dwm	Host	···	MMT	Blue Channel
2013 Dec. 29	56655	PS1-13ess	Host	···	Magellan-Clay	LDSS3

[a] Rest-frame days since observed $g-$band maximum.

[b] ALFOSC = Andalucia Faint Object Spectrograph and Camera; Hectospec (Fabricant et al. 2005); Blue Channel (Schmidt et al. 1989); LDSS3 = Low Dispersion Survey Spectrograph-3 (Allington-Smith et al. 1994); GMOS = Gemini Multi-Object Spectrograph (Hook et al. 2004)

3.3 Sample Overview

The 14 rapidly-evolving transients we identify in the PS1-MDS can be usefully split into three groups based on (1) the quality of their observed light curves and (2) constraints available on their distances. For the rest of the manuscript these sub-groups will be designated “gold”, “silver”, and “bronze”.

3.3.1 Gold and Silver Samples

Together our gold and silver samples contain 10 objects. For these events, we obtained spectroscopic redshifts of their host galaxies, allowing us to constrain their true luminosity scale. Our gold sample is composed of six objects. These are our highest quality events, all of which satisfy the photometric selection criteria listed in Section 3.2.2. The absolute magnitude, rest-frame, light curves for these events are shown in Figure 3.1.

Our silver sample is composed of four objects. These are events that were noted as rapidly-evolving during the normal operations of the PS1-MDS but which possess sparser light curves (Figure 3.2). In all cases the observed light curves are sufficient to characterize them as rapidly-evolving, but sparse enough such that they fail the systematic selection criteria described above. For instance, PS1-13ess only has one band with a deep limit in the 9 days prior to observed maximum (as opposed to the requisite two). For a majority of this manuscript, the silver objects will be analyzed with our gold sample, as they further inform the properties of rapidly-evolving transients. However, in Section 3.7 when calculating volumetric rates, only objects which pass the well defined set of selection criteria outlined above will be considered.

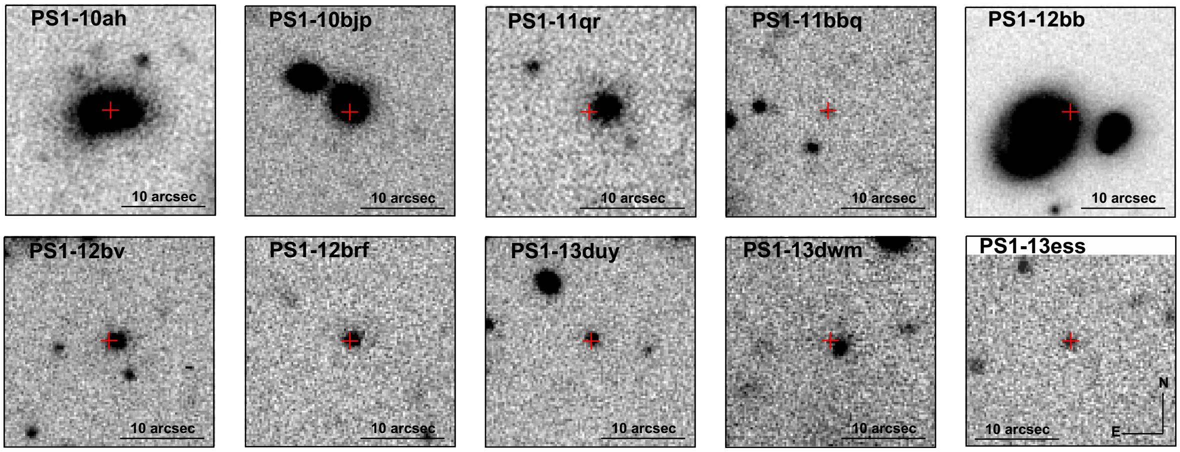

Figure 3.4.—: Gold and silver sample explosion environments. Images are from PS1 templates. Transient explosion sites are marked with red crosses.

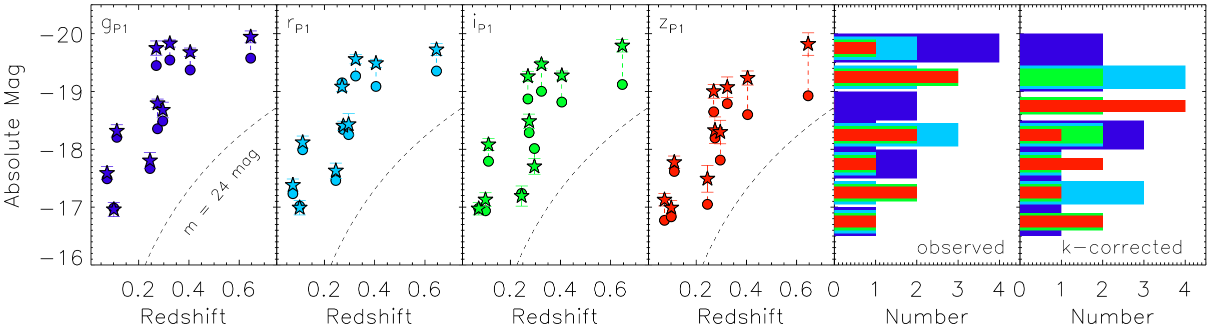

Figure 3.5.—: Peak absolute magnitude versus redshift for our gold and silver sample objects in four photometric bands (griz$_{\rm P1}$). Stars represent our observed values corrected for distance and extinction while circles have been roughly k-corrected to rest-frame bandpasses (see Section 3.4.3). Dashed lines represent a constant apparent magnitude of 24 mag. Histograms for both sets of magnitudes are given in the two right most panels (blue = g$_{\rm P1}$, cyan = r$_{\rm P1}$, green = i$_{\rm P1}$, red = z$_{\rm P1}$).

In Figure 3.4 we show the $25' \times 25'$ region surrounding the gold and silver transients, all of which have an associated host. Narrow emission and absorption lines were used to measure the redshift to each host. These range from z = 0.074 (PS1-10ah) to z = 0.646 (PS1-11bbq) with a median redshift of z = 0.275. In Table 3.1 we list the redshift, luminosity distance, and Milky Way reddening in the direction of each transient (Schlafly & Finkbeiner 2011). Throughout this paper we correct only for Milky Way extinction. All calculations in this paper assume a flat ΛCDM cosmology with $H_0 = 71$ km s^{-1} Mpc^{-1}, $\Omega_m = 0.27$, and $\Omega_\Lambda = 0.73$.

In Figure 3.5 we plot peak absolute magnitude versus redshift in griz$_{\rm P1}$ for the gold/silver transients. Stars represent our observed magnitudes corrected for distance and MW extinction. Circles represent absolute magnitudes that have been k-corrected to the rest-frame griz$_{\rm P1}$ bandpasses based on best fit blackbodies (see Section 3.4). We see that our sample spans a wide range of absolute peak magnitude ($-17 > M > -20$).

3.3.2 Bronze Sample

Our bronze sample is composed of four objects. These events have light curves that were flagged by the selection criteria in Section 3.2.2 but for which we were unable to spectroscopically confirm the extragalactic nature of their hosts. The $25' \times 25'$ region surrounding our bronze sample is shown in Figure 3.6. All four transients have a faint (25 mag $< m_i <$ 22 mag) underlying source visible in the PS1 deep stacks, although in several cases there is ambiguity about the true host (for instance, PS1-13aea exploded in the region between NGC4258 and NGC4248; see Figure 3.6). In Appendix A we quantify the most likely hosts and discuss the consequences of each probable host for the

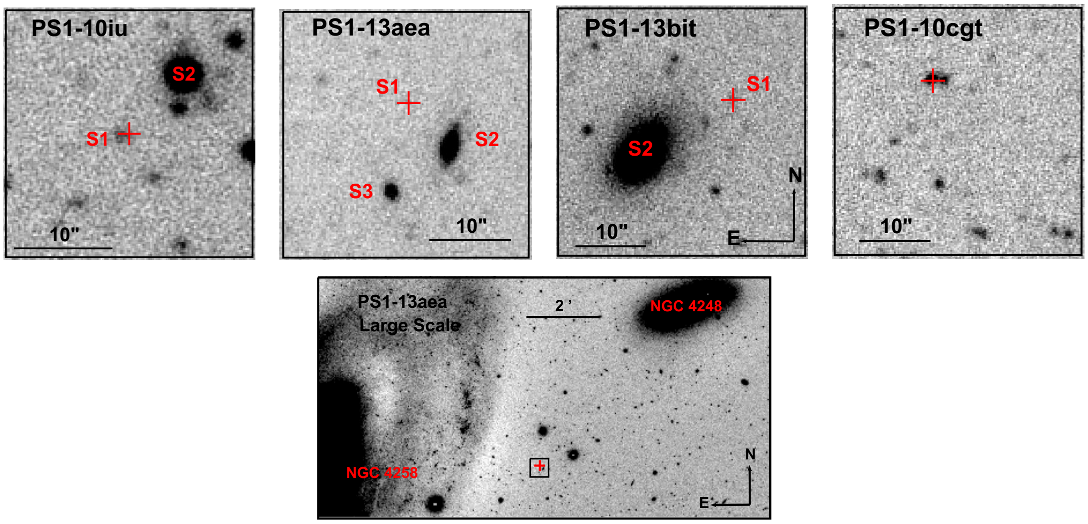

Figure 3.6.—: *Top:* Bronze sample explosion environments. All images are from PS1 templates. Nearby galaxies are labeled in red. The location of the transient is indicated by a red cross. *Bottom:* The large scale environment around PS1-13aea, which exploded between NGC 4258 and NGC 4248.

nature of these transients. We find it likely that a subset of our bronze sample events are extragalactic, and therefore additional rapidly-evolving and luminous transients. However, due to the uncertainty in the distance to any individual bronze event, for a majority of this manuscript we will focus on the properties of the gold and silver transients.

3.4 Photometric Properties

The gold and silver events presented in this work increase the number of known transients with $t_{1/2} \lesssim 12$ days by approximately a factor of three. This is illustrated in Figure 3.7 where we plot peak pseudo-bolometric luminosity versus $t_{1/2}$ for the objects presented in this work (red stars) and other rapid SN (red circles) in comparison to type Ia, Ia-x, "Calcium-rich" Ia, Ib/c, IIn, IIP, and type-I SLSN (see caption for references). The sample of PS1-MDS transients significantly increases the population of known objects at the shortest timescales and spans a wide range of peak luminosities. In the this section we discuss the photometric properties of the PS1-MDS identified transients.

3.4.1 Timescales

In Table 3.4 we summarize the photometric properties of the gold/silver transients, including their observed/absolute magnitudes and several measurement of their rise and decline timescales. The $t_{1/2,\mathrm{rise}}$ and $t_{1/2,\mathrm{decline}}$ timescales as well as the number of magnitudes the light curves decline in the first 15 days post-maximum (Δm_{15}) were determined by linearly interpolating our observed light curve[4]. All values are determined with respect to the time of *observed* maximum, and are therefore influenced by the three day cadence in each band. However, this should not strongly affect our qualitative assessment of these objects. The quoted rise time values encompass the entire range of values permitted by the observed photometry/limits in each band.

---

[4] Uncertainties were estimated using a Monte Carlo approach to produce 1000 realizations of our light curve, drawing from the uncertainties from of each data point.

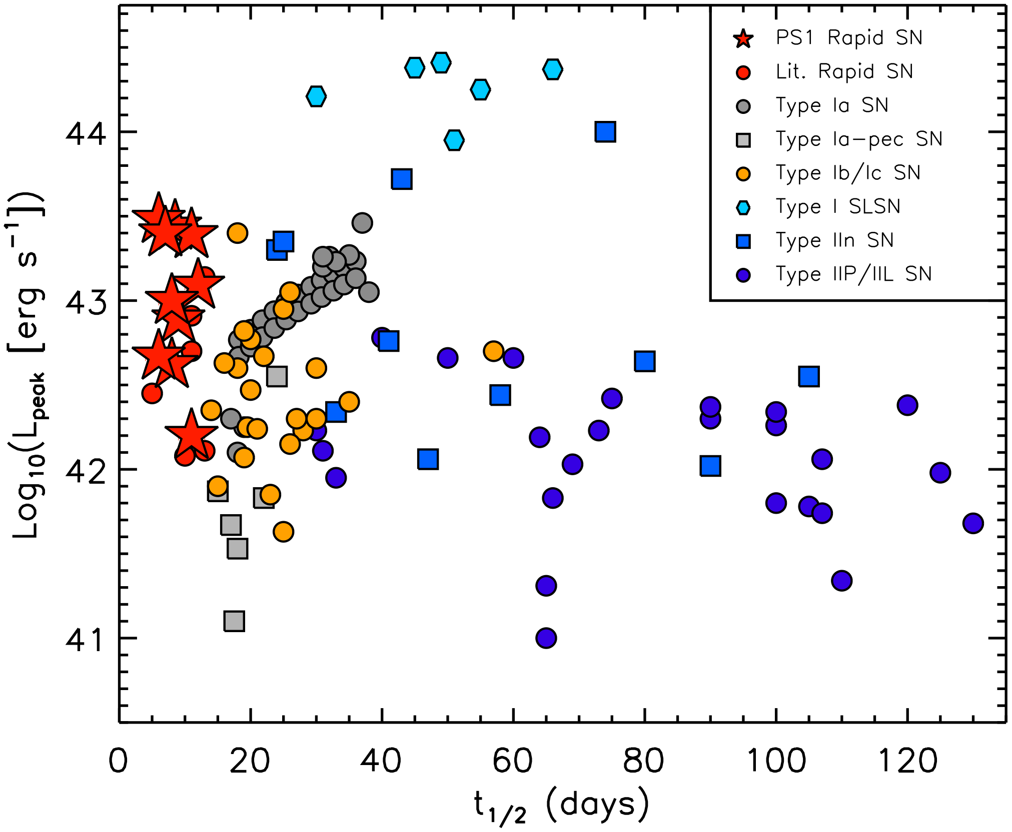

Figure 3.7.—: The phase space of SN: peak luminosity versus rest-frame time above half-maximum for a variety SN. The PS1-MDS transients described in this paper are shown as red stars. They span an order of magnitude in peak luminosity and significantly increase the number of known transients with short characteristic times. Other events from the literature are shown as colored circles/squares: type Ia SN (Nugent et al. 2002; Taubenberger et al. 2008; Scalzo et al. 2012), type Iax & “calcium-rich” Ia (Foley et al. 2013; Kasliwal et al. 2012; Perets et al. 2010), type Ib/Ic (Drout et al. 2011; Valenti et al. 2008; Campana et al. 2006; Taubenberger et al. 2006; Bersten et al. 2012; Olivares et al. 2012; Cobb et al. 2010; Valenti et al. 2012), type IIP/IIL (Arcavi et al. 2012; Hamuy 2003; Andrews et al. 2011; Botticella et al. 2009), type IIn (Kiewe et al. 2012; Margutti et al. 2014b), type I SLSN (Quimby et al. 2011b; Chomiuk et al. 2011; Lunnan et al. 2013), and other rapidly-evolving events (red; Drout et al. 2013; Kasliwal et al. 2010; Poznanski et al. 2010; Ofek et al. 2010; Matheson et al. 2000).

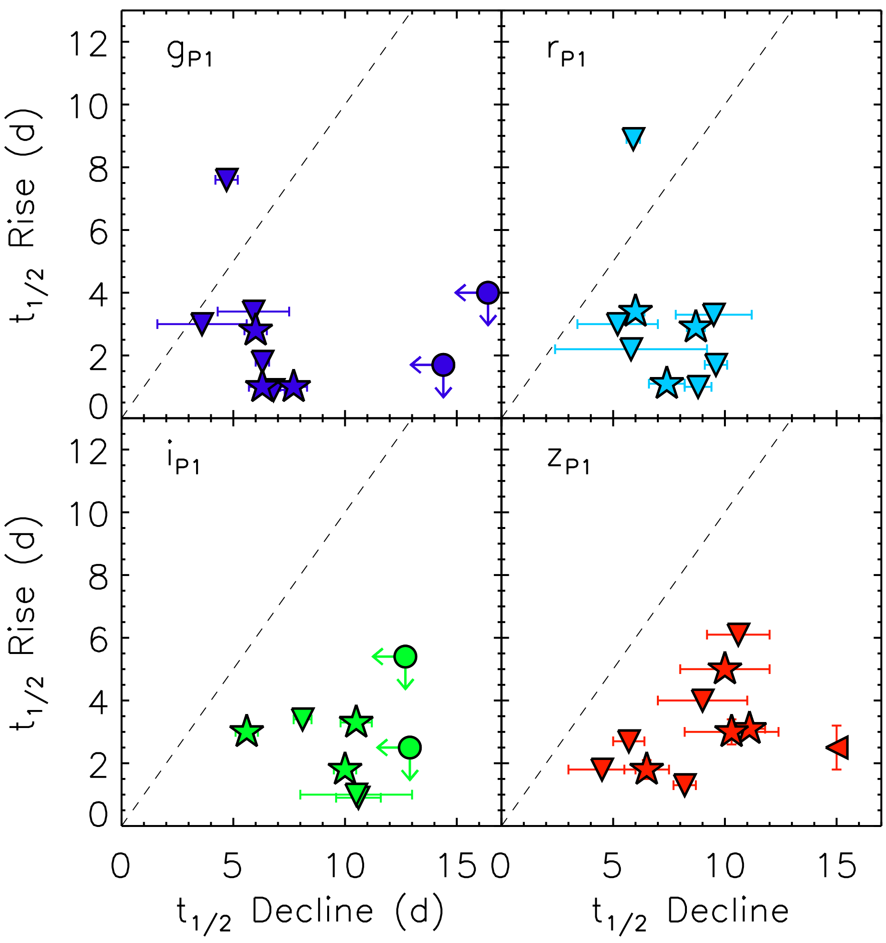

Figure 3.8.—: $t_{1/2,\rm rise}$ versus $t_{1/2,\rm decline}$ for the gold and silver transients in four photometric bands ($griz_{\rm P1}$). Stars represent objects with measured rise and decline timescales, triangles represent objects with an upper limit in one of the two timescales, and circles with arrows represent objects with upper limits for both timescales. In general, the PS1-MDS rapidly-evolving transients rise significantly faster than they decline.

In general the transients have faster rise than decline timescales. This is shown in Figure 3.8 where we plot the $t_{1/2,\mathrm{rise}}$ versus $t_{1/2,\mathrm{decline}}$ timescales. Most events fall well below the dashed line denoting equality, indicating that decline timescale is *not* a good proxy for overall timescale in these events. In fact, for six events, our data do not exclude a transient that rose on a timescale $\lesssim$1 day. In contrast, the typical Δm_{15} values for these transients ($1 - 2$ mags) are slightly more rapid than typical stripped envelope core-collapse SN ($\Delta m_{15} \sim 0.5 - 1.0$; Drout et al. 2011) but slower than the rapidly declining type I SN 2005ek, SN 2010X, and SN 2002bj (Drout et al. 2013; Kasliwal et al. 2010; Poznanski et al. 2010), which possess $\Delta m_{15} \gtrsim 3$ mag.

Three of the transients (PS1-10ah, PS1-12brf, PS1-13ess) show evidence for a change in decline timescale. PS1-10ah initially declines very rapidly, with a linear decline rate of $\sim$0.15 mag day^{-1}, which then shallows to ~ 0.02 mag day^{-1} around 10 days post-maximum. PS1-13ess shows an initial decline very similar to PS1-10ah, but then *rises* again as evidenced by our final i_{P1} and z_{P1} data points. This may liken it to the double peaked type IIb SN 1993J (see Section 3.8). The other objects in our sample show no discernible change in slope out to $\sim 10 - 20$ days post-maximum.

Table 3.4. Measured Photometric Properties (Gold and Silver Samples)

Event	Band	m$_{\rm obs,max}$ (mag)	M$_{\rm obs,max}$ (mag)	M$_{\rm rest,max}$ (mag)	t$_{\rm rise}$ (day)	t$_{1/2,\rm rise}$ (day)	t$_{1/2,\rm decline}$ (day)	Δm_{15} (mag)
PS1-10ah	$g_{\rm P1}$	19.95 (0.05)	-17.59 (0.11)	-17.5	1 − 3	1.0 (0.1)	6.3 (0.6)	1.7 (0.2)
PS1-10ah	$r_{\rm P1}$	20.15 (0.04)	-17.38 (0.10)	-17.2	1 − 3	1.1 (0.1)	7.4 (0.8)	1.4 (0.1)
PS1-10ah	$i_{\rm P1}$	20.56 (0.05)	-16.97 (0.11)	-17.0	1 − 3	< 0.9	10.6 (1.0)	1.0 (0.1)
PS1-10ah	$z_{\rm P1}$	20.40 (0.04)	-17.13 (0.11)	-16.8	1 − 3	< 2.7	5.7 (0.7)	1.2 (0.1)
PS1-10bjp	$g_{\rm P1}$	20.29 (0.02)	-18.34 (0.11)	-18.2	1 − 4	1.0 (0.1)	7.7 (0.6)	1.7 (0.2)
PS1-10bjp	$r_{\rm P1}$	20.45 (0.03)	-18.14 (0.11)	-18.0	3 − 5	3.4 (0.1)	6.0 (0.4)	1.8 (0.1)
PS1-10bjp	$i_{\rm P1}$	20.46 (0.01)	-18.10 (0.11)	-17.8	3 − 6	1.8 (0.1)	10.0 (0.5)	1.1 (0.1)
PS1-10bjp	$z_{\rm P1}$	20.75 (0.03)	-17.79 (0.11)	-17.6	2 − 6	3.1 (0.1)	11.1 (0.7)	1.0 (0.1)
PS1-11qr	$g_{\rm P1}$	21.05 (0.03)	-19.84 (0.06)	-19.5	2 − 5	2.8 (0.1)	6.0 (0.5)	2.1 (0.2)
PS1-11qr	$r_{\rm P1}$	21.31 (0.06)	-19.56 (0.08)	-19.3	2 − 5	2.9 (0.1)	8.7 (0.4)	1.7 (0.1)
PS1-11qr	$i_{\rm P1}$	21.39 (0.04)	-19.47 (0.07)	-19.0	3 − 6	3.0 (0.2)	5.6 (0.5)	2.0 (0.1)
PS1-11qr	$z_{\rm P1}$	21.78 (0.17)	-19.08 (0.18)	-18.8	1 − 6	3.0 (0.4)	10.3 (2.1)	1.1 (0.3)
PS1-11bbq	$g_{\rm P1}$	22.53 (0.09)	-19.96 (0.10)	-19.6	1 − 5	<1.7	< 14.4	> 0.7
PS1-11bbq	$r_{\rm P1}$	22.73 (0.09)	-19.73 (0.10)	-19.4	1 − 6	<3.3	< 9.5	> 0.9
PS1-11bbq	$i_{\rm P1}$	22.64 (0.10)	-19.80 (0.11)	-19.1	1 − 6	<5.4	< 12.7	> 0.9
PS1-11bbq	$z_{\rm P1}$	22.61 (0.20)	-19.83 (0.19)	-18.9	1 − 4	2.5 (0.7)	< 15.0	> 0.7
PS1-12bb	$g_{\rm P1}$	21.33 (0.03)	-16.97 (0.12)	-17.0	1 − 5	< 1.8	6.3 (0.3)	∼ 1.8
PS1-12bb	$r_{\rm P1}$	21.27 (0.04)	-17.00 (0.12)	-17.0	1 − 5	< 1.7	8 – 11.0	∼ 1.6
PS1-12bb	$i_{\rm P1}$	21.12 (0.02)	-17.14 (0.12)	-16.9	1 − 3	< 1.0	9.6 (0.5)	1.0 (0.07)
PS1-12bb	$z_{\rm P1}$	21.25 (0.04)	-16.99 (0.13)	-16.8	1 − 4	<1.3	8.2 (0.5)	1.8 (0.2)
PS1-12bv	$g_{\rm P1}$	21.69 (0.05)	-19.68 (0.07)	-19.4	3 − 7	< 3.4	4 – 8	> 1.6
PS1-12bv	$r_{\rm P1}$	21.87 (0.05)	-19.49 (0.07)	-19.1	3 − 7	< 2.2	3 – 9	> 1.5
PS1-12bv	$i_{\rm P1}$	22.07 (0.06)	-19.27 (0.08)	-18.8	2 − 6	< 3.4	8.1 (0.4)	1.6 (0.2)
PS1-12bv	$z_{\rm P1}$	22.12 (0.11)	-19.12 (0.12)	-18.6	3 − 7	< 4.0	9.0 (2.0)	>1.3
PS1-12brf	$g_{\rm P1}$	21.93 (0.05)	-18.84 (0.07)	-18.4	1 − 3	< 0.9	6.8 (0.5)	> 1.1
PS1-12brf	$r_{\rm P1}$	22.24 (0.06)	-18.43 (0.08)	-18.3	1 − 3	< 1.0	8.8 (0.6)	> 0.7
PS1-12brf	$i_{\rm P1}$	22.11 (0.11)	-18.50 (0.12)	-18.3	4 − 6	3.3 (0.2)	10.5 (0.7)	0.9 (0.2)
PS1-12brf	$z_{\rm P1}$	22.24 (0.22)	-18.34 (0.23)	-18.2	5 − 7	5.0 (0.2)	∼10.0	> 0.6
PS1-13duy	$g_{\rm P1}$	20.84 (0.10)	-19.75 (0.12)	-19.4	1 − 5	< 4.0	< 16.4	> 0.7

Table 3.4—Continued

Event	Band	$\mathrm{m_{obs,max}}$ (mag)	$\mathrm{M_{obs,max}}$ (mag)	$\mathrm{M_{rest,max}}$ (mag)	$\mathrm{t_{rise}}$ (day)	$\mathrm{t_{1/2,rise}}$ (day)	$\mathrm{t_{1/2,decline}}$ (day)	Δm_{15} (mag)
PS1-13duy	r_{P1}	21.46 (0.04)	-19.08 (0.08)	-19.1	···	···	< 17.3	> 0.7
PS1-13duy	i_{P1}	21.25 (0.05)	-19.26 (0.09)	-18.9	$1-3$	< 2.5	< 12.9	> 0.9
PS1-13duy	z_{P1}	21.49 (0.10)	-19.00 (0.12)	-18.6	$1-4$	1.8 (0.3)	6.5 (1.0)	> 1.3
PS1-13dwm	g_{P1}	22.56 (0.12)	-17.80 (0.14)	-17.7	$1-4$	< 3.0	$2-5$	> 0.5
PS1-13dwm	r_{P1}	22.69 (0.11)	-17.63 (0.13)	-17.5	$1-4$	< 3.0	$3-7$	> 0.5
PS1-13dwm	i_{P1}	23.09 (0.16)	-17.19 (0.17)	-17.2	$1-6$	···	···	> 0.5
PS1-13dwm	z_{P1}	22.78 (0.22)	-17.49 (0.23)	-17.0	$1-3$	< 1.8	$3-6$	> 0.5
PS1-13ess	g_{P1}	22.02 (0.12)	-18.68 (0.14)	-18.5	$1-6$	< 7.6	4.7 (0.5)	> 1.0
PS1-13ess	r_{P1}	22.69 (0.11)	-18.43 (0.18)	-18.3	$1-6$	< 8.9	5.9 (0.3)	> 1.2
PS1-13ess	i_{P1}	22.96 (0.12)	-17.70 (0.13)	-18.0	···	···	···	> 0.7
PS1-13ess	z_{P1}	22.34 (0.19)	-18.30 (0.20)	-17.8	$1-4$	< 6.1	10.6 (1.4)	> 1.0

3.4.2 Colors and SEDs

In the normal operation mode of the PS1-MDS only g_{P1} and r_{P1} observations are acquired on the same day, with i_{P1} and z_{P1} observations following on consecutive evenings. In the upper panel of Figure 3.9 we plot the $g_{P1} - r_{p1}$ colors from every epoch on which both bands were observed. The colors are generally blue ($g_{P1} - r_{p1} \lesssim 0.0$) and redden slightly with time. In the lower panel of Figure 3.9 we plot $\mathrm{g_{P1}} - \mathrm{r_{P1}}$ color at maximum as a function of transient redshift. A majority of objects possess $-0.2 > g_{P1} - r_{P1} > -0.3$. Only PS1-12bb shows significantly redder colors with $g_{P1} - r_{p1} = 0.0$. For comparison, we also show a randomly selected sample of PS1 type Ia SN (grey dots). The type Ia SN are significantly redder than our rapidly-evolving transients, especially at redshifts greater than z=0.2 where the $\mathrm{g_{P1}}$ and $\mathrm{r_{P1}}$ filters probe the portion of the type Ia spectrum where line blanketing greatly reduces the UV flux.

In order to gain a more complete view of the SED evolution of our sample, we interpolate our $griz_{P1}$ light curves to a set of common epochs. The uncertainly involved in such an interpolation is accentuated due to the rapidly-evolving nature of our sample, and we take care to only interpolate to epochs for which there was a cluster of $griz_{P1}$ observations within a few days. In Figure 3.10 we plot the SEDs. For a majority of the events, no turnoff is seen in the SED at blue wavelengths. This is true even for our highest redshift object, PS1-11bbq, for whom the $\mathrm{g_{P1}}$ extends out to a rest fame wavelength of ∼2500 Å.

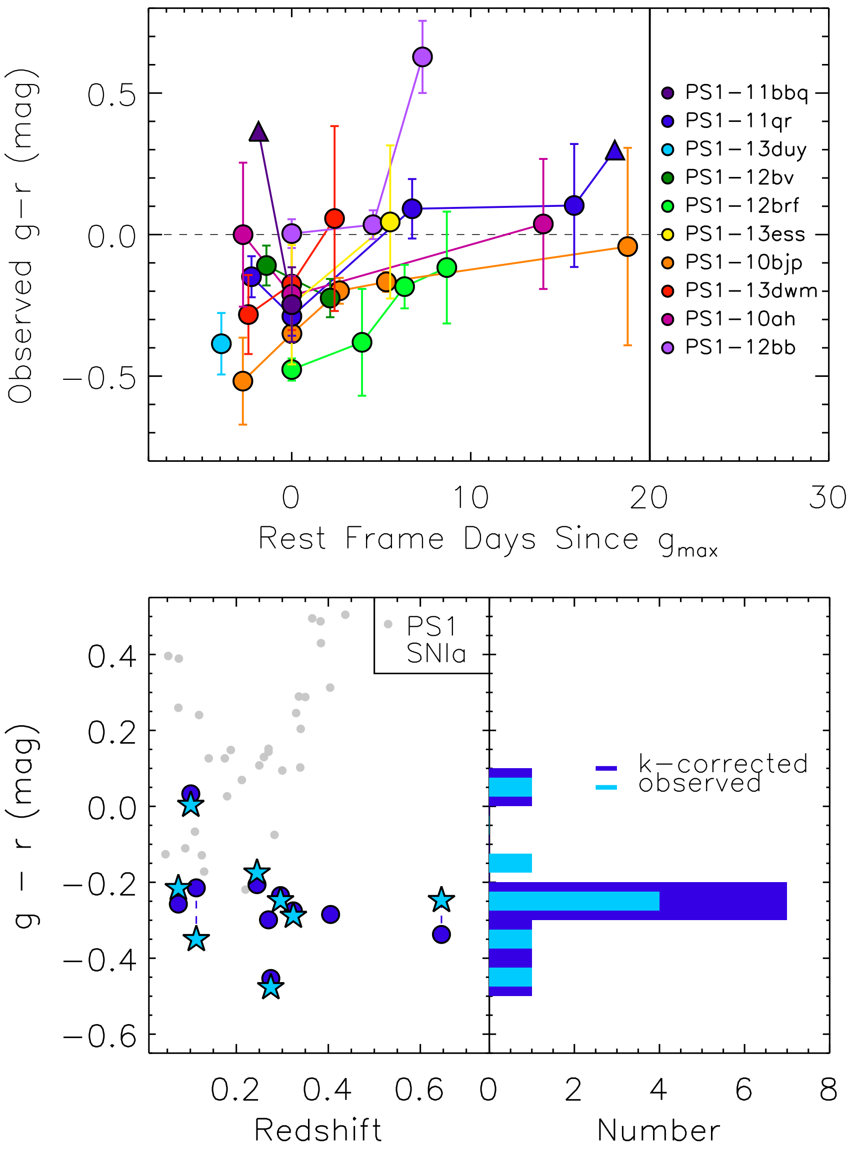

Figure 3.9.—: *Top Panel:* Observed $g_{P1} - r_{P1}$ color evolution for the gold and silver transients. Triangles mark lower limits. Colors are initially blue and redden slightly with time. The g_{P1} and r_{P1} bandpasses probe slightly different wavelength ranges for each transient. *Bottom Panel:* $g_{P1} - r_{P1}$ colors at maximum light versus redshift. Observed values are shown as cyan stars and values k-corrected to rest-frame bandpasses are shown as blue circles (see Section 3.4.3). Histograms of both are given in the right panel. A majority of our objects show blue colors with $-0.2 > g_{P1} - r_{P1} > -0.3$. Grey dots are a random selection of PS1-MDS type Ia SN.

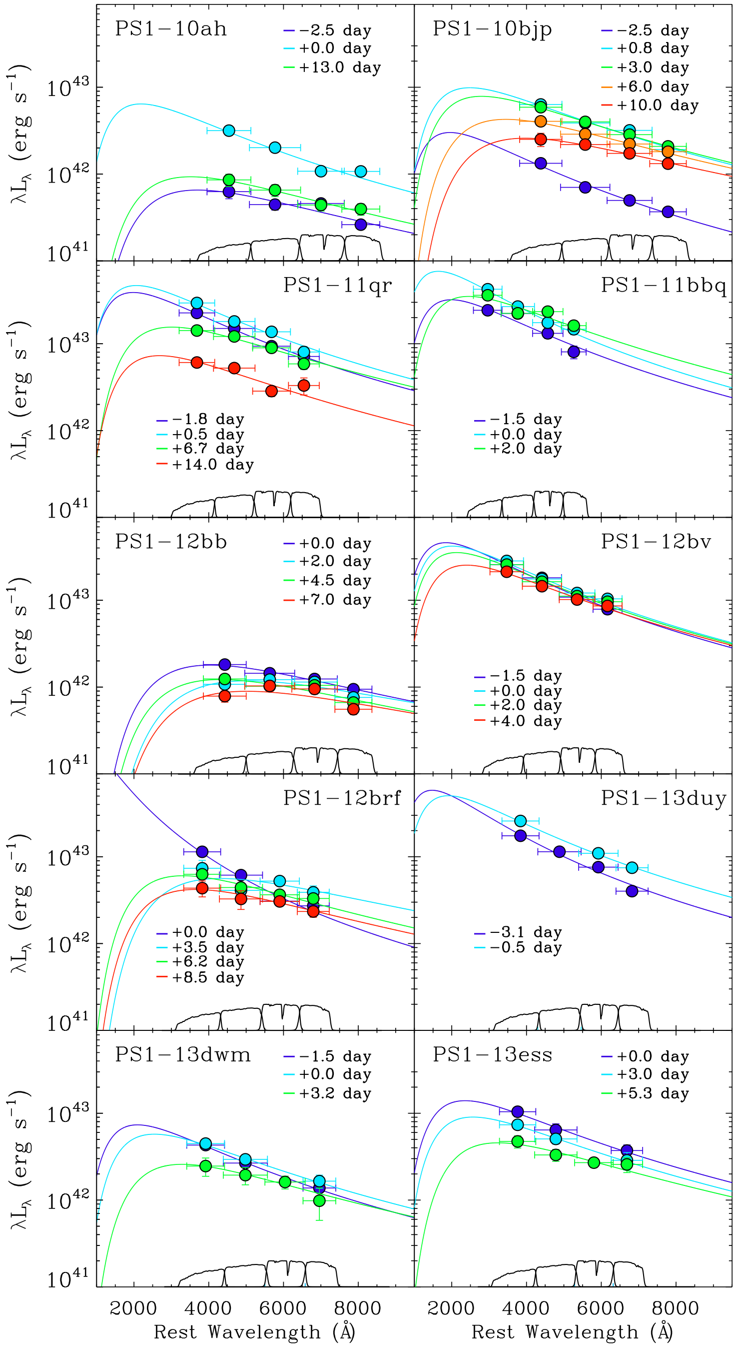

Figure 3.10.—: Multi-epoch SEDs for the gold and silver transients. Best fit blackbody curves are shown as solid lines. The griz$_{P1}$ bandpasses are plotted on the bottom axis for each event.

3.4.3 Temperature and Radius Evolution

Also shown in Figure 3.10 are the best fit blackbody curves for each epoch. For nine (of ten) transients the best fit blackbodies yield temperatures and radii that cool/expand with time, as one expects for an explosion with expanding ejecta (e.g. SN). The best fit blackbody temperatures and radii for these events are plotted as a function of time in Figure 3.11. On average, the temperatures cool from ∼20,000 K near maximum to ∼7,000 K at ∼20 days, and the radii expand from $\sim 10^{14}$ cm to a few $\times 10^{14}$ during the time period over which they are constrained. Dashed lines in Figure 3.11 show fiducial cooling rates and photosphere expansion speeds, which are based on our best observed object: PS1-10bjp (orange). The presence of extragalactic extinction along the line of sight would slightly increase these temperatures and radii, but would not affect our conclusion that their evolution is consistent with explosions that possess an expanding ejecta.

The temperature/radius evolution of three transients warrant further note: (1) PS1-12brf displays an initial best fit blackbody temperature of ∼50,000 K. This exact value is uncertain because our data lies far down the Rayleigh-Jeans tail, but from Figure 3.1 we see that it possesses extreme colors near maximum light. This is also the only transient for which our data shows longer wavelengths reaching maximum at later times. (2) PS1-10ah shows tentative evidence for a temperature that *rises* to maximum and then cools. (3) PS1-12bb is our only object that does not show a characteristic cooling/expanding behavior. The best fit blackbody temperature shows little variation and is consistent with $\sim 7{,}000$ K from $0 < t < 20$ days.

Finally, by assuming the spectra of our objects can be approximated by these best

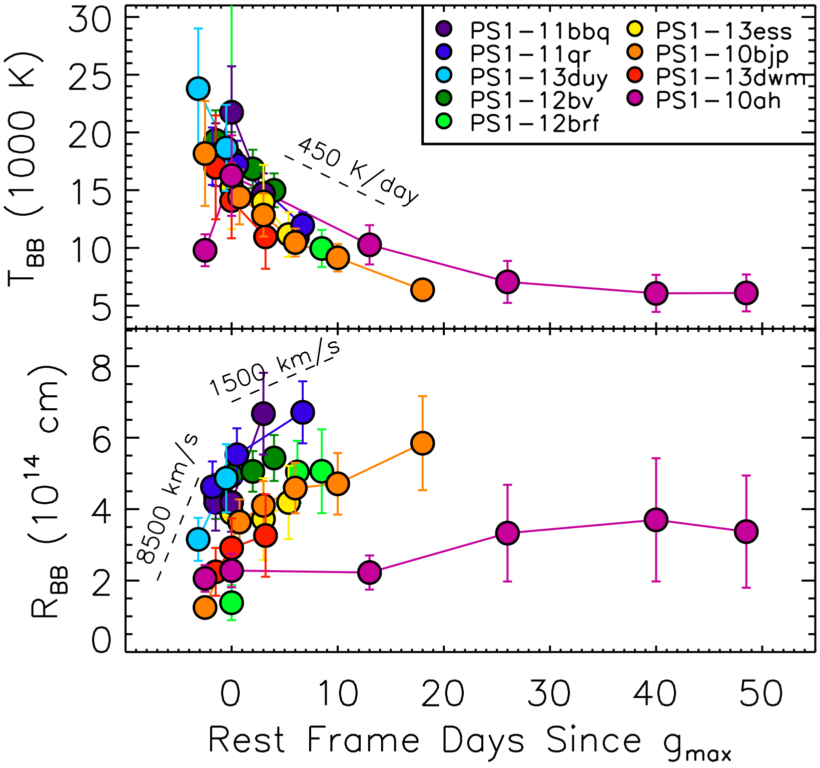

Figure 3.11.—: Best fit blackbody temperatures (top panel) and radii (bottom panel) as a function of time. In general, temperatures evolve from around 20,000 K near maximum to 7,000 K at later times. Exceptions include PS1-12brf (whose initial temperature is around 50,000 K), PS1-10ah (whose temperature rise to maximum light) and PS1-12bb (whose best-fit temperature remains constant around 8000 K; not plotted). Radii are a few time 10^{14} cm, and expand with time.

fit blackbodies, we can perform rough k-corrections on our observed magnitudes to rest-frame griz$_{\mathrm{P1}}$ bandpasses. This will allow us to directly compare the magnitudes observed for objects with differing redshifts. We perform synthetic PS1 photometry on these blackbodies and find the "rest" griz$_{P1}$ peak magnitudes listed in Table 3.4. These "k-corrected" peak magnitudes are shown as circles in Figure 3.5 and are used to produce "rest-frame" $\mathrm{g_{P1}} - \mathrm{r_{P1}}$ colors, which are plotted in Figure 3.9.

3.4.4 Pseudo-Bolometric Light Curves

To constrain the total energy radiated in these explosions, we construct pseudo-bolometric light curves from our multi-band data. We first perform a trapezoidal interpolation to our observed griz$_{P1}$ light curves and then account for missing IR flux by attaching a blackbody tail based on the best fit values described above. In order to account for missing UV flux and the varied wavelength coverage of our observations (due to differing redshifts) we then extend the same blackbody from the edge of the observed g$_{P1}$ band back to 2500 Å (rest-frame). This represents the blue edge of the wavelength range covered by our highest redshift event, and the approximate range of our spectra in Section 3.5.

Using this formulation, our peak pseudo-bolometric luminosities span a range of approximately 2×10^{42} ergs s^{-1} $<$ L $<$ to 3×10^{43} ergs s^{-1}, and are plotted in Figure 3.7. If we had instead utilized a UV bolometric correction that integrated the entire best fit blackbody, these values would be approximately a factor of 2 higher. In the left panel of Figure 3.12 we plot our derived pseudo-bolometric light curves. The number of epochs for which we can constrain the luminosity is limited for the silver transients. The energy radiated by the six gold transients between -3 and $+20$ days ranged from 2×10^{48} ergs (PS1-12bb) to 2×10^{49} ergs (PS1-11qr).

For comparison, we also show the pseudo-bolometric light curves of several other rapidly-evolving events (right panel): SN 2002bj (Poznanski et al. 2010), PTF 09uj (Ofek et al. 2010), SN 2010X (Kasliwal et al. 2010) and SN 2005ek (Drout et al. 2013), as well as the double peaked SN 1993J (Schmidt et al. 1993). The curves for SN 2005ek, SN 2002bj, and SN 1993J were calculated from multi-band photometry in a manner similar to that

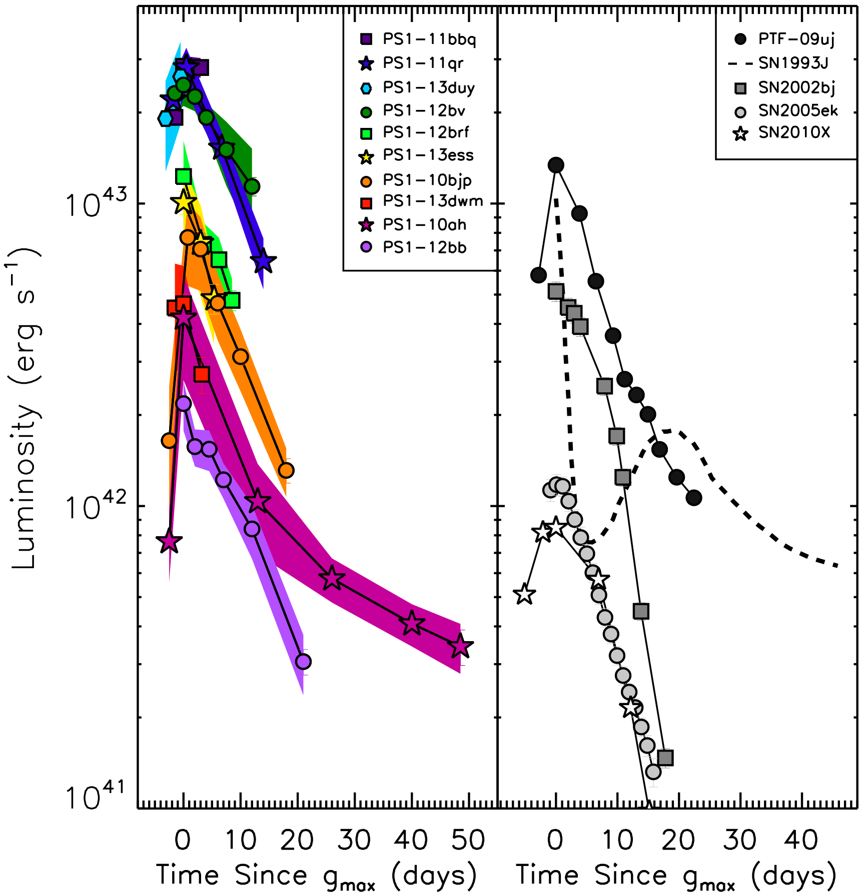

Figure 3.12.—: *Left Panel:* Pseudo-bolometric light curves for the gold and silver transients. *Right Panel:* Pseudo-bolometric light curves for other rapidly-evolving transients from the literature: the type Ic SN 2005ek (Drout et al. 2013) and 2010X (Kasliwal et al. 2010), the type Ib SN 2002bj (Poznanski et al. 2010), the type IIb SN 1993J (Schmidt et al. 1993), and the type IIn PTF09uj (Ofek et al. 2010).

utilized here, while the curves for SN 2010X and PTF 09uj were derived based on r-band data only. We note that SN 2005ek and SN 2010X, which have been proposed to be powered mainly by radioactive decay (Drout et al. 2013; Kasliwal et al. 2010; Tauris et al. 2013), are less luminous than the PS1-MDS events, while the more luminous PTF 09uj and the first peak of SN 1993J are thought to be powered by cooling envelope emission/interaction. These power sources will be discussed further in Section 3.8.

3.5 Spectroscopic Properties

We obtained spectra during outburst for five transients: PS1-11bbq, PS1-12bb, PS1-12bv, PS1-12brf, and PS1-13duy. These spectra are plotted in Figure 3.13. One spectrum was obtained between two and four days post maximum for each event and, in the case of PS1-12bb, a second spectrum was obtained at +33 days. The spectra shown for PS1-11bbq, PS1-12bv, PS1-12brf, and PS1-13duy still contain some contribution from their host galaxies, as evidenced from presence of nebular emission lines. However, both the lack of a 4000 Å break and the faint apparent magnitude of all four hosts ($23-25$ mag) give us confidence that a majority of the continuum is due to the transient itself.

3.5.1 Basic Properties and Comparison to other Events

From Figure 3.13 we see that the spectra are dominated by continua as opposed to strong P Cygni features. Four of the events, PS1-11bbq, PS1-12bv, PS1-12brf and PS1-13duy, show blue continua[5], while PS1-12bb is consistent with a blackbody of $6000-7000$ K. PS1-12bb also showed redder photometric colors and a distinct SED evolution (Section 3.4). Of the events, PS1-12bv shows the strongest evidence for broad spectral features, with the most evident near 3900 Å.

Spectra dominated by blue continua have been observed in previous SN. They are

---

[5] A spectrum of the bronze sample object PS1-13bit was obtained using the OSIRIS instrument at the Gran Telescopio Canarias under programme GTC2007-12ESO (PI: R. Kotak). Private communication from Rubina Kotak reveals that it is similarly dominated by a blue continuum with no narrow emission or absorption features.

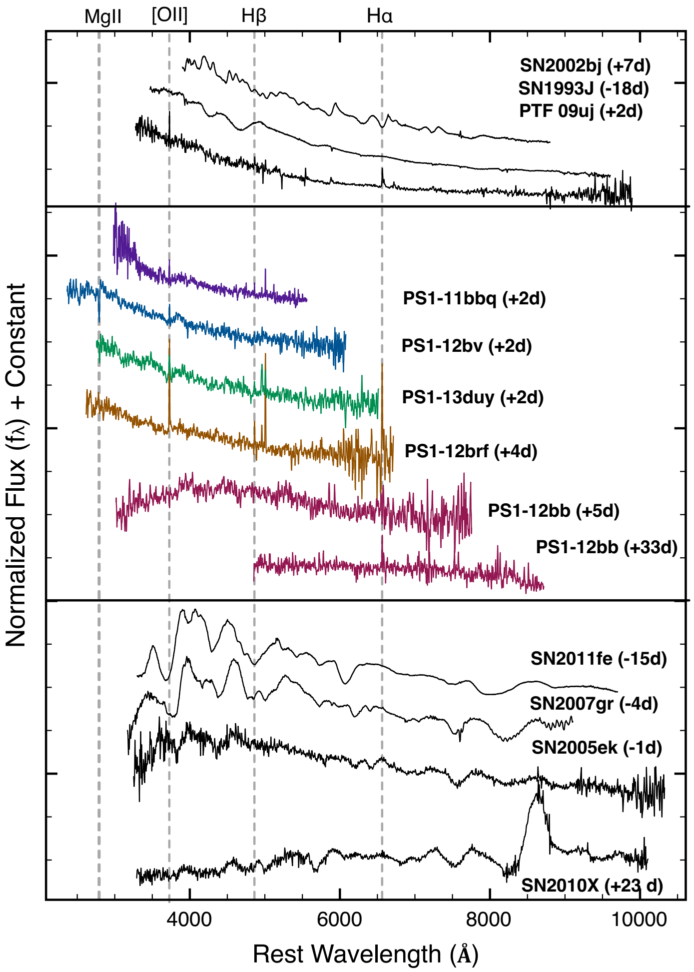

Figure 3.13.—: Explosion spectra for five PS1-MDS transients (colored) in comparison to events from the literature (black). With the exception of PS1-12bb our events are dominated by a blue continuum, with a lack of strong P Cygni features. Some contributions from the host galaxy (e.g. nebular emission lines) are still present in these events. PS1-12bb shows a redder continuum and a notable lack of broad nebular features at +33 days. The top panel shows literature objects thought to be powered by cooling envelope emission/interaction while the bottom panel shows objects powered by radioactive decay (type Ib SN 2002bj Poznanski et al. 2010; type IIb SN 1993J Barbon et al. 1995; type IIn PTF 09uj Ofek et al. 2010; type Ia SN 2011fe Pereira et al. 2013; type Ic SN 2007gr Valenti et al. 2008; type Ic SN 2005ek Drout et al. 2013; type Ic SN 2010X Kasliwal et al. 2010).

typically found in objects that are hot, optically thick, and powered by cooling envelope emission or interaction. For instance, although SN 1993J later went on to develop a plethora of P Cygni features indicative of a type IIb SN, during its initial light curve peak (attributed to cooling envelope emission and recombination) its spectrum was dominated by continua with only a few features between $4000 - 5000$ Å. Hydrogen lines were not evident in the early spectra. In addition, the rapidly-evolving type IIn SN PTF 09uj (attributed to shock breakout/interaction) has only weak narrow emission lines in its spectra near maximum, and is dominated by a blue continuum. Given the signal to noise of our spectra, it is unlikely that we would be able to identify similar emission features in our events if they were present. Thus, based on the quality and coverage of our spectra, *we are unable to conclude whether the objects in our sample are hydrogen-rich or hydrogen-poor.* We plot spectra of SN 1993J and PTF 09uj, as well as the blue rapidly-evolving SN 2002bj (whose power source is still under debate), in the top panel of Figure 3.13.

In contrast, SN that are powered mainly by radioactive decay (type Ia/b/c SN) are typically dominated by P Cygni features formed in the outer ejecta layers. In particular, they often possess strong line blanketing in the blue due to the presence of iron peak elements. We plot several examples in the lower panel of Figure 3.13. We see that our spectra more closely resemble events that are powered by interaction/recombination, as opposed to radioactive decay.

3.5.2 Lack of Nebular Features in PS1-12bb

We obtained two spectra for PS1-12bb. At the time of the second epoch (+33 days) the $i-$band light curve of PS1-12bb had declined by ∼3 mag. Similar to the spectrum obtained near maximum light, this spectrum is dominated by continuum (with some contribution from its host galaxy's light). This is in contrast to any other "late time" spectra of a rapidly-declining SN that has been obtained to date. Both SN 2005ek (Drout et al. 2013) and SN 2010X (Kasliwal et al. 2010) were observed between 10 and 35 days post-maximum. Both events (type Ic) displayed a growing emission component in the Ca II NIR triplet. By +23 days the spectrum of SN 2010X was dominated by the Ca II NIR triplet between 8000 and 9000 Å. This is not the case for PS1-12bb. We can place a limit on the luminosity in the Ca II NIR triplet between 8300−8700 Å at +33 days in PS1-12bb of $< 3 \times 10^{39}$ erg s^{-1}. This is approximately 4 times lower than the feature observed in SN 2010X at a similar time. PS1-12bb was also our only object whose best fit blackbodies did not show radii that expanded with time. Thus, this transient may be of a different kind than a SN with an expanding ejecta that eventually becomes optically thin.

3.5.3 Potential CSM absorption in PS1-12bv

The emission lines present in Figure 3.13 are unresolved and attributed to the host galaxies. However, in the spectrum of PS1-12bv there is tentative evidence for CSM absorption in the Mg II ($\lambda\lambda$ 2796,2803) feature. A view around this feature is shown in the left panel of Figure 3.14. The spectrum of PS1-12bv shows unresolved nebular emission lines of [OII] λ3727 and Hβ at a redshift of z = 0.405. In contrast, the two

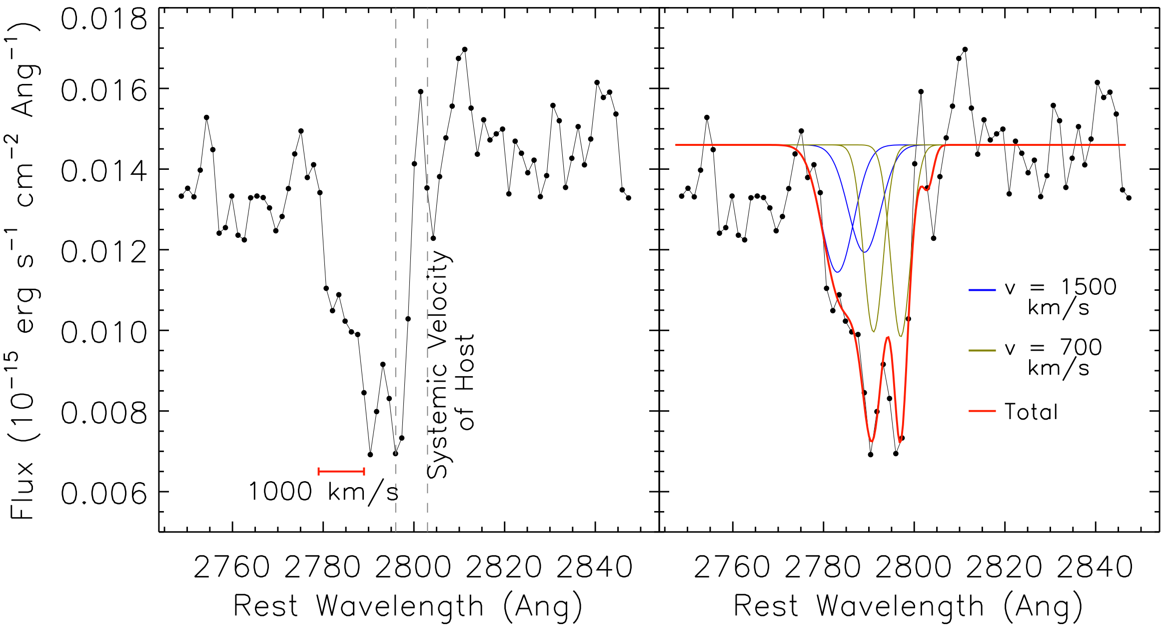

Figure 3.14.—: Mg II absorption in the spectrum of PS1-12bv. *Left:* Vertical lines mark the systemic velocities of the host galaxy as measured from [OII] λ3727 and Hβ in emission. The red line signifies the extent of the resolved blue "shelf", which may be due to absorption in the CSM surrounding the progenitor. *Right:* An example multiple component fit to the absorption feature. The green (blue) components are blue shifted $\sim$700 km s^{-1} (1500 km s^{-1}) with respect to the host galaxy and have a FWHM of 550 km s^{-1} (900 km s^{-1}). The galaxy [OII] λ 3727 feature has a FWHM of 300 km s^{-1}.

deepest features of the Mg II ($\lambda\lambda$ 2796,2803) absorption feature are blue shifted by $\sim$ 700 km s^{-1} relative to the galaxy emission lines (z = 0.402) and there is a resolved blue wing to the feature. This blue wing spans an *additional* $\sim$1000 km s^{-1} from the minimum of the absorption feature. Our resolution corresponds to $\sim$ 400 km s^{-1} in this wavelength region.

A similar blue absorption wing was seen in the spectra of the type IIn SN 1998S (Bowen et al. 2000), although in this case the wing spanned only ~ 350 km s^{-1} from the absorption minimum. Both Bowen et al. (2000) and Chugai et al. (2002) credit this "shelf" of absorption to the CSM around the explosion and Chugai et al. (2002) invoked radiative driving to accelerate relatively slow moving CSM material ($40 - 50$ km s^{-1}) to these velocities. In our case, if the blue component is due to CSM absorption, we would require either stronger radiative driving or a faster CSM wind speed. The CSM wind speed found for SN 1998S was typical for a RSG wind, whereas the speeds required for PS1-12bv would be more indicative of a wind from a WR or LBV star. PS1-12bv is one of our four most luminous objects and is very similar photometrically to PS1-11qr, PS1-11bbq, PS1-13duy and PTF 09uj (which was hypothesized to be due to the shock breakout from an optically thick wind; Ofek et al. 2010). This broad feature may therefore point to a progenitor star that possesses a strong wind in the years before explosion for these transients.

Alternatively, this feature could be explained by either a complex ISM absorption system along the line of sight or an outflow from the host galaxy. In order to investigate this possibility, we fit pairs of Mg II ($\lambda\lambda$ 2796,2803) doublets with varying redshifts and full-width at half-maximum (FWHM) to this portion of the spectrum. An example fit is shown in the right panel of Figure 3.14. Blue and green lines show the individual Mg II ($\lambda\lambda$ 2796,2803) doublets, and the red line shows their sum. In all cases, we required absorption components that were both resolved and significantly broader than typical ISM absorptions ($\lesssim 100$ km s^{-1}).

3.6 Host Galaxies

Our method of selecting rapidly-evolving SN was not designed to select transients from a single explosion mechanism/progenitor. However, on the whole, the objects we identified within the PS1-MDS have a similar set of photometric and spectroscopic properties (blue colors, spectra dominated by continua, etc.). We now turn to the host galaxies of these explosions to see what insight they can provide into their progenitor populations. In Figure 3.15 we display the host galaxy spectra obtained for six of the transients. These are supplemented by the host galaxy lines present in the explosion spectra (Figure 3.13). Nebular emission lines, indicative of active star formation, are found in the spectra of all ten galaxies. In the sections below we examine the masses, metallicities, star formation rates, and explosion site offsets of the host galaxies in comparison to the hosts of other classes of transients.

3.6.1 Mass

After correcting the host griz-band photometry for Milky Way extinction we use the FAST stellar population synthesis code (Kriek et al. 2009) to calculate the total stellar mass contained within our host galaxies. Our models utilized the Maraston (2005) stellar library and assumed an exponential star formation history and Salpeter IMF. The total extinction was restricted to < 0.05 (motivated by the Balmer decrement in our highest quality host spectra and the blue colors of our transients; the assumed extinction does not significantly affect the resulting mass). The results from this analysis are listed in Table 3.5.

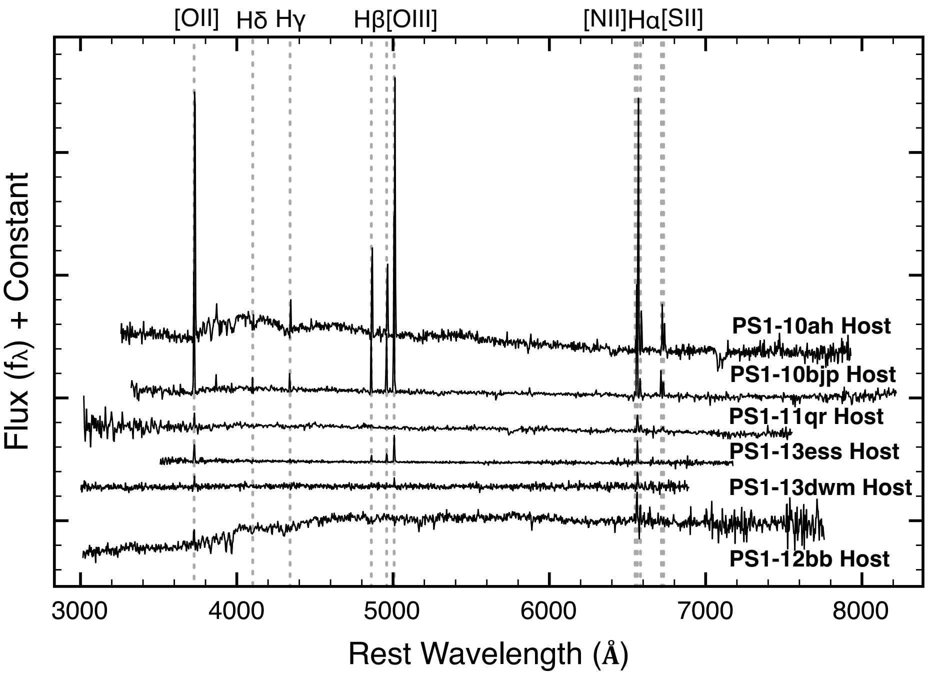

Figure 3.15.—: Host galaxy spectra for six of the gold/silver transients. Nebular emission lines are labeled by dashed vertical lines.

The total stellar mass in the host galaxies ranges from $8.0 < \log (M/M_\odot) < 10.6$ with a median value of $\log (M/M_\odot) = 9.0$. In the first panel of Figure 3.16 we plot the cumulative distribution of our host masses in comparison to the core collapse SN (CC-SN) and long gamma-ray burst (LGRB) samples from Svensson et al. (2010). A larger fraction of our sample's hosts appear at relatively low masses in comparison to the core collapse SN. A Kolmogorov-Smirnov (KS) test yields a 14% (37%) probability that the rapidly-evolving transients hosts are drawn from the same population as the CC-SN (LGRB) hosts. Thus, while our host galaxies skew slightly toward lower masses, there is no statistical evidence for a different parent population from either LGRBs or CC-SN.

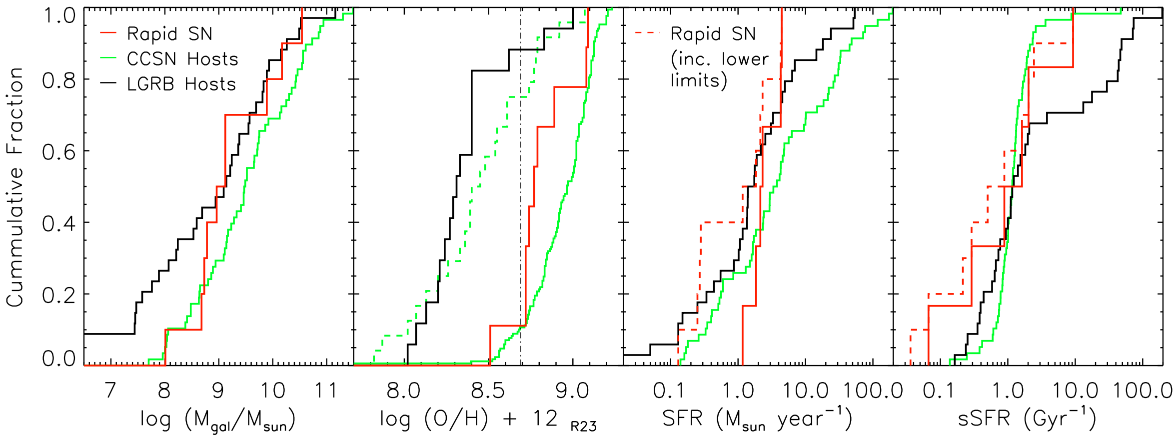

Figure 3.16.—: Cumulative distributions of various host galaxy properties: stellar mass, metallicity, star formation rate, and specific star formation rate. In all panels the red line(s) represents the rapid evolving SN presented in this work. In panels 3 and 4 the solid red line represents the six gold/silver objects with host galaxy spectra and the dashed red line includes lower limits based on the explosion spectra of the remaining four objects. Also shown are distributions from LGRBs and core-collapse SN (black and green lines, respectively; see text for references). The dashed green line in panel 2 is the *untargeted* Type Ibc SN from Sanders et al. (2012). The vertical dashed line in panel 2 signifies solar metallicity.

3.6.2 Metallicity

Using the Markov Chain Monte Carlo method described in Sanders et al. (2012) we measure the emission line fluxes and metallicities of nine of the host galaxies. Due to the varying wavelength coverage and quality of our spectra, it was not possible to use the same strong line diagnostic for all of the galaxies. In Table 3.5 we list both the measured value and the diagnostic utilized. For the purposes of comparison, we then convert all of the values to the R23 system of Kewley & Dopita (2002) using the calibration relations from Kewley & Ellison (2008).

Many of the host galaxies have metallicities that are roughly solar, with a median value of log (O/H) + 12 = 8.8. In the second panel of Figure 3.16 we plot their cumulative distribution. Our hosts are offset to a significantly higher metallicity than either LGRB hosts (Svensson et al. 2010; Savaglio et al. 2009; Levesque et al. 2010; Levesque et al. 2010; Graham & Fruchter 2013) or the untargeted type Ibc hosts from Sanders et al. (2012) (black line and dashed green line, respectively) with a $\lesssim$0.5% probability of being drawn from the same population. The entire core-collapse SN sample from Kelly & Kirshner (2012a) (solid green line) is shifted to even higher metallicities than our sample, although we caution a fraction of these events were discovered by targeted surveys (which bias towards higher metallicities).

3.6.3 Mass-Metallicity Relation

In Figure 3.17 we plot the stellar mass versus metallicity for nine of the transients (red stars) versus the $\sim$ 53000 SDSS star forming galaxies from SDSS (Tremonti et al. 2004, shaded regions). Also shown are the low redshift LGRB hosts from Levesque et al. (2010, black). *The hosts of the PS1-MDS rapidly-evolving SN appear to be consistent with the bulk of star-forming galaxies in SDSS.* This is in contrast to the hosts of LGRBs and type I SLSN, both of which have been shown to obey a relation in the mass-metallicity plane that is offset below the bulk of star-forming galaxies (Levesque et al. 2010; Lunnan et al. 2014).

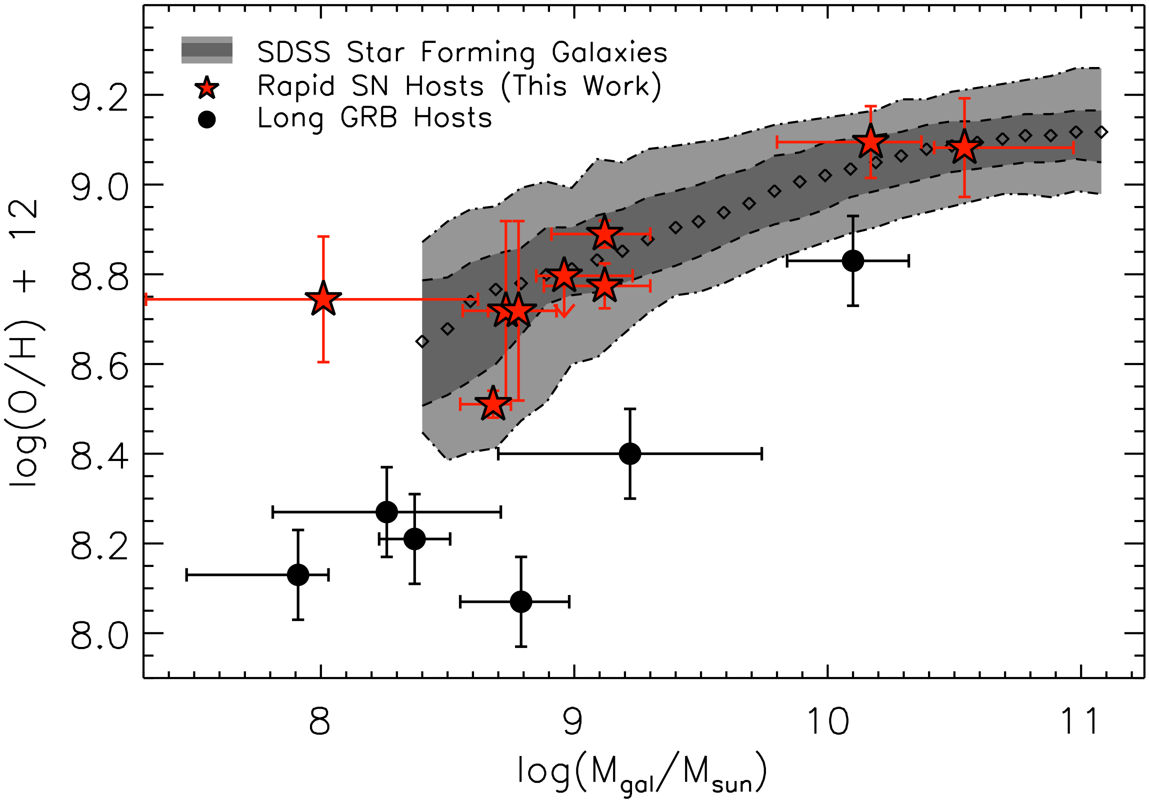

Figure 3.17.—: Mass-metallicity relation for nine gold/silver transients (red stars). Also plotted are contours representing the 53000 SDSS star forming galaxies from Tremonti et al. (2004) (shaded region, lines represent the 2.5, 16, 50, 84, and 97.5 percentile of the distribution in each bin) and the long duration GRB hosts from Levesque et al. (2010). Unlike the LGRB hosts, which are offset to lower metallicities, our sample is consistent with being drawn from the greater SDSS population.

3.6.4 Star Formation Rates

We estimate host galaxy star formation rates (SFRs) for the six events for which we possess galaxy spectra (Figure 3.15) by measuring their Hα line fluxes and applying the relation of Kennicutt (1998). In each case we apply a rough correction for the covering fraction of our spectra by scaling to our PS1 photometry of the hosts. We do not correct for intrinsic extinction. In the three cases where both Hα and Hβ are detected the decrement is reasonably consistent with zero extinction. The resulting SFRs range from $1 - 5$ M$_\odot$ yr^{-1} and are listed in Table 3.5. For the four remaining objects we may place lower limits on the SFR by measuring the Hβ emission line flux from the explosion spectra (Figure 3.13) and assuming zero extinction. We do not attempt to correct for the covering fraction in these cases. The lower limits range from $0.1 - 0.3$ M$_\odot$ yr^{-1}. In the second and third panels of Figure 3.16 we plot the cumulative distribution of our SFRs and specific SFRs in comparison to the CC-SN and LGRB hosts from Svensson et al. (2010). Although the small number of events limits the conclusions we can draw, there is no statistical evidence that the samples are drawn from different progenitor populations. The star formation rates measured for our hosts are clustered around the median value observed for both CC-SN and LGRBs.

3.6.5 Explosion Site Offsets

Using the PS1 centroid positions (good to $\sim 0.1''$) we measure the separation between the location of the transient and the center of its host galaxy. The cumulative distribution of these offsets (in physical units) are shown in the left panel of Figure 3.18 (red line). Also shown are distributions of type Ia, type Ibc and type II SN (Prieto et al. 2008, blue, green, and cyan, respectively), short-duration GRBs (Fong & Berger 2013, dashed black; SGRBs), and LGRBs (Bloom et al. 2002, solid black).

In the right panel of Figure 3.18 we normalize these offsets by the $g-$band half light radius of the host. Also shown are type Ia SN (Galbany et al. 2012, blue), type Ibc and type II SN (Kelly & Kirshner 2012a, green and cyan, respectively) and the same LGRB and SGRB samples as described above. For objects with high signal to noise SDSS detections, we use the Petrosian half-light radius from SDSS DR9. For others (PS1-11bbq, PS1-13duy, and PS1-13ess), we estimate the half light radius based on the light within a $3''$ radius of the centroid location within the PS1 deep stacks (we caution that these values are more uncertain). Both the physical and normalized offsets are listed in Table 3.5. Our sample most closely resembles the normalized offsets of type Ibc and type II SN, indicating that, at least in this context, our explosion sites are consistent with the environments in which one can expect to find massive stars.

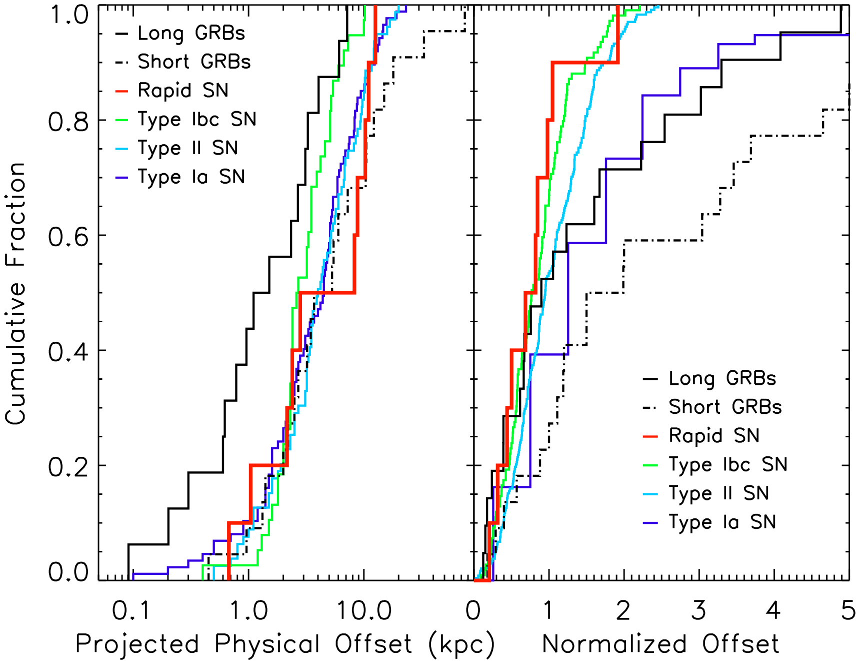

Figure 3.18.—: Projected host offsets for our sample (red) in comparison to other astronomical transients. *Left Panel:* physical offsets *Right Panel:* offsets normalized by the g-band half-light radii of the hosts. Our sample most closely traces the distribution of core-collapse SN offsets.

Table 3.5. Host Galaxy Properties

Event	$m_{\mathrm{obs,i}}$ (mag)	log (O/H) + 12[a] (measured)	Method[b]	$\log(M_{\mathrm{gal}}/M_{\odot})$	SFR $M_{\odot}$ yr^{-1}	sSFR Gyr^{-1}	Offset (arcsec)	Offset (kpc)	Norm. Offset[c]
PS1-10ah	18.08 (0.02)	8.49 (0.03)	PP04N2	$9.12^{+0.18}_{-0.21}$	∼1.2	∼0.9	0.42	0.68	0.21
PS1-10bjp	19.22 (0.03)	8.38 (0.05)	PP04N2	$9.12^{+0.18}_{-0.24}$	∼2.1	∼1.6	0.95	2.39	0.85
PS1-11qr	19.80 (0.06)	8.85 (0.08)	PP04N2	$10.17^{+0.20}_{-0.37}$	∼4.3	∼0.3	1.54	12.58	0.98
PS1-11bbq	24.40 (0.15)	8.67 (0.14)	Z94	$8.01^{+0.61}_{-0.70}$	>0.3	>2.4	0.47	8.81	1.05
PS1-12bb	16.59 (0.01)	8.79 (0.11)	PP04N2	$10.54^{+0.43}_{-0.12}$	∼2.3	∼0.06	4.93	10.99	1.92
PS1-12bv	22.01 (0.20)	···	···	$9.89^{+0.62}_{-0.52}$	>0.3	>0.03	0.97	10.29	0.50
PS1-12brf	22.04 (0.21)	8.6 (0.2)	KD02	$8.73^{+0.20}_{-0.17}$	>0.3	>0.5	0.42	2.90	0.69
PS1-13duy	22.20 (0.04)	8.6 (0.2)	KD02	$8.78^{+0.15}_{-0.12}$	>0.1	>0.2	0.33	2.16	0.44
PS1-13dwm	21.38 (0.08)	< 8.4	PP04N2	$8.96^{+0.27}_{-0.01}$	∼1.9	∼2.0	1.40	8.28	0.82
PS1-13ess	22.54 (0.08)	8.43 (0.03)	M91	$8.68^{+0.07}_{-0.13}$	∼4.5	∼9.3	0.14	1.04	0.32

[a] Metallicity measured from host galaxy spectra. Diagnostics utilized varied between objects

[b] Diagnostic used to obtain column 2. PP04N2 = Pettini & Pagel (2004); Z94 = Zaritsky et al. (1994); KD02 = Kewley & Dopita (2002); M91 = McGaugh (1991)

[c] Offset normalized by the g−band half light radius of the host galaxy.

3.7 Volumetric and Relative Rates

In this section we use information on the true cadence and sensitivity obtained by the PS1-MDS between Dec. 2009 and March 2014 to calculate the volumetric rate of rapidly-evolving transients similar to those presented in this work. Because these objects were identified based on their light curve morphology, rather than spectroscopic classification, we avoid the observer-dependent bias that results because resources limit our spectroscopic follow-up to roughly 10% of the transients discovered in the PS1-MDS.

Because their timescale is rapid, even short observing gaps due to poor weather or maintenance can have a significant effect on the efficiency with which the survey detects these transients. We therefore use a Monte Carlo approach similar to that utilized in Quimby et al. (2012, 2013) to calculate the efficiency with which each PS1-MDS field can recover these transients as a function of distance.

We begin by constructing light curve and temperature evolution templates based on the gold transients (Figure 3.1). We then construct a luminosity function which consists of an intrinsic gaussian distribution modified by an exponential function to account for host galaxy absorption. In following with Quimby et al. (2013) we adopt $\mathrm{P(A_V)} \propto \mathrm{e}^{\mathrm{A_V}/\tau}$ with $\tau = 0.6$ (Hatano et al. 1998) for the host galaxy absorption. As a starting point for the intrinsic distribution we adopt a gaussian with the same mean and variance as the (rest-frame) peak magnitudes of our gold sample after performing a V/Vmax correction for the Malmquist bias. As a check we performed several Monte Carlo simulations distributing 500 objects drawn from this distribution evenly in space. The objects with apparent magnitudes > 1.5 mag above the nominal PS1 detection limit (a rough proxy for detectability) agree well with our observed transients in both luminosity and distance.

The nominal values for the intrinsic (i-band) gaussian distribution we adopt below are $\mu = -17.2$ mag and $\sigma = 1.0$ mag.

For each PS1-MDS field we then determine the detection efficiency within 140 distance bins between z=0.005 and z=0.7. We performed 10,000 iterations of the following process *within each distance bin:* (i) randomly select one of the six templates; (ii) choose a peak absolute magnitude from the aforementioned luminosity distribution; (iii) choose a random distance *within* the distance bin; (iv) k-correct the template light curves, assuming the spectra can be approximated as a blackbodies described by the temperature evolution template; (v) choose a random explosion epoch between Dec. 2009 and March. 2014; (vi) map the resulting explosion onto the *actual dates* PS1 observed each filter for that PS1-MDS field; (vii) assign random noise to each epoch that is pulled from the actual distribution of noises obtained by transients found in the PS1-MDS on that epoch in that filter; and finally (viii) run the resulting synthetic data through the same light curve selection criteria described in Section 3.2. The efficiency within each distance bin is then calculated as the fraction of the 10,000 iterations that were recovered.

In Figure 3.19 we plot the resultant efficiencies for each PS1-MDS field (colored lines) as well as the survey as a whole (solid black line). The survey detection efficiencies range from $\sim$11% near z $\sim$ 0.1 to $\lesssim$0.1% at z $\sim$0.7. The quoted efficiencies are for the entire duration of the PS1 survey (Dec. 2009 to March 2014), while any given PS1-MDS field is only observed for roughly half of this time period. The in-season efficiency at z$\sim$ 0.1 for the survey was approximately 25%. This demonstrates how much influence small, in-season, observing gaps can have on the detection of such rapid transients.

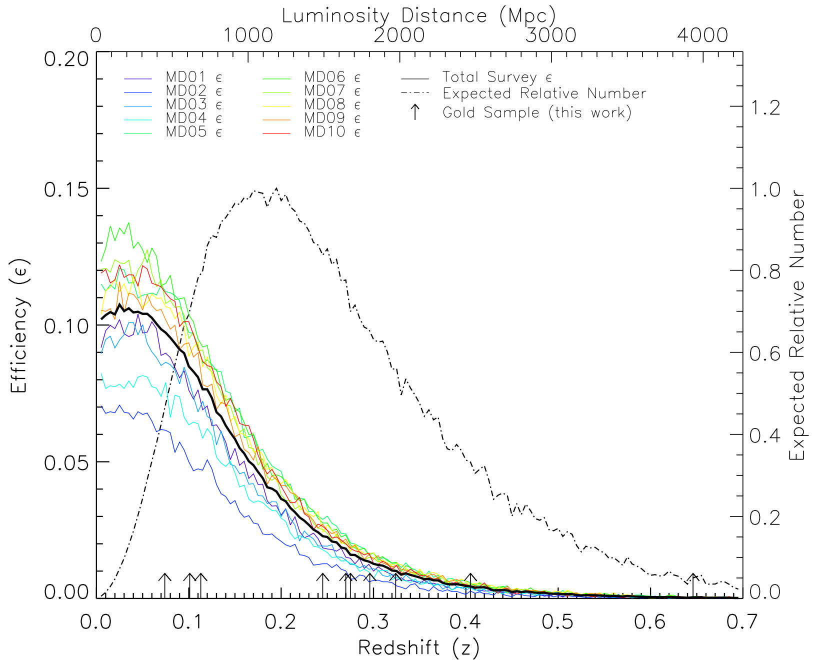

Figure 3.19.—: PS1-MDS rapid-transient detection efficiencies for our rate calculation. Solid lines indicate detection efficiencies for individual PS1-MDS fields as a function of redshift (bottom axis) or luminosity distance (top axis). A black solid line indicates the detection efficiencies for the survey as a whole, which peak around 11% at z=0.1. The dashed black line indicates the distance at which we expect our detections to be located. This peaks at z=0.2. The actual distances of the PS1-MDS transients are shown as arrows on the bottom axis.

Using these efficiencies we calculate the volumetric rate of these rapid and luminous transients as:

$$R = \frac{N}{\sum \epsilon_i V_i t_i} \tag{3.1}$$

where ϵ_i, V_i, and t_i are the efficiency, co-moving volume, and proper time within each distance bin and N is the number of transients actually detected in the PS1-MDS. We calculate a rapidly-evolving transient volumetric rate of $4800 - 8000$ events yr^{-1} Gpc^{-3}.

The quoted range comes from assuming either 6 detections (the gold transients) or 10 detections (the gold plus bronze transients). Our rate calculation does not include the silver transients because they would not be selected by the criteria given in Section 3.2 (which were the basis for how our efficiencies were derived). This rate is approximately $24 - 40$ times higher than the rate derived by Quimby et al. (2013) for super-luminous SN-like objects and is approximately $4 - 7\%$ of the core-collapse SN rate at z$\sim$0.2 found by Botticella et al. (2008).

In Figure 3.19 we also plot the expected relative number of detected events as a function of distance (dashed black line). This is calculated by multiplying the efficiency at each distance by the relative volume and relative proper time in that bin. We expect that a majority of the PS1-MDS detected transients should be found around z$\sim$0.2. Black arrows along the bottom axis represent the redshifts of our spectroscopic sample. A KS test between the observed and expected redshift distributions yields a 50% probability that they are drawn from the same population.

The largest sources of uncertainty in these derived rates are our assumed luminosity function and the effects of host galaxy extinction. In order to assess these errors, we run additional iterations of procedure described above, varying both the parameters that describe the intrinsic luminosity function and the parameter τ which describes host galaxy absorption. Varying τ between 0.5 and 0.7 produced ± 500 events yr^{-1} Gpc^{-3} in the derived rates (an $\sim 8\%$ variation), while neglecting host extinction entirely yields rates of $3500 - 5800$ events yr^{-1} Gpc^{-3}. Introducing small variations to the functional form of the intrinsic luminosity function (high and low luminosity cutoffs, a lognormal distribution, etc.) produces only slightly variations in the derived rates ($\lesssim$8%). Increasing the mean luminosity from -17.2 to -17.5 (which although less ideal, still produces reasonable agreement with our observed sample) lowers our derived rates to $3500 - 5800$ events yr^{-1} Gpc^{-3}, a factor of 1.4 decrease.

In addition, the `photpipe` pipeline requires a human to examine every potential detection and select real astronomical events. As a byproduct of this process, some fraction of real transients will be overlooked. The chance that a given event will be missed is likely higher for transients with shorter overall timescales. It is beyond the scope of the current paper to address this factor, but any such correction would act to increase our derived rates.

Finally, we address, from a rates perspective, the possibility that no objects of a similar class to the rapidly-evolving SN 2005ek and SN 2010X were discovered in the PS1-MDS. Only PS1-12bb possesses a similar luminosity and red colors but its spectra do not exhibit the strong early on-set of the Ca II NIR features that was a distinctive characteristic of those events. Using the data of Drout et al. (2013) we construct light curve and temperature templates for SN 2005ek and run them through a similar procedure as described above, pulling from a Gaussian luminosity distribution with $\mathrm{M_r} = -17.5 \pm 0.5$. We find that, due to the lower peak luminosity and red colors of SN 2005ek, the efficiency with which the PS1-MDS can detect similar transients plummets to zero by $z{\sim}0.2$. In addition, the PS1-MDS has a small effective volume at low redshifts. As a result, if the intrinsic rate of SN 2005ek-like events is similar to that for the bluer, more luminous, objects that make up our sample we would only expect to find $\lesssim$1 over the duration of the PS1-MDS. *The reason the PS1-MDS sample of rapidly-evolving SN is dominated by luminous, blue events (as opposed to previously discovered, faint, red events) is not due to differences in their intrinsic rates, but rather to the efficiency with which the pencil beam observing strategy of the PS1-MDS detects objects of each class.*

3.8 Discussion: Power Sources and Progenitors

In the sections above, we described the basic properties of the PS1-MDS rapidly-evolving transients, their host galaxies, and their volumetric rates. We now examine the nature of these transients. We discuss several means by which the optical emission may be powered, and the implications of each on the progenitor systems. Specifically, we examine SN powered by radioactive decay, SN powered by shock breakout emission/interaction, super-Eddington flares from tidal disruption events, and magnetars formed during NS-NS mergers.

3.8.1 Limits on Radioactive Decay

As described in Section 3.5, the continuum dominated spectra of our objects more closely resemble those of explosions powered by cooling envelope emission or interaction than those powered by radioactive decay. *In addition, the rapid timescale and high peak luminosity of several of our events are difficult to reconcile with an explosion powered entirely by* ^{56}Ni. This is demonstrated in Figure 3.20 where we plot the rise time versus peak luminosity for the gold/silver transients along with SN from the literature that are powered by radioactive decay. Using the models of Arnett (1982) and Valenti et al. (2008) we map these parameters onto a grid of ^{56}Ni mass ($M_{\rm Ni}$) and a parameter proportional to the total ejecta mass ($M_{\rm ej}$) and kinetic energy ($E_{\rm K}$) of the explosion. These results rely on the assumptions of spherical symmetry, centrally localized ^{56}Ni, and an optically thick ejecta.

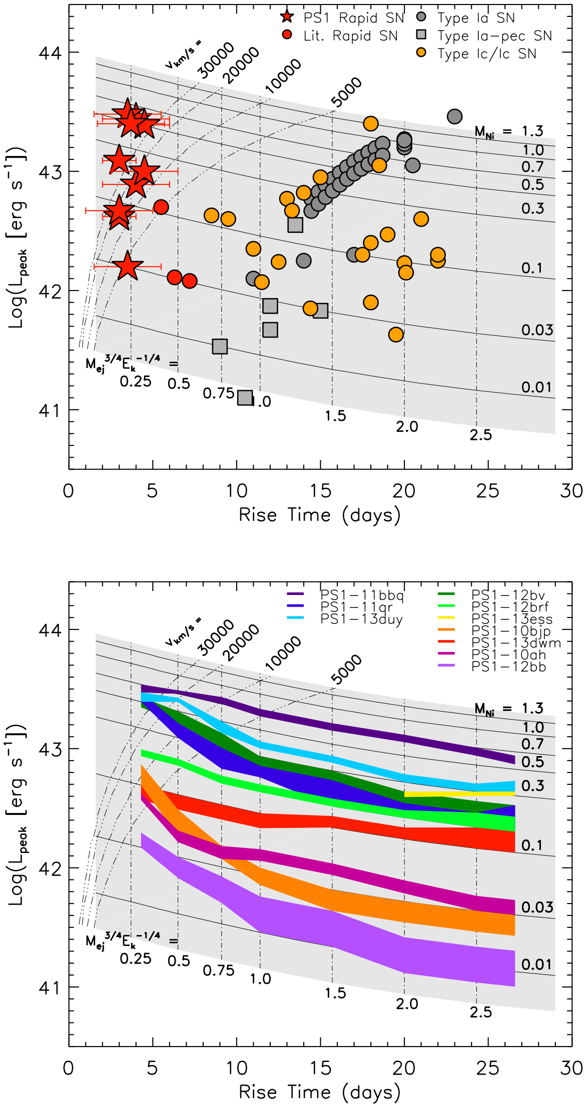

Figure 3.20.—: Physical constraints for ^{56}Ni powered explosions. *Top Panel:* We map the physical parameters M_{Ni} and $M_{ej}^{3/4}$ $E_K^{-1/4}$ onto the observable parameters of peak luminosity and rise time. On this we plot the gold/silver transients (red stars) and objects from the literature that are powered by radioactive decay (type Ia - grey circles; type Ib/Ic - orange circles; type Ia-pec - grey squares; rapid events - red circles). The curved lines represent locations where $M_{Ni} = M_{ej}$ for a given ejecta velocity. Any object above and to the left of a given line is unphysical for that velocity. *Bottom Panel:* Colored regions represent the upper limit on the amount of ^{56}Ni which could power a second peak (such as that observed in SN 1993J) in the light curves of our objects.

The M_{Ni} required to reproduce the peak luminosity of our events span a wide range ($0.03\ M_\odot < M_{Ni} < 0.7\ M_\odot$). This range is similar to that spanned by type Ib/Ic SN, however, the devil is in the details. The degeneracy between M_{ej} and E_K can be broken by using the photospheric velocity of the explosion near maximum light. For a given velocity, a smaller characteristic time implies a lower ejecta mass. Thus, for objects with short overall timescales, it is possible to obtain the unphysical result that $M_{Ni} > M_{ej}$.

The photospheric velocities of our objects are unknown, so in Figure 3.20 we plot curved lines that represent $M_{Ni} = M_{ej}$ for a variety of velocities. Any object to the upper left of a given line is physically disallowed for the simplified photospheric model. While the radioactively powered explosions from the literature fall comfortably in the region where $M_{Ni} << M_{ej}$, several of our transients would require relatively high ejecta velocities ($\gtrsim 0.1c$) to remain physical. In all cases the rise times and peak luminosities imply that the required nickel mass makes up a significant fraction of the total ejecta mass.

One caveat is that the models represented in Figure 3.20 assume the ejecta is optically thick. If this assumption breaks down, incomplete gamma-ray trapping at early times can produce a faster initial light curve evolution (Drout et al. 2013). For our objects, we can estimate the level of gamma-ray trapping required such that a $^{56}\mathrm{Co} \rightarrow {}^{56}\mathrm{Fe}$ decay tail would fall below our late-time PS1 photometry limits. For five of our ten gold objects, the late-time PS1 limits *require* incomplete gamma-ray trapping at early times if the peak is truly powered by ^{56}Ni. Using the parameterization of Valenti et al. (2008) to relate the level of trapping to M_{ej} and E_k we find that only two of our objects (PS1-10ah and PS1-12bb) have *lower limits* for M_{Ni}/M_{ej} that are less than 0.3.

Thus, if our objects are powered primarily by ^{56}Ni, they would require either (1) progenitors that can produce a relatively small ejecta mass composed almost entirely of ^{56}Ni — *a scenario that seems inconsistent with the lack of strong UV line blanketing in our spectra* — or (2) a explosion scenario in which either a significant amount of the radioactive material is mixed into the outer ejecta layers or there is a significant breakdown in spherical symmetry.

We are therefore converging on a situation where the early emission from many of our rapidly-evolving events is powered by a source other than radioactive ^{56}Ni. In this case, it is useful to place limits on the amount of ^{56}Ni that could power a subsequent peak in the light curve (such as that observed in SN 1993J or type Ibn SN iPTF13beo; Gorbikov et al. 2014) without exceeding our observed light curve points or late-time limits. SN 1993J possessed two peaks of similar optical luminosity. The first was due to cooling envelope emission and the second to the radioactive decay of $\sim$0.07 M$_\odot$ of ^{56}Ni. Only one of our objects, PS1-13ess, shows evidence for a second peak in its light curve. The $M_{\rm Ni}$ required to power this second peak for PS1-13ess is $0.2 - 0.3$ M$_\odot$ (depending on the rise time, which is not well constrained). This is approximately four times higher than the amount that powered SN 1993J. In Figure 3.20 we use our observations to put upper limits on the amount of ^{56}Ni that could power such a secondary peak in the remainder of our transients.

For each object, we present a colored region which represents the maximum nickel mass that could power an optically thick explosion with a given rise time. For three of our objects (PS1-10ah, PS1-10bjp, and PS1-12bb) we can put an upper limit on the amount of ^{56}Ni that could power a secondary peak to $\lesssim$0.03 M$_\odot$. This is lower than the amount inferred for all but a few type Ibc and peculiar type Ia SN. Several type II SN have been constrained to have $M_{Ni} < 0.03\ M_{\odot}$, although over half of those analyzed in Hamuy (2003) have M_{Ni} larger than this. The limits on the more luminous transients are less constraining in comparison to type Ib/Ic SN.

3.8.2 Shock Breakout and Interaction

The blue colors and spectra of several of our objects resemble those observed in SN powered by cooling envelope emission or interaction with a dense CSM (e.g. type IIb, type IIn and type Ibn SN, several of which have peak luminosities and timescales which also resemble the PS1 transients presented here). In this section we examine both the shock breakout from the surface of a star and a shock breakout that occurs within an optically thick wind surrounding the progenitor as possible power sources.

Shock Breakout from the Surface of a Star

First, we consider the case where these events are powered by the cooling envelope portion of the explosion of a massive star. While the shock breakout from a massive star lasts only a matter of seconds (WR stars) to hours (RSGs) the process shock heats the ejecta, which then cools and recombines, giving rise to optical emission which is independent from later emission powered by radioactive decay. The luminosity reached by the cooling envelope emission can give insight into the radius of the progenitor, with larger progenitors yielding more luminous events (due to both a larger emitting surface and reduced effects of adiabatic cooling), while the timescale of the event is related to the envelope mass that is cooling/recombining (see, e.g., Nakar & Sari 2010; Rabinak & Waxman 2011).

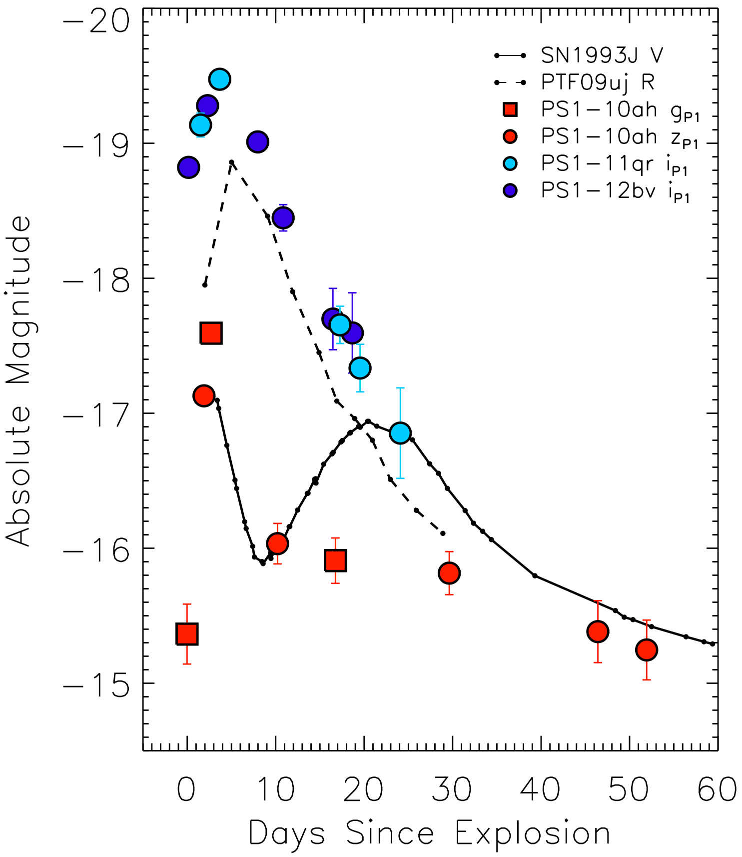

Figure 3.21.—: A comparison of the light curves of several gold transients to events from the literature thought to be powered by varieties of shock breakout/cooling envelope emission. PS1-10ah shows a similar initial decline to the type IIb SN 1993J, but lacks a later peak powered by radioactive decay. PS1-11qr, PS1-12bv, and a number of the other luminous events are very similar to PTF 09uj, which was hypothesized to be due to the shock breakout from an optically thick wind (Ofek et al. 2010).

Several of our transients (e.g. PS1-10ah, PS1-12brf, PS1-13dwm, PS1-13ess) have peak luminosities and timescales that are similar to those observed for the cooling envelope portion of type IIb SN with extended progenitors. In Figure 3.21 we compare the light curve of SN 1993J to several of our gold sample objects and see that the initial decline of SN 1993J is well matched to the initial decline of our object PS1-10ah. This is consistent with the initial light curve signature expected for the explosion of progenitors with extended low-mass envelopes (Nakar & Piro 2014). However, with the exception of PS1-13ess, we *do not* observe a second peak due to the decay of ^{56}Ni as is observed in other type IIb SN. In fact, these intermediate luminosity objects are the transients for which we can place the strictest limits on the amount of ^{56}Ni that powers a secondary peak. For PS1-10ah we constrain $M_{\rm Ni} \lesssim 0.03 M_\odot$, which is more than a factor of two lower than that found for the second peak of SN 1993J (Woosley et al. 1994). This implies that some *stripped envelope* core-collapse SN may eject a very small amount of radioactive isotopes. A similar point was raised in Kleiser & Kasen (2014) who modeled the rapidly declining type Ic SN 2010X as an *oxygen* recombination event.

While this power source seems reasonable for our intermediate luminosity events, a number of our other transients (PS1-11qr, PS1-11bbq, PS1-12bv, and PS1-13duy) possess peak luminosities that are a factor of ten higher than that observed for SN 1993J (see Figure 3.21). Woosley et al. (1994) invoked a progenitor radius of $\sim 4 \times 10^{13}$ cm in order to reproduce the light curve of SN 1993J. This is only a factor of two below the radii of the largest known RSGs (Levesque et al. 2009). Thus, if these events can be explained by the cooling envelope emission after shock breakout from the *surface* of a massive star, we would seem to require a progenitor that is both extremely extended, but also possesses a relatively low envelope mass. Alternatively, these events could represent cases where the shock breakout occurs not directly from a stellar surface, but inside a dense, optically thick, wind surrounding the star. This hypothesis was also put forth for the rapidly-evolving type IIn event, PFT09uj (Ofek et al. 2010), whose light curve bears striking resemblance to our higher luminosity events (Figure 3.21).

Shock Breakout within a Dense Wind

The case of a shock breakout from a dense wind has been examined from a theoretical perspective by Chevalier & Irwin (2011), Balberg & Loeb (2011), Ofek et al. (2010) and Ginzburg & Balberg (2014). For a wind environment, the density profile around the star goes as $\rho_w \propto r^{-2}$. While the actual situation for the case of an optically thick mass-loss region may be more complex (e.g. due to shell ejections), this approximation has been made in previous works and will also be utilized here. These models have been applied to explain a number of super-luminous SN (both type I and type II; Chevalier & Irwin 2011) as well other type IIn SN such as SN2009ip (Margutti et al. 2014b) and PTF 09uj (Ofek et al. 2010) and the first peak of type Ibn iPTF13beo (Gorbikov et al. 2014).

In their appendix, Margutti et al. (2014b) solve the equations given in Chevalier & Irwin (2011) for the case where the wind radius, R_w, is larger than the radius at which diffusion becomes important, R_d. These equations give the ejecta mass and kinetic energy of the explosion, as well as the opacity and density of the mass-loss region (as parameterized by a mass-loss rate $\dot{M}$) in terms of three observables: the rise time of the explosion ($t_{\rm rise}$), the energy radiated on the rise ($E_{\rm rad}$), and the radius at breakout ($R_{\rm bo}$). Using our first measured blackbody radius for each transient (Figure 3.22) as an order of magnitude estimate for $R_{\rm bo}$, we can utilize these models to estimate the physical parameters of the explosion and mass-loss region surrounding the progenitor. From Figure 3.22 we see that the breakout radius for our events is relatively small. All the events (including those whose first radius constraint was measured at maximum light) have values below that measured for SN 2009ip and an order of magnitude smaller than those measured for several SLSN (Chevalier & Irwin 2011).

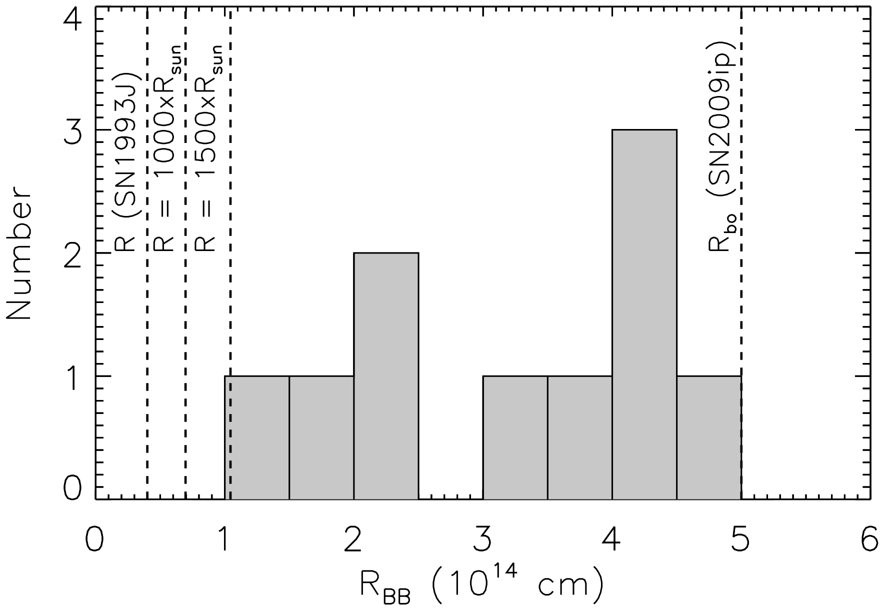

Figure 3.22.—: Histogram of the first radius constraint obtained for each transient in Section 3.4. Vertical lines mark the radius found for the progenitor of SN 1993J (Woosley et al. 1994), 1000 and 1500 $R_\odot$ (the largest known RSGs) and the radius of shock breakout found for the type IIn SN 2009ip (Margutti et al. 2014b).

These models are degenerate in $M_{ej}E^{-2}$ and we find values for the ejecta mass ranging from 1.0 $(\frac{E}{10^{51}\mathrm{ergs}})$ $M_\odot \lesssim M_{ej} \lesssim 45.0$ $(\frac{E}{10^{51}\mathrm{ergs}})$ $M_\odot$. In comparison, Margutti et al. (2014b) found $M_{ej} = 50.5$ $(\frac{E}{10^{51}\mathrm{ergs}})$ $M_\odot$ for the 2012b outburst of SN2009ip. In Figure 3.23 we plot diagonal lines which represent the value of $M_{ej}E^{-2}$ obtained for each object. The shaded gray region in each panel represents an excluded region where the explosion energy (vertical axis) is lower than the total radiated energy calculated in Section 3.4. Horizontal lines in each panel then represent explosion energies that are 10 and 100 times the radiated energy.

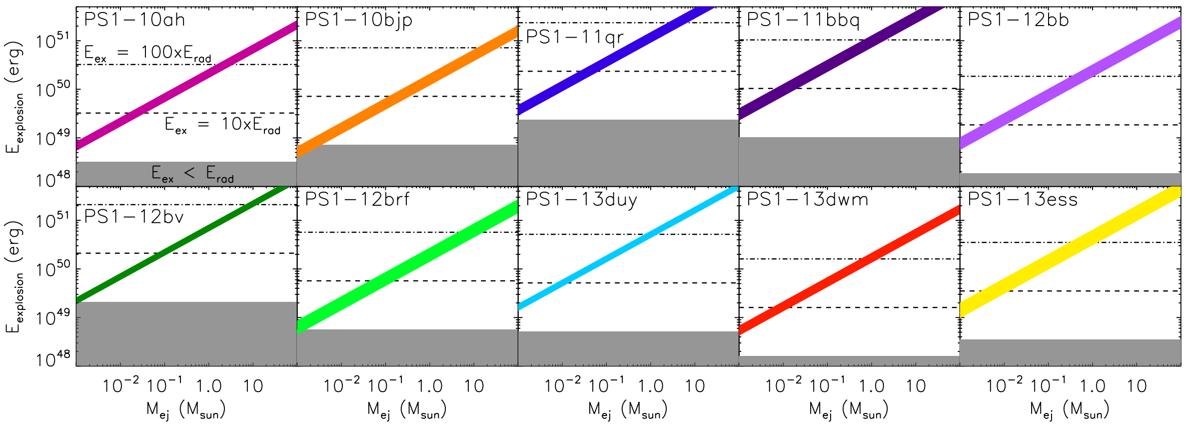

Figure 3.23.—: Values of $M_{ej}E^{-1/2}$ derived for the gold/silver transients for the case of a shock breakout from a dense, optically thick, wind. The width of the colored region gives the error inferred for $M_{ej}E^{-2}$ based on the errors for each of our observables. Grey shading represents an excluded region where the explosion energy is less than the observed radiated energy. Horizontal lines in each panel represent where $E_{explosion} = 10\times E_{rad}$ and $100\times E_{rad}$ for each object.

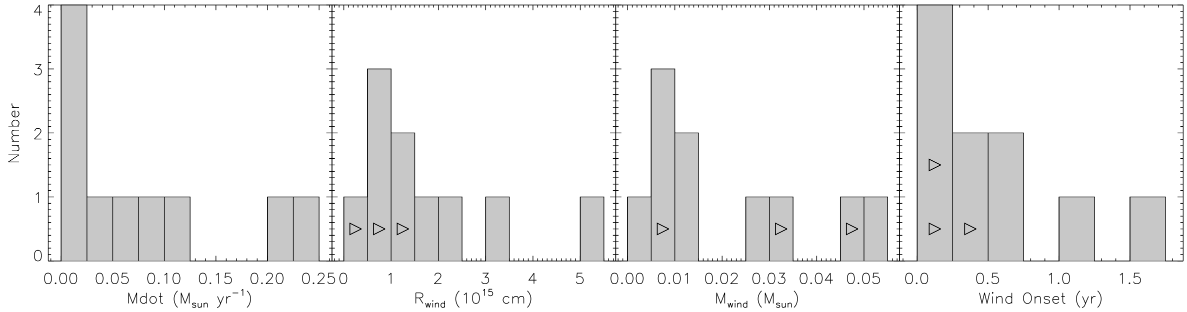

Figure 3.24.—: Histograms of the physical parameters derived for the mass-loss region surrounding each object in the case of a shock breakout from a dense, optically thick, wind. Panels 1,2,3 and 4 display the mass-loss rates inferred from the explosion, the outer radius of the region of dense mass-loss, the total mass contained in the region of dense mass-loss, and the inferred time for the onset of the mass-loss (prior to the main explosion), respectively. Both the mass-loss rates (panel 1) and wind onset times (panel 4) listed assume a wind velocity of 1000 km s^{-1} (as measured from a potential CSM absorption in the spectrum of PS1-12bv). The results scale linearly for other assumed velocities.

For these models we infer mass-loss rates ranging from 2 $\times 10^{-3}(\frac{\rm v_w}{1000 \rm kms^{-1}})$ $\rm M_\odot$ yr^{-1} $\lesssim \dot{\rm M} \lesssim$ 2 $\times 10^{-1}(\frac{\rm v_w}{1000 \rm kms^{-1}})$ $\rm M_\odot$ yr^{-1}. A histogram of these values are shown in the first panel of Figure 3.24. We have normalized to a wind speed of 1000 km s^{-1} based on the tentative CSM absorption observed in PS1-12bv (Section 3.5). These values exceed the mass-loss rates of WR stars (typically $\lesssim 10^{-4}$ $\rm M_\odot$ yr^{-1}) and may hint at a more complex or eruptive mass-loss history.

In order to obtain more information about the mass-loss environment implied by these models, we next use the time when the bolometric luminosity calculated in Section 3.4 falls below that expected from continued interaction (Chevalier & Irwin 2011 Eqn. 9; Margutti et al. 2014b Eqn. A6) to estimate the time at which the shock reaches the outer radius of the dense wind region. For all of our objects, with the exception of PS1-10ah, this occurs within a few days after maximum light. For PS1-10ah the flattening of the light-curve at +10 days is consistent with the emission expected for continued interaction. Using this information and Eqn. A7 from Margutti et al. (2014b), we find that the dense wind extends to a few × 10^{15} cm for all of our objects (second panel, Figure 3.24). For three events (PS1-11bbq, PS1-12brf, and PS1-13duy) we were only able to put lower limits on the extent of the mass-loss region. These values are comparable to the dense wind radius of 1.2 $\times 10^{15}$ cm found by Margutti et al. (2014b) for the 2012b explosion of SN 2009ip.

From this we find that the total mass contained within the region of dense mass-loss is only a few hundredths of a solar mass for most of our objects (third panel, Figure 3.24). This is an order of magnitude lower than the CSM mass found by Margutti et al. (2014b) for the 2012b explosion of SN 2009ip. In addition, the timescale over which the ejection of this mass from the progenitor would have occurred is very short. For wind speeds of

1000 km s^{-1} the mass-loss would have occurred in the $\lesssim 1$ year prior to explosion (fourth panel, Figure 3.24).

Chevalier & Irwin (2011) predict that the temperature of the explosion should *rise* to maximum in the case of shock breakout within a region of dense mass-loss. Unfortunately, for many of our objects we do not robustly constrain their temperature evolution on the rise. However, one of our best observed objects on the rise, PS1-10ah, does show evidence for a rise in temperature to maximum. Our best fit blackbody for this object at maximum light is $\sim$ 18,000 K, but several days before max is only 10,000 K. This trend is also reflected in the observed g−r colors, which get bluer at maximum light.

If this physical scenario is an accurate representation of our transients, then they (along with PTF09uj) add to the interesting picture painted by type IIn, type Ibn, SLSN-II and other transients about the (possibly eruptive) mass-loss that some massive stars undergo in the year(s) immediately prior to explosion. The rates of these short duration transients are not insignificant compared to the rates of longer duration type IIn SN (8−9% of core-collapse SN; Smith et al. 2011). While the mass-loss rates and dense wind radii required for our transients are similar to those derived for other type IIn events, the total mass contained in the dense CSM is a factor of ten lower than that inferred for a majority of of type IIn SN (see Smith 2014 and references therein). This, in turn, leads to a smaller break-out radius and shorter transient duration.

3.8.3 Super-Eddington Tidal Disruption Flares

We now turn our attention to a set of non-explosive transients whose predicted properties bear some resemblance to several of our objects: the super-Eddington phase of a tidal disruption flare. To date, a majority of tidal disruption event candidates have been discovered in the UV and X-rays. This is expected given the high predicted blackbody temperature of material close to the SMBH ($\sim 3\times10^5$ K; see, e.g., Lodato & Rossi 2011). However, for SMBHs with M $\lesssim 10^8$ M$_\odot$, there may be a period of time after the initial disruption when accretion is super-Eddington, which can drive an outflow of material. Strubbe & Quataert (2009) model the light curves and spectra for this type of emission. They find that the transients are short-lived ($\lesssim$ 30 days), luminous (L $\sim 10^{43}$ ergs s^{-1}), and peak in the optical/UV.

Cenko et al. (2012) argue that a super-Eddington outflow may explain the event PTF 10iya, which has several properties in common with the PS1-MDS transients. PTF 10iya has a rapid timescale ($\sim$ 10 days), high peak luminosity ($\sim 10^{44}$ ergs s^{-1}) and a blackbody temperature of ~20,000 K. However, there are several difficulties in interpreting our objects similarly. First, and most obviously, PTF 10iya was coincident with the nucleus of its host galaxy to within 350 mas. The same is not the case for many of the transients presented here. Only PS1-10ah lies in the very central region of its host. While, in principle, a non-nuclear event could be due to a tidal disruption by an intermediate-mass black hole (IMBH), in the models of Strubbe & Quataert (2009) a characteristic timescale of ~10 days requires a SMBH with a mass between 10^6 and 10^8 M$_\odot$. The timescale for an IMBH would be $\lesssim$ 1 day.

In addition, Strubbe & Quataert (2009) predict that the observed temperature should *increase* slightly as the transient declines. In contrast, our objects show ejecta which cool with time. Finally, Cenko et al. (2012) argued that the blackbody radii measured for PTF 10iya ($\sim 10^{15}$ cm) are too large for SN ejecta traveling at typical velocities to reach in such a short period of time. The same argument does not hold for our objects, whose blackbody radii are an order of magnitude smaller. Thus, despite sharing several observational properties with PTF 10iya, it is not obvious that any of our events are consistent with the emission predicted for the super-Eddington phase of a tidal disruption flare.

In contrast, Strubbe & Quataert (2009) predicted that the PS1-MDS should detect approximately 20 tidal disruption flares in their super-Eddington phase *per year*. Using their models and detection rates as a function of BH mass and the black hole mass function from Hopkins et al. (2007) we estimate that roughly 40% of these should fall in the rapidly-evolving parameter space that was systematically examined in this paper. In addition, Strubbe & Quataert (2009) calculate their rates using a limiting flux of 25 AB mag for the PS1-MDS, which is $1 - 1.5$ mag fainter than what the survey actually achieved. Using Equation 32 in Strubbe & Quataert (2009) to scale their derived rates to the true sensitivity obtained by PS1-MDS we produce a modified predicted detection rate of $1 - 2$ events per year within the parameter space we have examined. Thus, given the stringent detection criteria we utilized in Section 3.2.2 it is possible that our lack of detections in four years of the PS1-MDS is not in conflict with the models of Strubbe & Quataert (2009).

3.8.4 Magnetars formed during NS-NS Mergers

In some cases, the merger of two low mass neutron stars (NS) may produce a stable massive NS as opposed to collapsing to a black hole. Both Yu et al. (2013) and Metzger & Piro (2014) investigate the electromagnetic counterparts that would be produced from the formation of such a system if the magnetar spin-down energy is channeled into the ejecta from the merger, as opposed to a collimated jet. They predict optical/UV transients with peak bolometric luminosities of $10^{43} - 10^{44}$ erg s^{-1}, rise timescales of $\lesssim 1$ day and overall timescales of $\sim$10 days. Although these predicted luminosities and timescales are slightly higher/shorter than those observed for the PS1-MDS transients presented here, their properties are broadly comparable.

However, both the derived rates for the PS1-MDS transients and their explosion site offset distribution disfavor a significant fraction originating from this channel. The "realistic" NS-NS merger rate from Abadie et al. (2010) is 1000 events yr^{-1} Gpc^{-3} and the "high" rate is 10000 events yr^{-1} Gpc^{-3}. The rates we derive in Section 3.7 are 4800 $-$ 8000 events yr^{-1} Gpc^{-3}. Thus, if *all* of our events originated from this channel we would require a high NS-NS merger rate of which a significant fraction produce stable NS remnants. In addition, the offset distribution observed for our transients is consistent with that observed for CC-SN, rather than SGRBs (which are also thought to originate from NS-NS mergers). However, while this progenitor channel cannot explain the entire population of rapidly-evolving objects we identify in the PS1-MDS, we cannot rule it out for some individual objects. To do so, we would require models with more detailed radiation transport to determine if the blue colors and continuum dominated spectra we observe are consistent with predictions.

3.9 Summary and Conclusions

The Search: We have performed a search for transients with rapid timescales ($t_{1/2} \lesssim$ 12 days) and high peak luminosities ($-15 > M > -21$) within the ∼5000 transients discovered in the PS1-MDS. We identify 14 light curves of interest, 10 of which have confirmed peak magnitudes brighter than −16 mag. This sample increases the known number of events in this region of transient phase space by approximately a factor of three. The median redshift of our confirmed sample is 0.275.

Basic Properties: The PS1-MDS rapidly-evolving transients span a wide range peak magnitudes (-16.8 mag $< M < -20$ mag) and an order of magnitude in peak pseudo-bolometric luminosity (2×10^{42} erg s^{-1} $< L_{\rm peak} < 3 \times 10^{43}$ erg s^{-1}). In general, they possess much faster rise than decline timescales. Our data for six objects cannot exclude a transient that rose on a timescale of $\lesssim 1$ day. With the exception of PS1-12bb, all of the transients possess blue colors near maximum light ($g_{\rm P1} - r_{\rm P1} \lesssim -0.2$). Best fit blackbodies reveal photospheric temperatures/radii which cool/expand with time, consistent with explosions that involve expanding ejecta. The explosion spectra obtained near maximum light are dominated by a blue continuum, consistent with a hot optically thick ejecta. Based on these spectra we cannot conclude if the explosions are hydrogen-rich or hydrogen-poor.

Power Sources and Progenitors: The short timescales and high peak luminosities of the PS1-MDS transients are difficult to reconcile with explosions powered by the radioactive decay of ^{56}Ni. Either extreme ejecta velocities or significant outward mixing of ^{56}Ni would be required to avoid a situation where the required nickel mass is a significant fraction (>50%) of the total ejecta mass. However, the blue, continuum dominated, spectra are consistent with early spectra observed for transients powered by shock breakout cooling envelope emission or interaction with a dense CSM.

The luminosity and duration of several transients are consistent with the cooling envelope emission observed in type IIb SN with extended low-mass envelopes (e.g. SN 1993J). However, in all but one case we see no evidence for a second peak in the optical powered by radioactive decay. For the others, we can restrict the amount of ^{56}Ni which could power a subsequent peak to $\lesssim$0.03 $M_\odot$. In contrast, several of the more luminous transients may be produced by a shock breakout within a region of dense mass-loss surrounding the progenitor star. The mass-loss rates and dense CSM radii required are comparable to those derived for normal type IIn SN. However, the total mass contained within the dense CSM is an order of magnitude lower ($\sim$0.01 $M_\odot$).

Host Galaxies: The host galaxies of the PS1-MDS rapidly-evolving transients are consistent with the interpretation of massive star progenitors. They are all star-forming, possess roughly solar metallicity, and are consistent with the mass-metallicity relation observed for SDSS star forming galaxies (Tremonti et al. 2004). The explosion sites span a wide range of offsets from the galaxy centers, and their distribution most closely resembles that observed for core-collapse SN.

Volumetric Rates: Using information on the true cadence and sensitivity achieved by the PS1-MDS, we use a Monte Carlo code to calculate the efficiency of the PS1-MDS in detecting rapidly-evolving transients as a function of distance. For luminous blue transients (such as those presented here) we find in season efficiencies that peak around $\sim$25% at z=0.1. This demonstrates the large effect that small observing gaps (due to weather, maintenance, etc.) can have on the ability of optical SN searches to detect rapidly-evolving events. Using these efficiencies we calculate a volumetric rate for these transients of $4800 - 8000$ events $\mathrm{Gpc}^{-3}\ \mathrm{yr}^{-1}$. This is $4 - 7\%$ of the core-collapse SN rate at z=0.2 found by Botticella et al. (2008). In addition, we find that the efficiency with which PS1-MDS detects faint, red, transients (similar to the rapidly-declining events presented in the literature; SN 2010X, SN 2005ek) plummets to zero by z∼0.2. The PS1-MDS has a small survey volume at such low redshifts. Thus, the lack of similar objects in our sample does not reflect their intrinsic rate, but rather the efficiency with which the PS1 observing strategy can recover events of each subclass.

Implications and Future Directions: Both the event rates we derive for these transients and our interpretation for their progenitors have significant implications for our understanding of the final stages of stellar evolution. The rates are not insignificant compared to the core-collapse SN rate, and both the progenitor systems we favor imply non-standard final configurations of the star. Our interpretation of some events as cooling envelope emission from a progenitor with a low-mass extended envelope implies that some stripped envelope core-collapse SN eject very little radioactive material. This could either be due to fallback within a high mass progenitor whose outer envelope is stripped by winds, or due to binary stripping of the outer envelope in a lower mass progenitor. Our interpretation of some other events as a shock breakout within an optically thick wind adds to the complex picture painted by type IIn SN of the eruptive mass loss that seems to occur for some massive stars in the year(s) immediately prior to explosion. In view of these results, there are several future directions for both theorists and observers that will aid our ability to interpret these transients:

Theory: (1) Detailed models of these fast, blue, luminous transients. In particular, when detailed models (which treat outward mixing of ^{56}Ni, departures from spherical symmetry, and time varying opacity) are performed, do they confirm that the luminosities, timescales, and spectra are inconsistent with a transient powered mainly by radioactive decay? What stellar envelope parameters does a cooling envelope interpretation imply? Is it possible to reproduce the most luminous transients with a shock breakout from the surface of a star, or are the implied stellar radii unphysical? Can a model other than those investigated here reproduce all of the observed properties? (2) Updated models of the final stages of stellar evolution. What final state do stars which are stripped by binary interaction actually take? Can detailed models reproduce the mass-loss in the final year(s) before explosion implied by these events and other type IIn SN?

Observation: (1) Multi-band data taken on the same epoch with a ∼1 day cadence. This data will allow us to constrain both the true rise time of the transients ($\lesssim$ 1 day versus 2−3 days) and their temperature evolution on the rise. The shock breakout from the surface of a star and a shock breakout from within a region of dense mass loss give different predictions for these parameters. (2) Multiple epochs of spectroscopy, especially at late times. The spectra obtained for all of our blue transients were at maximum light. While spectra dominated by blue continua are consistent with a cooling envelope or shock breakout interpretation at these epochs, late time spectra should display features from either the SN ejecta or from interaction with the CSM.

M.R.D thanks Hagai Perets, Jerod Parrent, and Luke Zoltan Kelley for useful conversations regarding this manuscript. M.R.D. is supported in part by the NSF through a Graduate Research Fellowship. Support for this work was provided by the David and Lucile Packard Foundation Fellowship for Science and Engineering awarded to A.M.S.

E.K. acknowledges financial support from the Jenny and Antti Wihuri Foundation. S.J.S. acknowledges European Research Council funding under the European Union's Seventh Framework Programme (FP7/2007-2013)/ERC Grant agreement n^{o} [291222]

The Pan-STARRS1 Surveys (PS1) have been made possible through contributions of the Institute for Astronomy, the University of Hawaii, the Pan-STARRS Project Office, the Max-Planck Society and its participating institutes, the Max Planck Institute for Astronomy, Heidelberg and the Max Planck Institute for Extraterrestrial Physics, Garching, The Johns Hopkins University, Durham University, the University of Edinburgh, Queen's University Belfast, the Harvard-Smithsonian Center for Astrophysics, the Las Cumbres Observatory Global Telescope Network Incorporated, the National Central University of Taiwan, the Space Telescope Science Institute, the National Aeronautics and Space Administration under Grant No. NNX08AR22G issued through the Planetary Science Division of the NASA Science Mission Directorate, the National Science Foundation under Grant No. AST-1238877, the University of Maryland, and Eotvos Lorand University (ELTE)

This paper includes data gathered with the 6.5m Magellan Telescopes located at Las Campanas Observatory, Chile. Some observations reported here were obtained at the MMT observatory, a joint facility of the Smithsonian Institution and the University of Arizona. Some observations were obtained under Program IDs GN-2011B-Q-3 (PI: Berger) and GS-2012A-Q-31 (PI: Berger) at the Gemini Observatory, which is operated by the Association of Universities for Research in Astronomy, Inc., under a cooperative agreement with the NSF on behalf of the Gemini partnership: the National Science Foundation (United States), the National Research Council (Canada), CONICYT (Chile), the Australian Research Council (Australia), Ministerio da Ciencia, Tecnologia e Inovacao (Brazil) and Ministerio de Ciencia, Tecnologia e Innovacion Productiva (Argentina). The data presented here were obtained in part with ALFOSC, which is provided by the Instituto de Astrofisica de Andalucia (IAA) under a joint agreement with the University of Copenhagen and NOTSA. Some of the computations in this paper were run on the Odyssey cluster supported by the FAS Science Division Research Computing Group at Harvard University.

Facilities: PS1 (GPC1), Magellan Baade (IMACS), Magellan Clay (LDSS3), MMT (Blue Channel spectrograph, Hectospec), Gemini North (GMOS-N),Gemini South (GMOS-S), NOT (ALFOSC)

3.10 Appendix: Most Likely Host Analysis of Bronze Sample Objects

Our bronze sample is composed of four objects that passed all of the photometric selection criteria described in Section 3.2.2, but whose distance we were not able to constrain spectroscopically. As a result, we cannot confirm that they are "high luminosity" transients ($M < -15$ mag). We now attempt to assess this likelihood by examining the possible hosts for each event.

The region around each transient is shown in Figure 3.6, and we begin by assessing the most likely host for all four objects via the method outlined in Bloom et al. (2002) and Berger (2010). We calculate the probability of chance alignment, P(δR), with various galaxies in the surrounding area (labeled in red in Figure 3.6) based on their $i-$band magnitudes and δR from the explosion site. δR for underlying versus distant galaxies are calculated as described in Bloom et al. (2002). The results from this analysis are shown in Figure 3.25.

There are faint (25 mag $<$ m$_i$ $<$ 22 mag) sources located within $1''$ of the explosion site for all four bronze objects, as well as more luminous galaxies at slightly larger separations. In all four cases we find that the underlying, faint, source has the lowest probability of chance alignment with the transient ($\lesssim$ 4%). However, all four events have at least one other source with a <10% probability of chance alignment. We now examine, in turn, the consequences if each of these sources were the true host of the transient.

The additional sources with a <10% probability of chance alignment are bright (m$_i$ $>$ 19.5) and can morphologically be identified as galaxies. Thus, if our transients are associated with these sources, they would be analogous to our gold/silver transients, with larger offsets from their hosts. PS1-10iu S2, PS1-13aea S2, and PS1-13bit S2 possess SDSS photometric redshifts of 0.136, 0.290, and 0.134, respectively. If these are their true hosts, the transients would possess peak absolute magnitudes between -16.8 and -19.5, well in line with the range exhibited by the gold/silver samples. For PS1-13aea, the situation has the added complication that the transient exploded in the region between NGC 4258 and NGC 4248 (See Figure 3.6), with distances of 7.2 and 7.3 Mpc, respectively. If the transient were associated with either of these galaxies (NGC 4258 has roughly the same probability of chance alignment as PS1-13aea S2) then the peak magnitude of PS1-13aea would only be -8.5, and likely an extragalactic nova.

We now turn to the possibility that the hosts of the bronze transients are the faint sources located within $\sim 1''$ of the explosion site. If this is the case, then two possibilities exist. Either these sources are galaxies, and the bronze events represent additional

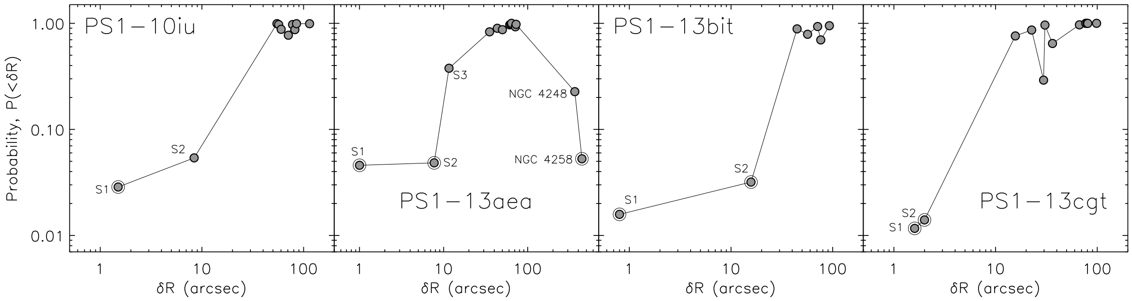

Figure 3.25.—: Most probable host analysis for the bronze transients. Vertical axis gives the probability of chance alignment with a given galaxy as a function of δR. Galaxies of particular note are labeled.

rapidly-evolving and luminous transients (likely at higher redshifts), or these sources are stellar and these events are less luminous (and likely known) classes of transients. Not one of the transients shows signs of prior or later outbursts in the four years of PS1-MDS data. Unfortunately, the signal to noise of the detections are not sufficient to do a definitive morphological assessment of the sources. However, for both PS1-10iu and PS1-13bit, the location of the transient (accurate to approximately $0.1''$) appears offset from the centroid of the underlying source. If the sources were located within the Milky Way (at distances <3 kpc) then the absolute magnitude of the *quiescent* sources would be only ~ 10 mag. While this is in line with magnitudes expected for quiescent cataclysmic variables, several of the sources also possess red colors, which is not.

Based on these arguments, we find it likely that at least some subset of our bronze objects represent additional members of this class of rapidly-evolving and luminous transients.

Chapter 4

The Double-Peaked SN 2013ge: a Type Ib/c SN with an Asymmetric Mass Ejection or an Extended Progenitor Envelope

M. R. Drout, D. Milisavljevic, J. Parrent, R. Margutti, A. Kamble, A. M. Soderberg, P. Challis, R. Chornock, W. Fong, S. Frank, N. Gehrels, M. L. Graham, E. Hsiao, K. Itagaki, M. Kasliwal, R. P. Kirshner, D. Macomb, G. H. Marion, J. Norris, M. M. Phillips

The Astrophysical Journal, Vol. 812, No. 57, 2016

Abstract

We present extensive multiwavelength (radio to X-ray) observations of the Type Ib/c SN 2013ge from −13 to +457 days relative to maximum light, including a series of optical spectra and *Swift* UV-optical photometry beginning $2-4$ days post-explosion. This data set makes SN 2013ge one of the best observed normal Type Ib/c SN at early times—when the light curve is particularly sensitive to the progenitor configuration and mixing of radioactive elements—and reveals two distinct light curve components in the UV bands. The first component rises over $4-5$ days and is visible for the first week post-explosion. Spectra of the first component have blue continua and show a plethora of moderately high-velocity ($\sim$15,000 km s^{-1}) but narrow ($\sim$3500 km s^{-1}) spectroscopic features, indicating that the line-forming region is restricted. The explosion parameters estimated for the bulk explosion ($M_{\rm ej} \sim 2-3$ M$_\odot$; $E_{\rm K} \sim 1-2 \times 10^{51}$ erg) are standard for Type Ib/c SN, and there is evidence for *weak* He features at early times—in an object which would have otherwise been classified as Type Ic. In addition, SN 2013ge exploded in a low metallicity environment ($\sim$0.5 Z$_\odot$) and we have obtained some of the deepest radio and X-ray limits for a Type Ib/c SN to date, which constrain the progenitor mass-loss rate to be $\dot{M} < 4 \times 10^{-6}$ M$_\odot$ yr^{-1}. We are left with two distinct progenitor scenarios for SN 2013ge, depending on our interpretation of the early emission. If the first component is cooling envelope emission, then the progenitor of SN 2013ge either possessed an extended ($\gtrsim$ 30 R$_\odot$) envelope or ejected a portion of its envelope in the final $\lesssim$1 year before core-collapse. Alternatively, if the first component is due to outwardly mixed ^{56}Ni, then our observations are consistent with the asymmetric ejection of a distinct clump of nickel-rich material at high velocities. Current models for the

collision of a SN shock with a binary companion cannot reproduce both the timescale and luminosity of the early emission in SN 2013ge. Finally, the spectra of the first component of SN 2013ge are similar to those of the rapidly-declining SN 2002bj.

4.1 Introduction

Type Ib/c supernovae (SN) are an observational subclass of stellar explosions. They are identified mainly by a lack of either strong hydrogen or strong silicon features in their optical spectra (see Wheeler et al. 1995, Filippenko 1997 for a review of SN classifications). This class can be further divided into Type Ib SN, which show conspicuous lines of helium in their spectra, and Type Ic SN, which do not. These events are physically understood to be the core-collapse of massive stars that were stripped of their hydrogen envelopes. Main progenitor channels include isolated Wolf Rayet (WR) stars with massive winds (Begelman & Sarazin 1986; Woosley & Weaver 1995) and lower mass helium stars stripped by binary companions (Wheeler & Levreault 1985; Podsiadlowski et al. 1992; Yoon et al. 2010).

Two of the main power sources that contribute to the rising phase of a SN light curve are the radioactive decay of ^{56}Ni synthesized in the explosion and the cooling envelope emission produced when the ejecta radiates away energy deposited by the SN shock (e.g. Piro & Nakar 2013). In stripped-envelope SN, ^{56}Ni powers a majority of the light curve, while cooling envelope emission is only predicted to be visible for a few days post-explosion. As a result, early observations of Type Ib/c SN provide a particularly sensitive probe of both the structure of the progenitor star prior to explosion (Nakar & Sari 2010; Rabinak & Waxman 2011) and the degree to which radioactive materials are mixed into the outer ejecta (Dessart et al. 2012; Piro & Nakar 2013).

Constraints on the structure of the progenitor star from cooling envelope emission are valuable as the final radii of putative Type Ib/c progenitors are predicted to vary by an order of magnitude or more depending on their initial conditions (mass, metallicity) and evolutionary history (single versus binary) (Yoon et al. 2010). While no cooling envelope emission has been observed for a normal (not broad-lined) Type Ic SN to date, non-detections have been used to place constraints on the progenitor radii in several objects (e.g. PTF10vgv; Corsi et al. 2012). In addition, when interpreted as shock breakout emission, the early X-ray/UV peak observed from the Type Ib SN 2008D constrains its progenitor radius to be $\lesssim 12\ \mathrm{R}_\odot$ (Soderberg et al. 2008; but see also e.g. Mazzali et al. 2008, Bersten et al. 2013 for alternative interpretations of this emission).

In addition, recent observations have highlighted gaps in our understanding of the final state of the progenitors for some SN. For example, a handful of SN with double-peaked optical light curves have been discovered. When interpreted as cooling envelope emission, the first peak requires that the progenitor star possessed a low-mass extended envelope, which differs from the standard hydrostatic models of stellar structure (Nakar & Piro 2014; Bersten et al. 2012; Nakar 2015). While a majority of these events are of Type IIb (e.g. SN 1993J Wheeler et al. 1993; SN 2011dh Arcavi et al. 2011; SN 2013df Van Dyk et al. 2014), a similar morphology has also been observed in the Type Ibn iPTF 13beo (Gorbikov et al. 2014) and the Ic-BL SN 2006aj associated with Gamma-Ray Burst (GRB) 060218 (Campana et al. 2006; Nakar 2015). Further, X-ray observations point to a subset of long GRB progenitors which either underwent enhanced mass-loss in the final years before explosion, or possess low-mass, extended, progenitor envelopes (Margutti et al. 2015).

Constraints on the mixing of radioactive material from rising light curves can also provide insight into the progenitor structure and explosion mechanism for various subclasses of Type Ib/c SN. Mixing in core-collapse SN can be accomplished by a number of mechanisms including a large-scale asymmetry of the explosion (e.g. a "jet"-like explosion), a large-scale asymmetry of the SN shock produced by the neutrino or magneto-rotational mechanism (e.g. Scheck et al. 2006; Marek & Janka 2009; Maeda et al. 2002; Burrows et al. 2007), and smaller-scale Rayleigh-Taylor and Kelvin-Helmholtz instabilities at the shock front (Kifonidis et al. 2006; Joggerst et al. 2009; Hammer et al. 2010). The observed signature of such mixing will vary depending on its origin, ranging from small modifications to the timescale and colors on the rise for well-mixed shallow deposits of ^{56}Ni (Dessart et al. 2012) to double-peaked light curves for asymmetric ejections of material. Models of the latter type have been investigated as a possible source for the double-peaked light curves observed in the Type Ib SN 2008D (Bersten et al. 2013) and SN 2005bf (Folatelli et al. 2006; but see also Maeda et al. 2007).

Understanding the mixing of radioactive material is especially vital for constraining what distinguishes whether a given progenitor will explode as a Type Ib or Ic SN. The production of He I lines in SN spectra requires non-thermal excitation of the helium atoms, likely from the γ-rays produced by the radioactive decay of ^{56}Ni (e.g. Lucy 1991; Dessart et al. 2012; Hachinger et al. 2012). Thus, in order to produce a Type Ib SN, mixing may be required, while the observation of a Type Ic SN may not necessarily imply that its progenitor was He poor. Early observations that constrain mixing in a normal Type Ic SN can therefore help to distinguish whether or not these events have an intrinsically lower helium abundance.

Thus, particularly when they are coupled with other multiwavelength observations, early light curves offer us insight into topics such as the evolutionary path of the progenitor, the explosion mechanism, and the properties that dictate whether a given star will explode as a Type Ib or Ic SN. In this paper we present detailed observations of the Type Ib/c SN 2013ge, which span radio to X-ray and include spectroscopy and UV-optical photometry beginning 2−4 days after the epoch of first light. These early observations show behavior which has not been observed in any Type Ib/c SN to date: a distinct light curve component visible in the blue bands for the first week after explosion, which—on its rising portion—shows spectral features with moderately high expansion velocities but *narrow* line widths.

In Section 4.2 we describe the observations obtained for SN 2013ge. In Sections 4.3 & 4.4 we describe the photometric and spectroscopic properties of SN 2013ge, respectively, while in Section 4.5 we examine the properties of the circumstellar medium (CSM) surrounding the progenitor star. In Section 4.6 we discuss the consequences of various observed properties on our understanding of the progenitor of SN 2013ge.

4.2 Observations

4.2.1 UV and Optical Photometry

We obtained UV and optical photometric observations of SN 2013ge from a wide variety of instruments, spanning 466 days. In the sections below we describe the data acquisition, reduction, and calibration for each instrument and in Section 4.2.1 we discuss the consistency of the combined light curve. The location of the transient on the outskirts of NGC 3287 is shown in Figure 4.1.

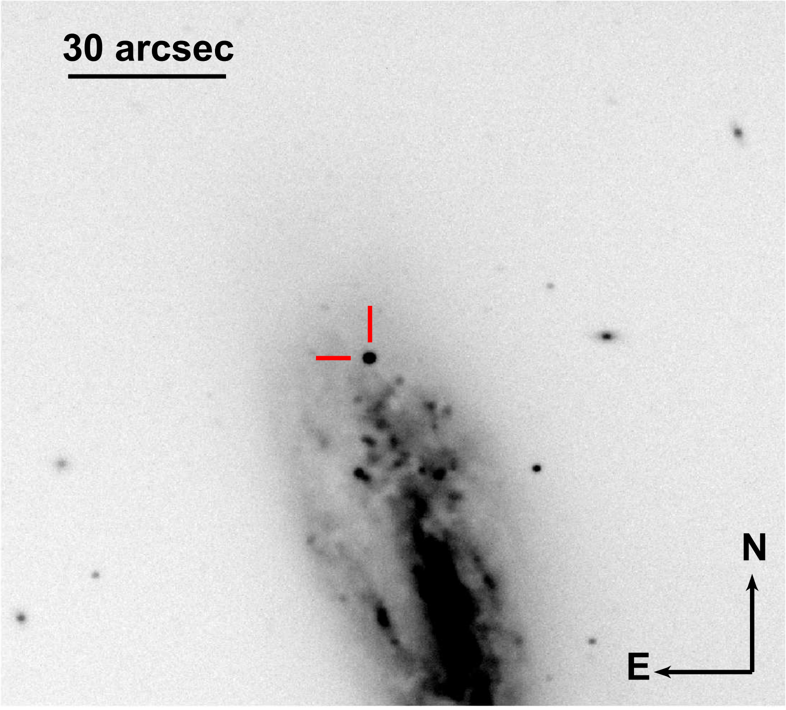

Figure 4.1.—: r-band image from MMTCam, obtained on 2014 Apr. 1, showing the location of SN 2013ge (red cross hairs) on the outskirts of NGC 3287.

Discovery Photometry and Pre-Explosion Limit

SN 2013ge was discovered by Koichi Itagaki on 2013 Nov. 8.8 (all times UT) using the 0.5-m reflector at the Takanezawa station, Tochigi-ken, and was undetected prior to discovery on 2013 Nov. 1.7 with the same instrument (CBAT 3601). We have reanalyzed these unfiltered images for this manuscript. We performed point spread function (PSF) photometry on the SN and nearby field stars in the discovery image using standard packages in IRAF[1], and absolute calibration was performed using Bessell R-band magnitudes of nearby field stars. No formal color correction to the Bessell system was performed. This same procedure was also carried out on fake sources injected into the pre-discovery image. This yields an unfiltered discovery magnitude of 16.9 ± 0.1 mag and a pre-explosion limit of 19.0 mag.

Swift UVOT Photometry

We observed SN 2013ge with the UV Optical Telescope onboard *Swift* (UVOT, Gehrels et al. 2004b, Roming et al. 2005) from 2013 Nov. 11 to 2013 Dec. 9 (-11 to $+17$ days). The *Swift*-UVOT photometric data were extracted following the prescriptions of Brown et al. (2009). We used a variable aperture with radius 3" – 5" to maximize the signal-to-noise ratio as the SN flux faded. The *Swift*-UVOT photometry is reported in Table 4.1 in the photometric system described in Breeveld et al. (2011).

---

[1] IRAF is distributed by NOAO, which is operated by the Association for Research in Astronomy, Inc. under cooperative agreement with the NSF.

Challis Observatory Optical Photometry

We observed SN 2013ge with the Challis Astronomical Observatory (CAO) on 12 nights spanning 2013 Nov. 12 to 2013 Dec. 14 (−10 to +22 days). CAO is located in central Idaho near the River of No Return Wilderness. The facility telescope is a 0.4−m f/10 Meade LX−200, equipped with an Apogee Alta U47-MB camera and UBVRI Bessell filters.

For each epoch, $5-10$ raw images were stacked and PSF photometry was performed in IRAF. Absolute calibration was performed using SDSS observations of field stars, which were converted to the Bessell BVRI system using the equations of Smith et al. (2002). A single nightly zeropoint offset was applied, as data was not available to fully calibrate color terms between the CAO and standard Bessell filters. However, no strong trends between zeropoint and color were evident in observations of ∼15 field stars on multiple epochs, and the observed color of SN 2013ge is well matched to the range of colors of the field stars used for calibration. We estimate that the error in our calibration (assuming a range of possible color terms) is $\lesssim$0.05 mag over the epochs we observed with CAO. This data is listed in Table 4.2 in the Bessell photometric system.

FLWO 1.2-m Optical Photometry

We obtained 55 epochs of BVri photometry of SN 2013ge spanning 2013 Dec. 7 to 2014 May 3 (+15 to +162 days) with the Fred Lawrence Whipple Observatory (FLWO) 1.2 meter telescope plus KeplerCam CCD. The KeplerCam data were reduced using IRAF, IDL and PERL procedures as described in Hicken et al. (2012) for the CfA4 Type Ia sample, with the exception that no host galaxy subtraction was performed. BVri instrumental magnitudes were measured using PSF fitting. For calibration, we applied a set of linear transforms, which account for zeropoint, atmospheric and color terms. These linear transforms were calibrated using Landolt (1992) standards for BV and Smith et al. (2002) standards for r and i bands on 5 photometric nights, while nightly zeropoints were determined by measuring the magnitudes of local comparison stars in the SN 2013ge field (see Hicken et al. 2012 for further discussion of the calibration applied). The resulting BV data in the Bessell photometric system and ri data in the SDSS photometric system are listed in Table 4.3.

MMTCam, LBT and IMACS Optical Photometry

In addition, we obtained eight epochs of ri−band photometry and two epochs of z−band photometry with the MMTCam instrument mounted on the 6.5m MMT telescope, one epoch of ri−band imaging with the Large Binocular Camera (LBC; Speziali et al. 2008) mounted on the Large Binocular Telescope (LBT), and two epochs of r−band imaging with IMACS on Magellan-Baade. One epoch was obtained on 2013 Nov. 19 (−3 days), and the other epochs span 2013 Apr. 1 to 2015 Apr. 16 (+129 to +510 days). Bias and flat field corrections were made to all images and nightly stacks were produced using standard routines in IRAF. Dark frame corrections were also applied to images taken with MMTCam. PSF photometry was performed and absolute calibration was carried out using SDSS observations of field stars. A single nightly zeropoint offset was performed. These data listed in the SDSS photometric system in Table 4.4.

Table 4.1. *Swift* UVOT Photometry

UT Date	MJD	*uvw*2 (err) mag	*uvm*2 (err) mag	*uvw*1 (err) mag	*u* (err) mag	*b* (err) mag	*v* (err) mag
2013 Nov 11	56607.0	···	···	16.66 (0.08)	15.34 (0.06)	···	···
2013 Nov 11	56607.8	17.32 (0.07)	17.37 (0.06)	16.20 (0.06)	15.03 (0.04)	15.79 (0.04)	15.69 (0.06)
2013 Nov 12	56608.7	17.21 (0.07)	17.36 (0.07)	16.18 (0.06)	14.94 (0.04)	15.61 (0.04)	15.54 (0.06)
2013 Nov 13	56609.8	17.29 (0.07)	17.40 (0.07)	16.11 (0.05)	14.87 (0.04)	15.56 (0.04)	15.32 (0.05)
2013 Nov 14	56610.8	17.37 (0.08)	17.46 (0.10)	16.25 (0.06)	15.03 (0.05)	15.55 (0.04)	15.20 (0.05)
2013 Nov 15	56611.3	17.53 (0.08)	17.50 (0.08)	16.44 (0.07)	15.05 (0.05)	15.46 (0.04)	15.26 (0.05)
2013 Nov 16	56612.1	17.54 (0.08)	17.70 (0.08)	16.55 (0.07)	15.21 (0.05)	15.43 (0.04)	15.15 (0.05)
2013 Nov 17	56613.1	17.57 (0.08)	17.93 (0.12)	16.69 (0.07)	15.26 (0.05)	15.46 (0.04)	15.11 (0.05)
2013 Nov 18	56614.6	17.72 (0.08)	···	16.79 (0.07)	15.30 (0.05)	15.47 (0.04)	14.98 (0.05)
2013 Nov 19	56615.1	17.76 (0.08)	18.07 (0.09)	16.80 (0.07)	15.39 (0.05)	15.42 (0.04)	14.94 (0.04)
2013 Nov 20	56616.7	17.86 (0.09)	17.92 (0.09)	16.82 (0.07)	15.39 (0.05)	15.51 (0.04)	14.95 (0.05)
2013 Nov 21	56617.1	17.75 (0.08)	17.94 (0.09)	16.85 (0.07)	15.42 (0.05)	15.36 (0.04)	14.83 (0.04)
2013 Nov 22	56618.6	···	···	16.83 (0.06)	15.46 (0.04)	15.39 (0.04)	14.78 (0.06)
2013 Nov 23	56619.2	···	···	16.98 (0.06)	15.47 (0.04)	15.38 (0.04)	14.87 (0.08)
2013 Nov 24	56620.1	···	···	17.15 (0.07)	15.61 (0.04)	15.54 (0.04)	14.76 (0.07)
2013 Nov 27	56623.1	···	···	17.25 (0.08)	15.84 (0.05)	15.55 (0.04)	14.81 (0.04)
2013 Nov 29	56625.9	···	···	17.40 (0.08)	16.16 (0.05)	15.77 (0.05)	14.93 (0.06)
2013 Dec 1	56627.7	···	···	17.39 (0.07)	16.49 (0.05)	16.07 (0.04)	15.00 (0.05)
2013 Dec 3	56629.5	···	···	17.38 (0.07)	16.70 (0.05)	16.10 (0.04)	15.03 (0.06)
2013 Dec 5	56631.1	···	···	17.61 (0.08)	16.77 (0.06)	16.30 (0.05)	15.24 (0.06)
2013 Dec 7	56633.5	···	···	17.74 (0.10)	16.91 (0.07)	16.46 (0.06)	15.36 (0.06)
2013 Dec 9	56635.2	···	···	17.90 (0.10)	17.08 (0.07)	16.62 (0.06)	15.48 (0.07)

Note. — Data is presented in the photometric system of Breeveld et al. (2011).

Table 4.2. CAO Photometry

UT Date	MJD	B (err) mag	V (err) mag	R (err) mag	I (err) mag
2013 Nov 12	56608.5	···	15.62 (0.09)	15.67 (0.13)	15.43 (0.22)
2013 Nov 22	56618.5	15.51 (0.10)	14.88 (0.08)	14.70 (0.05)	14.41 (0.05)
2013 Nov 23	56619.5	15.46 (0.09)	14.80 (0.07)	14.55 (0.04)	14.33 (0.06)
2013 Nov 24	56620.5	15.53 (0.09)	14.83 (0.07)	14.51 (0.06)	14.30 (0.05)
2013 Nov 25	56621.5	15.64 (0.14)	14.87 (0.06)	14.68 (0.06)	14.35 (0.08)
2013 Nov 26	56622.5	15.63 (0.09)	14.82 (0.10)	14.66 (0.05)	14.33 (0.05)
2013 Nov 28	56624.5	15.83 (0.10)	14.94 (0.06)	14.58 (0.04)	14.25 (0.05)
2013 Nov 29	56625.5	15.93 (0.12)	14.96 (0.10)	14.58 (0.05)	14.27 (0.06)
2013 Dec 5	56631.5	···	15.41 (0.14)	14.80 (0.10)	14.42 (0.16)
2013 Dec 11	56637.5	···	15.60 (0.21)	14.98 (0.15)	14.56 (0.19)
2013 Dec 12	56638.5	···	15.85 (0.09)	15.09 (0.06)	14.63 (0.09)
2013 Dec 14	56640.5	···	15.87 (0.09)	15.10 (0.06)	14.64 (0.09)

Note. — Data is presented in the Bessell photometric system.

Table 4.3. FLWO Photometry

UT Date	MJD	B (err) mag	V (err) mag	r' (err) mag	i' (err) mag
2013 Dec 7	56633.4	16.70 (0.02)	15.54 (0.02)	15.15 (0.03)	15.06 (0.03)
2013 Dec 7	56633.5	16.71 (0.03)	15.55 (0.03)	15.15 (0.05)	15.08 (0.04)
2013 Dec 8	56634.4	16.70 (0.02)	15.54 (0.02)	15.14 (0.01)	15.04 (0.01)
2013 Dec 14	56640.3	17.16 (0.02)	15.93 (0.02)	15.47 (0.02)	15.35 (0.03)
2013 Dec 23	56649.5	17.36 (0.03)	16.27 (0.01)	15.85 (0.01)	15.72 (0.01)
2013 Dec 24	56650.5	17.57 (0.03)	16.35 (0.02)	15.91 (0.03)	15.78 (0.03)
2013 Dec 26	56652.5	17.54 (0.02)	16.36 (0.01)	15.93 (0.01)	15.84 (0.02)
2013 Dec 27	56653.5	17.53 (0.02)	16.40 (0.01)	15.95 (0.01)	15.85 (0.01)
2013 Dec 28	56654.5	17.62 (0.02)	···	16.02 (0.03)	15.91 (0.03)
2013 Dec 29	56655.5	···	···	···	15.92 (0.05)
2013 Dec 30	56656.3	17.52 (0.02)	16.42 (0.01)	15.96 (0.01)	15.84 (0.01)
2014 Jan 1	56658.5	17.65 (0.02)	16.48 (0.02)	16.08 (0.02)	···
2014 Jan 2	56659.5	···	16.49 (0.01)	16.07 (0.01)	15.99 (0.01)
2014 Jan 3	56660.3	17.71 (0.04)	16.54 (0.03)	16.13 (0.04)	15.93 (0.02)
2014 Jan 6	56663.5	17.71 (0.02)	16.58 (0.05)	16.19 (0.05)	16.10 (0.06)
2014 Jan 9	56666.4	17.76 (0.03)	16.64 (0.02)	···	16.19 (0.03)
2014 Jan 11	56668.3	17.76 (0.02)	16.65 (0.01)	16.29 (0.02)	16.23 (0.02)
2014 Jan 12	56669.5	17.80 (0.03)	16.70 (0.03)	16.30 (0.03)	16.27 (0.04)
2014 Jan 13	56670.5	17.78 (0.02)	16.70 (0.03)	16.34 (0.02)	16.31 (0.03)
2014 Jan 14	56671.4	17.83 (0.03)	16.73 (0.04)	16.38 (0.04)	16.32 (0.04)
2014 Jan 15	56672.5	···	16.70 (0.01)	16.32 (0.01)	16.29 (0.01)
2014 Jan 16	56673.5	17.88 (0.04)	16.78 (0.03)	16.44 (0.05)	···
2014 Jan 17	56674.4	···	16.69 (0.01)	16.27 (0.02)	16.35 (0.01)
2014 Jan 18	56675.4	17.85 (0.03)	16.77 (0.02)	16.44 (0.03)	16.44 (0.03)
2014 Jan 19	56676.5	···	16.82 (0.03)	···	16.50 (0.04)
2014 Jan 20	56677.4	17.92 (0.04)	16.85 (0.03)	16.49 (0.03)	16.48 (0.03)
2014 Jan 21	56678.4	17.89 (0.02)	···	16.50 (0.02)	16.49 (0.02)
2014 Jan 23	56680.4	17.86 (0.02)	16.87 (0.02)	16.53 (0.03)	16.55 (0.03)
2014 Jan 26	56683.5	17.92 (0.02)	16.91 (0.03)	16.59 (0.03)	16.61 (0.02)

Table 4.3—Continued

UT Date	MJD	B (err) mag	V (err) mag	r' (err) mag	i' (err) mag
2014 Jan 28	56685.4	17.90 (0.02)	16.95 (0.02)	16.60 (0.03)	16.63 (0.03)
2014 Feb 3	56691.3	17.97 (0.02)	17.00 (0.02)	16.70 (0.02)	16.77 (0.03)
2014 Feb 6	56694.4	···	17.05 (0.03)	···	···
2014 Feb 9	56697.4	18.08 (0.02)	17.13 (0.02)	16.81 (0.02)	16.89 (0.02)
2014 Feb 12	56700.3	18.14 (0.02)	17.20 (0.02)	16.87 (0.02)	16.96 (0.02)
2014 Feb 13	56701.4	18.16 (0.03)	17.21 (0.03)	16.89 (0.03)	17.01 (0.04)
2014 Feb 14	56702.3	18.20 (0.03)	17.21 (0.03)	16.90 (0.02)	17.03 (0.03)
2014 Feb 15	56703.5	18.18 (0.04)	···	···	···
2014 Feb 18	56706.4	18.20 (0.02)	17.28 (0.03)	16.97 (0.03)	17.09 (0.04)
2014 Feb 20	56708.5	18.11 (0.02)	17.31 (0.02)	17.02 (0.02)	17.15 (0.03)
2014 Feb 25	56713.2	18.19 (0.03)	17.34 (0.04)	17.05 (0.03)	17.15 (0.02)
2014 Feb 25	56713.3	18.30 (0.03)	17.42 (0.05)	17.07 (0.03)	···
2014 Feb 27	56715.2	18.24 (0.03)	17.35 (0.02)	17.07 (0.02)	17.22 (0.02)
2014 Feb 27	56715.5	18.28 (0.03)	17.39 (0.02)	17.11 (0.02)	17.25 (0.03)
2014 Mar 5	56721.5	···	···	17.08 (0.02)	17.24 (0.02)
2014 Mar 6	56722.3	18.38 (0.03)	17.54 (0.04)	17.19 (0.04)	17.35 (0.03)
2014 Mar 14	56730.5	18.50 (0.04)	17.67 (0.03)	17.29 (0.02)	17.60 (0.04)
2014 Mar 15	56731.4	···	17.63 (0.03)	···	···
2014 Mar 17	56733.3	18.63 (0.04)	17.77 (0.03)	17.38 (0.03)	17.62 (0.03)
2014 Mar 19	56735.3	18.50 (0.05)	17.77 (0.07)	17.33 (0.07)	17.61 (0.13)
2014 Mar 25	56741.3	18.68 (0.03)	17.88 (0.04)	17.50 (0.04)	17.71 (0.03)
2014 Mar 30	56746.3	18.73 (0.10)	17.75 (0.05)	···	···
2014 Apr 2	56749.3	18.64 (0.03)	18.00 (0.02)	17.58 (0.02)	17.71 (0.02)
2014 Apr 7	56754.3	18.64 (0.03)	18.00 (0.02)	17.57 (0.02)	17.91 (0.03)
2014 Apr 30	56777.2	···	···	···	···
2014 May 3	56780.2	19.46 (0.03)	18.70 (0.02)	18.12 (0.03)	18.39 (0.03)

Note. — BV data is presented in the Bessell photometric system and ri data is presented in the SDSS photometric system.

Table 4.4. MMTCam, LBT, and IMACS Photometry

UT Date	MJD	r (err) mag	i (err) mag	z (err) mag	Instrument
2013 Nov 19	56615.5	15.01 (0.03)	14.98 (0.04)	15.04 (0.05)	MMTCam
2014 Apr 1	56748.1	17.59 (0.05)	17.85 (0.02)	···	MMTCam
2014 Apr 4	56751.3	17.69 (0.03)	17.91 (0.02)	17.04 (0.01)	MMTCam
2014 May 21	56798.2	18.41 (0.02)	18.71 (0.03)	···	MMTCam
2014 June 7	56815.1	18.71 (0.04)	18.92 (0.01)	···	MMTCam
2014 Oct 22	56952.1	20.48 (0.05)	20.96 (0.02)	···	LBT
2014 Nov 20	56981.5	21.18 (0.03)	21.62 (0.03)	···	MMTCam
2014 Dec 18	57009.3	21.36 (0.02)	···	···	IMACS
2015 Jan 15	57037.3	21.65 (0.03)	···	···	IMACS
2015 Feb 10	57063.4	22.13 (0.06)	22.58 (0.04)	···	MMTCam
2015 Apr 16	57128.1	> 22.3	> 22.4	···	MMTCam

Note. — Data is presented in the SDSS photometric system.

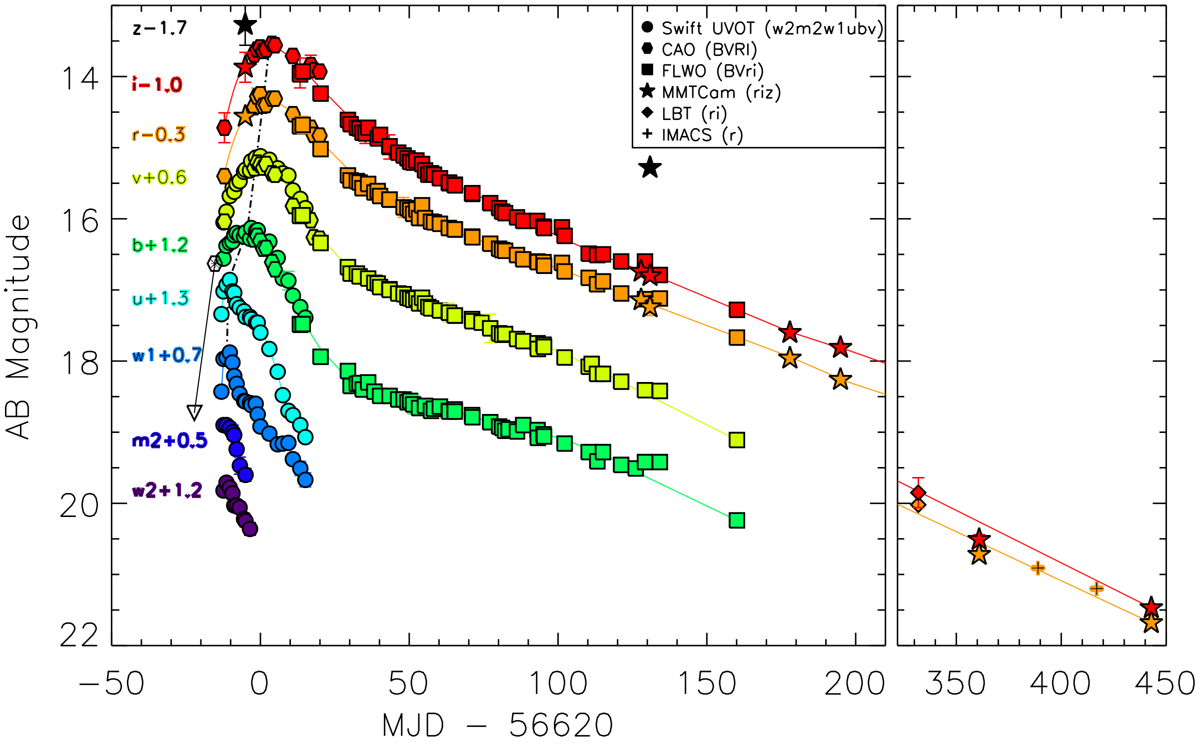

Figure 4.2.—: Multi-band photometry for SN 2013ge. Symbol shape indicates the source of the photometry and color indicates the observed band, as labeled. The unfiltered discovery photometry and pre-explosion limit are shown as a hexagon with an asterisk and an open downward facing triangle, respectively. See Section 4.2.1 for further information on the procedures applied to place data on this plot. The dashed-dotted line traces the epoch of maximum light for each observed band.

Combined UV-Optical Light Curve

As a result of the extensive observations described above, we possess *Swift*-UVOT data in the Breeveld et al. (2011) photometric system, CAO BVRI and FLWO BV data in the Bessell photometric system, and FLWO ri, MMTCam riz, LBT ri and IMACS r−band data in the SDSS photometric system. We plot the resulting UV/optical light curve in Figure 4.2. In this Figure color signifies the observed band and the shape of the symbol signifies the source of the photometry (see legend). In order to place data from different photometric systems on the same plot, we have shifted the photometric zeropoint of all data to the AB magnitude scale (m $= -2.5\log_{10}(F_{\rm Jy}/3630)$) and have corrected for the extinction in each observed band based on the total E(B−V)=0.067 mag derived in Section 4.2.6, below. We find good agreement between our data from different sources. Slight variations, on the order of 0.05−0.1 mag, are observed between the *Swift* bv data and CAO BV data, as expected for the different filter curves. We note that the overlapping epochs of CAO/FLWO V−band data and FWLO/MMTCam ri−band data agree within the quoted uncertainties, consistent with the conclusion that the color corrections between the CAO/MMTCam filters and the standard Bessell/SDSS filters are small.

The unfiltered discovery photometry and pre-explosion limit are shown as a hexagon with an asterisk and an open downward facing triangle in Figure 4.2, respectively. These points have been processed in the same manner as the R−band data for placement on this plot, but we caution that some variations likely exist between this data and the standard Bessell R-band at early times when the SN is very blue. We do not attempt to transform all of our data to a single photometric/filter system. In the analysis below, each point is treated appropriately for the filter in which it was originally observed.

4.2.2 Chandra X-ray Observations

We obtained deep X-ray limits for SN 2013ge with the *Chandra* X-ray Observatory on 2013 Dec. 7 under an approved Director Discretionary Time Proposal (PI: Margutti). The total exposure time was 18.8 ks. *Chandra* ACIS-S data were reduced with the `CIAO` software package (v4.5) and relevant calibration files, applying standard filtering criteria. Using `wavedetect` we find no evidence for X-ray emission at the location of SN 2013ge. The $3\,\sigma$ count-rate upper limit is 3.1×10^{-4} s^{-1} in the 0.5-8 keV energy band.

The neutral hydrogen column density in the direction of the SN is $\mathrm{NH_{gal}} = 1.9 \times 10^{20}$ cm^{-2} (Kalberla et al. 2005). From our optical spectra we estimate $\mathrm{E(B\text{-}V)_{host}} = 0.047$ mag (Section 4.2.6). For a Galactic dust to gas ratio, this value corresponds to an intrinsic neutral hydrogen column density of $\mathrm{NH_{host}} \sim 3 \times 10^{20}\,\mathrm{cm^{-2}}$. For an assumed simple power-law spectral model with spectral photon index $\Gamma = 2$ we find an unabsorbed flux limit 3.4×10^{-15} erg s^{-1} cm^{-2} (0.3-10 keV). At the distance of 23.7 Mpc (Section 4.2.6), this flux translates into a luminosity limit of 2.3×10^{38} erg s^{-1}.

4.2.3 Very Large Array Radio Observations

We obtained three epochs of deep radio limits for the emission from SN 2013ge at 4.8 and 7.1 GHz with the Very Large Array (VLA)[2]. Observations were obtained on 2013 Nov. 16, 25, and 2014 Jan. 14 (−6, +3, and +53 days), when the VLA was in B configuration, under program 13A-270.

All observations were taken in standard continuum observing mode with a bandwidth of $16 \times 64 \times 2$ MHz. During the reduction we split the data in two basebands of approximately 1 GHz each[3]. We used 3C286 for flux calibration, and calibrator J1018+3542 for phase referencing. The data were reduced using standard packages within the Astronomical Image Processing System (AIPS). No radio emission was detected from SN 2013ge in any of these observations. We measured the RMS noise at the location of SN 2013ge in each image using the task 'JMFIT' in AIPS. The resulting 3σ upper limits for each frequency and epoch are listed in Table 4.5.

---

[2] The National Radio Astronomy Observatory is a facility of the National Science Foundation operated under cooperative agreement by Associated Universities, Inc.

[3] 8 IF × 64 (channels/IF) × 2 (MHz/channel)

Table 4.5. VLA Observations

UT Date	MJD	Frequency GHz	F_ν[a] μJy
2013 Nov 16	56612.8	4.8	<45.6
⋯	⋯	7.1	<42.0
2013 Nov 26	56622.4	4.8	<36.0
⋯	⋯	7.1	<30.9
2014 Jan 4	56661.3	4.8	<36.0
⋯	⋯	7.1	<29.3

[a] All quoted flux limits are 3σ.

4.2.4 Optical Spectroscopy

We obtained 29 epochs of low resolution optical spectra for SN 2013ge, spanning −13 to +447 days. In addition, one moderate resolution (R∼3400) spectrum was obtained at −12 days in the region of Na ID. All optical spectra are listed in Table 4.6 and shown in Figure 4.3. All long slit observations were carried out with the slit oriented at the parallactic angle, with the exception of those obtained on Magellan/IMACS, which possesses an atmospheric dispersion corrector.

Initial reduction (overscan correction, flat fielding, extraction, wavelength calibration) for all long slit spectra was carried out using the standard packages in IRAF. The MODS/LBT spectrum was taken in the dual channel mode with gratings G400L and G670L, and we used the modsCCDRed suite of python programs to perform bias subtraction, flat-field correction, and adjust for bad columns, before extracting the spectrum using standard packages in IRAF. Flux calibration and telluric correction for all long slit spectra were performed using a set of custom idl scripts (see, e.g., Matheson et al. 2008; Blondin et al. 2012) and standard star observations obtained the same night as the science exposures. Spectra obtained with the Hectospec multi-fiber spectrograph (Fabricant et al. 2005) were reduced using the IRAF package “hectospec” and the CfA pipeline designed for this instrument. In all cases, when possible, spectroscopic flux calibration has been checked against observed photometry.

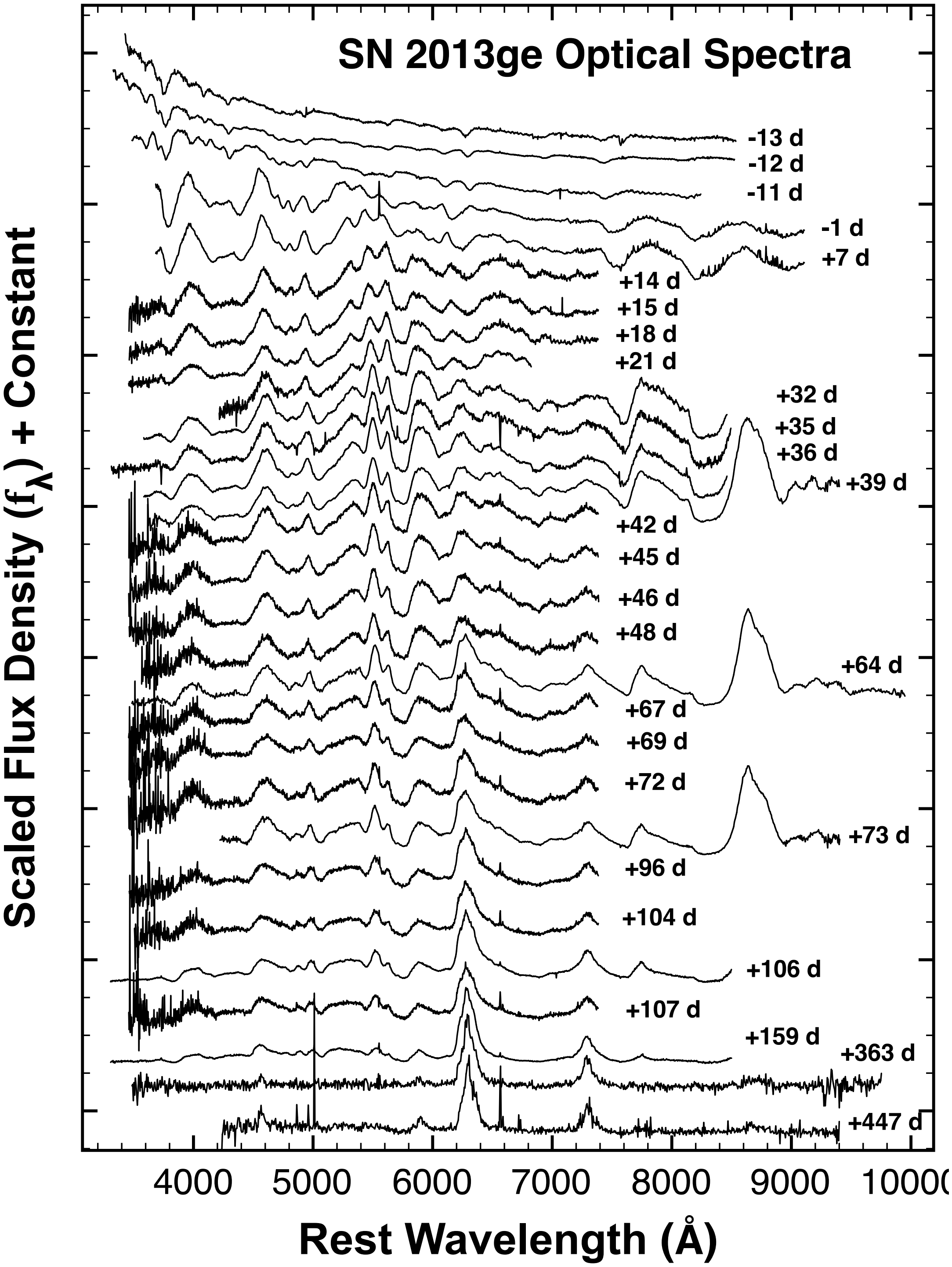

Figure 4.3.—: Normalized optical spectra spanning −13 to +447 days with respect to V-band maximum.

4.2.5 Infrared Spectroscopy

We obtained 8 epochs of NIR spectra for SN 2013ge with the Folded-port InfraRed Echellette spectrograph (FIRE; Simcoe et al. 2013) on Magellan-Baade spanning −2 to +123 days. All observations were obtained in longslit mode with the slit orientated at the paratactic angle. These data were reduced following standard procedures (see, e.g. Hsiao et al. 2015) using an IDL pipeline designed specifically for FIRE (`firehose`)[4]. A0V standards observed with each science exposure were used to correct for telluric absorption using the IDL tool `xtellcor` (Vacca et al. 2003). A model spectrum of Vega was used to remove stellar absorption features from the telluric standards and the resulting spectra were also used for flux calibration. All NIR spectra are listed in Table 4.6 and shown in Figure 4.4.

---

[4] Available at http://web.mit.edu/ rsimcoe/www/FIRE/

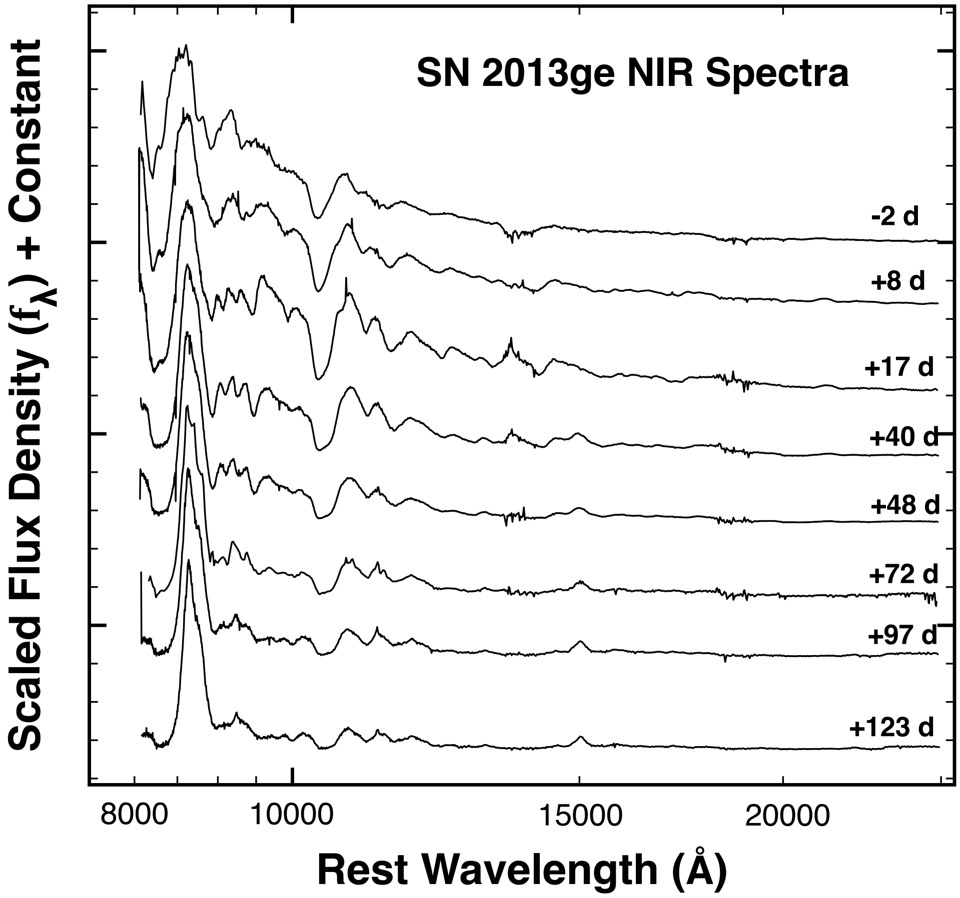

Figure 4.4.—: Normalized NIR spectra spanning −2 to +123 days with respect to V-band maximum.

Table 4.6. Optical and Infrared Spectroscopy

UT Date	MJD	Telescope	Instrument[a]
2013 Nov 9	56605	MMT	BC
2013 Nov 10	56606	MMT	BC[b]
2013 Nov 10	56606	MMT	BC
2013 Nov 11	56607	MMT	BC
2013 Nov 20	56616	Magellan-Baade	FIRE
2013 Nov 21	56617	MMT	Hectospec
2013 Nov 29	56625	MMT	Hectospec
2013 Nov 30	56626	Magellan-Baade	FIRE
2013 Dec 6	56632	Tillinghast 60-in	FAST
2013 Dec 7	56633	Tillinghast 60-in	FAST
2013 Dec 9	56634	Magellan-Baade	FIRE
2013 Dec 10	56636	Tillinghast 60-in	FAST
2013 Dec 13	56639	MDM 2.4-m	OSMOS
2013 Dec 24	56650	MMT	BC
2013 Dec 27	56653	MMT	BC
2013 Dec 28	56654	MMT	BC
2013 Dec 31	56657	Magellan-Clay	LDSS-3
2014 Jan 1	56658	Magellan-Baade	FIRE
2014 Jan 3	56660	Tillinghast 60-in	FAST
2014 Jan 6	56663	Tillinghast 60-in	FAST
2014 Jan 7	56664	Tillinghast 60-in	FAST
2014 Jan 9	56666	Tillinghast 60-in	FAST
2014 Jan 9	56666	Magellan-Baade	FIRE
2014 Jan 25	56682	Shane 3-m	Kast
2014 Jan 28	56685	Tillinghast 60-in	FAST
2014 Jan 30	56687	Tillinghast 60-in	FAST
2014 Feb 2	56690	Tillinghast 60-in	FAST
2014 Feb 2	56690	Magellan-Baade	FIRE
2014 Feb 3	56691	Magellan-Baade	IMACS
2014 Feb 26	56714	Tillinghast 60-in	FAST

Table 4.6—Continued

UT Date	MJD	Telescope	Instrument[a]
2014 Feb 27	56715	Magellan-Baade	FIRE
2014 Mar 4	56720	Tillinghast 60-in	FAST
2014 Mar 6	56722	MMT	BC
2014 Mar 7	56723	Tillinghast 60-in	FAST
2014 Mar 25	56741	Magellan-Baade	FIRE
2014 Apr 28	56775	MMT	BC
2014 Oct 23	56953	LBT	MODS
2015 Jan 15	57037	Magellan-Baade	IMACS

[a] Instrument References: FAST spectrograph (Fabricant et al. 1998) on the FLWO 60-inch Tillinghast telescope; Blue Channel (BC) spectrograph (Schmidt et al. 1989) on the 6.5 MMT; hectospec multi-fiber spectrograph (Fabricant et al. 2005) on the MMT; Low Dispersion Survey Spectrograph-3 (LDSS-3; Allington-Smith et al. 1994) on Magellan-Clay, the Inamori-Magellan Areal Camera & Spectrograph (IMACS; Dressler et al. 2006) on Magellan-Baade, OSMOS on the MDM 2.4-m (Martini et al. 2011), the Kast spectrograph (Miller & Stone 1993) on Shane 3-m at Lick Observatory, and the Multi-Object Double Spectrograph (MODS; Pogge et al. 2010) mounted on the 2 × 8.4-m LBT; Folded-port InfraRed Echellette spectrograph (FIRE; Simcoe et al. 2013) on Magellan-Baade

[b] Observation with the 1200 lines/mm grating.

4.2.6 Distance and Reddening

SN 2013ge exploded on the outskirts of NGC 3287. In this paper we adopt of distance of 23.7 ± 1.7 Mpc, corresponding to the NED distance after correction for Virgo, Great Attractor, and Shapley Supercluster infall, assuming $H_0 = 73$ km s^{-1} Mpc^{-1} (Mould et al. 2000).

Milky Way reddening in the direction of SN 2013ge is $E(B-V)_{MW} = 0.020$ mag (Schlafly & Finkbeiner 2011). To estimate the intrinsic absorption due to dust within NGC 3287, we examine our moderate resolution spectra obtained on 2014 Nov. 10 for narrow Na ID absorption lines. We identify two Na ID $\lambda\lambda$5889.9, 5895.9 doublets, one corresponding to Milky Way absorption, and one at the redshift of NGC 3287. The total equivalent width of the Na ID doublet at the redshift of NGC 3287 is ∼0.45 Å. Using the empirical relation of Poznanski et al. (2012) this implies a host galaxy contribution to the total reddening of $E(B-V)_{host} = 0.047$ mag. As a check, we apply the same procedure to the observed Milky Way Na ID absorption which yields an $E(B-V)_{MW}$ value of 0.037 mag. This value is slightly higher than that found by Schlafly & Finkbeiner (2011), but within the quoted errors of the relation from Poznanski et al. (2012). Throughout this paper we adopt an $R = A_V/E(B-V) = 3.1$ Milky Way extinction curve with a total reddening of $E(B-V)_{tot} = 0.067$ mag. This value is consistent with that derived from the V−R color method described in Drout et al. (2011).

4.3 Photometric Properties

4.3.1 Light Curve Evolution

A deep pre-explosion limit for SN 2013ge was obtained 7 days prior to its initial discovery. However, the rapid rise observed in the *Swift* u− and w1−bands (photometric coverage in these bands began ∼2 days after first detection; see Figure 4.5) indicates that our constraints on the epoch of first light may be more stringent than allowed by this non-detection alone. Extrapolating polynomial fits of the rising phase of these light curves backward in time, we infer an epoch of first light only ∼2 days prior to first detection. Power-law fits of the form $L_\lambda \propto t^{1.5}$ and $L_\lambda \propto t^2$ yield similar results. The former power law is expected for the rising phase of cooling envelope emission (e.g. Piro & Nakar 2013) and the latter is expected for early radioactive heating in the fireball model (Nugent et al. 2011). Throughout this paper we adopt an epoch of first light of 2014 Nov. 6.5 = MJD 56602.5 ± 2 days. An epoch of first light prior to this date would be inconsistent with the early u− and w1−band light curves unless the rate of rise *increased* some time post-explosion. Such behavior is not typically observed in SN light curves, and would have implications for the early emission source, which will be discussed in Section 4.6. The possibility of a "dark period" separating the epoch of first light from the explosion epoch (Piro & Nakar 2013) will be also discussed in Section 4.6.

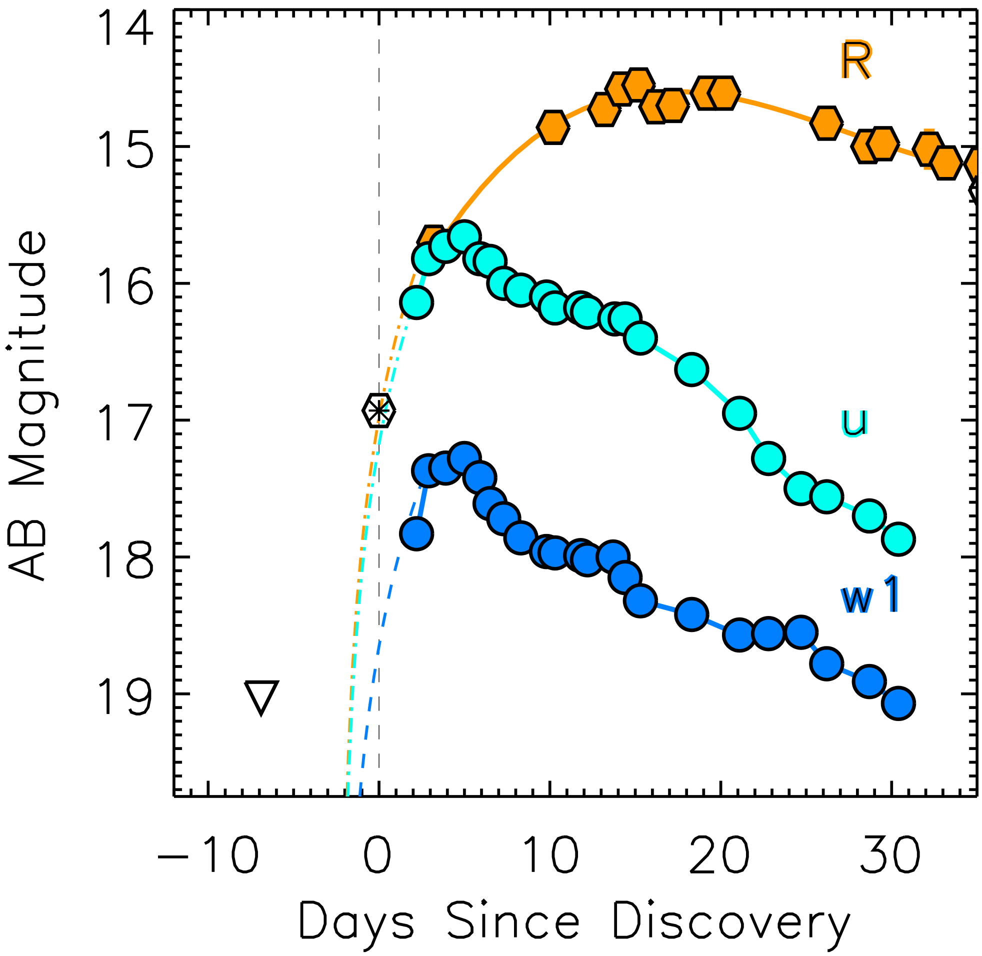

Figure 4.5.—: Characterization of the epoch of first light. Shown are the R-band (orange), u-band (cyan), and w1-band (blue) light curves, shifted to the AB system in the same manner as for Figure 4.2 (see Section 4.2.1). The rapid rise observed in the u− and w1−band light curves puts a tight constraint on the epoch of first light. Dashed colored lines are power law fits of the form $t^{1.5}$ to the rising phase of each band, all of which imply an epoch of first light 2 days prior to first detection. The unfiltered discovery and pre-explosion limit are shown as a hexagon with an asterisk and an open triangle, respectively.

In Table 4.7 we list basic properties for the UV and optical light curves of SN 2013ge, which were measured based on low order polynomial fits[5]. Throughout this paper, the phase of the SN will be given with respect to V-band maximum light: MJD 56618.6. This time of maximum implies a rise time in the V-band of ∼16 days. As is observed in other Type I SN, the time of maximum light cascades through the UV and optical bands (as shown by the dashed dotted line in Figure 4.2). SN 2013ge peaks at an absolute magnitude of approximately -17.3 mag (AB) in the optical, and declines between 1.1 mag and 0.38 mag in the first 15 days post maximum light (b−through−I bands, respectively). This places SN 2013ge at both the low luminosity and slowly-evolving end of Type I SN.

The BVRI light curves are characterized by a smooth rise to maximum light, followed by an initial decline and then a shallowing of the slope between 20 and 30 days post maximum light. Linear fits to the BVRI light curves between 60 and 120 days post-maximum reveal linear decline rates between 0.01 and 0.02 mag day^{-1}. This light curve morphology is typical for Type I SN.

---

[5] Polynomial fits for each band were performed based on photometry for a single source, as listed in Table 4.7.

Table 4.7. Basic Photometric Properties

Band	T_{max} (MJD)	$m_{\mathrm{obs,max}}$ (AB mag)	$M_{\mathrm{abs,max}}$ (AB mag)	Δm_{15} (mag)	Neb. Decline Rate[a] (mag day^{-1})
*w*2	56608.7 (1.1)	18.51 (0.06)	−13.36 (0.05)	>0.65	···
*m*2	56607.7 (1.0)	18.40 (0.05)	−13.47 (0.05)	>0.70	···
*w*1	56608.8 (1.0)	17.18 (0.04)	−14.69 (0.04)	1.23 (0.08)	···
u	56609.4 (1.1)	15.56 (0.04)	−16.31 (0.04)	1.16 (0.05)	···
b	56615.7 (1.5)	14.93 (0.03)	−16.94 (0.03)	1.11 (0.05)	0.0119 (0.0004)
v	56618.6 (1.5)	14.52 (0.05)	−17.35 (0.05)	0.74 (0.11)	0.0156 (0.0003)
R	56621.1 (1.5)	14.55 (0.03)	−17.32 (0.03)	0.44 (0.05)	0.0155 (0.0003)
I	56623.1 (1.5)	14.54 (0.03)	−17.33 (0.03)	0.38 (0.06)	0.0198 (0.0004)

Note. — Values for peak magnitudes, time of maximum, and Δm_{15} were measured from low order polynomials to photometry from a single source for each band. For w2−through−v bands, the polynomial was fit to the data from *Swift* UVOT, while for R−band and I−band the polynomial was fit to CAO data. The peak magnitudes presented here have been shifted to the AB photometric zeropoint as described in Section 4.2.1.

[a] Measured from a linear fit to the FLWO data between +60 and +120 days.

4.3.2 Early UV Light Curves

In contrast, the u− and w1−band light curves observed for SN 2013ge show a distinctly non-standard evolution. They display an early "bump" which is characterized by a rapid rise and decline over the first week of observations, before plateauing and then falling off rapidly again. In the top panel of Figure 4.6 we demonstrate that the u−band light curve can be decomposed into two components: a main component which peaks ∼11 days after discovery superimposed with an early peak of emission which rises rapidly over ∼4 days and declines rapidly after ∼1 week. This particular decomposition is for illustrative purposes only, as we do not constrain the rising behavior of the second component. Vertical dashed lines mark our first three epochs of spectroscopy, which probe the early rising portion of the first component.

Although well sampled u−band light curves between −14 and −7 days are still quite rare for Type I SN, no previous object has shown two distinct components with these timescales. This is demonstrated in the lower panel of Figure 4.6 where we compile u−band light curves from the literature. A majority of the events peak ∼4 days prior to V−band maximum and then decline rapidly, consistent with our inferred time of maximum and subsequent evolution for the *second* component in SN 2013ge.

Prior to this maximum, the evolution of the literature events is varied. Both SN 2008D and SN 2005bf also show double-peaked u−band light curves, but with timescales significantly different than those observed in SN 2013ge. The first peak in the light curve of SN 2008D rises on a timescale of ∼1 day from the observed X-ray flash, while the first light curve component of the peculiar Type Ib SN 2005bf has a rise time $\gtrsim$13 days. The early emission from SN 2008D has been interpreted as both adiabatic

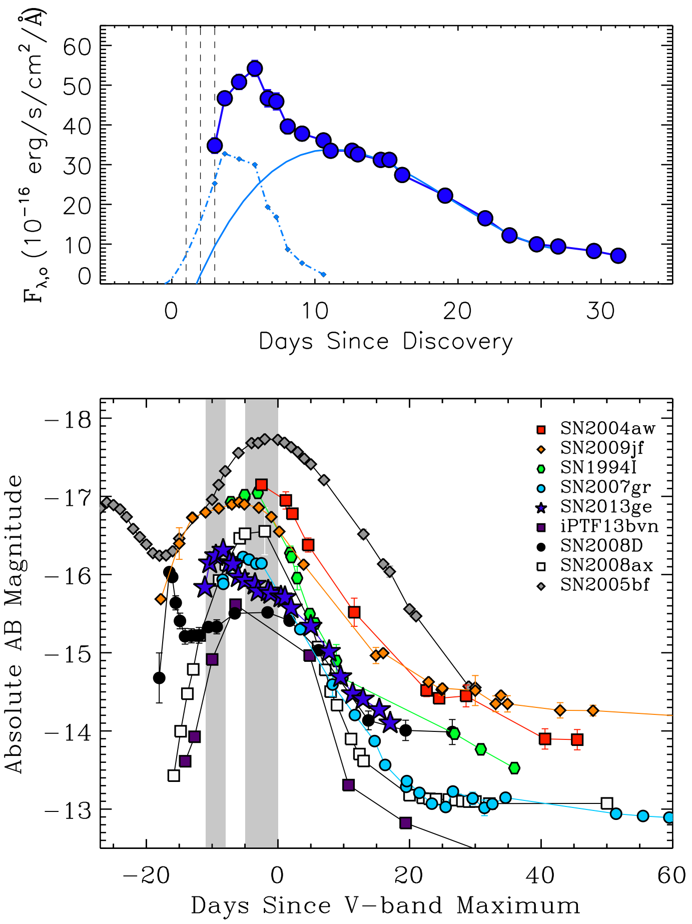

Figure 4.6.—: *Top:* Example decomposition of the u-band light curve into two components. This should be taken as representative only as we do not constrain the rising behavior of the second component. Dashed vertical lines represent our first three epochs of spectroscopy, which occur on the early rising portion of the first light curve component. *Bottom:* Comparison of the u-band light curve of SN 2013ge to other stripped core-collapse SN. Shaded regions highlight the time of maximum for both components of SN 2013ge. Most events peak on a timescale similar to that observed for the second component in SN 2013ge. The light curve of SN 2009jf shows a plateau that may be indicative of an early component similar to that observed in SN 2013ge. *References:* SN 2005bf (Folatelli et al. 2006), SN 2004aw (Taubenberger et al. 2006), SN 2009jf (Valenti et al. 2011), SN 2007gr (Hunter et al. 2009), SN 2008ax (Pastorello et al. 2008), SN 2008D (Soderberg et al. 2008), iPTF 13bvn (Fremling et al. 2014; Cao et al. 2013). Photometry for all objects was converted to the AB system zeropoint before plotting.

cooling emission and as emission associated with a double-peaked ^{56}Ni distribution. In contrast, in the model of Maeda et al. (2007), the first peak of SN 2005bf is powered by the radioactive decay of ^{56}Ni while the second peak requires an additional power source such as a central engine. Intriguingly, the U−band light curve of the Type Ib SN 2009jf shows a plateau which could be consistent with two components similar to those in SN 2013ge if the luminosities were comparable.

Finally, we note that the w1−band light curve of SN 2013ge shows tentative evidence for multiple changes in slope over ∼30 days. However, additional observations would be necessary to discern if the behavior between +20 and +30 days is due to a change in input power source or variations in spectral features/line blanketing.

4.3.3 Color Evolution and SEDs

In Figure 4.7 we plot the U−B and B−V colors of SN 2013ge and several other Type Ib/c SN. The grey shaded region highlights the time of the u−band excess described above. During these epochs, the u−b color of SN 2013ge is relatively flat for 3 days before rapidly reddening from ∼0.4 mag to ∼0.9 mag over 4 days. The $B - V$ color evolution of SN 2013ge is similar to other Type Ib/c SN.

In Figure 4.8 we plot the spectral energy distribution (SED) of SN 2013ge for epochs on the rising phase of the initial u−band peak (including our first three epochs of spectroscopy). The first spectroscopic observations are characterized by a very blue continuum, while from day −11 onward the *Swift*-UVOT photometry shows that the SED falls off significantly in the UV−bands. As shown in the lower panel of Figure 4.8, it is not possible to fit both the slope of the optical SED and the low flux level in the

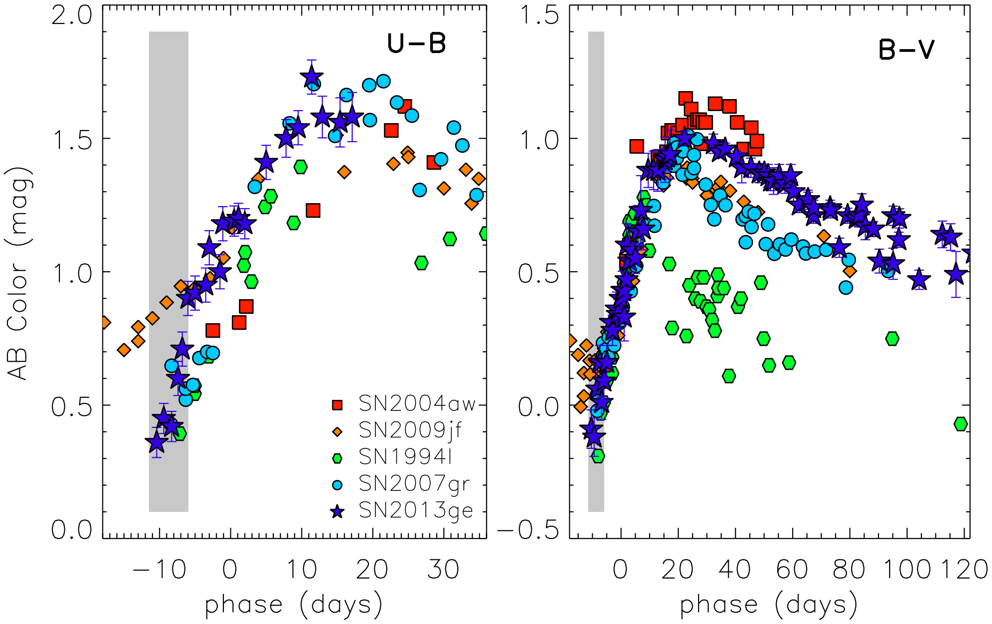

Figure 4.7.—: u−b and B−V color evolution of SN 2013ge in comparison to other Type Ib/c SN. Shaded regions indicate the time of the first light curve component. During the declining portion of the first light curve component (−8 to −5 days) the u−b color reddens drastically. The B−V evolution of SN 2013ge is very similar to other Type Ib/c SN. Photometry for all objects was converted to the AB system zeropoint before plotting. SN 2013ge data contains u−b and b−v observations from *Swift*-UVOT as well as Bessell B−V data from CAO and FLWO. All literature objects were observed with Bessell filters (see Figure 4.6 for references).

UV−bands with a single blackbody. Such behavior may indicate that line blanketing is significantly depressing the UV−flux, even at these very early epochs.

Fitting blackbodies to the BVRI−bands only we find color temperatures which fall from around 13,000 K at −12 days to around 7000 K at V−band maximum. The precise temperature evolution during the initial u-band peak is difficult to assess due to (1) the depressed UV flux and (2) our lack of dense R− and I-band photometry at the earliest epochs.

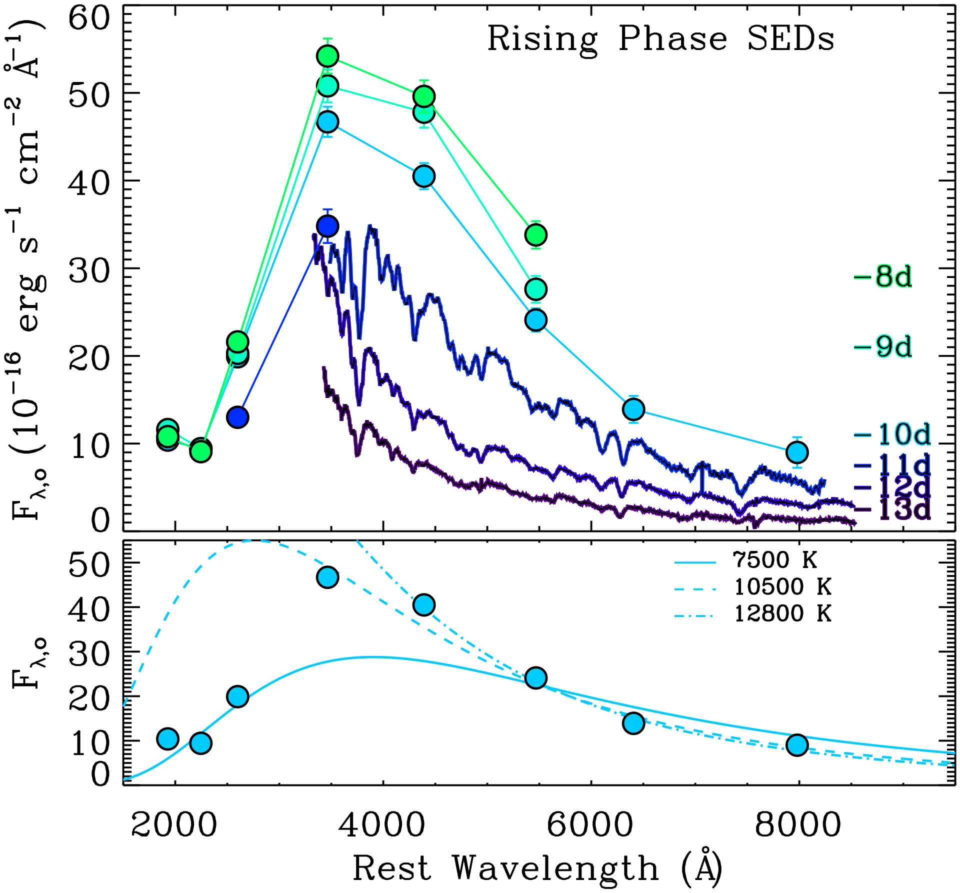

Figure 4.8.—: *Top:* Spectra and broadband photometry obtained on the rising phase of the first light curve component. Our earliest spectra, obtained before broadband photometry, show a steep blue continuum with narrow superimposed spectral features. Our first epoch of *Swift*-UVOT photometry (−11 days) constrains the peak of the SED to be around 3500 Å. Early spectra have been multiplied by a constant for clarity. *Bottom:* The −10 day SED with superimposed blackbody fits. It is not possible to fit both the slope of the SED in the optical and the depressed UV flux with a single temperature blackbody, indicating that line blanketing may be important even at these early epochs.

4.3.4 Pseudo-Bolometric Light Curve

To create a pseudo-bolometric light curve, we first sum our UV-optical photometry by means of a trapezoidal integration. To account for missing IR flux, we attach a blackbody tail from the best-fit blackbody to the BVRI data. This method of accounting for IR flux is equivalent to adding an IR contribution which monotonically increases from 15% at early times to ∼50% at late times. This is in line with what is found for Type I SN with well-observed IR light curves (see, e.g., Valenti et al. 2008; Lyman et al. 2016). To account for UV contributions at later epochs (beyond our *Swift*-UVOT coverage) we extrapolate the observed w2, m2, w1, and u−band light curves until they account for less than 0.5% of the pseudo-bolometric luminosity, at which point they are dropped from the integration. We note that the flux contained in the w2/m2−bands and w1/u−bands accounts for $\lesssim 1\%$ and only a few % of the bolometric luminosity at the epoch of their final observed data points, respectively. Thus, ambiguity in the morphology of the late-time UV light curve should not significantly impact the derived light curve.

The resulting pseudo-bolometric light curve is shown in Figure 4.9, along with the pseudo-bolometric light curves of other SN. Although two distinct peaks are not evident, an excess "shoulder" of emission can be seen at early times corresponding to the first u−band component described above. The bolometric light curve peaks at $2.1 \pm 0.1 \times 10^{42}$ erg s^{-1} and the total radiated energy between −12 and +120 days is $8.1 \pm 0.3 \times 10^{48}$ erg.

Assuming SN 2013ge is powered mainly by the radioactive decay of ^{56}Ni, we use the analytic models of Arnett (1982) and Valenti et al. (2008), with the corrections of Wheeler et al. (2015), to extract estimates of the explosion parameters from this

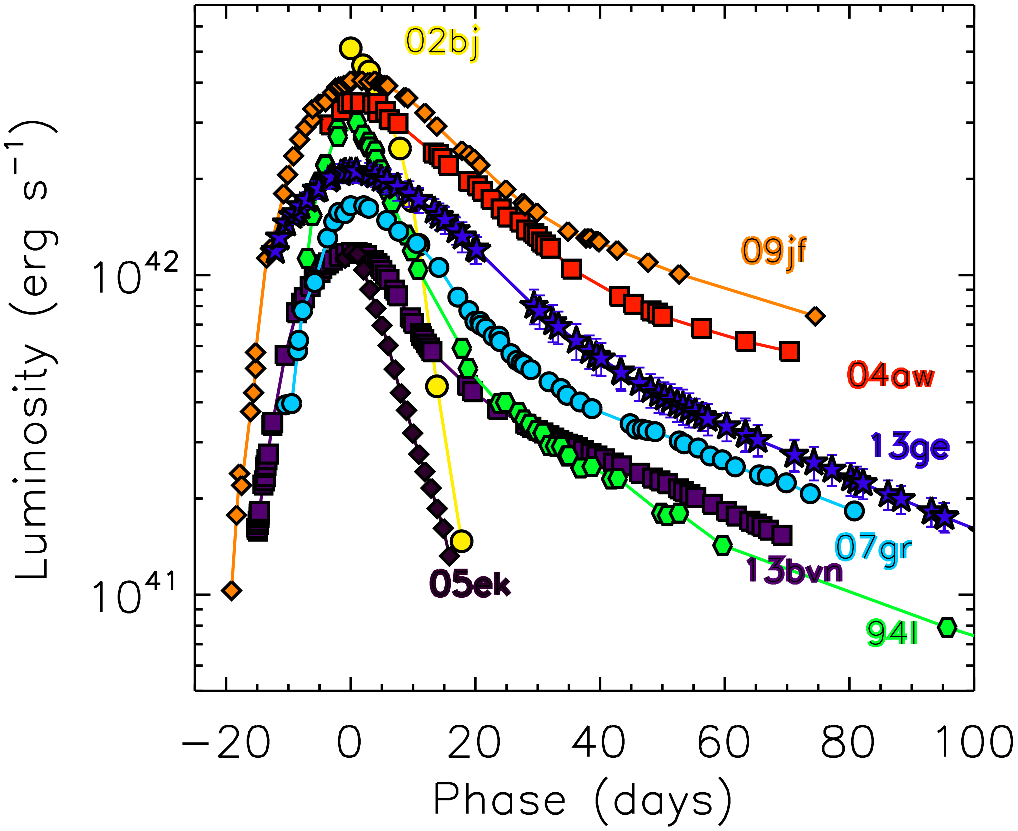

Figure 4.9.—: Pseudo-bolometric Light Curve of SN 2013ge in comparison to other Type Ib/c SN. SN 2013ge is relatively faint and slowly evolving. Two distinct peaks are not visible in the pseudo-bolometric light curve, but the morphology of the early UV light curves results in a "shoulder" of excess emission at early times. References for comparison objects: SN 2005ek (Drout et al. 2013), SN 2002bj (Poznanski et al. 2010), SN 2004aw (Taubenberger et al. 2006), SN 2009jf (Valenti et al. 2011), SN 2007gr (Hunter et al. 2009), SN 1994I (Richmond et al. 1996), iPTF13bvn (Fremling et al. 2014). U-band photometry was available for all comparison objects with the exception of SN 2002bj. When NIR photometry was available, UBVRIJHK data was summed to produce the comparison light curves. When NIR photometry was not available, a black body tail was added to an integration of the UBVRI data. The comparison light curves shown here do not account for UV flux emitted blueward of the U-band.

pseudo-bolometric light curve. We assume that from −8 to +20 days SN 2013ge is in the optically thick photospheric phase (we neglect the earliest data, during the "UV bump", when performing our fit), and utilize a constant opacity of 0.07 cm^2 g^{-1} (corresponding to the case of electron scattering). Under these assumptions we find best-fit explosion parameters of $\mathrm{M_{Ni}} \approx 0.12\ \mathrm{M_\odot}$, $\mathrm{M_{ej}} = 2 - 3\ \mathrm{M_\odot}$, and $\mathrm{E_K} = 1 - 2 \times 10^{51}$ erg. We have assumed a photospheric velocity at maximum of 10,000 − 11,000 km s^{-1} in order to break the degeneracy between $\mathrm{M_{ej}}$ and $\mathrm{E_K}$ (see Section 4.4).

Inserting these best-fit parameters from the photospheric phase in the nebular model from Valenti et al. (2008) we find a predicted luminosity which is relatively consistent with our late-time (> 60 days post-maximum) pseudo-bolometric light curve, although the predicted model declines more rapidly than the observed light curve. Such a trend has been noted in the literature when attempting to model Type Ib/c SN with single zone models (see, e.g., Maeda et al. 2003 and Valenti et al. 2008), and may indicate that SN 2013ge could be better described by a two-zone model with a high-density inner region and a low-density outer region. Alternatively, this could be evidence for an asymmetry in the explosion.

4.4 Spectroscopic Properties

4.4.1 Type Ib/c versus Type Iax

SN 2013ge can be immediately identified as a Type I SN since it lacks *conspicuous* hydrogen emission, and can further be sub-classified as a Type Ib/c from the lack of a strong Si II λ6355 feature (Wheeler et al. 1995). Near maximum light, the spectral features are relatively narrow and resemble maximum light spectra of both normal (not broad-lined) Type Ib/c SN and Type Iax SN (Foley et al. 2013). In order to resolve this degeneracy, in Figure 4.10 we compare spectra of SN 2013ge (red) to spectra of several normal Type Ib/c SN (black) and Type Iax SN (blue) at three phases: maximum (panel A), intermediate/transitional (panel B) and nebular (panel C).

Taken in conjunction, it is clear that from maximum light onwards SN 2013ge follows a spectral evolution typical for normal Type Ib/c SN. Near maximum light, iron peak elements are visible at bluer wavelengths as well as O I and the Ca II NIR triplet in the red. By +39 days, SN 2013ge has entered a transitional phase, marked by the onset of increased emission in the Ca II NIR triplet. This growth of the Ca II NIR feature has been observed in numerous Type Ib/c SN. Finally, at nebular phases SN 2013ge is dominated by emission from forbidden transitions of intermediate mass elements such as [O I], [Ca II], and Mg I].

This is in stark contrast to Type Iax SN, which do not show growth of the Ca II NIR triplet at intermediate phases and whose late-time spectra are dominated by forbidden Ca II and Fe II lines with no obvious contribution from [O I]. However, it is worth emphasizing the strong similarity between some Type Iax spectra and normal Type Ic spectra at maximum light—especially in the wavelength range $4200 - 7500$ Å. The main differentiating spectral features seem to be at wavelengths shorter than 4200 Å, where SN Iax show a plethora of lines which are not evident in normal Type Ib/c SN. Caution should be taken in classifying a Type Iax SN from a single maximum light spectrum.

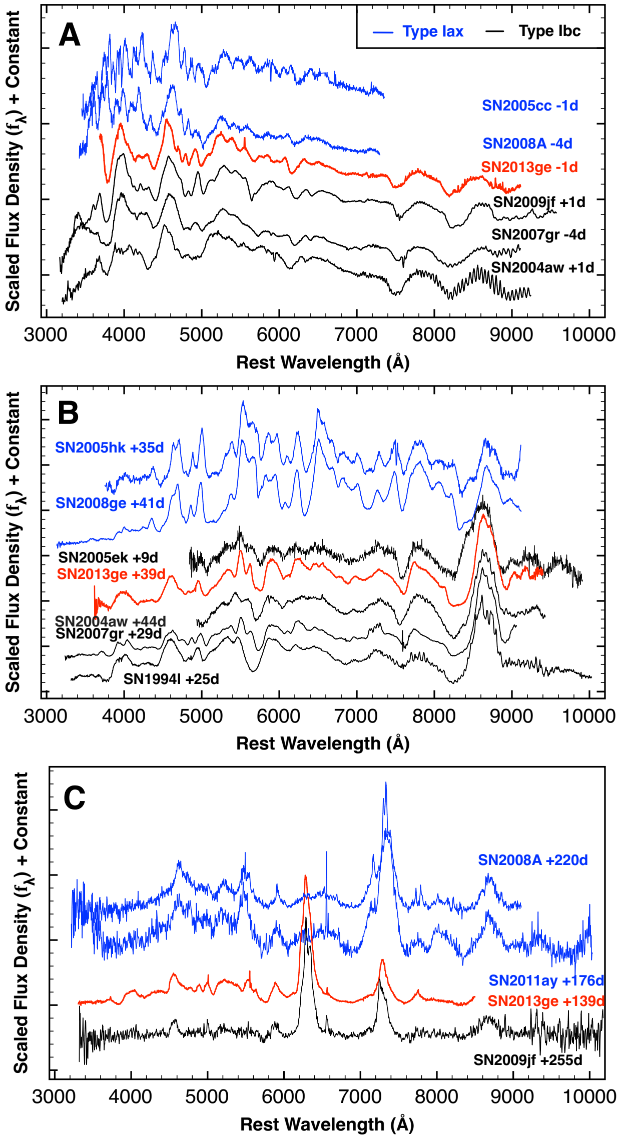

Figure 4.10.—: Comparison of the spectrum SN 2013ge at maximum light (panel A), intermediate phases (panel B) and nebular epochs (panel C) to spectra of Type Ib/c SN (black) and Type Iax SN (blue). Although there is significant overlap between both classes of objects at maximum light, at intermediate and late phases the evolution of SN 2013ge is similar to Type Ib/c SN. *References:* SN 2005cc and SN 2008A (Blondin et al. 2012), SN 2005hk (Phillips et al. 2007), SN 2008ge (Silverman et al. 2012), SN 2011ay (Foley et al. 2013), SN 2009jf (Valenti et al. 2011), SN 2007gr (Valenti et al. 2008), SN 2004aw (Taubenberger et al. 2006), SN 2005ek (Drout et al. 2013), SN 1994I (Filippenko et al. 1995).

4.4.2 Early Spectra

Despite evolving similarly to normal Type Ic SN from maximum onward, the early spectra of SN 2013ge are unusual for Type Ib/c SN. Our earliest three spectra, obtained between -13 and -11 days, are characterized by a blue continuum, superimposed with relatively shallow and *narrow* features (FWHM $\lesssim$ 3500 km s^{-1}). These spectra were obtained during the early rising phase of the first u−band component described in Section 4.3. Spectroscopic observations of Type Ib/c SN at such early epochs are rare, but a majority of events show *broad* high-velocity features at early times, which narrow as the photospheric velocity deceases. Indeed, these spectra vary significantly from the earliest spectra obtained for SN 2008D, SN 2009jf, PTF 12gzk, and iPTF 13bvn, all of which showed broad spectral features at similar epochs (see Figure 4.11).

During its first light curve peak, the spectrum of the peculiar Type Ib SN 2005bf did show several narrow spectroscopic features between 4500 Å and 5300 Å (see Figure 4.11; phases are given with respect to both the first and second peak). However, features in the rest of the spectrum were broader and more comparable to the other Type Ib/c SN shown in Figure 4.11. Folatelli et al. (2006) interpret this as the combination of an underlying photosphere (broad) and high-velocity iron and calcium features (narrow). In contrast, in the early spectra of SN 2013ge, *all* of the features observed have similarly narrow widths. Intriguingly, the "super-Chandra" Type Ia SN 2006gz (Hicken et al. 2007) also showed narrow spectroscopic features with blue-shifted absorption minima similar to SN 2013ge at early times. However, by maximum light SN 2006gz developed a very prominent Si II λ6355 feature, indicative of Type Ia SN, which was not observed in SN 2013ge.

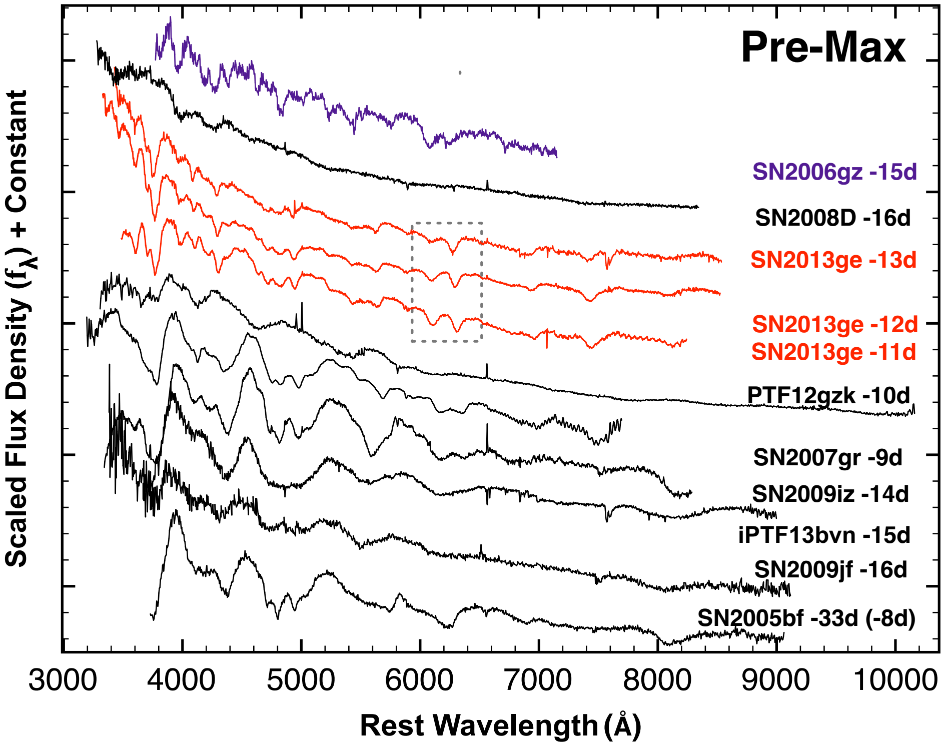

Figure 4.11.—: Very early spectra of SN 2013ge (red) compared to other Type Ib/c SN (black) and one "super-Chandra" Type Ia SN (purple). The spectra of SN 2013ge are characterized by blue continua and *narrow* spectroscopic features. In contrast, most other Type Ib/c SN with spectra at similar epochs show very broad features. One exception is the Type Ib SN 2005bf which during its first light curve peak showed both broad underlying features and narrow high-velocity features of Fe II and Ca II (phases are listed for SN 2005bf with respect to *both* light curve peaks). Interestingly, the "super-Chandra" Type Ia SN 2006gz also showed narrow spectroscopic features with blue-shifted absorption minima—similar to SN 2013ge—at early times. The dashed grey box highlights two features in the spectra of SN 2013ge whose ratio shows significant evolution over ∼2 days. *References:* SN 2006gz (Hicken et al. 2007), SN 2008D (Modjaz et al. 2009a), PTF 12gzk (Ben-Ami et al. 2012), SN 2007gr (Valenti et al. 2008), SN 2009iz (Modjaz et al. 2014), iPTF 13bvn (Milisavljevic et al. 2013), SN 2009jf (Sahu et al. 2011), SN 2005bf (Folatelli et al. 2006).

In addition, we observe rapid evolution in both the slope of the continuum and photospheric velocity over the two days in which these early spectra of SN 2013ge were obtained. Two absorption features between 6000 and 6500 Å also undergo a large change in their ratio over this time period. These features are highlighted by a grey box in Figure 4.11.

4.4.3 Assessing the Presence of Unburned Material

For many models, fully stripping the H/He layers from putative Type Ib/c progenitors has proved challenging. This makes possible identifications of trace amounts of these elements in Type Ib/c SN both important and long debated (see Parrent et al. 2014 for a review). Unfortunately, the identification of such contaminants is particularly complicated in the optical photospheric spectra of Type Ib/c SN where a number of degeneracies exist, most notably between H I $\lambda6563$, C II $\lambda6580$, and Si II $\lambda6355$, and He I $\lambda5876$ and Na I $\lambda5889$. These degeneracies can be partially alleviated if NIR spectra are available.

Early phase spectra probe the outermost regions of the ejecta where unburned material such as hydrogen and helium are most likely to be present, if at all. We therefore begin by examining our earliest three optical spectra (days −13, −12, −11) as well as our IR spectra at later epochs. In Figure 4.12 we shift the spectra from rest frame wavelength to the projected Doppler velocities of commonly found lines in order to examine preliminary matches between spectral features and dominant candidate lines of hydrogen, helium, and carbon. Each panel will be discussed in turn, below.

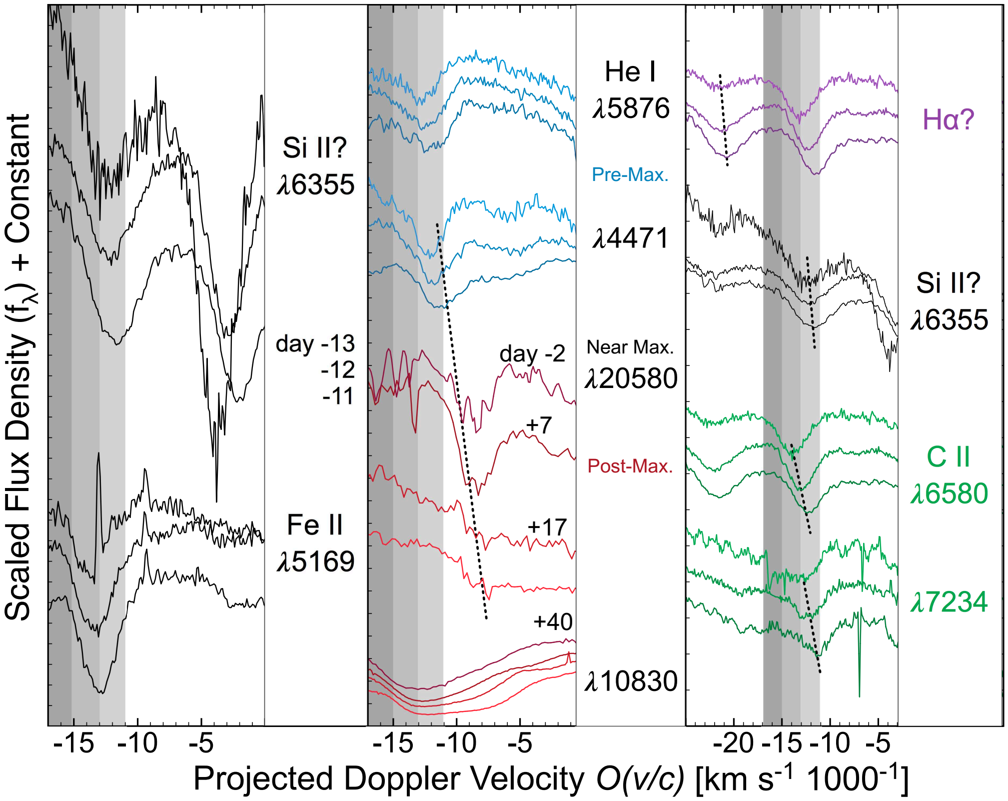

Figure 4.12.—: Projected Doppler velocities around key features in the spectra of SN 2013ge. These are used to assess the presence of unburned material (hydrogen, helium, and carbon). Grey regions mark particular velocities and are placed to guide the eye. Dashed lines highlight the velocity evolution of certain features with time. *Left:* The regions around Si II λ6355 and Fe II λ5169 in the −13, −12, and −11 day spectra. *Middle:* Assessing the presence of helium in the early optical spectra (top; blue) and maximum light NIR spectra (bottom; red). See text for details. *Right:* Assessing the degeneracy between Hα, Si II λ6355, and the presence of C II λ6580. See text for details.

Hydrogen

When we associate lines with Si II λ6355 and Fe II in the left panel of Figure 4.12, we see that the velocity of the absorption minima is ∼14,000 km s^{-1} (grey vertical bands are placed to guide the eye, and correspond the the same velocities in each panel). At the top of the right panel of Figure 4.12 we show the spectral region around Hα (purple). While the feature observed at ∼6300 Å appears at similar velocities to Fe II when interpreted as Hα, we find that the velocity overlap and implied velocity evolution is more consistent with the interpretation of C II λ6580 (see below for further discussion of carbon). However, this does not preclude very weak contributions from Hα to the observed feature.

We next investigate the possibility of high-velocity Hα in these early spectra. In particular, we note that the feature most often associated with Si II λ6355 appears at slightly lower velocities than Fe II, which would seem to suggest that photons from deeper layers are escaping opaque resonance line regions of iron. This model-independent discrepancy between the line velocities of Si II and Fe II absorption minima is frequently encountered for Type Ib/c SN (e.g. Branch et al. 2006; Elmhamdi et al. 2007; Milisavljevic et al. 2015; see Parrent et al. 2016 for a comprehensive examination), and may indicate that another ion is contributing to the observed line(s). In core-collapse SN, a candidate line in the wavelength region around Si II λ6355 is high-velocity Hα (Wheeler et al. 1995; Benetti et al. 2011; Parrent et al. 2016). In the top of the right panel of Figure 4.12 we show the velocities of Si II (black) versus H I (purple) which would be necessary to overlap with the feature observed at ∼ 6100 Å (dashed lines indicate the relevant feature in each case). If Hα contributes, it requires velocities in excess of 20,000 km s^{-1}. Unfortunately, we lack certain detections of either Si II $\lambda5972$ or Hβ in the early spectra of SN 2013ge, and therefore we cannot definitely confirm the presence or relative contributions of H I versus Si II to the observed feature.

Helium

In the middle panel of Figure 4.12, we examine the case for He I in the spectra of SN 2013ge. In the top portion of the panel, we show the earliest optical spectra in the region of He I $\lambda\lambda5876$, 4471 and find evidence for both lines at velocities which are consistent with the composite Fe II feature. A slight notch is also present at ∼6400 Å, consistent with He I $\lambda6678$ at a similar velocity (see Figure 4.14).

In the lower portion of the panel, we examine four NIR spectra (−2 to +40 days; red) and focus on the features near 1μm and 2μm. The large 1μm feature is significantly broader than the 2μm feature, and is often attributed to a blend of multiple ions including C I and Si I (Millard et al. 1999; Taubenberger et al. 2006). We detect a feature near 2μm, which is consistent with faint He I at ∼8000−9000 km s^{-1}. This is comparable to the photospheric velocities at these epochs (the dotted line is placed to guide the eye between the relevant features). Thus, we find that there is room for the existence of He I $\lambda\lambda4471$, 5876, 6678, 10830, and 20580 in the spectra of SN 2013ge. In addition, the identification of weak optical signatures of He I is consistent with either weak or absent signatures of He I $\lambda6678$ and 7065 (Branch et al. 2002; Hachinger et al. 2012).

We therefore conclude that our data is consistent with the identification of weak He I in the early spectra of SN 2013ge. We emphasize that these lines are weak and fade with time; they are distinct from the strong He I features observed in many SN classified as Type Ib, which are strongest a few weeks past maximum (e.g. Filippenko 1997; Liu et al. 2015). *SN 2013ge may therefore represent the detection of weak helium features in an event which would generally be classified as Type Ic.*

Carbon

Finally, in the lower portion of the right panel of Figure 4.12 we identify signatures of C II λλ6580, 7234 in the early spectra of SN 2013ge (green). We also examine our NIR spectra for evidence of C I features at later epochs (Figure 4.13). While we cannot rule out weak contamination from C I, the influence must be substantially weaker than that observed in the NIR spectra of the "carbon-rich" SN 2007gr (Hunter et al. 2009).

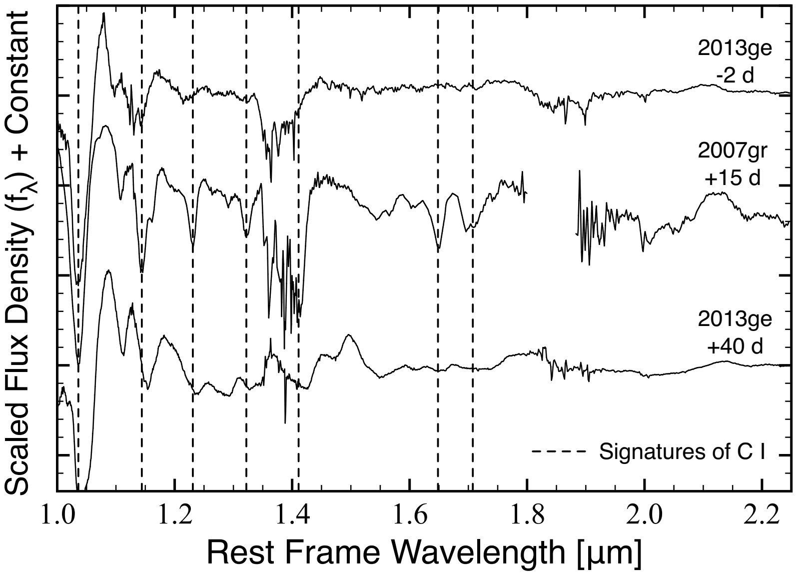

Figure 4.13.—: A comparison between the NIR spectra of SN 2007gr and SN 2013ge. Vertical dashed lines denote C I lines marked by Hunter et al. 2009 in their Fig. 12. Lines of a comparable strength are not observed in SN 2013ge.

4.4.4 Species Identification and Velocity Estimation

In order to further constrain the full set of ions present in the spectra of SN 2013ge, as well as the evolution of the velocity of the line-forming region, we utilize the fast and publicly available spectral synthesis code `SYN++` (Thomas et al. 2011)[6]. Line formation in `SYN++` is assumed to be dominated by pure resonant scattering with Boltzmann statistics determining relative lines strengths for a given ion. We use an exponential optical depth profile that begins at the (sharp) photospheric velocity, which is set by hand for each epoch. See Parrent (2014) for general fitting methods and procedures.

In Figure 4.14 we present detailed line identifications inferred with `SYN++` and show example `SYN++` fits (red lines) for both the early phase and maximum light spectra. For the photospheric spectra of SN 2013ge, we tested a full list of ionization species (H I through Fe III). Colored ticks at the top of each panel mark the wavelengths where a given ion is believed to be influencing the spectrum. Main contributors to the model fits include He I, C II, and O I as well as Mg II, Si II, Ca II, Ti II, Fe II, and possible S II and Fe III. In the `SYN++` models shown, only Si II contributes to the feature observed at ~6100 Å (we have not included high-velocity hydrogen).

The velocity of the line-forming region is estimated to decrease from ~15,000 km s^{-1} to ~13,000 km s^{-1} between −13 days and −11 days. This is similar to the early velocity evolution observed in SN 2008D (Modjaz et al. 2009b). In order to simultaneously reproduce the relatively high blueshift and narrow width of the features at these early epochs with `SYN++`, we set the minimum velocity parameter, $\mathtt{v}_{min}$, for all of the ions to ~15,000 km s^{-1} while the model photosphere, $\mathtt{v}_{phot}$, was set to 10,000 km s^{-1}. Within

---

[6] This is an updated version of `SYNOW`; https://c3.lbl.gov/es/.

the semi-empirical parameter space of `SYN++`, this is equivalent to the process by which one typically adds "detached" high-velocity features to a spectrum. We emphasize that in this case this process was applied to *all* of the ions and is not necessarily meant to suggest a region which is physically detached from a luminous source; the physical interpretation of these early spectra will be discussed in Section 4.6.

A similar set of ions is inferred for the maximum light spectrum, although significant evolution is observed. For instance, the spectrum is now significantly redder, a substantial Ti II absorption trough has formed between 4000 Å and 4500 Å, and the strength of the He I and C II identified features has decreased significantly with respect to the 6250 Å feature (which may be influenced by both Si II λ6355 and trace amounts of hydrogen, as described above). In addition, the velocity of the line-forming region has decreased to $\sim$11,000 km s^{-1}—typical for Type Ib/c SN at maximum light—and the width of the features is relatively well matched to the velocity of their absorption minima. Unfortunately, poor weather prohibited us from obtaining any spectra between -11 and -1 days. As a result, we were unable to observe the evolution from narrow high-velocity features in the early spectra toward moderate width and velocity features in the maximum light spectra.

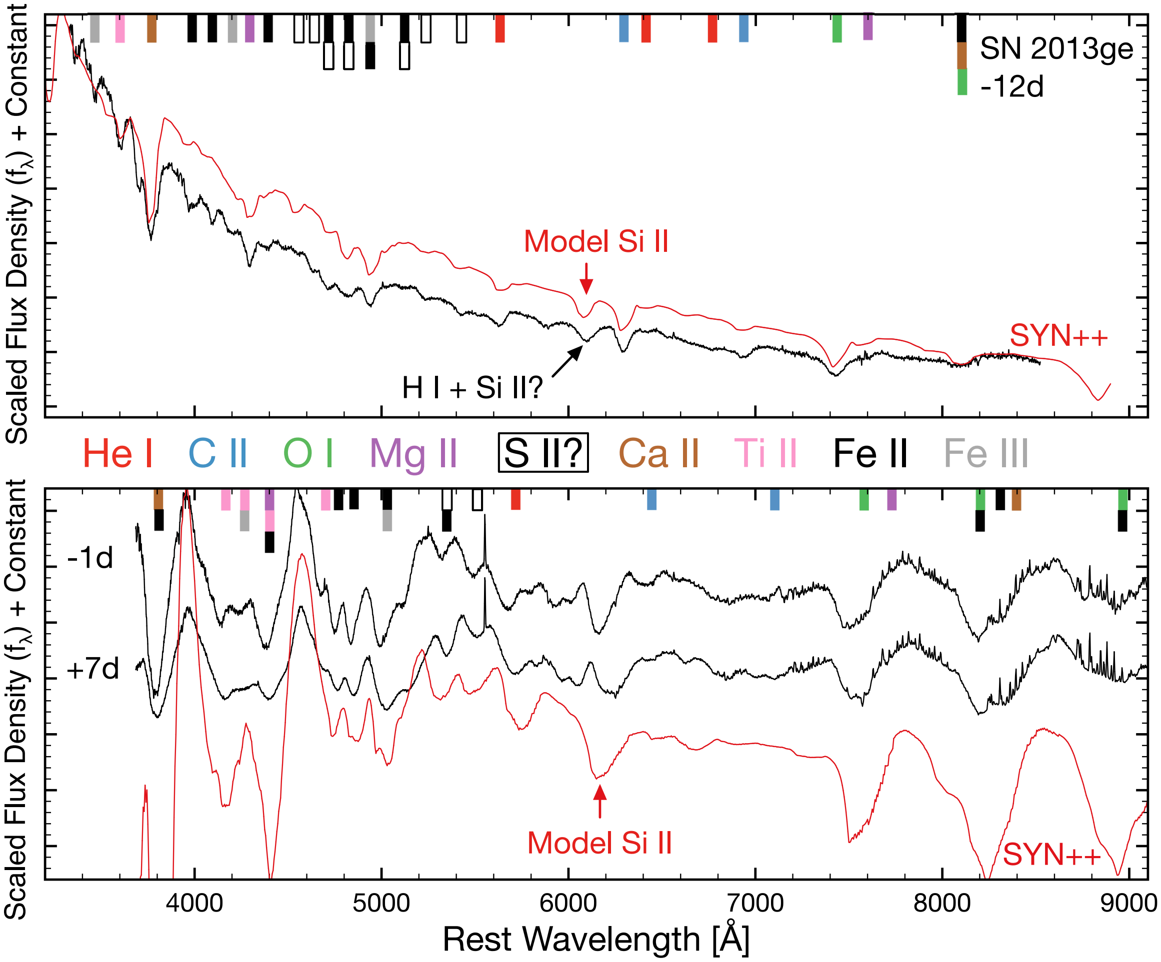

Figure 4.14.—: Ion identifications in the early (top panel) and maximum light (bottom panel) spectra of SN 2013ge. Observed spectra are shown in black while SYN++ models are shown in red. Colored rectangles designate the ions that contribute to each feature in the model spectra, as labeled between the panels. Species identified include He I, C II, and O I as well as contributions from Mg II, Si II, Ca II, Ti II, Fe III, and possibly S II and Fe III. Between −12 days and maximum light the blue continuum is significantly depressed. See text for more details.

4.4.5 Nebular Spectra Analysis

In the left panel of Figure 4.15 we plot the nebular spectra of SN 2013ge in comparison to SN 2007gr and SN 2009jf. The late-time spectra of SN 2013ge show conspicuous features due to [O I], [Ca II], and Mg I]. The flux contained in the [O I] $\lambda\lambda6300, 6364$ feature is significantly larger than that in either [Ca II] $\lambda\lambda7291, 7324$ or Mg I] $\lambda4571$, with ratios of ~0.3 and ~0.12, respectively. Notably, these ratios show very little evolution between +150 and +450 days.

The [Ca II]/[O I] ratio may be an indicator of progenitor core mass, with lower values implying a larger core mass, although mixing can also play a role (Fransson & Chevalier 1989). The ratio measured in SN 2013ge is on the low end of values observed in stripped core-collapse SN, comparable to that observed in SN 2009jf.

Hunter et al. (2009) examined the Mg I]/[O I] ratio for a large number of stripped core-collapse SN and the ratio observed in SN 2013ge is on the extreme low end when compared to this sample. It is also notable for its lack of evolution; a majority of events show a Mg I]/[O I] ratio that grows with time. For example, in SN 2007gr the Mg I]/[O I] ratio grows from ~0.1 to ~1 between 150 and 450 days post-maximum. This growth is *not* observed in either SN 2013ge or SN 2009jf (see Figure 4.15). To explain a weak Mg I] feature at late times in comparison to other SN we require that either the abundance of Mg produced in SN 2013ge is lower, or that the Mg I] line itself is suppressed due to other effects. For instance, Hunter et al. (2009) invoke mixing in the ejecta to explain the decreasing Mg I]/[O I] trend observed in SN 1998bw and SN 2006aj. In addition, in spectral models of Type IIb SN, Jerkstrand et al. (2015) find that the Mg I] $\lambda4571$ line is very sensitive to clumping in the O-Ne-Mg layer, with denser clumps favoring brighter

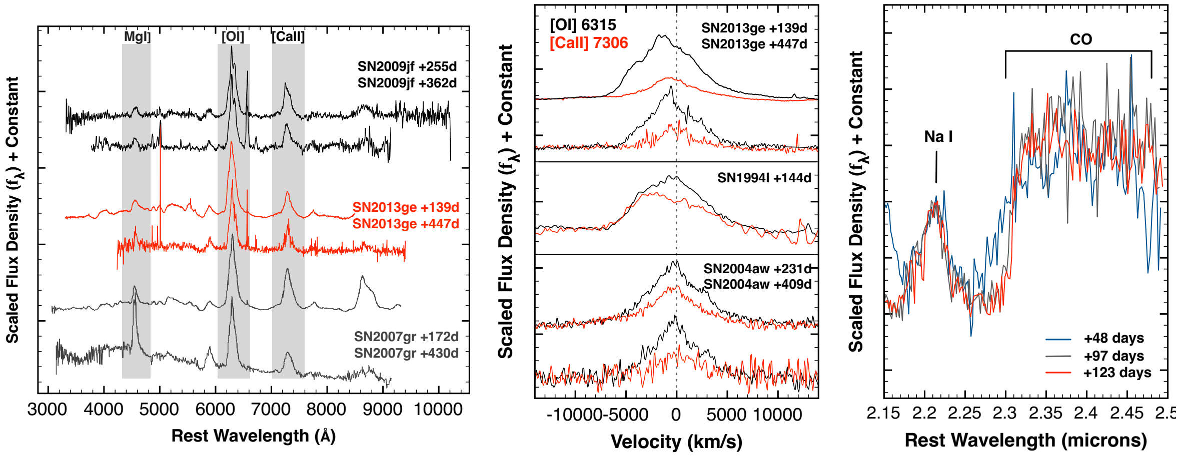

Figure 4.15.—: *Left:* A comparison between the nebular spectra of SN 2013ge, SN 2007gr, and SN 2009jf at multiple epochs. At ∼150−250 days, all have a Mg I] λ4571 to [O I] λλ6300, 6364 ratios of ∼0.15. However, by ∼450 days, the ratio in SN 2007gr has grown substantially to ∼1, while it has remained relatively constant in both SN 2013ge and SN 2009jf. *Center:* Nebular line profiles of SN 2013ge in comparison to SN 1994I and SN 2004aw at a variety of epochs. By late times the [O I] feature in SN 2013ge more closely resembles the peaked structure observed in SN 2004aw. *Right:* The CO band-head observed in SN 2013ge at three epochs. We observe evolution of the profile between +48 and +97 days. *References:* SN 2009jf (Valenti et al. 2011), SN 2007gr (Chen et al. 2014), SN 2004aw (Taubenberger et al. 2006), SN 1994I (Filippenko et al. 1995).

emission. In this context, the small Mg I]/[O I] ratio observed in SN 2013ge at late times could indicate a relative lack of high density enhancements due to clumping.

In Figure 4.15 we plot the [O I] λλ6300, 6364 and [Ca II] λλ7291, 7324 profiles of SN 2013ge in comparison to those of SN 2004aw and SN 1994I. The shape of the profiles in the +139d spectrum of SN 2013ge appears intermediate between the rounded profiles of SN 1994I and the highly peaked profiles of SN 2004aw, while at +447 days the spectrum of SN 2013ge appears more heavily peaked, with slightly blue-shifted velocity. Mazzali et al. (2005b) found that a sharp peak in the [O I] feature is consistent with viewing a jet on axis, although we emphasize that a sharp ejecta density profile can also produce a peaked nebular profile in the absence of a large asymmetry.

4.4.6 The Detection of CO Emission

We identify CO-band emission from the first overtone ($\Delta v = 2$) at $\sim$2.3μm in the NIR spectra of SN 2013ge. Although CO has been detected in the spectra of a number of Type II SN, SN 2013ge is only the third Type Ib/c SN in the literature, to date, with reported molecular CO emission. Previous identifications were reported in SN 2007gr (Hunter et al. 2009) and SN 2000ew (Gerardy et al. 2002). In the right panel of Figure 4.15 we plot the spectral region between 2.1 μm and 2.5 μm for three epochs of SN 2013ge NIR spectra (+48, +97, and +123 days). The CO band-head and Na I are labeled. Only marginal emission above the continuum was present in our previous NIR spectrum, indicating significant growth of the CO emission between +40 and +48 days.

It is also evident that there is evolution of the emission profile between +48 days and +97 days. The feature dramatically narrows, an effect that—to our knowledge—has not previously been observed. The width of the emission feature observed in SN 2007gr did not evolve over a similar range of epochs. This behavior may be linked to different clumping/mixing properties in the ejecta of SN 2013ge and SN 2007gr, as evidenced by their nebular line ratios, above. Detailed modeling of the CO-band will be presented in Milisavljevic et al. (*in prep*).

4.5 Local Environment Properties

4.5.1 Host Galaxy Environment

SN 2013ge exploded on the outskirts of NGC 3287, an SB(s)d galaxy, approximately 51 arcseconds north-east of the galaxy core. This corresponds to an offset—normalized by the g−band half-light radius—of 2.33. The north-east portion of NGC 3287 is characterized by a large number of blue stellar knots (see Figure 4.1). In our 2015 Jan. 15 IMACS spectrum the SN flux had fallen enough to reveal an unresolved knot of star formation (in the form of narrow emission lines) at the SN position.

We measured the fluxes of these emission lines at the SN explosion site using the MCMC method of Sanders et al. (2012). The measured Hα luminosity of $\sim$1.0 $\times$ 10^{38} erg s^{-1} leads to an explosion site star formation rate of $\sim 8.0 \times 10^{-4}$ $M_{\odot}$ yr^{-1} (Kennicutt 1998). This value is on the low end of the HII regions associated with core-collapse SN studied by Crowther (2012).

Using the PP04N2 diagnostic (Pettini & Pagel 2004), we find an explosion site metallicity for SN 2013ge of $\log(O/H) + 12 = 8.40 \pm 0.05$. This value is approximately half-solar (assuming $\log(O/H)_{\rm solar} + 12 = 8.69$; Asplund et al. 2005) and does not deviate strongly from a metallicity measured with an SDSS spectrum taken near the galaxy core. This places the host environment metallicity of SN 2013ge in roughly the bottom 25% of the distribution measured for Type Ib and Type Ic SN and the top 25% measured for Type Ic-BL in Sanders et al. (2012).

4.5.2 Non-Thermal Limits on Progenitor Mass-Loss Rate

We observed SN 2013ge in both the radio and X-ray bands during the main part of the optical outburst. Although we obtained only non-detections, these limits are among the deepest ever obtained for a Type Ib/c SN (Figure 4.16). Only the nearby (d $\sim$ 10 Mpc) Type Ic-BL SN 2002ap has intrinsically fainter emission which was detected in both regimes. Particularly notable, our radio observations constrain SN 2013ge to be fainter than SN 2007gr at similar epochs.

For SN that explode into a relatively low-density CSM (as is the case for Type Ib/c SN) X-ray emission near maximum light is due to Inverse Compton (IC) up-scattering of optical photospheric emission by electrons accelerated at the SN shock. In contrast, radio emission is characterized by a synchrotron self-absorbed spectrum, created when the electrons accelerated by the SN shock interact with shock-amplified magnetic fields (Chevalier & Fransson 2006). As such, radio and X-ray emission (or lack thereof) provide *independent* constraints on the density of the CSM surrounding the progenitor star.

X-ray IC Limits

To model the X-ray upper limit in the context of IC up-scattering, we utilize the models of Margutti et al. (2012, 2014a) which are based on the formalism of Chevalier & Fransson (2006). The luminosity of the IC signal is proportional to the bolometric luminosity ($L_{\rm bol}$) and additionally depends on the outer density structure of the SN ejecta, the density structure of the CSM, the energy spectrum of electrons which up-scatter the optical photons, the fraction of post-shock energy in relativistic electrons ($\epsilon_{\rm e}$), and the explosion properties of the SN (ejecta mass, kinetic energy). The IC signal

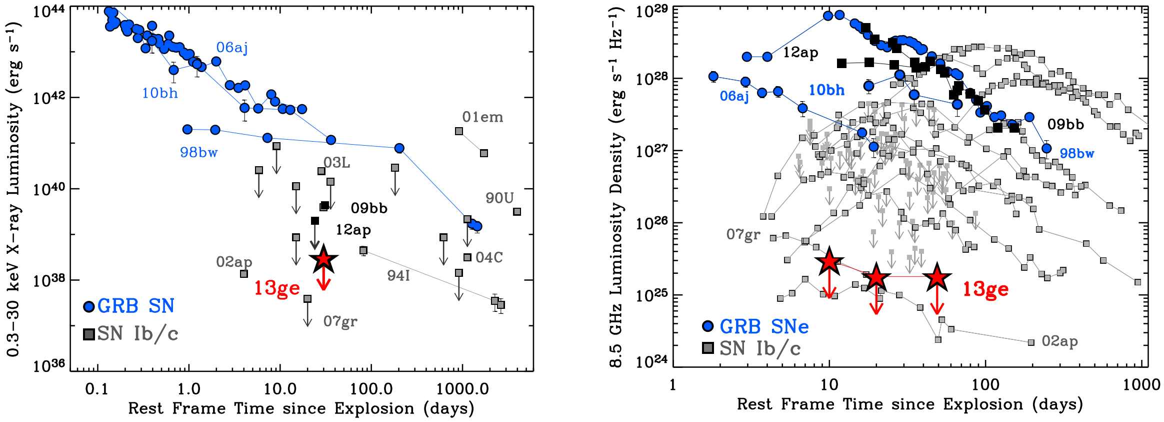

Figure 4.16.—: X-ray (left) and Radio (right) upper limits obtained for SN 2013ge (red stars) in comparison to other Type Ib/c SN. GRB-SN are shown in blue, relativistic SN in black and other Type Ib/c SN in grey (labels for notable objects are shown in the same color as the data points). The limits obtained for SN 2013ge are among the deepest to date for a Type Ib/c SN.

does *not* depend on the fraction of energy in magnetic fields (ϵ_B) and because $L_{IC} \propto L_{bol}$ the mass-loss rate we derive is independent of any uncertainty in the distance to the SN.

Throughout our analysis we use the bolometric light curve derived in Section 4.3 and assume $M_{ej} = 2.5\ M_\odot$ and $E_K = 1.5 \times 10^{51}$ erg. We additionally assume that the accelerated elections possess a power law structure of the form $n(\gamma) \propto \gamma^{-p}$ with p=3 (γ is the Lorentz factor of the electrons) and that ϵ_e=0.1. These values are motivated by the study of Type Ib/c SN in the radio (e.g. Chevalier & Fransson 2006; Soderberg et al. 2006b). The outer portion of the SN ejecta is assumed to follow a steep power law of the form $\rho_{SN} \propto R^{-n}$ with n=10 (e.g. Matzner & McKee 1999). Finally, we consider the case where the density of the CSM can be described as a wind environment with a steady mass-loss rate $\dot{M}$ ($\rho = \dot{M}/4\pi r^2 v_w$ where v_w is the wind velocity). Using these input parameters our X-ray limit leads to an upper limit on the progenitor mass-loss rate of $\dot{M} < 2.3 \times 10^{-5}\ (\frac{v_w}{1000\,\mathrm{km\,s^{-1}}})\ M_\odot\ \mathrm{yr}^{-1}$.

Radio Synchrotron Limits

To model the radio upper limits in the context of self-absorbed synchrotron emission, we use the models outlined in Kamble et al. (2014), which are based on those of Chevalier (1998). For the radio spectrum characterized by synchrotron self-absorption (SSA), the peak spectral flux ($F_{\nu_{\rm a}}$) and SSA frequency ($\nu_{\rm a}$) are given by:

$$\begin{aligned} F_{\nu_a}(\mathrm{mJy}) &= 0.16\, A_*^{1.36} \left(\frac{\epsilon_B}{0.1}\right)^{0.64} \left(\frac{\beta}{0.15}\right)^{4.14} \\ \nu_a(\mathrm{GHz}) &= 6.0\, A_*^{0.64} \left(\frac{t}{10\,\mathrm{day}}\right)^{-1.0} \left(\frac{\epsilon_B}{0.1}\right)^{0.36} \left(\frac{\beta}{0.15}\right)^{1.86} \end{aligned}$$

where β is the shock velocity in the units of speed of light and A_* is a dimensionless constant used to parameterize the density of the CSM. As described above, for a stellar wind environment, the density surrounding the progenitor star can be parameterized as $\rho = \dot{\mathrm{M}}/4\pi \mathrm{r}^2 \mathrm{v_w}$. Normalizing to a constant mass loss rate and wind velocity of $\dot{M} = 10^{-5}\,\mathrm{M_\odot\,yr^{-1}}$ and $\mathrm{v_w} = 1000\,\mathrm{km\,s^{-1}}$, this can further be expressed as $\rho = 5 \times 10^{11}$ $\mathrm{A}_*\ \mathrm{r}^{-2}$ g cm^{-3} (e.g. $\mathrm{A}_* = (\frac{\dot{\mathrm{M}}}{10^{-5} M_\odot\,\mathrm{yr}^{-1}})\ (\frac{\mathrm{v_w}}{1000\,\mathrm{km\,s^{-1}}})^{-1}$). As above, we have also assumed, $n(\gamma) \propto \gamma^{-p}$ and $p = 3.0$ for the distribution of relativistic electrons.

Assuming that the shocked material is in equipartition ($\epsilon_e = \epsilon_B$) we can calculate the predicted radio flux for various values of $\dot{\mathrm{M}}$. Each of our radio upper limits place a constraint on the mass-loss rate of the progenitor system. We find that our 3σ upper limit from 9 days post-explosion at 4.8 GHz is the most constraining, leading to an upper limit on the progenitor mass-loss rate of $\dot{\mathrm{M}} < 4.0 \times 10^{-6}\ (\frac{\mathrm{v_w}}{1000\mathrm{kms^{-1}}})\ (\frac{\epsilon_B}{0.1})^{-0.39}\ \mathrm{M_\odot\ yr^{-1}}$. We have scaled to a fiducial value of $\epsilon_B = 0.1$. Combining this with our X-ray limit (which does not depend on ϵ_B) we place the following constraints on the mass-loss from the progenitor of SN 2013ge:

$\dot{\mathrm{M}} < 4.0 \times 10^{-6}\ \mathrm{v}_{w,1}\ (\frac{\epsilon_B}{0.1})^{-0.39}\ \mathrm{M}_\odot\ \mathrm{yr}^{-1}$ for $\epsilon_B > 0.001$

$\dot{\mathrm{M}} < 2.3 \times 10^{-5}\ \mathrm{v}_{w,1}\ \mathrm{M}_\odot\ \mathrm{yr}^{-1}$ for $\epsilon_B < 0.001$

where $\mathrm{v}_{w,1}$ is v_w normalized by 1000 km s^{-1}.

Comparison to Other Core-Collapse SN

In Figure 4.17 we plot progenitor mass-loss rate versus wind speed to show how the mass-loss constraints obtained for SN 2013ge compare to those based on radio observations of 15 other stripped-envelope core-collapse SN (Type IIb, Ib, Ic, and Ic-BL; see caption for references). Radio observations only constrain $\dot{M}/\mathrm{v_w}$ so each SN appears as a diagonal line in this representation. The SN presented span over four orders of magnitude in $\dot{M}/\mathrm{v_w}$. A horizontal line designates a wind speed of 1000 km s^{-1}, which is often taken as a fiducial value for progenitors of Type Ib/c SN. Also shown (colored squares) are regions of this phase space occupied for various classes of (apparently single) evolved massive stars.

In interpreting the data presented in Figure 4.17 several caveats must be mentioned. First, we plot a single value of $\dot{M}/\mathrm{v_w}$ for each SN, representing the CSM at a physical scales of a few × 10^{15} cm. Detailed modeling of many Type Ib/c radio light curves reveals a more complex morphology, with some events showing signs of density modulations at larger physical scales or density profiles which vary from the $\rho \propto \mathrm{r}^{-2}$ characteristic of a steady wind (Wellons et al. 2012). Similarly, the colored squares represent the locations of known, apparently single, massive stars. How the values of $\dot{M}$ and $\mathrm{v_w}$ may change in the final years of a star's life is an open area of study (e.g. Smith 2014), with mass-loss due to binary interaction and eruptive mass-loss events potentially creating complex

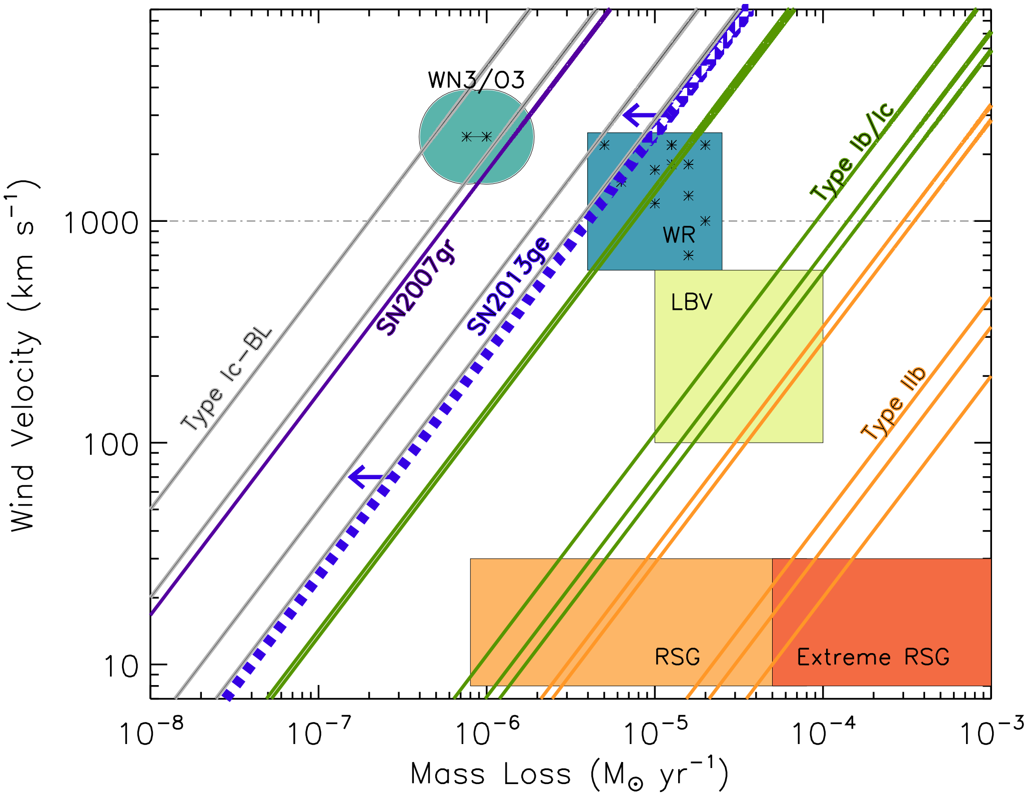

Figure 4.17.—: Wind Speed versus Mass-loss rate. Locations of galactic WR stars come from Crowther (2007), WN3/O3 stars from Massey et al. (2015), normal and extreme RSGs from Marshall et al. (2004), van Loon et al. (2005) and de Jager et al. (1988), and LBV wind (not outburst) properties from Smith (2014). Overplotted are measurements of progenitor mass-loss rate as a function of wind speed for SN 2013ge (this work), SN 2007gr Soderberg et al. (2010), SN 2002ap (Berger et al. 2002), SN 2006aj (Soderberg et al. 2006c), SN 2009bb (Soderberg et al. 2010), SN 2012ap (Chakraborti et al. 2015), SN 1994I (Weiler et al. 2011), SN 1990B (van Dyk et al. 1993), SN 1983N (Sramek et al. 1984), SN 2003L (Soderberg et al. 2005), SN 2008D (Soderberg et al. 2008), SN 2001ig (Ryder et al. 2004), SN 2003bg (Soderberg et al. 2006a), SN 2008ax (Roming et al. 2009), SN 2011dh (Krauss et al. 2012), and SN 2013df (Kamble et al. 2016). We emphasize that the colored boxes represent the wind parameters measured for known, apparently single, evolved massive stars. Binary interaction may play a role in producing the progenitor systems of a significant fraction of stripped SN.

CSM environments. This is particularly relevant here, as a significant fraction of the observed population of stripped SN may have progenitors formed via binary interaction (see, e.g. Smartt 2015, and references therein), although only a small fraction ($\sim 6.5\%$; Margutti et al. 2016) of Type Ib/c progenitors are expected to undergo mass transfer during the final stages of their evolution ("Case-C" mass transfer). Finally, the SN shown in Figure 4.17 are events which have been *detected* at radio wavelengths and published in the literature, and therefore may be biased towards brighter events.

Nevertheless, despite these caveats, several trends emerge. The Type IIb SN all appear at the high end of the CSM density range. They have values of $\dot{M}/\mathrm{v_w}$ that intersect with the red/yellow supergiants, as might be expected if their progenitors have not fully lost their hydrogen envelopes[7]. Five of the Type Ib/c SN fall at intermediate densities, while the Type Ic-BL SN appear to preferentially explode in regions of low CSM density. However, it appears that SN 2007gr and SN 2013ge, represent examples of *normal* Type Ib/c SN that exploded into particularly low density environments, similar to those observed for the broad-lined (including engine-driven) SN.

It is possible that this trend is partially due to metallicity. Type Ic-BL events preferentially occur in low metallicity environments (Sanders et al. 2012) and SN 2013ge and SN 2007gr also occurred in low metallicity regions of their hosts[8]. In addition, there

---

[7] The progenitors of several Type IIb SN have been identified as Yellow Supergiants (YGSs) in pre-explosion images (Maund et al. 2004; Elias-Rosa et al. 2009, 2010; Fraser et al. 2010; Van Dyk et al. 2014). The mass-loss rates and wind speeds of YSGs are not well characterized in the literature, but likely fall between RSGs and LBVs.

[8] The explosion site metallicity of SN 2007gr was $\log(\mathrm{O/H}) + 12 = 8.5$ (Modjaz et al. 2011), comparable to the LMC.

are both empirical observations and theoretical predictions (for line-driven or partially line-driven winds) that WR mass-loss rates are metallicity dependent (Crowther 2007). However, the relativistic[9] SN 2009bb and SN 2012ap were both Type Ic-BL events with low CSM densities that occurred in solar or super-solar environments (Levesque et al. 2010; Milisavljevic et al. 2015).

Intriguingly, several Type Ic-BL SN and SN 2007gr have measured values of $\dot{M}/\mathrm{v_w}$ which are a factor of 3 to 10 lower than any Galactic or LMC WR star examined in Crowther (2007). They are consistent with the mass-loss properties inferred for a new class of WR stars recently discovered in the LMC (Massey et al. 2015). Dubbed WN3/O3, these stars are both fainter in optical bands than "normal" WN/WC stars, and have inferred mass-loss rates an order of magnitude lower. The formation mechanism of these new WR stars is not fully understood, but they demonstrate that some evolved massive stars in the Local Group have mass-loss properties consistent with the very low densities inferred from radio observations of several Type Ic events.

4.6 Discussion

In this Section we discuss the observations outlined above in the context of their implications for the physical configuration of the progenitor system and explosion mechanism of SN 2013ge. From maximum light onward, the optical emission from SN 2013ge is fairly standard for a Type Ib/c SN. Its explosion parameters ($\mathrm{M_{ej}}$ = 2−3

---

[9] The term "relativistic" SN refers to events whose radio emission reveals a substantial relativistic outflow—likely powered by a central engine—but for which no associated GRB was observed (see Soderberg et al. 2010).

$M_\odot$, $E_K = 1 - 2 \times 10^{51}$ erg) are well within the range observed for other SN and its maximum light spectra are characterized by ions of various intermediate mass and iron peak elements at velocities of ∼10,000 km s^{-1}.

However, the early UV and spectroscopic observations of SN 2013ge are unusual. The u−band light curve shows an extra component of emission, which rises on a timescale of ∼4−5 days. During the rising phase of this initial peak the optical spectra are characterized by a blue continuum superimposed with a plethora of P Cygni features, which are both rapid (∼15,000 km s^{-1}) and *narrow* (FWHM $\lesssim$ 3500 km s^{-1}). Below, we discuss the physical interpretation of these early spectra, possible origins for the excess UV emission, and progenitor scenarios which can explain both these observations and the other properties of SN 2013ge.

4.6.1 Physical Interpretation of the Early Spectra

When a SN shock reaches the low density outer regions of the progenitor envelope it will accelerate, leading to a high-velocity gradient in the outer regions of the SN ejecta (Matzner & McKee 1999; Piro & Morozova 2014). The high velocities, rapid velocity evolution, and rapid evolution of observed line ratios in the early spectra of SN 2013ge indicate that we are probing these outer regions. However, for a spherically symmetric explosion in which the differential optical depth of the ejecta decreases monotonically outward from the photosphere, a high-velocity absorption minimum should be accompanied by a broad P Cygni feature. A departure from this picture (as we see in the early spectra of SN 2013ge) implies that the line formation is limited in some sense and likely requires either a modification to the geometry of the explosion or to the optical depth profile of the ejecta.

The high-velocity, narrow, absorption features observed in the early spectra of SN 2013ge could be understood in terms of an asymmetric explosion in which a fraction of the ejecta was launched at high velocities along the line of sight to the observer. In this case, the widths of the lines are affected by the opening angle of the ejection. After some time, this material becomes transparent, revealing the underlying photosphere of the bulk explosion. Folatelli et al. (2006) suggest a similar model for the double-peaked SN 2005bf, which displayed both high-velocity Fe II and Ca II lines and broader features (associated with the underlying photosphere) at early times. The presence of both features was understood in terms of the asymmetric explosion being close, but slightly off from the observer angle. In contrast, in SN 2013ge *all* ions observed in the earliest spectra show narrow, high-velocity features; no underlying photosphere with broader components is visible. This has implications for both the ions present in such an asymmetric ejection, as well as the angle at which we observe the outflow.

Alternatively, it may be possible to recreate the spectral features in SN 2013ge if the line absorption coefficient does not decrease monotonically with radius. In this case, the main line-forming region at early epochs could be "detached" above the photosphere. Physically, this could be due to an actual increase in density or to a change in the ionization state of ejecta at a certain distance above the photosphere, resulting in an increased line opacity. The latter argument was used by Tanaka et al. (2009) to explain the high-velocity Ca II and Fe II lines in SN 2005bf. They note that these lines coincide with high-velocity Hα, indicating that they were formed in a thin hydrogen shell that remained on the progenitor star at the time of explosion. They argue that the high electron density in this (solar abundance) hydrogen shell enhances the recombination of

Ca III and Fe III (Mazzali et al. 2005b; Tanaka et al. 2009), allowing narrow, high-velocity Ca II and Fe II lines to be formed in the outer portions of the ejecta. In the case of SN 2013ge, a plethora of high-velocity ions are observed at these early epochs which would have implications for the composition of the outer layers of the progenitor star.

4.6.2 The Nature of the early UV emission

The early rising light curves of Type I SN are powered by a combination of two primary sources: energy deposited by the SN shock and the radioactive decay of ^{56}Ni. Excess emission can also be produced by external sources, such as the collision of the SN shock with a binary companion. We now examine the likelihood that the excess UV emission observed in the early light curve of SN 2013ge is powered by each of these sources, and the implications for the explosion in each case.

Cooling Envelope Emission

After shock breakout, the shock heated ejecta cool, giving rise to a light curve component independent from that powered by ^{56}Ni. During this phase, both the bolometric luminosity of the transient and the color temperature should decline with time (Nakar & Sari 2010), with the exact values depending on the radius of the progenitor star, the explosion energy, the ejecta mass, and the ejecta opacity. The luminosity observed in any given optical/UV band will rise as long it is located on the Rayleigh-Jeans tail of the temperature spectrum. As a result, one expects a rise in the UV/optical bands proportional to $t^{1.5}$ if the emission is powered by shock heated cooling (Piro & Nakar 2013; Nakar & Sari 2010).

In the case of SN 2013ge, *the observed rise time for the first u−band component is abnormally large for cooling envelope emission from a stripped progenitor star.* A power-law of the form $t^{1.5}$ can be fit to the initial rise observed in the u− and w1−bands (see Figure 4.5; although this solution is not unique), yielding a rise time of 4−6 days from the epoch of explosion. In contrast, the first light curve components of both SN 2008D and SN 2006aj (which some authors associate with cooling envelope emission; Soderberg et al. 2008; Campana et al. 2006) rise in the UV/optical on timescales $\lesssim$1 day. By $\sim$5 days post explosion, emission from the radioactive decay of ^{56}Ni likely comprises a non-negligible fraction of the total light, making it difficult to assess whether the temperature and luminosity evolution of the first component is consistent with cooling envelope emission. The u−b color remains roughly constant during the rising portion of the first u−band component (before rapidly reddening during the decline phase), which is consistent with the peak of the blackbody passing through the observed band. However, we caution that the UV flux was also depressed compared to a single blackbody during this time period, and the rapid reddening could therefore be due to increased UV line blanketing.

Under the assumption that this emission is caused by shock-heated cooling then, when compared with theoretical models, the long rise time implies that SN 2013ge *cannot have a standard WR progenitor*. In order to account for the 4−6 day rise in the u−band, we require that the temperature remain above 10^4 K ($\sim$ 0.9 eV) *at a minimum* for this time period. In contrast, in the WR model of Nakar & Sari (2010) the temperature has already fallen below this level by $\lesssim$1 day post-explosion. Using the parameterization from Piro & Nakar (2013) for a progenitor with a hydrogen-free radiative envelope, in Figure 4.18 we plot the color temperature versus time for a range of progenitor radii, assuming $M_{ej} = 2-3\ M_\odot$ and $E_K = 1-2 \times 10^{51}$ erg (as derived from the bulk explosion). We see that for this envelope structure, we require a progenitor radius of *at least* 50 $R_\odot$ to account for the observed u−band rise. The cooling envelope luminosity at 4 days post-explosion for this model is $4 - 5 \times 10^{41}$ erg s^{-1}, compatible to the shoulder of excess emission observed at early times.

The modest ejecta mass and extended progenitor radius derived above lead us to also consider the models of Nakar & Piro (2014) for double-peaked SN. These models employ a non-standard progenitor envelope structure, in which a massive compact core is surrounded by extended low-mass material. In this picture, the luminosity of the emission is mainly a function of the radius of the extended material while the time to maximum is related to the total mass in the extended envelope. Both also depend on the velocity and opacity. For a peak time of 4 days, peak luminosity of $0.6 - 1.2 \times 10^{42}$ erg s^{-1}, a characteristic velocity of ∼12,000 km s^{-1}, and Eqns. 10 and 12 of Nakar & Piro (2014) we find an extended envelope mass of ∼0.1 $M_\odot$ at a radius of $15 - 25$ $R_\odot$. Although less extreme than the value derived for a standard progenitor envelope structure, this is still more extended than a typical WR progenitor star.

Outwardly Mixed ^{56}Ni

Alternatively, the early emission from SN 2013ge could be due to ^{56}Ni mixed outward in the explosion. In this case, our rising light curve can give constraints on the radial distribution of the outwardly mixed material.

For any given light curve point, there is a degeneracy between the depth of the contributing ^{56}Ni and the explosion epoch. For deep deposits, there will be a "dark

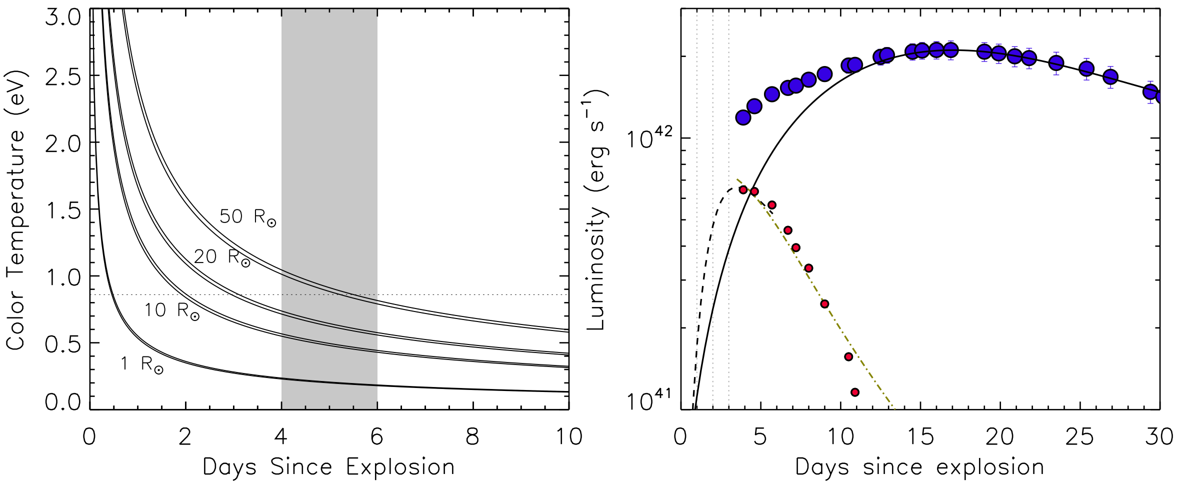

Figure 4.18.—: *Left:* Color temperature versus time since explosion for cooling envelope emission from hydrogen-poor progenitors with radii between 1 $R_\odot$ and 50 $R_\odot$. Bands for each radius assume explosion parameters of $M_{ej} = 2 - 3\ M_\odot$ and $E_K = 1 - 2 \times 10^{51}$ erg. If the early emission from SN 2013ge is due to cooling envelope emission, then the temperature remain must above 10,000 K (0.9 eV) *at a minimum* for 4−6 days post-explosion, implying an extended progenitor. *Right:* Decomposition of the bolometric luminosity of SN 2013ge (blue) into two components. The solid black line represents our best fit ^{56}Ni decay model to the bulk explosion. Red points show the excess emission above this model at early times. The black dashed line is an Arnett model fit to the rise time and luminosity of this early component and the gold line is a model for the decline phase based on the instantaneous energy deposition from the $^{56}\text{Ni} \rightarrow {}^{56}\text{Co} \rightarrow {}^{56}\text{Fe}$ decay chain, allowing for incomplete gamma-ray trapping. Dotted lines indicate the epochs of our early spectra.

period" between the explosion and the epoch of first light (Piro & Nakar 2013). Our spectroscopic observations from ∼3 days after the epoch of first light displayed high velocities and rapid velocity evolution which argue against any significant dark period for SN 2013ge. This is compatible with our first measurement of the luminosity, temperature and photospheric velocity which, using Eqn. 17 of Piro & Nakar (2013) only require that the explosion was ∼2 days prior to our first bolometric light curve point. In this model, the lack of a significant dark period in SN 2013ge requires that some amount of ^{56}Ni was mixed into the outer portions of the ejecta.

The morphology of the early bolometric light curve also has implications for the distribution of this outwardly mixed ^{56}Ni. A radial distribution of ^{56}Ni which is monotonically decreasing should yield a smoothly rising light curve (e.g. Dessart et al. 2012). In contrast, the "shoulder" of emission as seen in SN 2013ge may require a distinct deposit of ^{56}Ni at shallower depths, qualitatively similar to the model used by Bersten et al. (2013) to explain the first light curve component of SN 2008D. If a small clump of ^{56}Ni-rich material was ejected at high velocities, we can obtain a rough order of magnitude estimate for the ejecta mass, nickel mass, and kinetic energy of this material by decomposing the bolometric light curve into two components. This is done in the right panel of Figure 4.18, where the solid line is our model for the bulk explosion (Section 4.3) and the red points are the excess above this model at early times.

Using the models of Arnett (1982) to fit the rise time and luminosity of this excess—and assuming a velocity of $\sim$12,000 km s^{-1}—yields an ejected mass of $\sim$0.06 M$_{\odot}$, a ^{56}Ni mass of $\sim$0.012 M$_{\odot}$, and a kinetic energy of $\sim 6 \times 10^{49}$ erg. To investigate if a ^{56}Ni-powered explosion with these parameters is consistent with the rapid post-maximum decline inferred for the early light curve component we use the model of Drout et al. (2013), which was developed for the rapidly-declining SN 2005ek. It fits the entire post-maximum evolution of an explosion based on the instantaneous rate of energy deposition from the $^{56}\mathrm{Ni} \rightarrow {}^{56}\mathrm{Co} \rightarrow {}^{56}\mathrm{Fe}$ decay chain, including incomplete trapping of gamma-rays produced during $^{56}\mathrm{Ni} \rightarrow {}^{56}\mathrm{Co}$ decay. This is appropriate for the declining phase of SN with very low ejecta masses, which become optically thin quickly, making the models of Arnett (1982) inapplicable.

Using this model with the explosion parameters found above yields the gold curve shown in the right panel of Figure 4.18, which is well matched to the decline timescale inferred for the early light curve component in SN 2013ge. However, we emphasize that these explosion parameters should be taken as order of magnitude estimates only. We do not uniquely decompose the bolometric light curve into multiple components and the analytical models used here do not account for variations in geometry, opacity, or contributing radioactive species.

Shock Collision with a Binary Companion

Finally, we consider an external source for the early UV emission: a collision between the SN ejecta and a binary companion. During such a collision a bow shock will form, compressing and shock-heating the SN ejecta in the direction of the interaction. This heating can lead to an extra source of UV/optical emission for several days post explosion (Kasen 2010). The observed properties of this emission depend on several parameters (e.g. binary separation, ejected mass) and are highly viewing angle dependent. Using a binary population synthesis model for core-collapse SN, Moriya et al. (2015) find that only $\sim$0.53 % of Type Ib/c SN light curves should have a detectable visible brightening due to this mechanism. As such, any detection of this collision would be rare.

Using the models of Kasen (2010), we assess whether both the luminosity and timescale of the early emission observed in SN 2013ge can be reproduced by this mechanism. Using their Eqn. 22 and the explosion parameters derived in Section 4.3 we find that the luminosity of the excess emission in SN 2013ge would require a binary separation of $\lesssim 10^{12}$ cm ($\sim 15\ R_\odot$). However, reproducing the timescale of the early emission is challenging. The source of the UV/optical emission in this model is shock-heated cooling, analogous to the cooling envelope emission described above. Thus, in this model, the u-band rise time of 4−6 days similarly requires that the u−band remain on the Rayleigh-Jeans tail of the temperature spectrum for this time period. In contrast, none of the models presented in Kasen (2010) have rise times longer than ∼2 days. Using Eqn. 15 in Kasen (2010) for the effective temperature of the emission, we find that a separation of *at least* 10^{13} cm is required to have $T_{\rm eff} > 10^4$ K at 5 days post-explosion. This is inconsistent with the required separation found above. Thus, we find that (for the current set of theoretical models) the early observations of SN 2013ge are inconsistent with the collision of SN ejecta with a companion star.

4.6.3 The Progenitor of SN 2013ge

SN 2013ge was the explosion of a stripped massive star with a moderate ejecta mass, *weak* He features in its optical/IR spectra, a low pre-SN mass-loss rate, and a local environment metallicity of ∼0.5 solar. However, we are left with two distinct scenarios depending on our interpretation of the early emission. Either SN 2013ge was the explosion of a star with an extended envelope or it was the result of an explosion in which a clump of ^{56}Ni was mixed outward in the ejecta, possibly coupled to the ejection of a small amount of mass along the line of sight to the observer. We now examine the consistency and consequences of each of these progenitor models. We emphasize that although SN 2013ge is a relatively unique object, the results presented here potentially have general implications for the progenitors of Type Ib/c SN. Without either our early spectroscopic or UV observations *SN 2013ge may not have been flagged as unusual.*

Extended Progenitor Surface

If we interpret the early emission from SN 2013ge as cooling envelope emission, it implies that shock breakout occurred from an extended surface. Our estimates for the extent of this surface range from $15 - 25$ $R_\odot$, for a low-mass envelope on a compact core, to > 50 $R_\odot$ for a standard envelope structure. In principle, this surface could either be a genuinely extended progenitor envelope, or it could be located within a dense optically thick wind region surrounding the progenitor star.

While some WR stars have particularly dense wind regions, which extend their photospheric radii by up to a factor of 10 (Li 2007), the interpretation of SN 2013ge as the explosion of such a star is complicated by the need to reconcile it with the radio observations obtained $\sim$9 days post-explosion. These observations indicate that by $\sim 10^{15}$ cm (for a standard SN shock velocity of $v_{\rm sh} = 0.15c$) the progenitor of SN 2013ge is characterized by a *low* density wind region. Thus, if the shock breakout occurred within a dense CSM, *the progenitor star must have either experienced a significant change in its mass-loss properties or ejected a portion of its envelope during the final stages of its evolution.* This process must have occurred within the final $\lesssim$100 days before core-collapse in order to be contained within the region probed by our radio observations or the final $\lesssim$0.5 days if the breakout radius we derive is the outer extent of this mass. These timescales are normalized to an ejection velocity of 1000 km s^{-1}, and are consistent with models that predict that instabilities and internal gravity waves can be induced during the final advanced nuclear burning stages, possibly leading to enhanced mass-loss/eruptions during the final year(s) before core-collapse (e.g. Shiode & Quataert 2014; Smith & Arnett 2014).

Alternatively, SN 2013ge could be explained by the explosion of a stripped star with a low final mass-loss rate and an inflated stellar envelope. Several of the Type Ib/c binary progenitor models from Yoon et al. (2010) have radii inflated to ∼30 $R_{\odot}$, low pre-SN mass-loss rates ($\dot{M} \lesssim 10^{-6}$ $M_{\odot}$ yr^{-1}), final masses between 3−4 $M_{\odot}$ (consistent with our derived ejecta masses), and sub-solar metallicity. However, the helium envelopes for these progenitors are relatively large (∼1.5 $M_{\odot}$; significantly higher than the mass Hachinger et al. 2012 find is necessary to produce observable features) and are therefore likely inconsistent with the *weak* He I features observed in SN 2013ge. In particular, these low-mass, extended, progenitors are predicted to be more efficient at mixing ^{56}Ni into the He-rich layers via RT-instabilities (Yoon et al. 2010; Hammer et al. 2010; Joggerst et al. 2009), which should lead to *stronger* observed He lines. Thus, the observations of SN 2013ge likely require a progenitor which differs from any presented in Yoon et al. (2010) in having an extended envelope but *low* final He mass.

Finally, we consider if this progenitor scenario can account for the unusual spectra observed during the rise of the first light curve component. In particular, while this scenario requires a high effective temperature, the ions present in these spectra are standard singly ionized species. It is possible that this, as well as the unusual velocity profile of the lines, could be understood if there was a change in ionization state in the outer portion of the ejecta, associated with either the low-mass extended envelope or a density enhancement due to a pre-explosion mass ejection. In the former case, the presence of even a very small amount of hydrogen could increase the electron density enough to lead to enhanced recombination (Mazzali et al. 2005a; Tanaka et al. 2008).

Asymmetric Ejection

Alternatively, if we interpret the early emission as heating due to ^{56}Ni, then an asymmetric ejection of a small amount of ^{56}Ni-rich material at high velocities could explain both the early light curve peak and the unusual velocity profile in the early spectra. Intriguingly, our observed velocity ($\sim$15,000 km s^{-1}) and estimated mass ($\sim$0.06 M$_{\odot}$) for this material are comparable to those observed in the high-velocity clumps in the northwest portion of the Cassiopeia A (Cas A) SN remnant (Fesen 2001; Laming et al. 2006). This material in Cas A has an opening angle of $\sim$45 degrees and has been argued by some to originate in the stellar core (Hwang et al. 2004; Laming et al. 2006; Milisavljevic & Fesen 2013).

While the moderately peaked nebular emission line profiles and low-CSM density observed for SN 2013ge also show similarities to jet-driven explosions in the literature, the observations obtained do not necessarily *require* a highly asymmetric explosion mechanism. They could also potentially be understood if viewing one of the nickel and silicon-rich plumes of material observed in 3D simulations of mixing instabilities in neutrino driven explosions (e.g. Hammer et al. 2010). In these models, fast clumps of metal-containing material are able to penetrate through the outer layers of the ejecta, possibly leading to asymmetric variations in the ejecta velocity. Indeed, velocity variations of $\sim$4000 km s^{-1} were detected in light echoes from the explosion of Cas A, depending on viewing angle (Rest et al. 2011). However, resolved imaging of titanium in Cas A indicates that the explosion mechanism was dominated by slightly asymmetric, low-mode, convection, as opposed to a highly asymmetric/bipolar explosion mechanism (Grefenstette et al. 2014).

In this scenario, the weak helium features observed in the spectra of SN 2013ge also have implications for the true helium abundance of the progenitor star. In particular, they suggest a different scenario than that observed in SN 2005bf, where Tanaka et al. (2009) proposed that a ^{56}Ni-rich plume penetrated only slightly into a nearly intact helium envelope. In this case, both the strength and velocity of the observed helium features grew with time as more of the helium envelope fell within a γ-ray optical depth of the ^{56}Ni deposit. In the models of (Dessart et al. 2012), the asymmetric ejection of a single blob of ^{56}Ni-rich material to high-velocities is only predicted to produce weak helium features. However, if this blob is part of a larger scale mixing instability, as described above, then it would favor a scenario where the progenitor of SN 2013ge was genuinely He-poor, containing only a thin layer at the time of explosion.

4.6.4 Comparison of the Early Emission to the Rapidly-Declining SN 2002bj

While investigating the early spectra of SN 2013ge, we found that the first spectrum obtained for the rapidly declining SN 2002bj (Poznanski et al. 2010) displayed a similar blue continuum and narrow spectroscopic features. In Figure 4.19 we show this spectrum along with the −11 day spectrum of SN 2013ge. The spectrum of SN 2002bj was obtained at +7 days, when its photospheric velocity was only ∼4000 km s^{-1}, and we have linearly blue-shifted it by 8000 km s^{-1} for comparison with SN 2013ge. We emphasize that, unlike in the early spectra of SN 2013ge, there is no mismatch between the widths the features in this spectrum and the blueshifts of their absorption minima. From modeling its SED as a blackbody, Poznanski et al. (2010) found that the velocity of SN 2002bj was higher at earlier epochs—consistent with a photosphere rapidly receding into a low-mass envelope. Unfortunately, no spectrum of SN 2002bj is available to assess whether its spectroscopic features were similarly narrow at earlier epochs. However, the similarity between the spectrum of SN 2002bj and spectra obtained during the first emission component of SN 2013ge is still striking.

The nature of the explosion which produced SN 2002bj is still a mystery. The rapid light curve and unusual spectrum lead Poznanski et al. (2010) to hypothesize that it was due to the detonation of a He shell on the surface of a WD. Comparing the early emission of SN 2013ge (as shown in Figure 4.18) to the light curve of SN 2002bj (see Figure 4.9) we find that the first emission component in SN 2013ge is nearly an order of magnitude fainter and also declines a factor of ∼1.4 faster than the bolometric light curve of SN 2002bj. Thus, even neglecting the second (main) light curve component of SN 2013ge (which is entirely lacking in SN 2002bj) the energetics of these explosions are very different. However, Figure 4.19 demonstrates that the ions and ionization state present in the ejecta of SN 2002bj can also be produced during the core-collapse of a massive star. It has already been shown that massive stars may be able to produce rapidly-evolving Type I SN, either due to very low ejecta masses (Drout et al. 2013; Tauris et al. 2013) or through the combination of a large progenitor radius and a lack of ejected radioactive elements (Kleiser & Kasen 2014). More detailed modeling attempting to ascertain whether SN 2002bj may be a more extreme example of the first emission component in SN 2013ge in an explosion which lacks the second, main, light curve component powered by ^{56}Ni would be warranted.

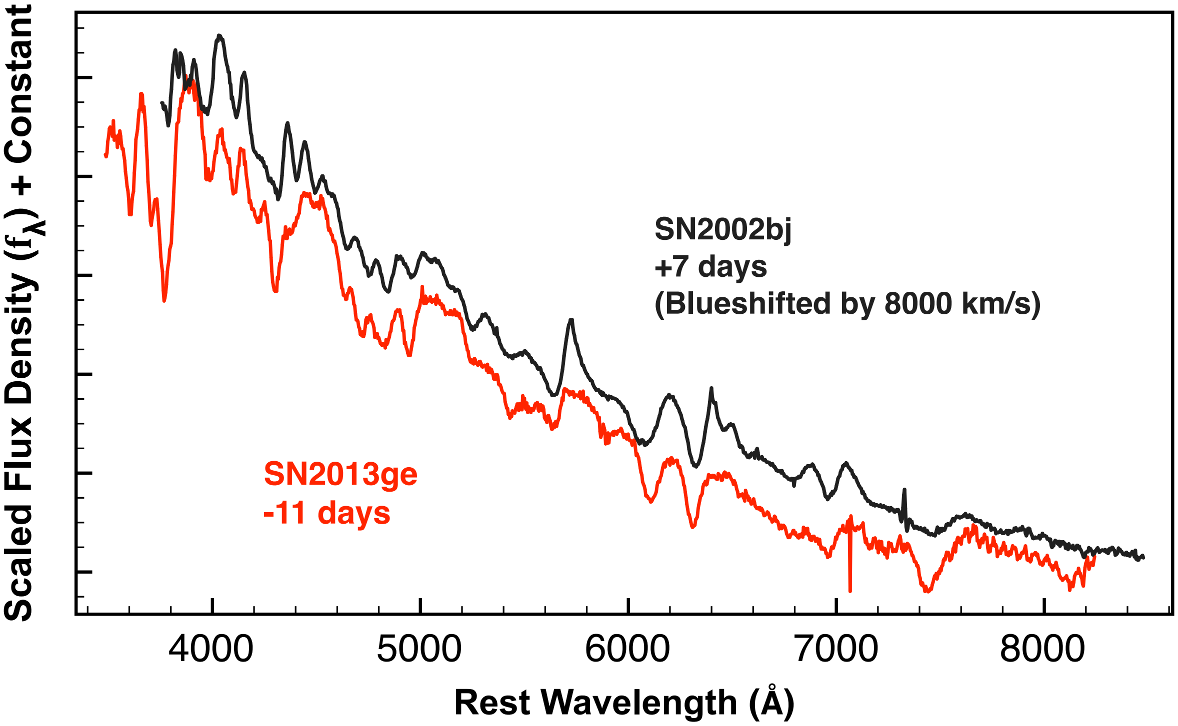

Figure 4.19.—: A comparison of an early spectrum of SN 2013ge to a spectrum of the rapidly evolving SN 2002bj (Poznanski et al. 2010). The spectrum of SN 2002bj has been linearly blueshifted by 8000 km s^{-1}.

4.7 Summary and Conclusions

We have presented extensive observations of the Type Ib/c SN 2013ge beginning ∼2 days post-explosion, when the light curve is particularity sensitive to both the progenitor configuration and mixing within the ejecta. Here we summarize our main conclusions.

Early Emission: The rapid velocity evolution and rapid rise observed in the early spectra and UV light curves, respectively, indicate that our first observations probe the outer regions of the ejecta shortly after explosion. The early u−band and UV light curves show two distinct components. The first component has a rise time of ∼4−5 days and is visible for the first week post-explosion. This manifests itself as a "shoulder" of excess emission in the bolometric light curve with a luminosity of $\sim 6 \times 10^{41}$ erg s^{-1}. Spectra of the first component display a blue continuum and are unusual in possessing features which are both moderately high-velocity ($\sim$15,000 km s^{-1}) and *narrow* ($\sim$3500 km s^{-1}). This indicates that the line formation region is limited in some sense, possibly due to an asymmetric geometry or a change in ionization state in the outer portions of the ejecta.

Bulk Explosion: With $\mathrm{M_{R,peak}} = -17.5$ and $\Delta \mathrm{m_{15,R}} = 0.4$, SN 2013ge is relatively faint and slowly evolving, but the derived ejecta mass ($2 - 3$ $\mathrm{M_\odot}$) and kinetic energy ($1 - 2 \times 10^{51}$ erg) are well within the distribution observed for Type Ib/c SN. *Weak* He I lines, which fade with time, are detected in early optical and NIR spectra. These are distinct from the conspicuous He I lines which are usually used to classify Type Ib SN. Near maximum light the spectra are dominated by a plethora of intermediate mass and iron peak elements. The late-time spectral evolution of SN 2013ge is also distinctive, showing a lack of evolution in the Mg I]/[O I] ratio and a shifting CO-emission profile.

Environment Properties: SN 2013ge exploded on the outskirts of a star forming galaxy. There is an unresolved HII region at the explosion site, which has a metallicity of $\sim$0.5 solar. The radio and X-ray limits for SN 2013ge are among the deepest ever obtained for a stripped-envelope SN and constrain the progenitor mass-loss rate to be $\dot{\mathrm{M}} < 4.0 \times 10^{-6}$ $\mathrm{M_\odot}$ yr^{-1} for $\epsilon_\mathrm{B} = 0.1$.

Power Sources and Progenitors: SN 2013ge was the explosion of a stripped massive star with a moderate ejecta mass. However, we are left with two distinct progenitor scenarios depending on our interpretation of the early emission. In both cases, we find it likely that the progenitor of SN 2013ge had only a thin layer of helium remaining at the time of core-collapse.

1. If the early emission is due to post-shock-breakout cooling envelope emission, then its relatively long rise time ($\sim$4$-$6 days) requires that the progenitor of SN 2013ge either had an extended envelope or that it ejected a small portion of its envelope in the final $\lesssim$1 year before core-collapse.
2. If the early emission is due to outwardly mixed ^{56}Ni then we require that a distinct clump of ^{56}Ni was mixed into the very outer portions of the ejecta. Coupled with the early spectra, this may imply an asymmetric ejection of a small amount of nickel-rich material at high-velocities.

More detailed modeling beyond the scope of this work will be necessary to fully distinguish between or rule out one of these two progenitor scenarios. In particular, it would be useful to ascertain whether either scenario can actually reproduce the plethora of high-velocity and narrow features observed in the early spectra, with the cooling envelope model facing the additional challenge of explaining the depressed UV flux at early epochs. We note that if the epoch of first light is earlier than that derived in Section 4.3 from power law fits to the early UV light curves, then the cooling envelope/extended progenitor scenario would be put under additional tension, or ruled out entirely. In contrast, the model of a high-velocity clump could be naturally extended to explain a rise in the UV light curve after the epoch of first light. Finally, we find that current theoretical models for the collision of a SN shock with a binary companion cannot reproduce both the luminosity and timescale of the early emission observed in SN 2013ge.

Rapidly-Evolving SN 2002bj: The early spectra of SN 2013ge are similar to the spectrum of the rapidly-evolving SN 2002bj, demonstrating that the ions and ionization state present in the ejecta of SN 2002bj can also be produced by the core-collapse of a massive star.

We thank the anonymous referee for numerous comments that improved this manuscript. M. R. D. thanks L. Z. Kelley, D. Kasen, and E. Ramirez-Ruiz for useful discussions. We thank N. Morrell for obtaining some of the observations reported here. M. R. D. is supported in part by the NSF Graduate Research Fellowship. M.L.G.'s position in the supernova research group at U.C. Berkeley is supported by Gary and Cynthia Bengier and NSF grant AST-1211916. E. Y. H. acknowledges the generous support provided by the Danish Agency for Science and Technology and Innovation through a Sapere Aude Level 2 grant.

This paper includes data gathered with the 6.5 m Magellan Telescopes located at Las Campanas Observatory, Chile. Some observations reported here were obtained at the MMT observatory, a joint facility of the Smithsonian Institution and the University of Arizona. This paper uses data taken with the MODS spectrographs built with funding from NSF grant AST-9987045 and the NSF Telescope System Instrumentation Program (TSIP), with additional funds from the Ohio Board of Regents and the Ohio State University Office of Research.

Facilities: Swift-UVOT, Magellan:Baade (IMACS, FIRE), Magellan:Clay (LDSS3), MMT (Blue Channel spectrograph, Hectospec, MMTCam), LBT (MODS), CAO, FLWO (FAST, KeplerCam), Chandra, VLA, Lick:Shane (Kast), MDM (OSMOS)

Chapter 5

Luminous Interacting Transients I: Background and Motivation

5.1 Introduction

Approximately 10% of core-collapse SN exhibit narrow hydrogen emission lines in their spectra (dubbed Type IIn; Schlegel 1990), indicative of the SN blast wave interacting with a *dense* CSM (Smith et al. 2011; Chevalier & Fransson 1994; Chugai & Danziger 1994). The light curves and spectra of Type IIn SN can be used to estimate pre-SN mass-loss rates and, in many cases, the derived values of 10^{-4} to 10^{-2} $M_\odot$ yr^{-1} are orders of magnitude higher than steady winds observed in evolved massive stars (Vink et al. 2001; Crowther 2007). The origin of this dense CSM poses a challenge for models of stellar evolution, as it implies that a subset of massive stars undergo intense (possibly violent/eruptive) mass-loss in the years immediately preceding core-collapse.

These challenges have been accentuated by the recent discovery that some Type IIn SN reach luminosities 10−100 times that of normal core-collapse SN, with total radiated energies $\gtrsim 10^{51}$ erg (e.g. Smith et al. 2007, 2008; Rest et al. 2011). If powered primarily by shock heating due to ejecta-CSM interaction, these super-luminous SN require intense mass-loss episodes of up to a $M_\odot$ yr^{-1} and dense CSM shells of $\gtrsim$10 $M_\odot$ (e.g. Smith & McCray 2008; van Marle et al. 2010; Chatzopoulos et al. 2013). Such mass-loss is not *a priori* predicted, and both the progenitor stars and physical mass-loss mechanism are debated (e.g. Smith et al. 2007; Woosley et al. 2007).

Our current observational capabilities offer two main routes to advance our understanding of the progenitors and physical mass-loss mechanism which operates in luminous Type IIn SN:

1. Modeling observed light curves and spectra in order to constrain the full range CSM parameters (physical scale, density profile) and explosion properties.
2. Studying host galaxies and sub-galactic environments in order to investigate the physical conditions present in their progenitor star populations.

Both of these endeavors require large and unbiased samples of events, and motivate the remainder of this thesis. In this chapter, we provide some brief additional background regarding both Type IIn SN and luminous SN (Sections 5.2 and 5.3) and outline the definition of a “luminous” interacting transient which will be used in the following chapters (Section 5.4).

5.2 Background: Type IIn SN Progenitors

Type IIn SN are an incredibly heterogeneous class of explosions. They show wide variety in both their peak luminosities (-16 to -22 mag) and timescales (few days to multiple years) which, in turn, lead to a wide variety in their inferred pre-SN mass-loss rates and histories. However, as reviewed by Smith (2014), a number of observations have led many to associate Type IIn SN with the explosion of Luminous Blue Variable (LBV) stars. These include the typical masses, energies and velocities inferred for the dense mass-loss regions surrounding Type IIn SN, a growing number of events observed to exhibit pre-explosion outbursts (e.g. Pastorello et al. 2007; Foley et al. 2011; Mauerhan et al. 2013a; Ofek et al. 2014b) and the identification of luminous progenitor systems in pre-explosion images of SN 2005gl and SN 2009ip (Gal-Yam et al. 2007; Gal-Yam & Leonard 2009; Smith et al. 2010; Foley et al. 2011). This hypothesis is in direct conflict with the traditional view of LBVs as a short-lived *transitionary* phase in the evolution of the most massive single stars (Conti 1976; Humphreys & Davidson 1994).

Additional insight into the progenitor stars and physical conditions required to produce Type IIn SN can be gained by studying their sub-galactic environments, and the results of several initial studies are intriguing. For example, Anderson & James (2009) and Kelly & Kirshner (2012b) did not find any statistically significant difference between a sample of $\sim$20 Type IIn SN and the more common Type IIP SN when considering a variety of host environment properties (explosion site offset, metallicity, specific star formation rate). Further, Anderson et al. (2012) and Habergham et al. (2014) found the surprising result that Type IIn SN are *not* strongly correlated with the Hα emission in their host galaxies. These results seem to contradict the idea that Type IIn SN come primarily from massive LBV stars. If Type IIn SN result predominantly from more massive progenitors than the bulk of Type IIP SN (the explosions of red supergiants with initial masses between 8 and 15 $M_\odot$; Smartt 2009) then we would expect this to manifest in their host environments. Specifically, they would be expected to more closely trace the sites of active star formation in their host galaxies. Such a trend *is* observed for Type Ic SN, which are also thought to arise from more massive progenitors (Anderson & James 2009; Anderson et al. 2012; Kelly & Kirshner 2012b; Habergham et al. 2014).

Motivated by these studies, Smith & Tombleson (2015) examined the locations of known LBVs in Milky Way and Magellanic Clouds and found that LBVs were more isolated on average than Wolf-Rayet (WR) stars, a result which is *also* in conflict with the idea that LBVs represent a short transitionary phase between massive O−stars and WRs. They further proposed proposed that some LBVs are actually mass gainers in binary systems that have been kicked from their natal positions, which offers a potential resolution between the interpretation of Type IIn SN as the explosion of LBVs with their apparent isolation. However, the heterogeneity of Type IIn SN must again be emphasized. It is likely that different subclasses of Type IIn SN can be tied to different progenitor systems, with other possibilities including extreme red supergiants (RSGs; Fransson et al. 2002), asymptotic giant branch stars (Mauerhan et al. 2013b), and a wide array of binary channels, such as common-envelope evolution (Chevalier 2012) and photoionizition/confinement of a steady wind (Mackey et al. 2014).

The likelihood of multiple progenitor systems hidden within the broad class of Type IIn emphasizes the need to incorporate information about the explosion and CSM properties into any study of Type IIn sub-galactic environments in order to draw robust conclusions about their progenitor populations. Until recently, such an exercise had been limited by the availability of well-sampled light curves and spectra for a large sample of events. Many of the early studies described above are based on heterogeneous samples which are drawn from the circulars, including objects for which no public information other than a single classifying spectra and discovery magnitude were known. This highlights the need for large and *unbiased* samples of Type IIn SN with well-sampled light curves in order to perform a systematic comparison between the explosion properties and host environment.

5.3 Background: Luminous Supernovae

Luminous supernovae are a rare class of stellar explosions whose discovery was facilitated by the advent of wide-field untargeted transients surveys. They are characterized by peak luminosities $10-100$ times that of typical core-collapse SN, and total radiated energies on the order of $\sim 10^{51}$ erg. These extreme luminosities require either a very energetic explosion, or a particularly efficient means of converting explosion energy into radiation. Proposed mechanisms include the radioactive decay of large amounts of ^{56}Ni following a pair-instability SN (Gal-Yam & Leonard 2009), magnetar spin-down (Kasen & Bildsten 2010), and interaction with a dense CSM (Chatzopoulos & Wheeler 2012).

Luminous SN can be divided into at least two spectroscopic classes (Gal-Yam 2012): hydrogen-poor (SLSN-I) and hydrogen-rich (SLSN-II). A majority of the hydrogen-rich events discovered are of Type IIn, displaying narrow and intermediate width Balmer emission lines in their spectra, indicative of a dense CSM. Thus, while the process(es) which produce the extreme luminosity observed in SLSN-I are still hotly debated, a consensus is emerging that the conversion of kinetic energy to radiation through CSM interaction plays an important role in many SLSN-II. Powering the extreme luminosity of these events predominately via CSM interaction requires a dense CSM ($\sim$10 $M_\odot$) at a physical scale of $\sim10^{15}$ cm (e.g Smith & McCray 2008). Accordingly, several theoretical mass-loss mechanisms have been proposed specifically for luminous Type IIn SN. These include LBV-like eruptions (Smith et al. 2007), instabilities or wave-driven mass-loss during late nuclear burning stages (Smith & Arnett 2014; Shiode & Quataert 2014), common-envelope evolution (Chevalier 2012), pulsational-pair instability (Woosley et al. 2007), or the presence of a relic proto-stellar disk (Metzger 2010).

However, even asserting that a dense CSM produces the extreme luminosity of luminous Type IIn SN, questions still remain about the nature of the underlying explosions, as well as how the progenitor stars and physical conditions required to produce these luminous interacting transients relate to those of "standard luminosity" Type IIn SN, and to other classes of energetic explosions. These questions motivate the studies and preliminary results presented remaining chapters of this thesis. Due to their relative rarity, luminous Type IIn SN have generally not been included in the statistical studies of Type IIn host environments described above, and studies of the explosion/CSM properties have mainly focused on individual events (e.g. Smith et al. 2007, 2008; Chatzopoulos et al. 2011; Gezari et al. 2009; Drake et al. 2010; Rest et al. 2011; Fransson et al. 2014) or small samples of $\sim$5 events (e.g. Chatzopoulos et al. 2013). In is only in recent years that the number of events identified have allowed for statistical analysis of their progenitor populations and explosion properties.

5.4 Definition of a “Luminous” Interacting Transient

5.4.1 Basic Definition

An important concept for the remaining chapters of this thesis will be the definition of a “luminous” interacting transient. For the purposes of this work, we define an interacting transient to be an event which shows narrow hydrogen emission lines in its spectra (e.g. a Type IIn SN). With regards to luminosity, a fiducial cutoff of -21 mag (in any observed band) is often quoted for official classification as a “super-luminous” supernovae (e.g. Gal-Yam 2012). However, such a cutoff is arbitrary and does not necessarily represent a distinct explosion mechanism or progenitor channel. For example, when SLSN-I are selected based on their *spectroscopic* features, identified members have peak magnitudes ranging from ~ -20.5 to < -23 mag (Quimby et al. 2011b; Lunnan et al. 2013; Nicholl et al. 2015). The classification of luminous interacting transients is even less clear, in large part because the interaction often masks any spectroscopic information about the underlying explosion. As a result, there is no clear break in spectral class with luminosity as there is for SLSN-I.

Based on the distance-limited sample of the Lick Observatory Supernova Search (LOSS), Li et al. (2011) derive a luminosity function for Type IIn SN of -16.86 ± 1.61 mag. Kiewe et al. (2012) quote a slightly higher peak magnitude range of $\mathrm{M_V} = -18.4 \pm 1.0$ mag based on 4 objects from the Caltech Core-Collapse Project (CCCP), which is unbiased in the sense that follow-up is not based on explosion properties. Motivated by these findings for the “typical” luminosity of interacting transients, in this work we have chosen to define a “luminous” interacting transient as any event whose peak luminosity is comparable or above that of the Type IIn SN 2010jl.

SN 2010jl was an extensively studied Type IIn SN (see, e.g. Stoll et al. 2011; Ofek et al. 2014c; Fransson et al. 2014) whose peak magnitude $M_{\rm I} = -20.5$ mag was well above the typical values found by LOSS or CCCP. SN 2010jl had a peak luminosity of $\sim 3 \times 10^{43}$ erg s^{-1}, and a slow evolution, resulting in a total radiated energy on the order of $6-9 \times 10^{50}$ erg. Modeling of multi-wavelength data shows that the CSM surrounding the progenitor of SN 2010jl possessed mass in excess of $3-10$ $M_{\odot}$, ejected in the final decades before collapse. In short, despite falling below a fiducial cutoff of $M_{\rm p} < -21$ mag, SN 2010jl was an extreme explosion and we base our definition of "luminous" interacting transients on its properties, requiring $M_{\rm p} < -20$ mag (or $L_{\rm bol,p} > 3 \times 10^{43}$ erg s^{-1}). Figure 5.1 shows the absolute R-band magnitude for a range of interacting transients, to place this definition in context.

5.4.2 Connection to Type IIn/Ia-CSM

We note that our adopted definition would not only include SN such as SN 2010jl and the extreme SN 2006gy (Smith et al. 2007), but also several members of the ambiguous/controversial class of events dubbed "Type IIn/Ia-CSM". These are transients which show narrow hydrogen emission lines in their spectra, indicative of CSM interaction, but also broad and diluted SN-like features, and have been hypothesized to be Type Ia SN exploding into a dense CSM (e.g Hamuy et al. 2003). While several members of this class show only relatively weak interaction and are unambiguously Type Ia SN (e.g. PTF11kx; Dilday et al. 2012), others are significantly more luminous, long-lived, and dominated by interaction (e.g. SN 1997cy, Figure 5.1), and their

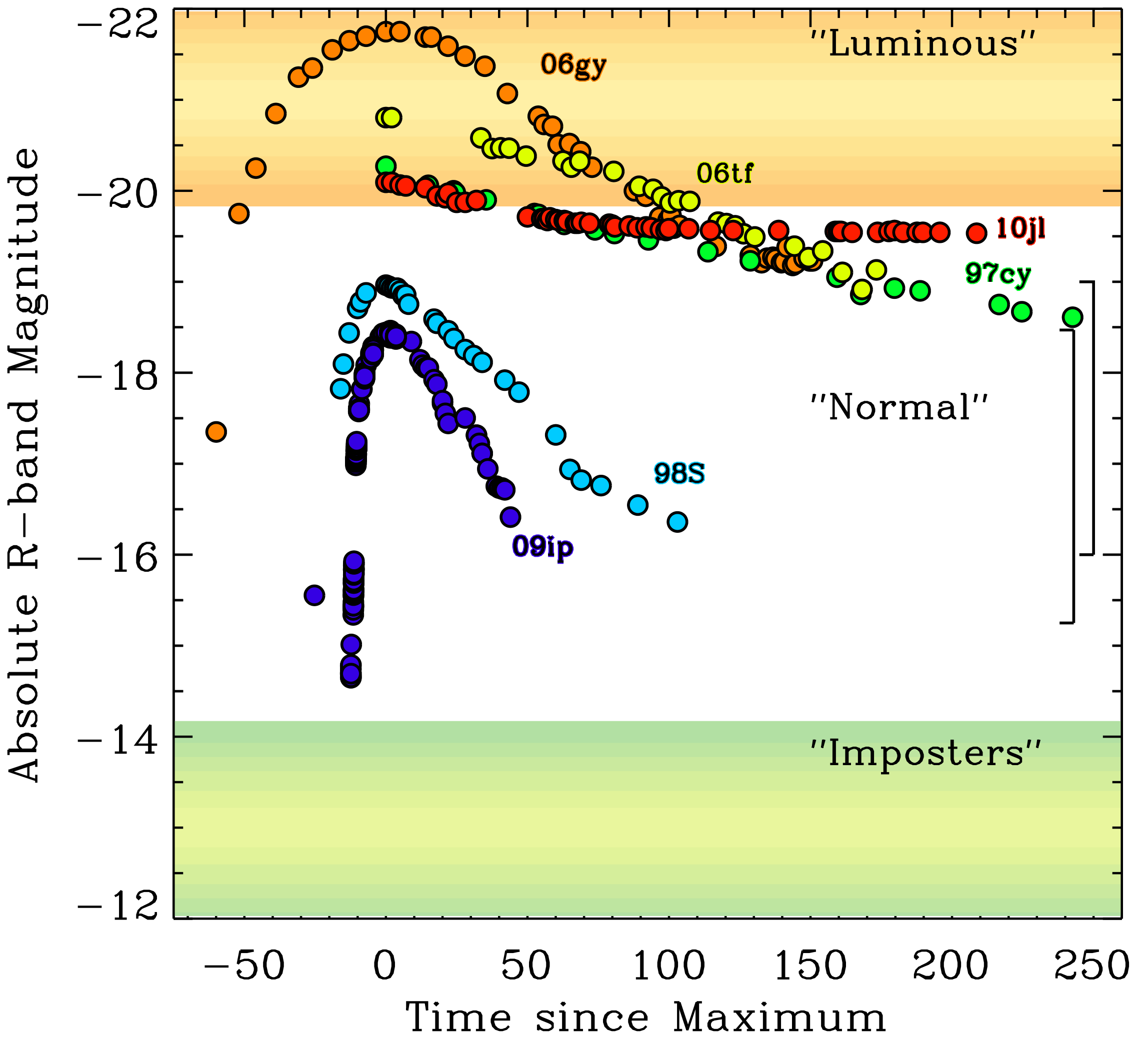

Figure 5.1.—: Luminosity Range of Interacting Transients. Bars on the right designate the typical peak luminosity for Type IIn SN as derived from the Lick Observatory SN Search and the Caltech Core Collapse SN Project. In the remaining chapters of this thesis we adopt a cutoff of ∼−20 mag for designation of a transient as "luminous". *References:* SN 1998S (Liu et al. 2000), SN 2009ip (Margutti et al. 2014b), SN 2010jl (Fransson et al. 2014), SN 2006tf (Smith et al. 2008), SN 1997cy (Germany et al. 2000), SN 2006gy (Smith et al. 2007).

interpretation as Type Ia SN has been debated (e.g Benetti et al. 2006; Trundle et al. 2008). In a systematic search Silverman et al. (2013) identified objects with spectral similarity to members of this class with peak magnitudes ranging from -19.0 mag $>$ $M_R > -21.3$ mag. At the high luminosity end, the broad SN-like features are heavily diluted, and Leloudas et al. (2015b) find that Type IIn SN brighter than -20.1 mag may be able to hide Type Ia SN. On the other hand, Inserra et al. (2016) argue that many of the luminous events now classified as Type IIn/Ia-CSM are difficult to reconcile with a thermonuclear explosion from an energetics perspective–requiring nearly 100% efficiency in converting explosion energy into radiation. In addition, Benetti et al. (2014) note strong spectral similarities at late times between the super-luminous transient CSS121015 and SN 2005gj (which has been classified as a Type IIn/Ia-CSM; Aldering et al. 2006). CSS121015 had a peak luminosity and total radiated energy in excess of 10^{44} erg s^{-1} and 10^{51} erg, respectively, and a Type Ia progenitor can be excluded based on energetics.

The Type IIn/Ia-CSM class of events therefore highlights the difficulty in assessing the underlying explosions and progenitor systems of interaction-powered SN. Jointly assessing the explosion properties and host environments of transients which have been explicitly classified as Type IIn/Ia-CSM along with other luminous interacting transients can provide insight into the progenitor populations of each. These events will be considered in addition to other luminous interacting transients in Chapter 7 when we investigate sub-galactic environments.

Chapter 6

Luminous Interacting Transients II: Type IIn SN from the PanSTARRS1 Medium Deep Survey

M. R. Drout, E. Berger and the Pan-STARRS1-MDS Transient Group

In Preparation

Abstract

We present the light curves, spectra, and basic properties for the full sample of Type IIn SN discovered during the PanSTARRS1 Medium Deep Survey. These 25 events span a wide range in peak luminosity (-16 mag $>$ M > -21 mag) and timescale (12 days $<$ $t_{\rm char}$ $<$ 200 days). The sample includes 10 events with peak luminosities above 6×10^{43} erg s^{-1} and total radiated energies in excess of (0.3$-$1.0) $\times10^{51}$ erg. This represents a significant contribution to the total number of luminous interacting transients with well-sampled, multi-band light curves available. When modeled as a shock breakout and interaction within a dense wind, the bolometric light curves for these luminous events require pre-SN mass-loss rates on the order of $\sim$$M_\odot$ yr^{-1} and dense CSM shells of $\sim$10 $M_\odot$. This sample, supplemented with events from the literature, will be used in Chapters 7 and 8 to study the host-galaxies and sub galactic environments of interacting transients, with an emphasis on luminous events.

6.1 Introduction

As outlined in Chapter 5, a large and unbiased sample of events is a key asset in advancing our understanding of the progenitor stars and mass-loss mechanism of Type IIn SN. In this chapter we present the full sample of Type IIn SN discovered by the PanSTARRS1 Medium-Deep Survey (PS1-MDS). This sample is unbiased in the sense that it comes from a single, untargeted, transient survey, and it includes events which span a wide range of luminosities and timescales. In addition, due to its volume and depth, the PS1-MDS is particularly efficient at identifying luminous transients. This sample includes a significant contribution to the total number of luminous interacting transients with well sampled, multi-band light curves presently available. These events also form the core of the sample which we will use in Chapters 7 and 8 to investigate the global host galaxy properties and sub-galactic environments of luminous interacting transients in comparison to both "standard luminosity" Type IIn SN and other energetic transients.

This chapter is organized as follows: In Section 6.2 we describe the selection process for the PS1-MDS sample of interacting transients, in Section 6.3 we describe the basic properties of the full sample of 25 Types IIn SN discovered in the PS1-MDS, in Section 6.4 we provide preliminary estimates of the CSM densities inferred, and in Section 6.5 we briefly discuss future work.

6.2 Sample Selection

Approximately 25% of the PS1 observing time was devoted to the Medium-Deep Survey, which operated between late 2009 and early 2014. The PS1 imager is an array of sixty 4800 × 4800 pixel detectors with a pixel scale of $0.''258$, mounted on a 1.8-m primary with a $3^{\circ}.3$ diameter field of view (Kaiser et al. 2010; Tonry & Onaka 2009). Details of the filters and photometric system are given in Tonry et al. (2012) and Stubbs et al. (2010). The PS1-MDS consisted of 10 single-footprint fields distributed throughout the sky, which were imaged in $g_{P1}r_{P1}i_{P1}z_{P1}$—with a nominal cadence of 3 days per filter—to a typical 5σ depth of 23.3 mag. y_{P1} was observed during times of full moon to a depth of ~ 21.7 mag. Standard initial reductions, astrometric solution, and stacking of nightly PS1-MDS images were carried out with the PS1 Image Processing Pipeline (IPP;

Magnier 2006; Magnier et al. 2008). The nightly PS1-MDS stacks were then transferred to the Harvard FAS Research Computing cluster where difference images were produced and potential transients identified by the `photpipe` pipeline (Rest et al. 2005, 2014).

Throughout its 4.5 years of operation, the PS1-MDS identified ∼5000 transients. Of these, ∼10% were selected for spectroscopic follow-up. which was primarily preformed using the Blue Channel spectrograph on the 6.5-m MMT telescope (Schmidt et al. 1989), the Inamori-Magellan Areal Camera and Spectrograph (IMACS; Dressler et al. 2006) and Low Dispersion Survey Spectrograph (LDSS3) on the 6.5−m Magellan telescopes, and the Gemini Multi-Object Spectrograph (GMOS; Hook et al. 2004) on the 8-m Gemini telescopes. Over the duration of the PS1-MDS, we spectroscopically confirmed ∼25 interacting transients. For formal classification as a Type IIn SN, we required that a transient showed resolved hydrogen emission but lacked the broad P Cygni absorption features associated with standard Type II SN. While a subset of events have only a single classifying spectrum, a majority have 2−3 spectra acquired over 1−2 observing seasons.

Due to its pencil beam observing strategy, most of PS1-MDS volume is at moderate redshift. This has several important consequences for the identification and properties of our sample of interacting transients. As we detail below, particular care must be taken both to eliminate possible contaminants and to assess sample completeness.

6.2.1 Contamination

At moderate spectral resolution and signal-to-noise, a number of transients can resemble Type IIn SN. This is particularly true in the central regions of galaxies. Some active galactic nuclei (AGN) possess spectra remarkably similar to Type IIn SN (Filippenko

1989) and in recent years a number of "changing look" AGN have been identified in which the broad-line components of Hα and Hβ are observed to either appear or disappear (see Shappee et al. 2014, and references therein). In addition, several tidal disruption event (TDE) candidates have been observed with broad/intermediate width hydrogen emission lines (van Velzen et al. 2011). In Chapter 8, we present precise astrometry on our PS1-MDS selected interacting transients. While none of the events in this sample are coincident with their galaxy centers within the 1σ uncertainties, several lie in the inner regions of their hosts. We have therefore taken several steps to examine our sample for possible contamination by AGN/TDEs. These include:

1. Transient Color Evolution: Most optically-selected TDEs in the literature exhibit blue colors and a distinct *lack* of color evolution with time. (van Velzen et al. 2011; Gezari et al. 2012; Chornock et al. 2013). In is in contrast to most SN, which are blue at early times but quickly evolve to colors significantly redder than those found in TDE candidates. We have examined the photometric color evolution for all transients in our sample. We observe reddening in most events after maximum light (consistent with a cooling and expanding photosphere) and none display the distinctive color evolution found in TDE candidates.

2. Host Galaxy Spectra: We have obtained host galaxy spectra for a many of the events in our sample. In all cases, the resolved component of the hydrogen emission has disappeared at late times. In addition, after measuring the nebular emission lines fluxes in the galaxy spectra of events that exploded in the central regions of their hosts, we find that they show emission line ratios similar to star-forming galaxies in a BPT diagram.

3. Pre- and Post-explosion Variability: We examined the full 4.5 year PS1-MDS light curves of events in our sample for evidence of AGN-like variability. In all cases, the main outburst is the only transient event/variability observed above the detection threshold of the PS1-MDS.

6.2.2 Completeness

We are interested in understanding the progenitor stars and mass-loss mechanism of luminous interacting transients, and it is therefore useful to assess our ability to identify these events in the PS1-MDS. Due to its pencil beam observing strategy, the PS1-MDS is well suited to identify luminous and blue transients at moderate redshift. However, luminous Type IIn SN have several properties which make them difficult to spectroscopically classify at moderate redshift. In particular, many luminous Type IIn SN only possess *weak* hydrogen emission emission lines in their spectra, which—in some cases—do not develop until weeks post-maximum (Benetti et al. 2014; Smith et al. 2008, 2007). This spectral evolution is often interpreted as the CSM interaction being so optically thick that the energy must first diffuse outward from an opaque shell. This results in a spectrum dominated mainly by a blue continuum (e.g Smith et al. 2007). Indeed, for many of the luminous Type IIn SN we identified in the PS1-MDS, the first observed spectrum was featureless and blue, and only in later epochs do resolved Balmer emission lines become apparent.

These weak emission features complicate the spectral identification of luminous interacting transients, *especially at redshift* $z > 0.4$ when Hα is redshifted out of the range of most optical spectrographs. This is in contrast to SLSN-I, whose UV spectroscopic features are favorable for identification at high-z[1]. We therefore examined all events from the PS1-MDS spectroscopic sample whose spectra showed only blue continua for candidate interacting transients. We required that any objects identified pass the following cuts:

1. Are luminous. This avoids contamination from other classes of core-collapse SN, whose early spectra can also be blue and featureless.
2. Lack the UV absorption features used to classify SLSN-I.
3. Pass the same cuts for AGN/TDEs listed above (i.e. color evolution, lack of pre− and post−explosion variability).

This process yielded two additional transients, both at z>0.68 (PS1-13byi and PS1-13cvy). We consider these likely, but non-confirmed, luminous interacting transients, and analyze their basic properties alongside rest of the sample below.

6.3 Basic Properties

Our final sample of PS1-MDS selected interacting transients consists of 25 events. We list their basic properties in Table 6.1. The transients span a redshift range of $0.04 < z < 0.780$ with a median value of $z = 0.259$.

---

[1] for comparison the PS1-MDS discovered SLSN-I all fall at z>0.5

Table 6.1. Basic Photometric Properties

Event	Redshift	$M_{p,g}$ (err) (mag)	$M_{p,r}$ (err) (mag)	$M_{p,i}$ (err) (mag)	$M_{p,z}$ (err) (mag)	L_p (err) (erg s^{-1})	E_{rad} (err) (erg)
PS10acl	0.259	-18.78 (0.09)	-18.84 (0.07)	-18.92 (0.04)	-19.07 (0.06)	1.24e+43 (1.06e+42)	6.70e+49 (2.43e+48)
PS10caa	0.092	-15.96 (0.11)	-16.13 (0.07)	-16.30 (0.05)	-16.10 (0.07)	9.40e+41 (1.67e+41)	4.72e+48 (2.78e+47)
PS11ad	0.422	-19.98 (0.06)	-20.47 (0.04)	-20.72 (0.04)	-20.73 (0.03)	6.21e+43 (6.64e+42)	1.00e+51 (3.59e+49)
PS11jf[a]	0.282	-18.51 (0.07)	-19.33 (0.04)	-20.14 (0.02)	-19.95 (0.05)	2.52e+43 (2.19e+42)	2.71e+50 (1.17e+49)
PS11jg[a]	0.082	-14.14 (0.32)	-14.92 (0.31)	-16.35 (0.05)	-15.23 (0.14)	3.13e+41 (6.71e+40)	1.92e+48 (2.18e+47)
PS11kj	0.400	-19.64 (0.07)	-20.17 (0.05)	-20.29 (0.05)	-20.35 (0.07)	5.15e+43 (5.44e+42)	6.65e+50 (5.16e+49)
PS11vo	0.116	-20.24 (0.01)	-20.44 (0.01)	-20.52 (0.02)	-20.45 (0.01)	5.02e+43 (1.53e+42)	5.65e+50 (9.53e+48)
PS11aop	0.218	-20.14 (0.02)	-20.47 (0.02)	-20.69 (0.03)	-20.69 (0.05)	5.42e+43 (2.54e+42)	8.42e+50 (1.72e+49)
PS12dm	0.201	-18.65 (0.04)	-18.50 (0.03)	-18.35 (0.04)	-18.31 (0.07)	1.35e+43 (2.96e+42)	3.50e+49 (1.12e+48)
PS12gy[a]	0.285	-16.50 (0.33)	-17.73 (0.18)	-18.29 (0.18)	-18.63 (0.11)	1.22e+43 (6.96e+42)	1.56e+50 (5.26e+49)
PS12kn	0.473	-20.07 (0.10)	-20.17 (0.07)	-20.16 (0.04)	-20.23 (0.06)	5.09e+43 (7.56e+42)	2.57e+50 (7.18e+48)
PS12zc[a]	0.167	-19.96 (0.01)	-19.78 (0.01)	-19.58 (0.02)	-19.43 (0.09)	5.33e+43 (6.49e+42)	6.30e+50 (7.09e+49)
PS12apa	0.528	-19.96 (0.10)	-20.32 (0.07)	-20.58 (0.06)	-20.61 (0.08)	6.02e+43 (6.69e+42)	1.05e+50 (5.65e+48)
PS12bli	0.189	-18.64 (0.04)	-19.01 (0.06)	-19.07 (0.03)	-18.97 (0.03)	1.34e+43 (1.01e+42)	1.26e+50 (1.05e+49)
PS12bub[a]	0.325	-17.90 (0.13)	-19.26 (0.20)	-18.26 (0.10)	-19.44 (0.07)	1.42e+43 (3.89e+42)	2.82e+50 (3.59e+49)
PS12ces	0.193	-18.24 (0.07)	-18.38 (0.05)	-18.59 (0.04)	-18.48 (0.05)	9.24e+42 (1.14e+42)	2.73e+49 (1.57e+48)
PS12car	0.680	-20.43 (0.07)	-20.46 (0.08)	-20.62 (0.15)	-20.60 (0.07)	7.50e+43 (1.00e+43)	2.14e+50 (1.27e+49)
PS12cht	0.148	-19.66 (0.02)	-19.47 (0.01)	-19.51 (0.01)	-19.42 (0.02)	3.71e+43 (5.02e+42)	9.83e+49 (4.22e+48)
PS13hi[a]	0.040	-16.39 (0.05)	-17.09 (0.22)	-17.40 (0.03)	-17.74 (0.03)	2.55e+42 (9.16e+40)	1.51e+49 (2.34e+47)
PS13adh	0.137	-18.35 (0.03)	-18.07 (0.04)	-17.96 (0.03)	-17.73 (0.07)	1.05e+43 (2.31e+42)	1.35e+49 (8.24e+47)
PS13byi	0.682	-20.46 (0.06)	-20.56 (0.08)	-20.69 (0.13)	-20.65 (0.15)	7.32e+43 (1.03e+43)	2.49e+50 (1.19e+49)
PS13cvy	0.780	-20.19 (0.11)	-20.42 (0.08)	-20.68 (0.11)	-20.56 (0.21)	6.38e+43 (8.74e+42)	3.30e+50 (2.45e+49)
PS13ecp	0.184	-18.68 (0.04)	-18.90 (0.03)	-18.93 (0.02)	-19.07 (0.03)	1.30e+43 (1.50e+42)	4.57e+49 (1.42e+48)
PS13epq	0.261	-18.67 (0.07)	-18.53 (0.09)	-18.68 (0.06)	-18.84 (0.09)	1.22e+43 (1.77e+42)	1.84e+49 (2.82e+48)
PS13epy	0.294	-19.61 (0.06)	-19.59 (0.05)	-19.63 (0.04)	-19.66 (0.08)	3.09e+43 (5.69e+42)	4.24e+49 (4.92e+48)

[a] Peak of the light curve was not constrained. Values listed are peak *observed* magnitudes/luminosities. These events are plotted as open symbols in Figure 6.4

6.3.1 Observed Light Curves and Spectra

The full $g_{\rm P1}r_{\rm P1}i_{\rm P1}z_{\rm P1}$ light curves are presented in Figures 6.1 and 6.2. Representative spectra are shown in Figure 6.3. For 19 (of 25) events our photometric coverage includes the epoch of peak brightness.

In Figure 6.4 we plot the peak observed absolute magnitudes in $g_{\rm P1}r_{\rm P1}i_{\rm P1}z_{\rm P1}$ versus redshift for the entire sample. All calculations in this paper assume a flat ΛCDM cosmology with $\rm H_0 = 71$ km s^{-1} Mpc^{-1}, $\Omega_m = 0.27$, and $\Omega_\Lambda = 0.73$. Events for which we do not observe the epoch of peak brightness are shown as open symbols. We do not perform full bandpass k−corrections, but correct the measured magnitudes for cosmological expansion by adopting $\rm M = m - 5\ \log_{10}\ (\frac{d_L}{10pc}) + 2.5\ \log_{10}\ (1+z)$ (Chomiuk et al. 2011; Hogg et al. 2002). We have corrected our sample for Milky Way extinction (Schlafly & Finkbeiner 2011), but do not currently adopt any correction for host galaxy absorption.

Peak absolute magnitudes for the PS1-MDS sample range from -16 mag $>$ M $>$ -21 mag. There are two significant groupings of events: one with -18 mag $>$ M $>$ -19.5 mag and another with M $>$ -20 mag.

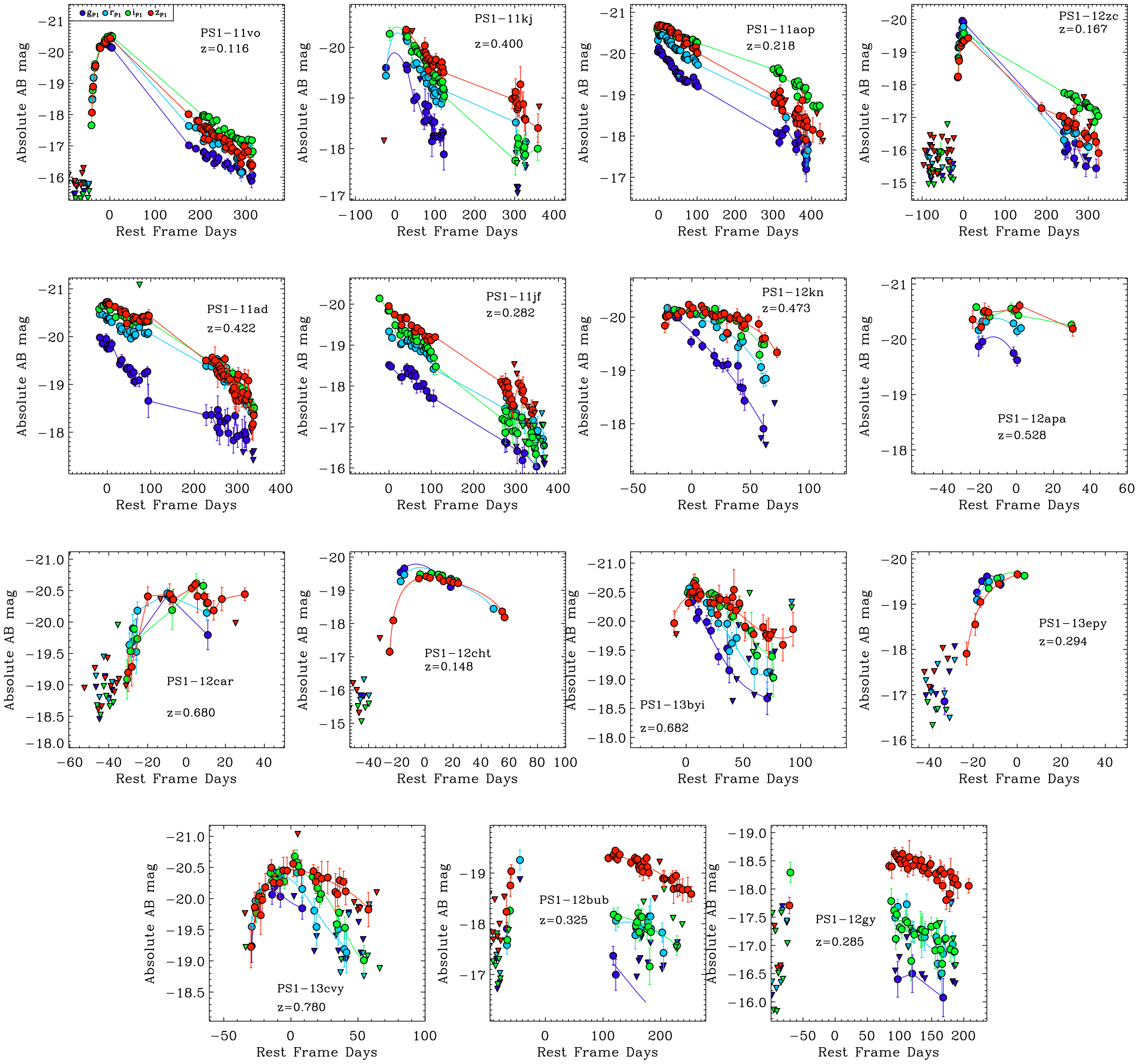

Figure 6.1.—: $g_{\rm P1}, r_{\rm P1}, i_{\rm P1}, and z_{\rm P1}$ light curves for the sample of PS1-MDS Type IIn SN with peak magnitudes which approach or exceed −20 mag (blue, cyan, green, and red, respectively). Upper limits are plotted as triangles. For PS1-12bub and PS1-12gy the epoch of maximum light occurred between observing seasons and the peak magnitude is not well constrained.

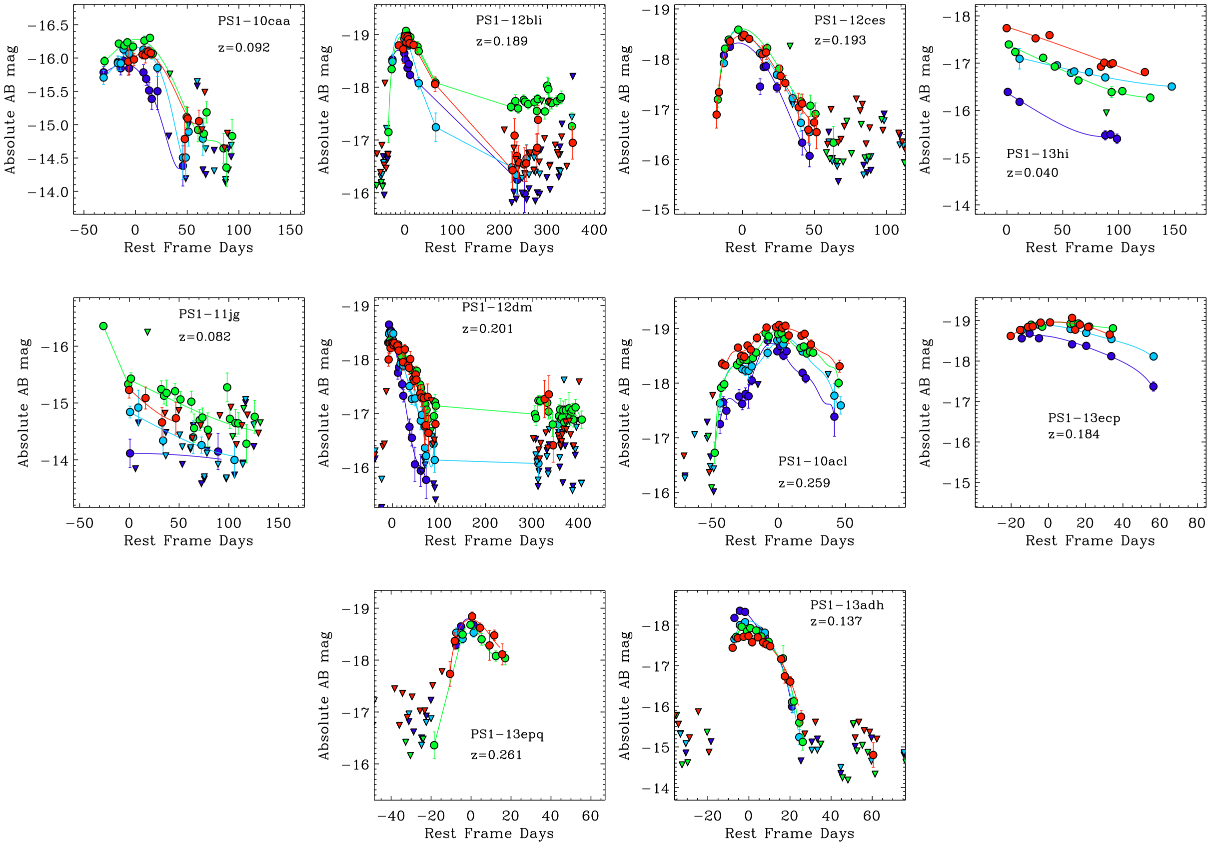

Figure 6.2.—: $g_{\rm P1}, r_{\rm P1}, i_{\rm P1}, and z_{\rm P1}$ light curves for the sample of PS1-MDS Type IIn SN with peak magnitudes below −20 mag (blue, cyan, green, and red, respectively). Upper limits are plotted as triangles.

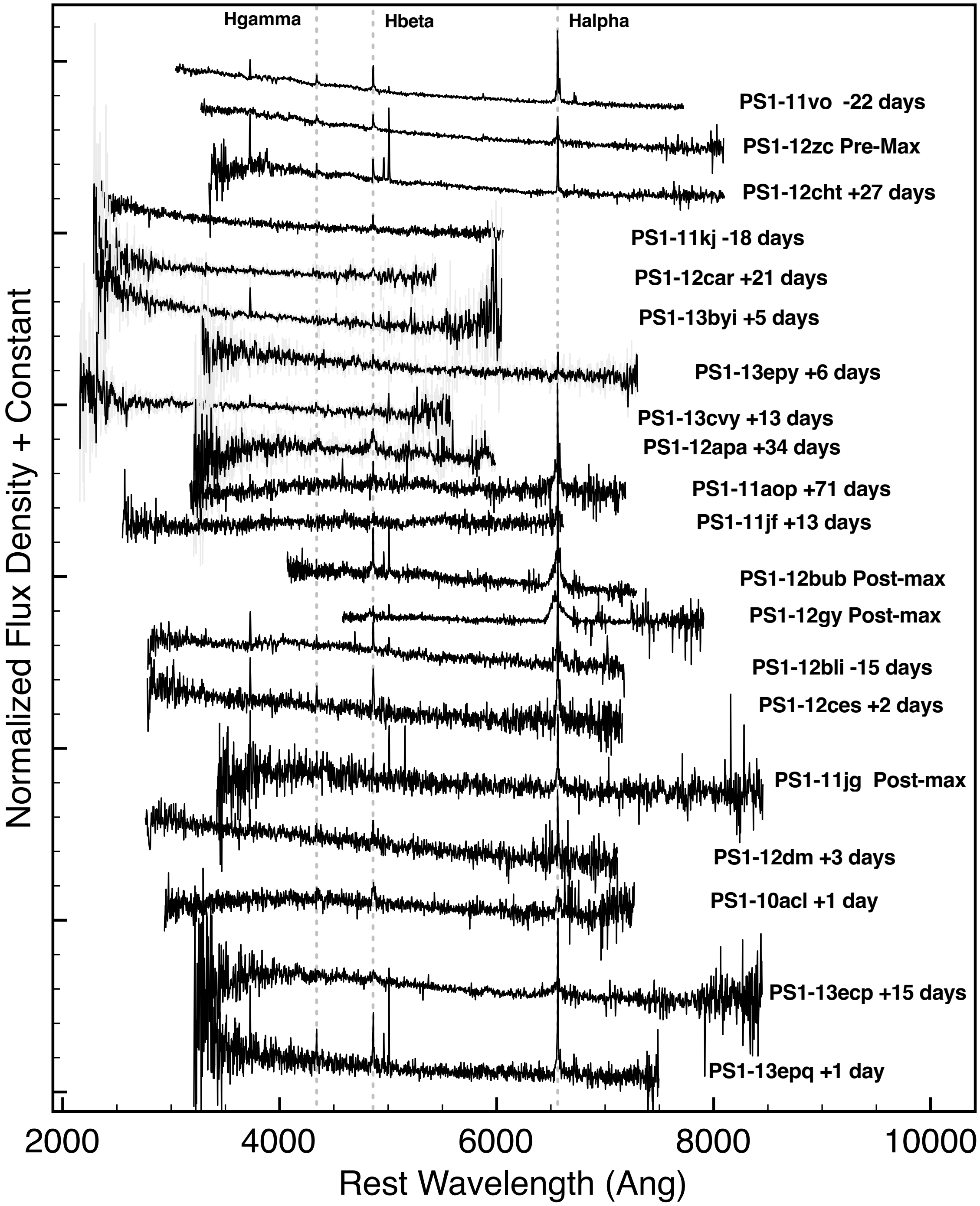

Figure 6.3.—: Representative spectra for the sample of PS1-MDS Type IIn SN.

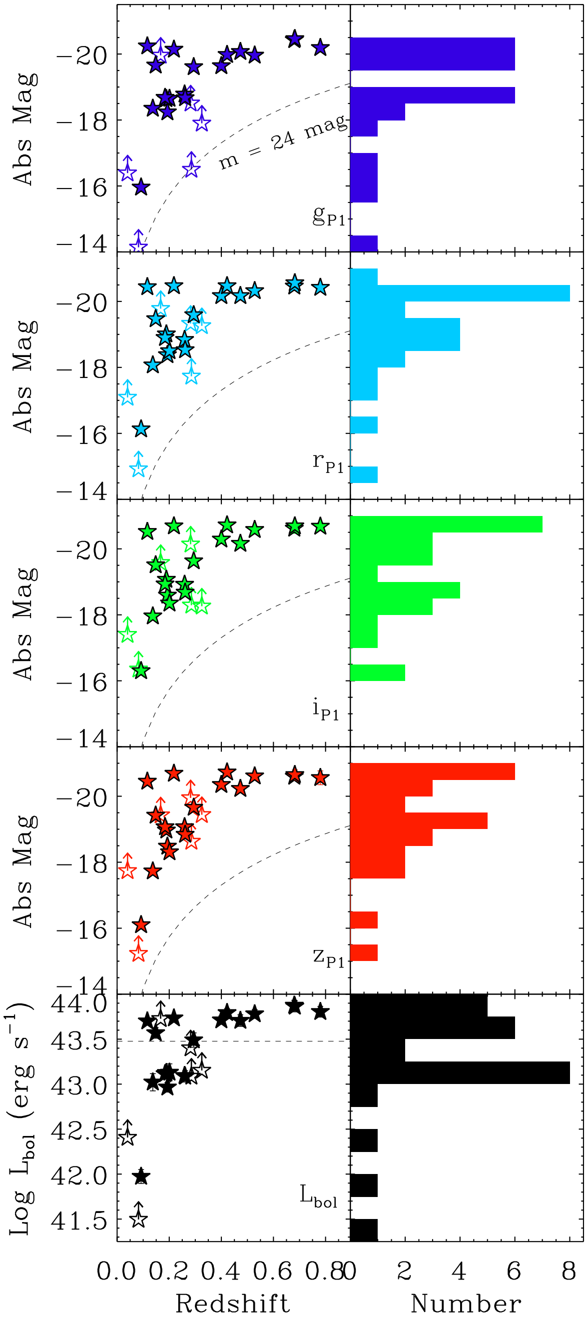

Figure 6.4.—: Peak absolute magnitudes and peak bolometric luminosities for the PS1-MDS sample of Type IIn SN as a function of redshift. Thirteen events could be classified as "luminous" by the definition outlined in Chapter 5.4.

6.3.2 Pseudo-Bolometric Light Curves

In order to constrain the true energy scale of the PS1-MDS Type IIn SN, we use the $g_{\rm P1}r_{\rm P1}i_{\rm P1}z_{\rm P1}$ light curves to construct pseudo-bolometric light curves for the entire sample. As $g_{\rm P1}r_{\rm P1}i_{\rm P1}z_{\rm P1}$ are not all observed concurrently during the PS1-MDS, we begin by fitting low-order polynomials to our observed data in each band, and use these polynomials to interpolate our data to a set of common epochs. In choosing our interpolation epochs, we require that all bands were observed within a time period of $\sim$3 days. We then sum the observed flux in these interpolated bands and attach a blackbody tail (based on a fit to the $g_{\rm P1}r_{\rm P1}i_{\rm P1}z_{\rm P1}$ data) to account for missing IR flux. The resulting peak bolometric luminosities are shown in the bottom panel of Figure 6.4 and span the range 10^{42} erg s^{-1} $<$ L $<$ 10^{44} erg s^{-1}. These values are listed in Table 6.1.

None of our transients are as extreme as the prototypical super-luminous Type IIn SN 2006gy[2], which had an derived peak bolometric luminosity of 1.7×10^{44} erg s^{-1} (Smith & McCray 2008). However, 13 events meet our definition of "luminous" outlined in Chapter 5 in having $L_{\rm bol,p} > 3 \times 10^{43}$ erg s^{-1}. Of these 13 transients, one (PS1-11jf) is spectroscopically classified as a Type IIn/Ia-CSM and two (PS1-12cht and PS1-13epy) have peak luminosities which just reach our cutoff. The remaining 10 objects all have $L_{\rm bol} > (5-6) \times 10^{43}$ erg s^{-1}, similar to luminous events such as SN 2003ma (Rest et al. 2011) and SN 2006tf (Smith et al. 2008). In Figure 6.5 we plot the pseudo-bolometric light curves for the entire sample.

---

[2] Although we note that SN 2006gy has an estimated $A_{\rm R} = 1.25$ mag of extinction from its host-galaxy (Smith et al. 2007). Our events have only been corrected for Milky Way reddening.

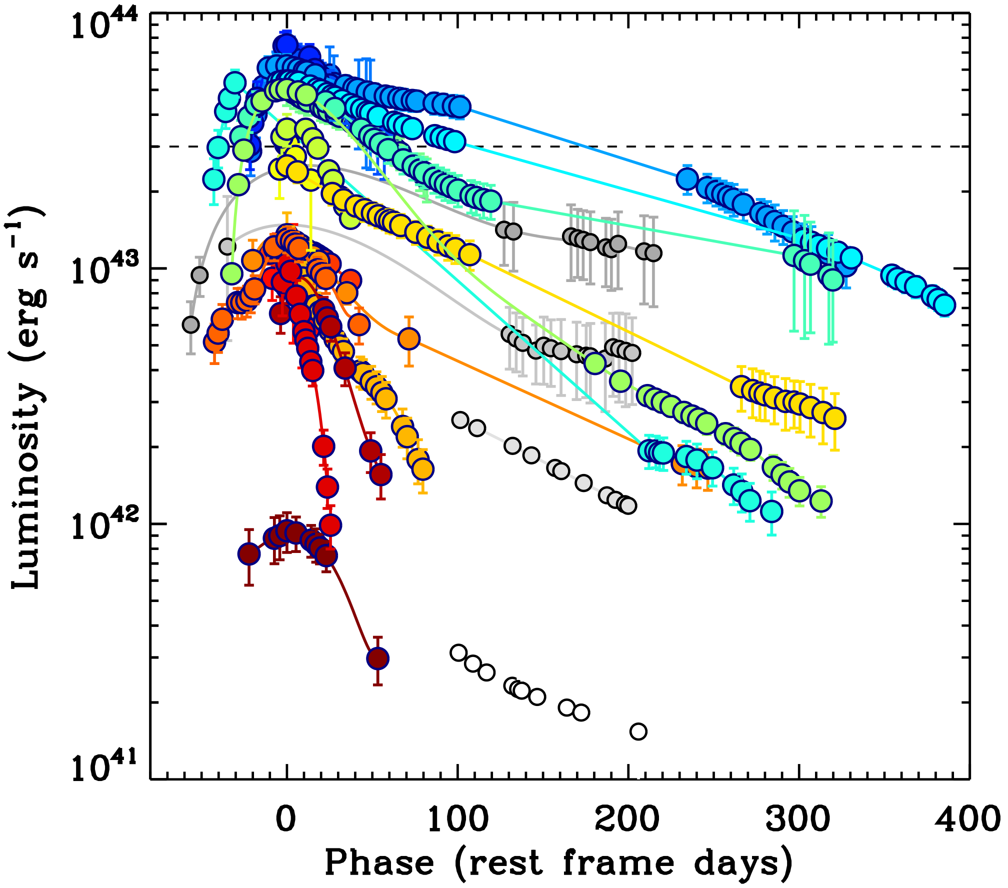

Figure 6.5.—: Bolometric light curves for the PS1-MDS sample of interacting transients. Events span two orders of magnitude in both peak luminosity and characteristic timescale. A number of events have luminosities which exceed 10^{43} erg s^{-1} ~1 year post-explosion. Objects for which we do not constrain the peak magnitude are plotted in grey.

6.3.3 Timescales

As can be seen in Figure 6.5, the SN display a wide range of observed timescales. These range from PS1-13adh, which declines by $\sim$2.5 magnitudes in the first 20 days post-maximum, to PS1-11ad, which decays by only $\sim$0.5 mag over >100 days. Of the luminous transients in our sample two (PS1-11vo and PS1-12zc) appear to show bell-shaped light curves reminiscent of SN 2006gy, while others exhibit slow and linear declines after peak that span multiple observing seasons. Eight SN have dense light curve coverage $\sim$1 year post explosion. At these epochs their luminosities are still in excess of $10^{42}-10^{43}$ erg s^{-1} (i.e. the typical *peak* luminosity of a Type Ib/c SN; Drout et al. 2011).

By contrast, many of the "non-luminous" Type IIn SN in our sample have peak luminosities of $L_p \sim 10^{43}$ erg s^{-1} and decline significantly over $50-100$ days, similar to the prototypical events SN 1998S (e.g Liu et al. 2000) and SN 2009ip (e.g Margutti et al. 2014b). In several cases, we observe a rapid post-maximum decline followed by a plateau in the observed band which includes Hα (e.g. PS1-12bli; See Figure 6.2)—possibly indicative of continued interaction.

6.3.4 Pre-Explosion Outbursts

A number of Type IIn SN have been observed to exhibit pre-explosion outbursts. We have examined the full 4.5-year light curves of the PS1-MDS transients for evidence of such eruptions. While we do not detect any precursor events in the years prior to explosion, several transients in the PS1-MDS sample show multiple peaks/undulations in their light curves. In Figure 6.6 we highlight one event, PS1-10acl, whose light curve displayed two peaks in all observed bands. The separation between these peaks is $\sim 30-40$ days, similar to separation observed between the pre-cursors and "main" explosions in SN 2009ip (Margutti et al. 2014b) and SN 2010mc (Ofek et al. 2013). The strong similarity between the light curves of SN 2009ip and SN 2010mc has been argued to imply that that the physical mechanism which leads to these peaks is fundamental to stellar evolution, rather than the fine-tuned details of any individual progenitor system (Margutti et al. 2014b). While PS1-10acl shows several differences in comparison to SN 2009ip and SN 2010mc (most notably the increased luminosity of the initial light curve peak), it represents an additional example of this characteristic timescale in Type IIn SN.

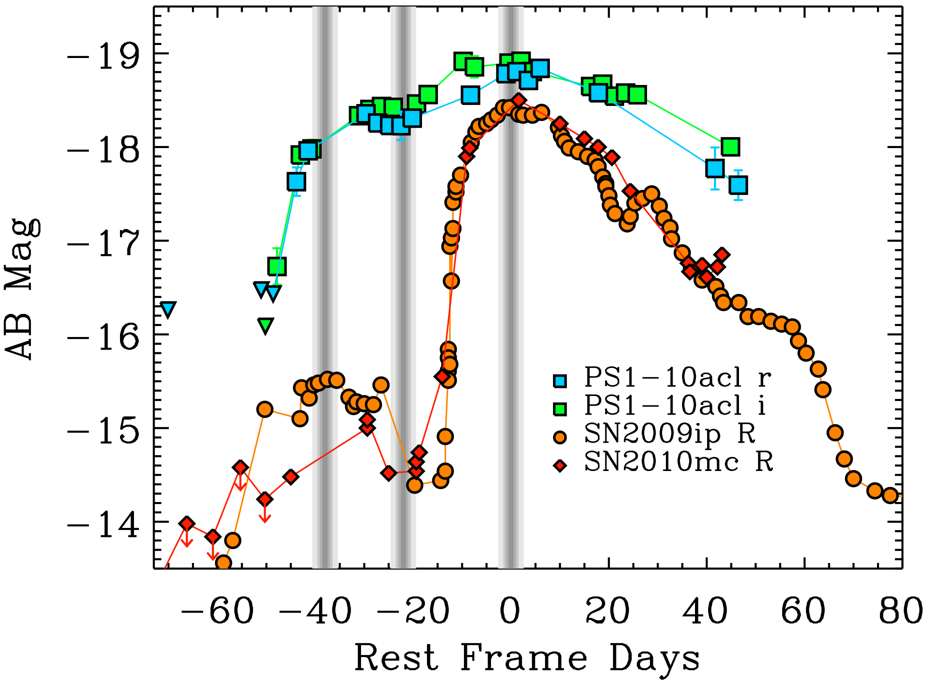

Figure 6.6.—: The light curve of PS1-10acl in comparison to those of the Type IIn SN 2009ip (Margutti et al. 2014b) and SN 2010mc (Ofek et al. 2013). PS1-10acl shows two peaks in its light curve with a similar temporal separation to the precursor and main explosions observed in SN 2090ip and SN 2010mc. Grey vertical lines highlight epoch of maximum for the two light curve peaks and the epoch of minima between them.

6.3.5 Total Radiated Energies

Finally, we put lower limits on the total radiated energy for each of the PS1-MDS transients by integrating our bolometric light curves. A histogram of these values in shown in Figure 6.7. For many of our luminous transients these *limits* approach or exceed 10^{51} ergs, therefore requiring either very energetic explosions, very high efficiency in converting explosion energy to radiation, or both. These values are listed in Table 6.1.

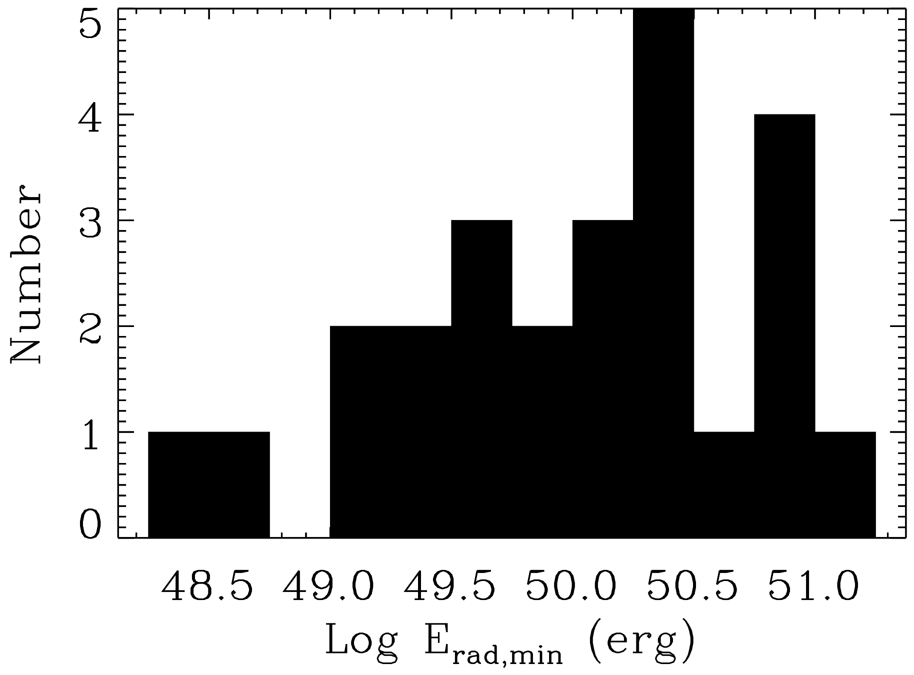

Figure 6.7.—: Histogram of lower limits on the total radiated energies for the PS1-MDS Sample of Type IIn SN. Many objects approach or exceed 10^{51} erg.

6.4 Preliminary Estimates of CSM Densities

The wide array of luminosities and timescales displayed by the PS1-MDS interacting transients are consistent with a similar diversity in the underlying explosions and properties of the CSM surrounding the progenitor systems. Detailed modeling of these parameters for the full sample of PS1-MDS interacting transients (including luminosity, temperature, and spectral evolution, multiple power sources and CSM density profiles, and constraints from late-time multi-wavelength (radio and X-ray) observations) will be presented in future work. Here, in order to provide context for how observed properties can translate to physical parameters, we provide order-of-magnitude estimates for the density of the CSM surrounding the progenitor systems of the PS1-MDS Type IIn SN, under the assumption that the observed luminosity is dominated by energy production from ejecta-CSM interaction.

To first order, a basic interaction model can be constructed by assuming that the observed luminosity directly tracks the instantaneous rate of energy generation from the ejecta-CSM interaction. Smith et al. (2010) construct such a model for the luminous Type IIn SN 2006gy, adopting $\mathrm{L} = (\eta/2)wv^3$ where η is the efficiency which which kinetic energy is converted to radiation, v is the expansion velocity of the shock into the CSM, and w is a parameterization of the density of the CSM. Specifically, $w = \rho_{\mathrm{CSM}} \times 4\pi\mathrm{R}^2 = \dot{\mathrm{M}}/\mathrm{v}_w$ where ρ_{CSM} is the density of the CSM, $\dot{\mathrm{M}}$ is the pre-SN mass-loss rate, and v_w is the pre-SN wind speed. Applying a similar model to the PS1-MDS Type IIn SN, assuming a shock velocity of $\mathrm{v}_{\mathrm{shock}} = 5000$ km s^{-1} and $\eta = 0.5$, yields inferred pre-SN mass-loss rates spanning $1 \times 10^{-3}\ \mathrm{M}_\odot\ \mathrm{yr}^{-1} < \dot{\mathrm{M}} \times (\frac{v_w}{150\mathrm{kms}^{-1}}) < 1\ \mathrm{M}_\odot\ \mathrm{yr}^{-1}$. This is consistent with the range of CSM densities found in the literature for both "standard

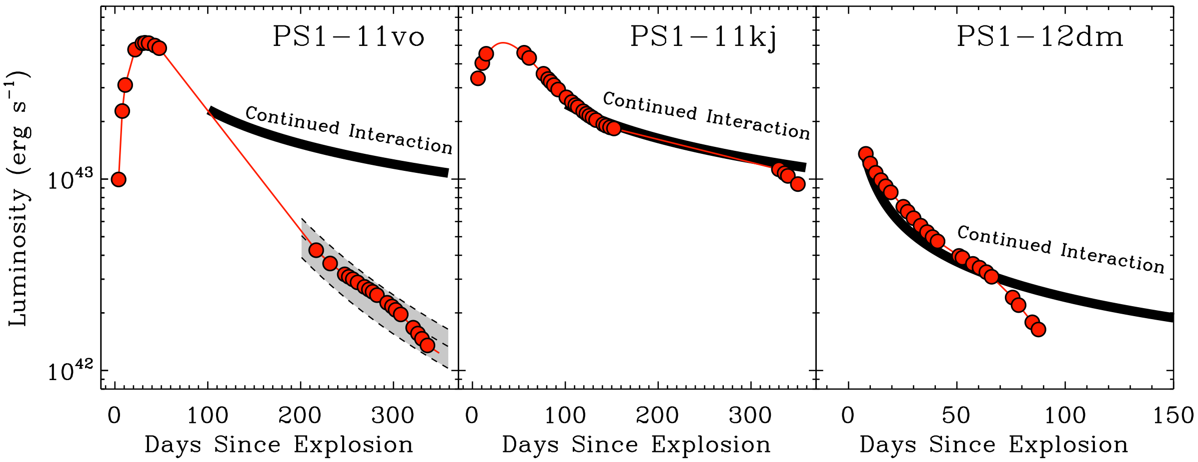

Figure 6.8.—: Pseudo-bolometric light curves for three representative examples of the PS1-MDS Type IIn sample in comparison to the luminosity predicted by the models of (Chevalier & Irwin 2011) for continued interaction within a dense CSM shell after shock break-out in an optically thick wind region. PS1-11vo (left panel) and PS1-11kj (middle panel) are both luminous Type IIn SN. However, at late times (t ∼ 1 year post-explosion) the luminosity of PS1-11kj is consistent with the prediction for continued interaction while the luminosity of PS1-11vo falls an order of magnitude below this level. When modeled with the CSM-interaction/diffusion model, the light curves of both PS1-11vo and PS1-11kj require dense CSM masses of $\gtrsim$10 $M_\odot$. PS1-12dm (right panel) is a lower luminosity Type IIn SN whose light curve can be fit by shock-breakout/interaction with a CSM characterized by a pre-SN mass-loss rate of a few $\times 10^{-2}$ $M_\odot$ yr^{-1} and a total CSM mass of ∼0.3 $M_\odot$.

luminosity” and luminous Type IIn SN (e.g Smith 2014).

The assumption of an optically-thin CSM-ejecta interaction will be violated at early times if radiative diffusion of the shock generated luminosity through an optically thick shell is important. In this case, we can model the rising and portion of the light curve as a shock breakout within a dense wind (see, e.g. Chevalier & Irwin 2011; Ofek et al. 2010; Balberg & Loeb 2011; Chatzopoulos et al. 2012). We now present a preliminary analysis for three of the PS1-MDS Type IIn SN that span the range of behavior observed in the sample. We use the analytic shock-breakout models of Chevalier & Irwin (2011) as parameterized by (Margutti et al. 2014b) for the case where the radius of the dense wind region is larger than the radius where diffusion becomes important ($R_w > R_d$). These models assume a wind environment density profile ($\rho \propto r^{-2}$), and relate the explosion kinetic energy, ejecta mass, and CSM density to three observable quantities: the rise time of the transient ($t_{\rm rise}$), the total energy radiated on the rise ($E_{\rm rad}$), and the shock-break out radius ($R_{\rm bo}$). $E_{\rm rad}$ and $t_{\rm rise}$ can be measured directly from many of the PS1-MDS light curves, while an estimate of $R_{\rm bo}$ can be derived from the radius evolution of the blackbody SED fits.

6.4.1 PS1-11vo

PS1-11vo is a luminous SN, reaching a peak magnitude in excess of −20.5 mag. The PS1-MDS observed its rise over a dynamic range of ∼5 mag, and its bolometric light curve is shown in the left panel of Figure 6.8. With an observed $t_{\rm rise} \sim 38$ days, $E_{\rm rad}$ $\sim 1.15 \times 10^{50}$ erg, and estimated $R_{\rm bo} \sim 8 \times 10^{14}$cm, the models of (Chevalier & Irwin 2011) yield an explosion ejecta mass of ~ 30 $(\frac{\rm E}{10^{51}{\rm erg}})$ $M_\odot$ and a CSM density which can be described by a pre-SN mass-loss rate of ~ 1.5 $(\frac{v_w}{150{\rm kms}^{-1}})^{-1}$ $M_\odot$ yr^{-1}.

The models of Chevalier & Irwin (2011) also predict the luminosity evolution for the SN after breakout as the blastwave continues to interact the region of dense mass-loss. Once the SN ejecta emerges from the edge of the dense wind region its luminosity will drop (e.g van Marle et al. 2010), and we can use the time when the observed bolometric luminosity falls below the predicted luminosity to estimate the outer radius of the dense shell and total mass contained within the CSM. For PS1-11vo, the bolometric luminosity observed in the second observing season is an order of magnitude lower than that predicted for continued interaction (see Figure 6.8). This allows us to infer a radius and mass for the dense wind region in this physical model of 2×10^{15} cm $< \mathrm{R}_w < 6 \times 10^{15}$ cm, and 8 $\mathrm{M}_\odot < \mathrm{M}_w <$ 20 $\mathrm{M}_\odot$ (Equation A7, Margutti et al. 2014b).

6.4.2 PS1-11kj

PS1-11kj is another luminous SN. It reached a similar peak luminosity to PS1-11vo, but displayed a slower post-maximum decline. Approximately 1 year post-explosion the luminosity of PS1-11kj was an order of magnitude higher than PS1-11vo at similar epochs (see Figure 6.8). Using the models Chevalier & Irwin (2011), in the same manner as above, we find an ejecta mass of $\sim 5\ (\frac{\mathrm{E}}{10^{51}\mathrm{erg}})$ $\mathrm{M}_\odot$ and a pre-SN mass-loss rate of $\sim$0.2 $(\frac{v_w}{150\mathrm{kms}^{-1}})^{-1}$ $\mathrm{M}_\odot$ yr^{-1}.

While these values are less extreme than those derived for PS1-11vo, unlike the case above, we find that the late-time bolometric luminosity is consistent with the prediction from Chevalier & Irwin (2011) for continued interaction (see Figure 6.8). This allows us to put lower limits on the radius and CSM mass contained within the dense shell of $\sim 3.5\times10^{16}$ cm and $\sim$9 $\mathrm{M}_\odot$, respectively. In this case, our constraint on the breakout radius is weaker than for PS1-11vo, as our photometric coverage on the rise is sparse. However, the late-time luminosity predicted by Chevalier & Irwin (2011) is a function primarily of $\mathrm{E}_{\mathrm{rad,r}}$ and $\mathrm{t}_{\mathrm{rise}}$, so this uncertainty does not affect the conclusion that the slow photometric evolution observed for PS1-11kj is consistent with continued interaction. If R_{bo} is smaller than 1.5×10^{15}cm, the main effect would be to increase the derived mass-loss rate and ejecta mass.

6.4.3 PS1-12dm

PS1-12dm is a Type IIn SN with a peak magnitude of ∼−18.5 mag. It was very blue at early times ($T_{BB} > 15,000$ K), showed rapid cooling, and declined linearly by ∼2.5 mag over 100 days. We have deep pre-explosion limits which constrain its rise time to be $\lesssim$8 days. For this event, the breakout models of (Chevalier & Irwin 2011) yield a pre-explosion mass-loss rate of $\sim 3.5\times10^{-2}\ (\frac{v_w}{150\mathrm{kms}^{-1}})^{-1}\ M_\odot\ \mathrm{yr}^{-1}$. As shown in the right panel of Figure 6.8 the bolometric light curve follows the prediction for continued interaction until ∼65 days post-explosion. This timescale implies a radius for the dense material of $\sim4\times10^{15}$ cm and a total CSM mass of ∼0.33 $M_\odot$.

6.4.4 Ongoing and Future Work

These preliminary models highlight the diverse range of CSM parameters which can inferred from PS1-MDS Type IIn SN, and the extreme nature of the inferred mass-loss regions surrounding luminous interacting transients. The values we find above are broadly consistent with other models for luminous transients based primarily on interaction (e.g. Chatzopoulos et al. 2013; van Marle et al. 2010; Chevalier & Irwin 2011). Full characterization of the explosion properties and CSM densities at a range of physical scales will require inclusion of other input power sources (^{56}Ni decay, magnetar spin-down), density profiles, and constraints from temperature evolution and multi-wavelength observations. This analysis is ongoing and will be presented in future publications. The PS1-MDS sample represents a significant increase in the number of luminous interacting SN for which multi-band light curves are available, facilitating this modeling process.

A particular research direction offered by this sample is late-time follow-up at radio wavelengths. Radio synchrotron emission is produced when the SN shock interacts with the surrounding medium. This emission is heavily absorbed at early times (due to synchrotron self-absorption and free-free absorption) but eventually enters the optically thin phase and brightens. Both the radio luminosity and the time of peak brightness at a given frequency are proportional to CSM density (Chevalier & Fransson 2006). As a result, luminous Type IIn SN—with their high inferred mass-loss rates—are predicted to be bright radio sources on a timescale of *years.*

As demonstrated by the preliminary models presented above, optical emission in the first year post-explosion probes the progenitor environment on physical scales of $\sim 10^{16}$ cm (corresponding to mass ejected in the final decade prior to explosion). In contrast, late-time ($\sim 2-5$ years) radio observations can probe the density profile on scales that are ten times larger, and hence reach back centuries in the mass loss history of the progenitors. Coupled with inferences from the optical data, this information will give us further leverage to distinguish between CSM geometries predicted by various mass-loss mechanisms such as a steady dust- driven wind, pulsational pair instability (which leads to multiple dense shells; Woosley et al. 2007), and unsteady late nuclear burning (which operates only in the final decade before collapse; Smith & Arnett 2014). We are currently undertaking a late-time radio survey of the luminous Type IIn SN discovered by the PS1-MDS.

6.5 PS1-MDS Sample: Summary

In this section, we have presented the identification and basic observed properties of the sample of interacting transients discovered by the PS1-MDS. These events represent an unbiased sample of interacting transients in that they were selected from a single, untargeted, transient survey. The sample spans a wide range of redshift, peak luminosity, and timescale. It is notable in including 13 events with peak luminosity's above 3×10^{43} erg s^{-1} (10 events above $5-6 \times 10^{43}$ erg s^{-1}). This represents a significant increase in the number of luminous type IIn SN with multi-band light curves available.

Using this sample, supplemented by events from the literature, in the following Chapters of this thesis we investigate the global host galaxy properties and sub-galactic environments of luminous interacting transients in comparison to standard luminosity Type IIn SN, and other classes of luminous transients.

Acknowledgments

The Pan-STARRS1 Surveys (PS1) have been made possible through contributions of the Institute for Astronomy, the University of Hawaii, the Pan-STARRS Project Office, the Max-Planck Society and its participating institutes, the Max Planck Institute for Astronomy, Heidelberg and the Max Planck Institute for Extraterrestrial Physics, Garching, The Johns Hopkins University, Durham University, the University of Edinburgh, Queen's University Belfast, the Harvard-Smithsonian Center for Astrophysics, the Las Cumbres Observatory Global Telescope Network Incorporated, the National Central University of Taiwan, the Space Telescope Science Institute, the National

Aeronautics and Space Administration under Grant No. NNX08AR22G issued through the Planetary Science Division of the NASA Science Mission Directorate, the National Science Foundation under Grant No. AST-1238877, the University of Maryland, and Eotvos Lorand University (ELTE). This work includes data gathered with the 6.5 m Magellan Telescopes located at Las Campanas Observatory, Chile. Some observations reported here were obtained at the MMT observatory, a joint facility of the Smithsonian Institution and the University of Arizona. This work is based on observations obtained at the Gemini Observatory, which is operated by the Association of Universities for Research in Astronomy, Inc., under a cooperative agreement with the NSF on behalf of the Gemini partnership: the National Science Foundation (United States), the National Research Council (Canada), CONICYT (Chile), the Australian Research Council (Australia), Ministerio da Ciencia, Tecnologia e Inovacao (Brazil) and Ministerio de Ciencia, Tecnologia e Innovacion Productiva (Argentina).

Chapter 7

Luminous Interacting Transients III: Global Host Galaxy Properties

M. R. Drout, E. Berger and the Pan-STARRS1-MDS Transient Group

In Preparation

Abstract

Using the PS1-MDS sample, supplemented with events from the literature, we present an analysis of the global host galaxy properties of 61 interacting transients, 37 of which are classified as luminous. The host galaxies of luminous interacting transients span a wide range in luminosity, mass and metallicity, with median values of $\langle \mathrm{M_B} \rangle = -18.5$ mag, $\langle \mathrm{M_{gal}} \rangle = 10^9$ $\mathrm{M_\odot}$, and $\langle 12 + \mathrm{Log(O/H)_{N2}} \rangle = 8.54$. We do not find any statistically distinguishable trends between the host galaxies of luminous interacting SN and the hosts of "standard luminosity" Type IIn SN. However, the host galaxies of luminous interacting transients are robustly distinguished from those of hydrogen-poor super-luminous SN (SLSN-I), in being more luminous, massive, and metal-rich. While a fraction of luminous interacting transients SN do explode in dwarf galaxies with sub-solar metallicities, the physical conditions present in these galaxies are not required to produce all luminous and interacting transients.

7.1 Introduction

Studies of host galaxy environments can provide important clues to the nature of the progenitors of various classes of transients. Early investigations of the host galaxies of luminous SN where primarily based on limited archival photometric data and included members of both the SLSN-I and SLSN-II spectroscopic classes. These concluded that luminous SN occur preferentially in dwarf galaxies (Neill et al. 2011; Stoll et al. 2011)—although the host of the "prototypical" luminous Type IIn SN 2006gy always served as a stark counter-example, as it exploded in the nuclear region of an S0 galaxy

(Smith et al. 2007). Since that time Lunnan et al. (2014) and Leloudas et al. (2015a) have presented detailed studies of the host galaxies of a large number of SLSN-I, demonstrating that they explode almost exclusively in dwarf galaxies with high specific star formation rates and low-metallicities. Similar trends have also been observed for the host galaxies of long-duration gamma-ray bursts (LGRBs) (e.g. Savaglio et al. 2009; Levesque et al. 2010). This strong environmental selection is thought to provide critical information about their progenitors, although it is debated whether the dominant ingredient is metallicity (Stanek et al. 2006; Lunnan et al. 2014), stellar mass (Leloudas et al. 2015a), or some other byproduct of star formation in these extreme environments (e.g. close binary interactions within dense star clusters; van den Heuvel & Portegies Zwart 2013).

In contrast to this recent comprehensive work on SLSN-I and LGRBs, studies of the host galaxies of luminous interacting SN remain limited. There exist individual examples of SLSN-II hosts that differ from those of SLSN-I/LGRBs (e.g. SN 2006gy) but a general preference for dwarf galaxies and/or low metallicities is often still cited (e.g. Neill et al. 2011; Stoll et al. 2011; Chatzopoulos et al. 2011; Gal-Yam 2012; Benetti et al. 2014). The most detailed study to date is by Leloudas et al. (2015a), who presented optical spectra for the host galaxies of six members of this class along side a larger sample of 17 SLSN-I. Based on these six events, they propose that hosts of SLSN-II have softer radiation fields and higher metallicities than those of of SLSN-I, but lower metallicities than standard luminosity Type IIn SN (Taddia et al. 2015). However, greater statistical significance is needed to test these hypotheses, and no large study of the global host galaxy properties of luminous interacting transients has yet been reported.

In this chapter, we present preliminary results from a statistical analysis of the global host galaxy properties (luminosity, mass, metallicity) of a large sample of luminous interacting transients. We aim to address whether their global properties are significantly distinct from (a) galaxies that host standard luminosity Type IIn SN and (b) galaxies that host other classes of energetic transients (SLSN-I and LGRBs).

The full sample of both luminous and standard luminosity interacting transients considered is described in section 7.2. Throughout this chapter, we will compare the empirical distribution functions found for our samples of interacting transients, as well as other classes of SN, using the Kolmogorov-Smirnov (KS) goodness-of-fit test. The main comparison samples considered are the SLSN-I sample from Lunnan et al. (2014), the LGRB sample from (Svensson et al. 2010) and the core-collapse SN (CCSN) sample from the GOODS survey (Fruchter et al. 2006; Svensson et al. 2010).

7.2 Sample Selection

In order to assess the global properties of the galaxies that host luminous interacting transients we have compiled a sample of 61 Type IIn SN, 37 of which are considered luminous by the definition outlined in Chapter 5. These transients are derived from three main sources:

1. The 25 Type IIn SN discovered in the PS1-MDS and described in detail in Chapter 6.
2. The 19 Type IIn SN discovered by the Palomar Transient Factory (PTF; Law et al. 2009) and presented in Ofek et al. (2014a). These Type IIn SN are complementary to the PS1-MDS sample in having well-constrained peak luminosities (albeit based

on single-band observations) which span the full range of 10^{42} erg $s^{-1} < L_p < 10^{44}$ erg s^{-1}. They were also identified by an untargeted survey, avoiding bias in host galaxy properties. The redshift range of the luminous events discovered by the PTF is similar to that of the PS1-MDS ($0.1 < z < 0.4$), though their standard luminosity Type IIn SN are identified mainly at lower redshift ($z < 0.1$).

3. 17 additional luminous interacting transients which are described in the literature. These events were discovered primarily by PTF, the Catalina Real-Time Transient Survey (CRTS Drake et al. 2009), the Robotic Optical Transient Search Experiment (ROTSE; Akerlof et al. 2003) and The PanSTARRS Survey for Transients (PSST; Huber et al. 2015b).

Basic properties for the full sample of interacting transient considered in this section are listed in Table 7.1. At this time we do not explicitly consider the host galaxies of luminous interacting transients which have been classified as Type IIn/Ia-CSM. These events are considered in our analysis of the sub-galactic environments of luminous interacting transients in Chapter 7, and their global host galaxy properties will be assessed in future work.

7.3 Observations and Data Reduction

7.3.1 Host Galaxy Optical Photometry

For objects discovered in the PS1-MDS, we possess deep images of their host environments in $grizy_{\mathrm{P1}}$ that were made by stacking pre-explosion survey images. The construction of these PS1-MDS "deep stacks" has been previously discussed in detail by Rest et al. (2014). On average, ∼30−80 high-quality nightly stacks are combined, weighted by the product of the inverse variance and the inverse area of the PSF. The typical depth achieved in the templates is ∼25.0 mag in $griz_{\rm PS1}$. All the host galaxies for all but one of the PS1-MDS Type IIn sample are detected in these template images. The observed apparent r-band magnitudes span a wide range (14 mag $< \rm m_r <$ 25 mag). In several cases, the PS1-MDS host galaxies are also detected in the Sloan Digital Sky Survey (SDSS), and we supplement the PS1 photometry with DR10 model magnitudes (Ahn et al. 2012). Images of the host environments of all 25 PS1-MDS interacting transients are shown in Figure 7.1. The location of the transient is marked with a red cross.

For the PTF Type IIn SN from Ofek et al. (2014a) and other literature events in our sample we compile multi-band host galaxy photometry from the SDSS and the PS1 3π survey, when possible. The PS1 3π survey provides templates covering most of the sky above Dec = −30 deg, and we use stacks constructed from pre-explosion images. In two cases (CSS201015, SMTJ0125) we have obtained additional imaging using IMACS and LDSS3 on the Magellan 6.5m telescopes. In these instances, all images were bias and flat-field corrected, trimmed, and stacked using standard tasks in IRAF. Aperture photometry was performed and image zero-points were determined from observations of standard star fields taken on the same night.

Finally, for a number of luminous Type IIn host galaxies, we do not carry out an independent analysis, but compile photometric measurements and host galaxy properties (masses, metallicities, etc.) quoted in the literature. These instances are clearly outlined in the sections below.

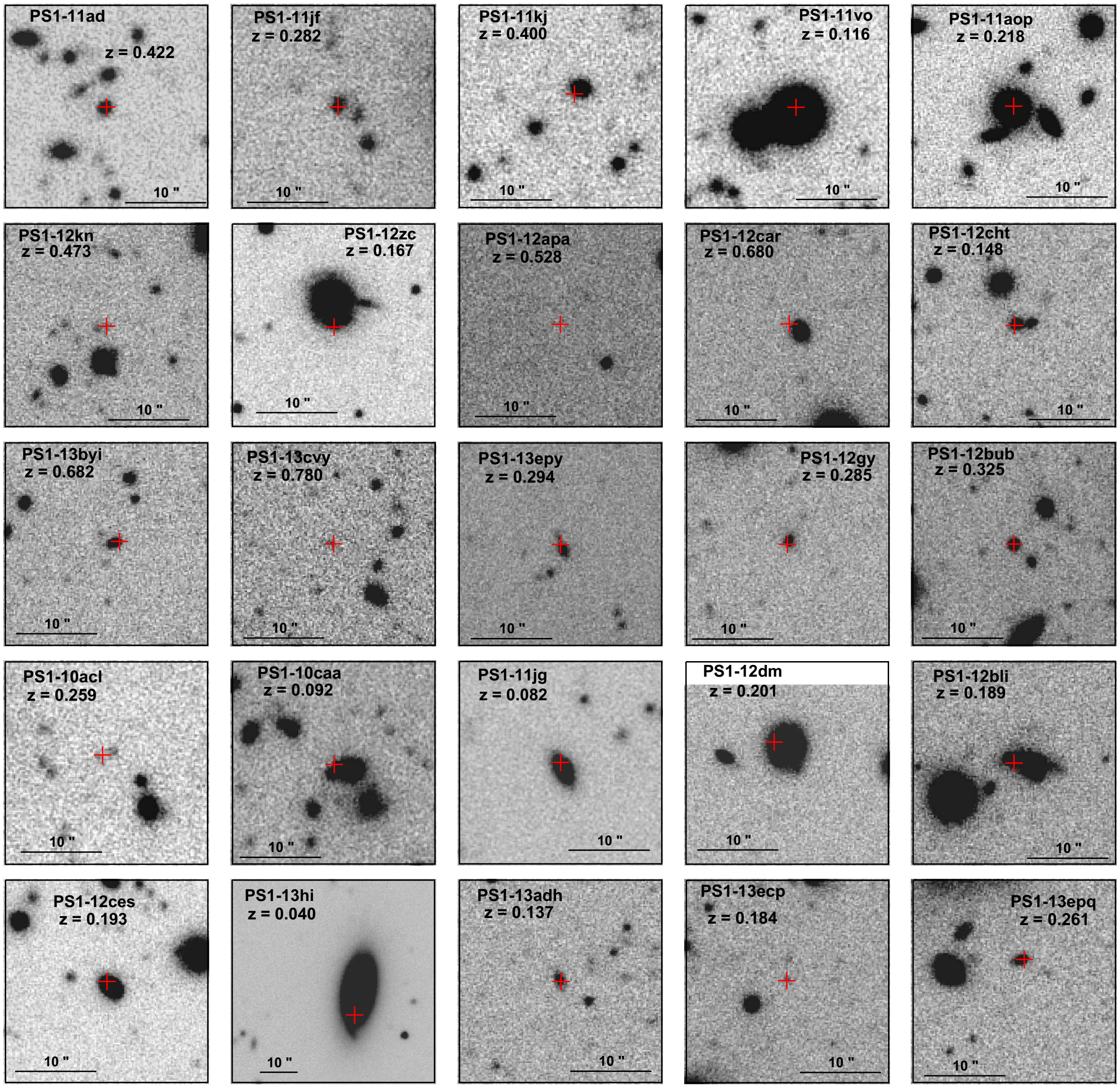

Figure 7.1.—: Host galaxy explosion environments for all PS1-MDS Type IIn SN. Images are from i_{P1}-band PS1 templates. Transient explosion sites are marked with red crosses. *Rows 1-3:* Host galaxies of transients classified as luminous. Row three also includes host environments of PS1-12gy and PS1-12bub. These two transients peaked between PS1-MDS observing seasons, and we cannot constrain whether they pass our definition for "luminous" transients outlined in Chapter 5. We analyze their host properties here, but they are not included in our statistical analysis. *Rows 5-6:* Host galaxies for Type IIn SN not classified as luminous.

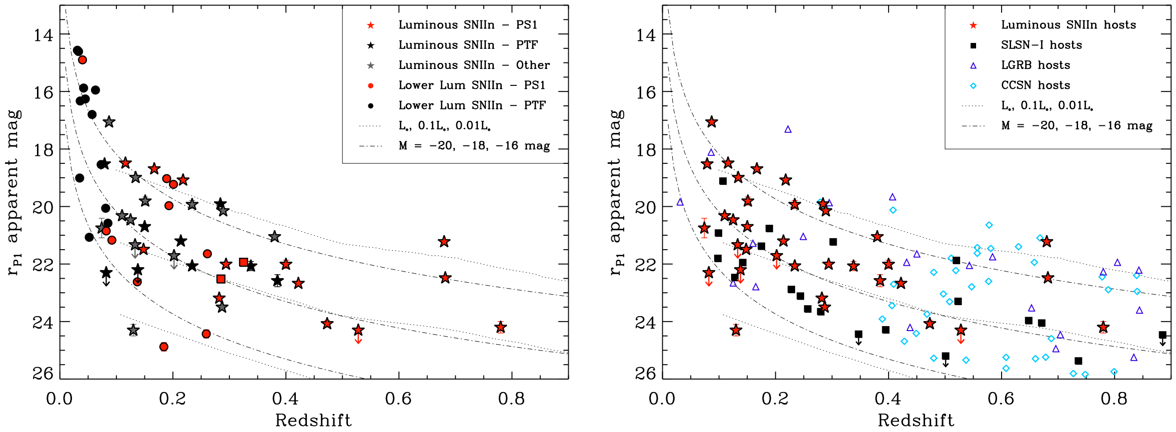

Figure 7.2.—: Apparent Magnitudes. *Left:* Host galaxies for the interacting transients considered in this section. Host galaxies of transients discovered by the PS1-MDS, PTF and other surveys are shown in red, black and grey, respectively. Host galaxies of luminous Type IIn SN are plotted as stars, while those of lower luminosity Type IIn SN are plotted as circles. Dashed-dotted lines show constant absolute magnitudes of −16, −18, and −20 mag, while dotted lines represent tracks of L_*, $0.1L_*$, and $0.01L_*$. *Right:* Same as left, but showing the host galaxies of all luminous interacting transients (red stars) in comparison to the hosts of SLSN-I (black squares; Lunnan et al. 2014), CCSN (cyan diamonds; Svensson et al. 2010) and LGRBs (blue triangles; Svensson et al. 2010).

In the left panel of Figure 7.2, we plot the apparent magnitudes for the Type IIn host galaxies considered in this chapter as a function of redshift. These values are listed in Table 7.1. In the right panel of Figure 7.2 we plot the host galaxies of the 37 luminous interacting transients (red stars) in comparison to the SLSN-I host galaxy sample of Lunnan et al. (2014, black squares), the LGRB sample of Svensson et al. (2010, blue triangles) and the GOODs CCSN sample Svensson et al. (2010, cyan diamonds).

Table 7.1. Sample and Host Properties

Event	Redshift	E(B−V)$_{\rm MW}$ (mag)	$L_{\rm p,SN}$[a] (erg s^{-1})	Disc. Survey	Reference	$m_{\rm obs}(err)$[b] (mag)	M_B (mag)	log(M_*) ($M_\odot$)	12+log(O/H) (PP04N2)
"Luminous" SNIIn									
PS11vo	0.116	0.0081	5.02e+43	PS1	···	18.49 (0.01)	-19.4	$9.72^{+0.34}_{-0.22}$	8.64
PS11kj	0.400	0.074	5.15e+43	PS1	···	22.01 (0.14)	-19.1	$9.31^{+0.67}_{-0.34}$	
PS11aop	0.218	0.0347	5.42e+43	PS1	···	19.08 (0.01)	-20.3	$10.37^{+0.24}_{-0.28}$	8.63
PS12zc	0.167	0.0208	>5.33e+43	PS1	···	18.69 (0.02)	-20.1	$9.89^{+0.56}_{-0.14}$	8.68
PS11ad	0.422	0.0060	6.21e+43	PS1	···	22.67 (0.027)	-18.6	$9.07^{+0.21}_{-0.11}$	
PS11jf[h]	0.282	0.0122	>2.52e+43	PS1	···	23.18 (0.039)	-17.0	$8.22^{+0.10}_{-0.09}$	
PS12kn	0.473	0.0100	5.09e+43	PS1	···	24.07 (0.12)	-17.5	$8.33^{+0.69}_{-0.22}$	
PS12car	0.680	0.0204	7.50e+43	PS1	···	21.22 (0.03)	-21.7	$10.48^{+0.56}_{-0.11}$	
PS12cht	0.148	0.0067	3.71e+43	PS1	···	21.49 (0.05)	-17.0	$8.67^{+0.04}_{-0.18}$	8.25
PS13byi	0.682	0.0662	7.32e+43	PS1	···	22.48 (0.04)	-20.4	$9.40^{+0.24}_{-0.12}$	
PS13epy	0.294	0.0316	3.09e+43	PS1	···	22.00 (0.04)	-18.2	$9.26^{+0.08}_{-0.19}$	8.55
PS13cvy	0.780	0.0211	6.38e+43	PS1	···	24.2 (0.2)	-18.7	$9.04^{+2.93}_{-1.34}$	
PS12apa	0.528	0.0069	6.02e+43	PS1	···	>24.3	>-17.9	<9.30	
PS15ces	0.134	0.0123	≈3.1d+43	PSST	[18]	18.92 (0.02)	-19.2	$9.46^{+0.04}_{-0.18}$	
PS15blq	0.125	0.0156	6.5d+43	PSST	[17]	20.46 (0.03)	-17.8	$8.68^{+0.16}_{-0.23}$	
PTF10heh	0.340	0.0237	≈6.6d+43	PTF	[13]	22.07 (0.16)	-18.00	$8.36^{+0.18}_{-0.17}$[e]	8.33[e]
PTF10oug	0.150	0.042	3.3d+43	PTF	[1]	20.7 (0.05)	-18.0	$9.06^{+0.04}_{-0.08}$	
PTF10qaf	0.284	0.074	1.7d+44	PTF	[1]	19.91 (0.02)	-21.3	$10.24^{+0.22}_{-0.17}$[e]	8.74[e]

Table 7.1—Continued

Event	Redshift	$E(B-V)_{MW}$ (mag)	$L_{p,SN}$[a] (erg s^{-1})	Disc. Survey	Reference	$m_{obs}(err)$[b] (mag)	M_B (mag)	$\log(M_*)$ ($M_\odot$)	12+log(O/H) (PP04N2)
PTF10yyc	0.214	0.046	5.1d+43	PTF	[1]	21.2 (0.06)	-18.4	$9.27^{+0.13}_{-0.22}$	
PTF10weh	0.138	0.032	5.8d+43	PTF	[1]	>22.2	> -16.0[i]	<7.76[j]	
PTF11dsf	0.385	0.0092	≈2.2d+44	PTF	[14]	22.58 (0.21)	-18.6	$8.97^{+0.11}_{-0.11}$[e]	8.18[e]
PTF11fzz	0.082	0.082	3.3d+43	PTF	[1]	> 22.3	> -15.2[i]	<7.44[j]	
PTF12efc[h]	0.234	0.012	6.8d+43	PTF	[1]	22.06 (0.01)	-17.3[i]	$8.47^{+0.51}_{-0.38}$[j]	
PTF12glz	0.079	0.131	3.3d+43	PTF	[1]	18.52 (0.02)	-18.7	$9.63^{+0.03}_{-0.04}$	
SN1999bd	0.151	0.0267	≈1.1e+44	SCP	[10]	19.81 (0.14)[g]	-18.99	$9.52^{+0.26}_{-0.24}$[e]	8.62[e]
SN2003ma	0.290	0.306	7.00e+43	SuperMACHO	[9]	20.15 (0.02)[d]	-19.9[f]	$9.73^{+0.42}_{-0.21}$[j]	8.45[d]
SN2006gy	0.020	0.136	1.70e+44	ROTSE	[8]	12.08 (0.01)[g]	-20.3[f]	···	
SN2006tf	0.070	0.027	6.30e+43	ROTSE	[7]	20.75 (0.34)[g]	-16.72	$7.70^{+0.04}_{-0.04}$[e]	8.27[e]
SN2008am	0.234	0.025	3.00e+44	ROTSE	[6]	19.93 (0.14)[g]	-20.12	$9.13^{+.19}_{-.14}$[e]	8.35[e]
SN2008es	0.210	0.012	2.1d+44	ROTSE	[5]	> 21.71[g]	>-17.1[f]	< 8.2[j]	
SN2008fz	0.130	0.136	1.9d+44	CRTS	[4]	> 21.33[g]	>-16.7[f]	< 8.0[j]	
SN2010jl	0.010	0.0234	3.80e+43	POSS	[11,12]	···	-19.3[f]	···	8.25[f]
SN2011cp	0.38	0.0478	9.90e+43	CRTS	[15]	21.05 (0.05)	-19.9	$10.16^{+0.67}_{-0.15}$	
SN2011eu	0.11	0.0458	5.70e+43	CRTS	[16]	20.32 (0.05)	-17.6	$9.13^{+0.38}_{-0.48}$	8.54
CSS121015	0.287	0.0748	3.1d+44	CRTS	[3]	23.5 (0.01)	-17.6[i]	$8.59^{+0.46}_{-0.49}$[j]	
SMTJ0125	0.130	0.0216	≈6.d+43	SMT	[2]	24.3 (0.2)	-14.5[i]	$7.16^{+0.29}_{-0.51}$[j]	
LSQ15abl	0.087	0.0372	5.5d+43	LSQ	[19]	17.06 (0.01)	-20.5	$9.82^{+0.13}_{-0.10}$	8.59

Table 7.1—Continued

Event	Redshift	$E(B-V)_{MW}$ (mag)	$L_{p,SN}$[a] (erg s^{-1})	Disc. Survey	Reference	$m_{obs}(err)$[b] (mag)	M_B (mag)	$\log(M_*)$ ($M_\odot$)	12+log(O/H) (PP04N2)
"Standard Luminosity" SNIIn									
PS10caa	0.092	0.0153	9.40e+41	PS1	···	21.17 (0.08)	-16.5	$8.05^{+0.28}_{-0.61}$	7.90
PS12bli	0.189	0.0486	1.34e+43	PS1	···	19.03 (0.02)	-20.1	$10.15^{+0.29}_{-0.30}$	8.57
PS12ces	0.193	0.0220	9.24e+42	PS1	···	19.97 (0.03)	-19.3	$9.29^{+0.54}_{-0.28}$	8.56
PS13hi	0.040	0.0134	>2.55e+42	PS1	···	14.90 (0.01)	-20.1	$10.71^{+0.43}_{-0.26}$	
PS11jg	0.082	0.0151	>3.13e+41	PS1	···	20.85 (0.06)	-16.4	$8.22^{+0.23}_{-0.28}$	8.30
PS12dm	0.201	0.0052	1.35e+43	PS1	···	19.23 (0.02)	-19.8	$10.33^{+0.37}_{-0.17}$	8.72
PS10acl	0.259	0.0324	1.24e+43	PS1	···	24.43 (0.14)	-15.9	$7.69^{+0.18}_{-0.18}$	
PS13ecp	0.184	0.0252	1.30e+43	PS1	···	24.87 (0.15)	-14.5	$7.17^{+0.19}_{-0.72}$	
PS13epq	0.261	0.0052	1.22e+43	PS1	···	21.64 (0.03)	-18.3	$8.94^{+0.07}_{-0.10}$	8.25
PS13adh	0.137	0.0118	1.05e+43	PS1	···	22.62 (0.04)	-15.57	$8.30^{+0.57}_{-0.62}$	
PS12bub[c]	0.325	0.0210	>1.42e+43	PS1	···	21.94 (0.04)	-18.7	$9.20^{+0.20}_{-0.58}$	8.47
PS12gy[c]	0.285	0.0122	>1.22e+43	PS1	···	22.52 (0.06)	-17.8	$8.32^{+0.10}_{-0.09}$	
PTF10vag	0.052	0.111	7.2d+42	PTF	[1]	21.07 (0.08)	-15.6	$7.13^{+0.74}_{-0.25}$	
PTF10achk	0.033	0.063	5.3d+42	PTF	[1]	14.61 (0.01)	-19.9	$11.01^{+0.11}_{-0.28}$	
PTF10tel	0.035	0.016	7.3d+42	PTF	[1]	19.01 (0.02)	-16.6	$8.14^{+0.15}_{-0.80}$	
PTF12ksy	0.031	0.043	5.2d+42	PTF	[1]	14.56 (0.01)	-20.2	$10.42^{+0.40}_{-0.79}$	
PTF10hbf	0.042	0.036	9.9d+41	PTF	[1]	15.88 (0.01)	-19.3	$10.35^{+0.28}_{-0.28}$	
PTF10cwx	0.073	0.025	7.2d+42	PTF	[1]	18.54 (0.01)	-18.5	$9.13^{+0.22}_{-0.28}$	

Table 7.1—Continued

Event	Redshift	E(B−V)$_{\mathrm{MW}}$ (mag)	L$_{\mathrm{p,SN}}$[a] (erg s^{-1})	Disc. Survey	Reference	m$_{\mathrm{obs}}$(err)[b] (mag)	M$_{\mathrm{B}}$ (mag)	log(M$_*$) (M$_\odot$)	12+log(O/H) (PP04N2)
PTF10gvf	0.081	0.011	1.0d+43	PTF	[1]	20.06 (0.05)	-17.1	$8.36^{+0.13}_{-0.18}$	
PTF10tyd	0.063	0.065	5.3d+42	PTF	[1]	15.95 (0.01)	-20.6	$10.32^{+0.45}_{-0.18}$	
PTF12cxj	0.036	0.011	2.6d+42	PTF	[1]	16.33 (0.01)	-18.8	$9.54^{+0.34}_{-0.22}$	
iPTF13agz	0.057	0.033	3.9d+42	PTF	[1]	16.80 (0.01)	-19.4	$9.93^{+0.45}_{-0.25}$	
PTF09drs	0.045	0.017	5.2d+42	PTF	[1]	16.26 (0.01)	-19.7	$9.47^{+0.24}_{-0.18}$	
PTF10cwl	0.085	0.022	9.1d+42	PTF	[1]	20.58 (0.08)	-16.7	$7.96^{+0.14}_{-0.18}$	

[a] Peak luminosity of the transient. PS1-MDS values are taken from Chapter 6 and most PTF discovered objects from Ofek et al. (2014a). Luminosities for other objects are taken from the literature. When only single band observations are available we convert to luminosity assuming zero bolometric correction. In several cases, literature luminous events have only a few photometric points publicly available in the ATELs, in which case the value we quote should be considered approximate (these are indicated with a ≈). This uncertainty in the true luminosity for some literature luminous events does not influence the results presented in this chapter.

[b] Observed magnitude of host galaxy, as plotted in Figure 7.2. For a majority of objects this is observed r−band photometry, with the following exceptions: PS1-13cvy is observed i-band. PTF12efc is observed i−band. SN2003ma is the SuperMACHO VR filter as described in Rest et al. (2011). SMTJ0125 is observed g-band.

[c] PS12bub and PS12gy peaked in between PS1 observing seasons and we do not constrain whether they qualify as luminous by our definition outlined in Chapter 5. We present their properties here, but do not include them in our statistical analysis.

[d] From Rest et al. (2011); [e] From Leloudas et al. (2015a); [f] From Stoll et al. (2011); [g] From Neill et al. (2011); [h] Possible Type IIn/Ia-CSM; [i] Calculated via a k-correction; [j] Calculated via a M/L ratio conversion.

Note. — *References:* [1] Ofek et al. (2014a); [2] Campbell et al. (2014); [3] Benetti et al. (2014); [4] Drake et al. (2010); [5] Gezari et al. (2009); [6] Chatzopoulos et al. (2011); [7] Smith et al. (2008); [8] Smith et al. (2007); [9] Rest et al. (2011); [10] Richards et al. (1999), [11] Stoll et al. (2011); [12] Fransson et al. (2014); [13] Quimby et al. (2010); [14] Quimby et al. (2011a); [15] Drake et al. (2011a); [16] Graham et al. (2011); [17] Huber et al. (2015a); [18] Foley et al. (2015); [19] Prajs et al. (2015) *Surveys:* SMT = Sky Mapper Transient and Supernova Survey (Scalzo et al. 2013); CRTS = Catalina Real-Time Transient Survey (Drake et al. 2009); PTF = Palomar Transient Factory (Law et al. 2009); PS1-MDS = PanSTARRS1 Medium Deep Survey (Kaiser et al. 2010); PSST = PanSTARRS Survey for Transients (Huber et al. 2015b); ROTSE = Robotic Optical Transient Search Experiment (Akerlof et al. 2003); SCP = Supernova Cosmology Project; POSS = Puckett Observatory Supernova Search (Newton & Puckett 2010); LSQ = La Silla Quest Survey (Hadjiyska et al. 2011); SuperMACHO = SuperMACHO Project microlensing survey

7.3.2 Host Galaxy Spectroscopy

We have obtained optical spectroscopy for the host galaxies of 19 of the PS1-MDS Type IIn SN, of which 15 are of sufficient quality for determination of the host galaxy metallicity (including the host galaxies of 7 luminous transients). We have also obtained spectra for 6 additional luminous Type IIn SN from the literature. These spectra were obtained primarily with Blue Channel and Hectospec on the 6.5m MMT telescope and IMACS and LDSS3 on the 6.5m Magellan telescopes. Initial reduction and extraction for all longslit spectra were performed using standard routines in IRAF. Flux calibration and telluric correction was performed using a set of custom IDL scripts and observations of spectrophotometric standards acquired on the same night as the science observations.

7.4 Host Galaxy Physical Properties

For events in our sample with multi-band photometry available, we have constructed preliminary galaxy models using the FAST stellar population synthesis code (Kriek et al. 2009). We use the Maraston (2005) stellar library and assume an exponential star formation history and Salpeter IMF. Extinction was allowed to vary freely and we have assumed $Z=Z_{\odot}$. When possible, both extinction and metallicity values will be constrained based on measurements from our spectroscopic sub-sample in future work.

7.4.1 Absolute Magnitudes

We use these synthetic galaxy models to calculate the absolute B-band magnitudes for the host galaxies in our sample. Models were shifted to the rest frame and synthetic

B-band photometry was performed. For galaxies where only upper limits or 1-2 photometric detections are available, we calculate an approximate $k-$correction from other galaxies in our sample at similar redshifts, which is then applied. These instances are indicated in Table 7.1. We supplement our measurements with the sample of $\mathrm{M_B}$ values for the host galaxies of luminous Type IIn SN listed in Stoll et al. (2011), also indicated in Table 7.1.

In Figure 7.3 we plot the resulting $\mathrm{M_B}$ values. The top-left panel displays $\mathrm{M_B}$ versus redshift for the 61 Type IIn SN we consider. The Type IIn host galaxies span a wide range in luminosity from -14 mag $< \mathrm{M_B} < -22$ mag. Notably, *both* the luminous and standard luminosity Type IIn host galaxies span this full range and have similar median values of $\langle \mathrm{M_B} \rangle \sim -18.6$ and $\langle \mathrm{M_B} \rangle \sim -18.5$, respectively ($\sim 0.1\mathrm{L_\odot}$; Willmer et al. 2006). Approximately $35-40\%$ of both the luminous and standard luminosity Type IIn SN samples explode in galaxies similar to or fainter than the LMC ($\mathrm{M_{B,LMC}} \sim -18$ mag; Stanek et al. 2006). In contrast, approximately 30% explode in galaxies brighter than $\mathrm{M_B}$ $= -20$ mag. In the bottom-left panel of Figure 7.3 we plot the cumulative distribution functions for the luminous and standard luminosity Type IIn SN (red and black, respectively) as well as several subsets of each sample. As KS-test between the luminous and standard luminosity Type IIn events yields a p-value of 0.28, indicating that we cannot exclude the null hypothesis that they are drawn from the same population.

However, subtle differences are observed between the samples identified by different surveys. In the PS1-MDS sample, the host galaxies of standard luminosity Type IIn SN are *fainter* on average than the host galaxies of luminous Type IIn SN. The host galaxies of the standard luminosity Type IIn SN discovered by PTF span a similar range in $\mathrm{M_B}$, but a higher fraction are observed with $\mathrm{M_B} < -18.5$ mag. We examine this further in

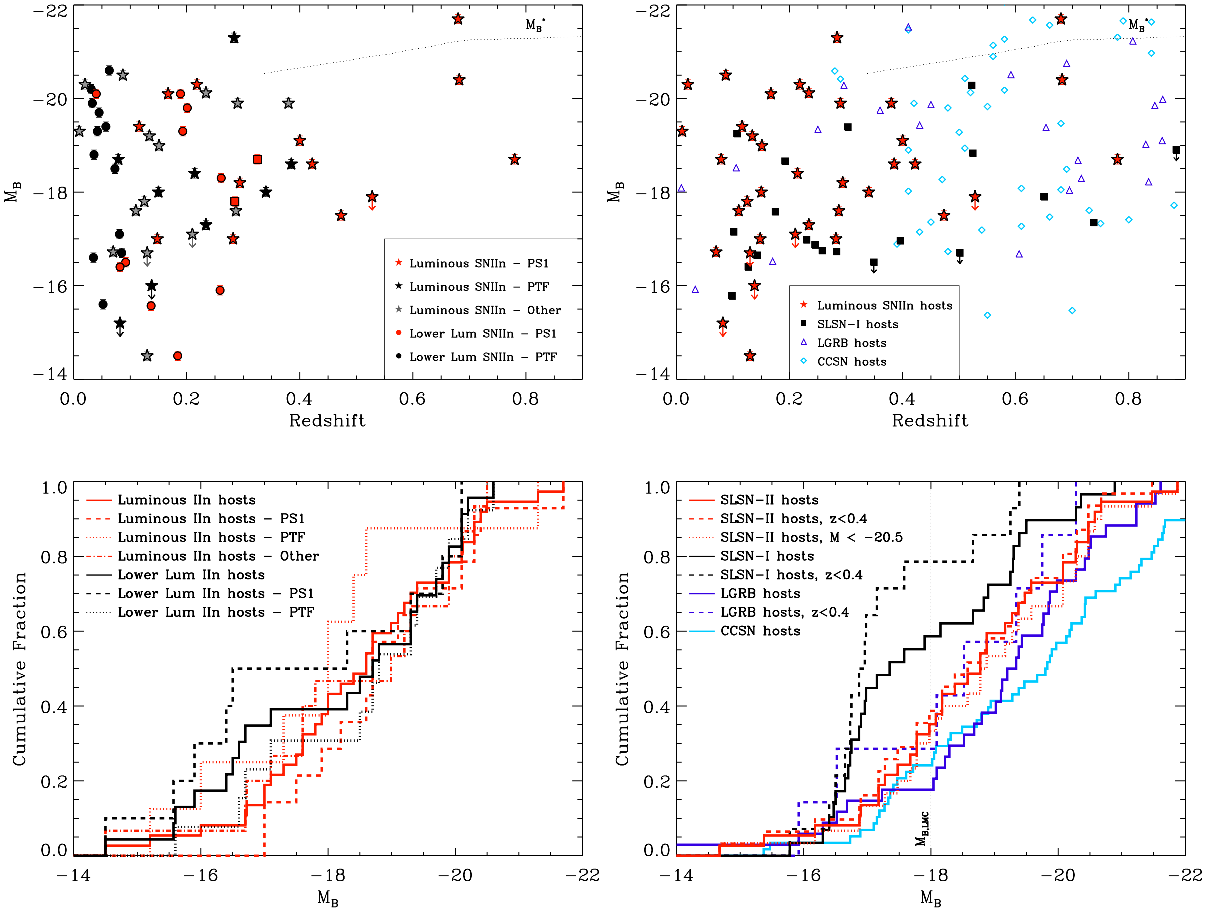

Figure 7.3.—: Absolute Magnitudes. Symbols and colors have the same meaning as in Figure 7.2. *Top Left:* Galaxy M$_B$ versus redshift for the full sample of interacting transients considered in this section. The host galaxies of both luminous and standard luminosity Type IIn SN span a wide range of luminosities (-14 mag $>$ M$_B$ $>$ -22 mag), and have similar median values $\langle M_B \rangle \approx -18.5$ mag. *Lower Left:* Cumulative Distributions for various subsets of events shown in the top left panel. While subtle differences are observed between samples of different surveys, the distributions of luminous and standard luminosity Type IIn host galaxies are not statistically distinguishable. *Top right:* Comparison of the host galaxies of luminous Type IIn SN to SLSN-I, LGRBs, and CCSN. *Lower right:* Cumulative distributions of samples shown in the top right panel. Luminous Type IIn SN explode in galaxies that are significantly more luminous than SLSN-I, a trend which is accentuated when the sample is restricted to events at z<0.4.

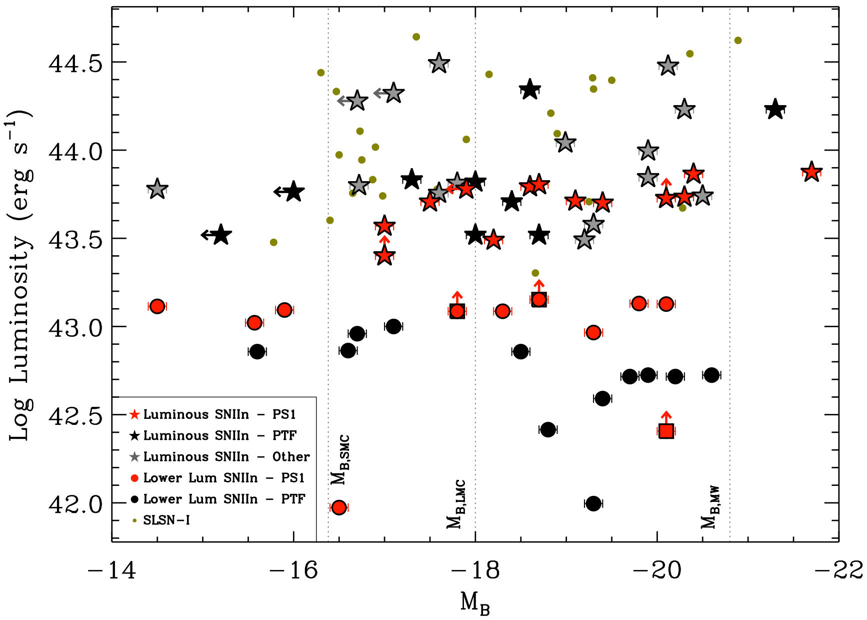

Figure 7.4.—: Host Galaxy M_B versus transient peak luminosity for Type IIn SN. Symbols and colors have the same meaning as in Figure 7.2. Also shown are a set of SLSN-I (gold circles). M_B values for the SLSN-I are from Lunnan et al. (2014) and transient luminosities from Lunnan et al. (2015a) and Nicholl et al. (2015). Vertical dotted lines mark the M_B values of the SMC, LMC, and Milky Way, for reference. A shift to lower galaxy magnitudes at the highest transient luminosities for Type IIn SN is not observed, although there is an apparent dearth of Type IIn SN with peak magnitudes below $\sim 6\times10^{42}$ erg s^{-1} which explode in dwarf galaxies. Our conclusion that the host galaxies of luminous interacting transients are statistically distinct from those of SLSN-I is not dependent on our adopted luminosity cutoff.

Figure 7.4 where we plot host galaxy M_B versus the *transient* peak luminosity. Based on this plot, it is *possible* that the difference between between the PS1 and PTF samples is partially driven by SN properties. The PS1 sample of "non-luminous" Type IIn SN is dominated by events with peak luminosities of $\sim 10^{43}$ erg s^{-1}, which uniformly span the full range of galaxy M_B. However, the Type IIn SN with peak luminosities below $\sim 6\ \times 10^{42}$ (which is dominated by PTF objects) explode almost exclusively in galaxies brighter than −18.5 mag. However, we note that redshift effects, sample selection, and/or small number statistics may also contribute to this observed trend.

In addition, all but one of the PTF-discovered luminous Type IIn SN occur in host galaxies fainter than −18.5 mag, while fully 50% of the luminous Type IIn SN identified both in the PS1-MDS and other surveys explode in more luminous galaxies. The redshift range in which luminous Type IIn SN are discovered is similar for all surveys considered here, and these differences may therefore reflect different survey follow-up and reporting strategies. A K−S test between the host galaxies of luminous Type IIn SN discovered by the PS1-MDS and those discovered by surveys other than PTF yields a p-value of 0.8, indicating that they are highly consistent.

In the right-hand panels of Figure 7.3, we compare the M_B values found for the hosts galaxies of luminous Type IIn SN (red) versus the host galaxies of the SLSN-I (black), LGRB (blue) and CCSN (cyan) samples described above. These are plotted versus redshift (top panel) and as cumulative distributions (bottom panel).

The host galaxies of luminous interacting transients are both more luminous and *statistically distinct* from the host galaxies of hydrogen-poor super-luminous SN ($p = 0.03$). This difference becomes even more pronounced if we consider the low redshift populations. The median M_B values for the host galaxies of luminous Type IIn SN and SLSN-I at $z<0.4$ are $\langle M_B \rangle = -18.57$ mag and $\langle M_B \rangle = -16.87$ mag, respectively. A KS-test between their distributions yields a p-value of 3×10^{-3}.

Critically, this difference is *not* driven by the luminosity cutoff we choose when defining a "luminous" interacting transient. This is demonstrated both in Figure 7.3 where we also plot a cumulative distribution for luminous transients whose peak magnitudes exceed −20.5 mag (the same range found for SLSN-I), and in Figure 7.4 where we plot host galaxy M_B versus the transient peak luminosity. Above $L_p = 10^{43}$ erg s^{-1}, no correlation with transient luminosity is found.

The host galaxies of luminous interacting transients are fainter on average than the hosts of both the LGRB and CCSN samples. This difference is marginally statistically significant in the case of the CCSN hosts ($p = 0.07$) but not versus the LGRB hosts ($p = 0.35$). However, we note that the redshift range probed by these samples is different. A majority of the GOODS sample is found at $z>0.4$, while a majority of luminous Type IIn SN are found at $z<0.4$ (and M_B^* evolves by ~ 1 mag between $z=0.3$ and $z=1.0$; Willmer et al. 2006). In Figure 7.3 we also plot the cumulative distribution of 7 LGRB host galaxies at $z<0.4$, which are fainter on average than the GOODS sample.

7.4.2 Masses

We next consider the total stellar mass contained within the interacting transient host galaxies. The FAST stellar populations synthesis code provides the mass of the best fit model, as well as 1σ confidence intervals derived from Monte Carlo simulations, which take uncertainties in both the models and measured fluxes into account (Brammer et al. 2008). We supplement our mass measurements with those of six luminous IIn SN given in Leloudas et al. (2015a). In addition, in order to avoid skewing our distribution to galaxies of higher mass, we use our models to calculate a median mass-to-light ratio as a function of M_B. This mass-to-light ratio is then applied to single-band photometric measurements for galaxies with too few detections for us to construct a synthetic galaxy model, in order to derive an estimate (or upper limit) for the galaxy mass. In these cases, uncertainties are taken as the range of observed mass-to-light ratios. We list our galaxy masses in Table 7.1, and explicitly state whether the value is derived from an SED model fit, estimated from a mass-to-light ratio conversion, or taken from the literature.

In the left hand panels of of Figure 7.5 we plot the resulting masses for the full sample of Type IIn SN. The host galaxies of luminous and standard luminosity Type IIn SN both span $\sim$4 orders of magnitude (10^7 $M_\odot$ < M_{gal} < 10^{11} $M_\odot$), and have similar median values of $\langle M_{gal} \rangle \sim 1 \times 10^9$ $M_\odot$ and $\langle M_{gal} \rangle \sim 2 \times 10^9$ $M_\odot$, respectively. As above, the distributions of host galaxy mass for luminous and standard luminosity Type IIn SN are not statistically distinguishable, although slight variations between surveys are present. In particular, the nine events in our sample with $L_p \lesssim 6 \times 10^{42}$ have a median stellar mass of $\langle M_{gal} \rangle \sim 10^{10}$ $M_\odot$.

As shown in the right hand panels of Figure 7.5, luminous Type IIn SN are robustly found in higher mass galaxies than SLSN-I ($p = 1 \times 10^{-3}$). The current sample of luminous Type IIn SN host galaxies appears shifted to lower masses than either the GOODS CCSN sample (cyan) or the low-redshift sample of CCSN discovered by *untargeted* surveys from (Kelly & Kirshner 2012b, green), although this is not formally statistically significant (KS test p-value of 0.1). As before, our results for the mass distribution of luminous Type IIn SN to do not heavily depend on either the redshift range examined or the transient luminosity cutoff adopted.

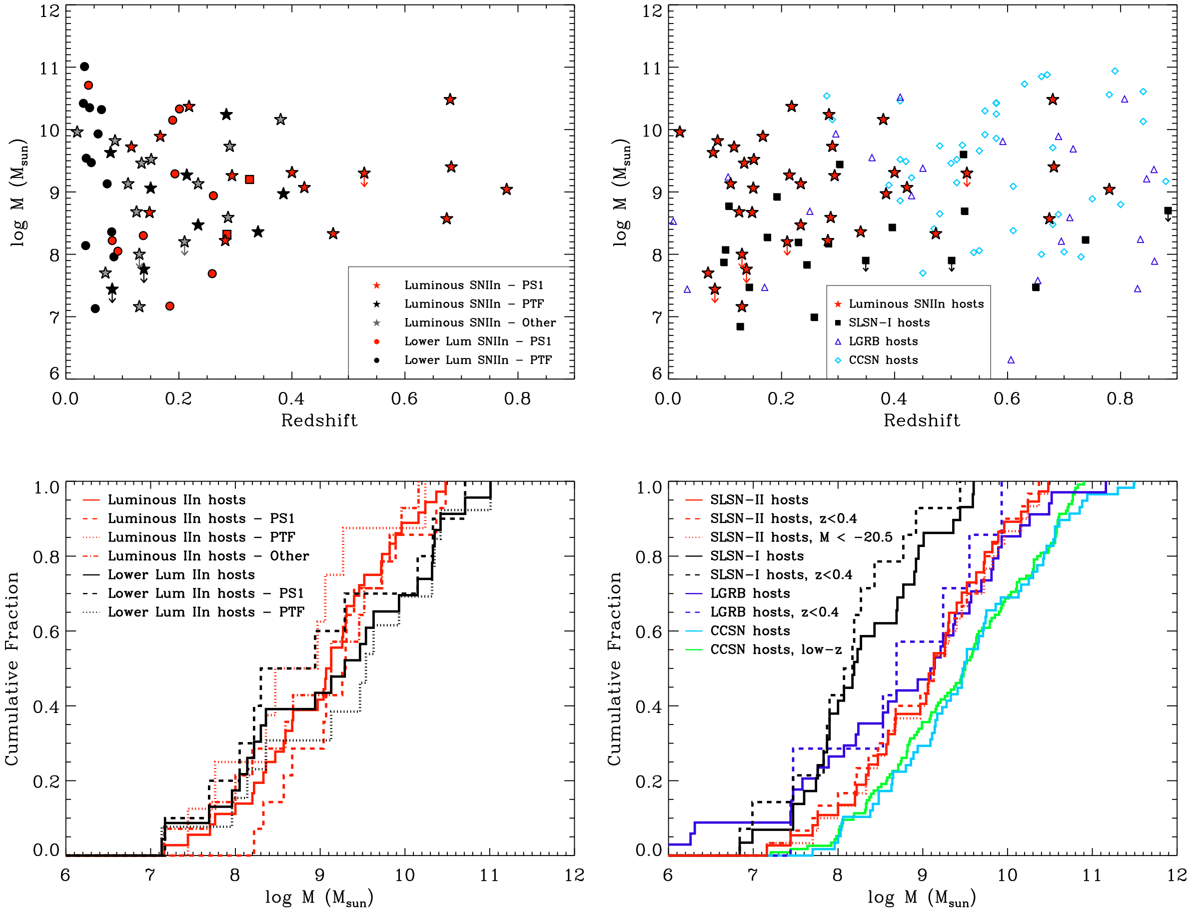

Figure 7.5.—: Same as Figure 7.3, but for host galaxy stellar masses. Symbols and colors have the same meaning as in Figure 7.2. *Left:* The host galaxies of luminous and standard luminosity Type IIn SN both span approximately 4 orders of magnitudes 10^7 $M_\odot$ < M_{gal} < 10^{11} $M_\odot$, and have similar median values of $\langle M_{gal} \rangle \sim \times 10^9$ $M_\odot$. *Right:* Luminous Type IIn SN host galaxies are robustly distinguished from the the host galaxies of SLSN-I.

7.4.3 Metallicities

This section presents preliminary results from of a subset of our spectroscopic sample, which includes the hosts galaxies of 7 luminous transients and 7 standard luminosity Type IIn SN discovered in the PS1-MDS (Figure 7.6). *This subsample doubles the number of luminous Type IIn hosts with metallicity measurements available in the literature.*

Several key comparisons can be made between our sample and the host galaxies of other luminous transients just by visual inspection. In particular, SLSN-I have been found to occur predominantly in extreme emission line galaxies with low-metallicities (Lunnan et al. 2014; Leloudas et al. 2015a). These galaxies possess strong [OIII] $\lambda\lambda$5007,4959 emission lines that dominate over Hβ and weak (often non-detected) lines of [NII] $\lambda\lambda$6583,6549. While examples of similar galaxies are found in the subset of our spectroscopic sample presented here (for both luminous *and* standard luminosity Type IIn host galaxies), many of the luminous Type IIn host galaxies are clearly distinct from this subclass, possessing weak features of [OIII] and and clear detections of [NII]—both indicative of higher metallicities.

We have calculated an initial estimate for the metallicities of the host galaxies shown in Figure 7.6 using the PP04N2 diagnostic (Pettini & Pagel 2004). Line fluxes were measured via gaussian fits in a custom IDL routine. The resulting metallicities are listed in Table 7.1, and span a range of $7.9 < 12 + \mathrm{Log(O/H)_{N2}} < 8.72$, corresponding to approximately $0.15Z_{\odot}$ to $Z_{\odot}$. Notably, half of the luminous Type IIn host galaxies in our spectroscopic sample have metallicities $\gtrsim 0.8Z\odot$.

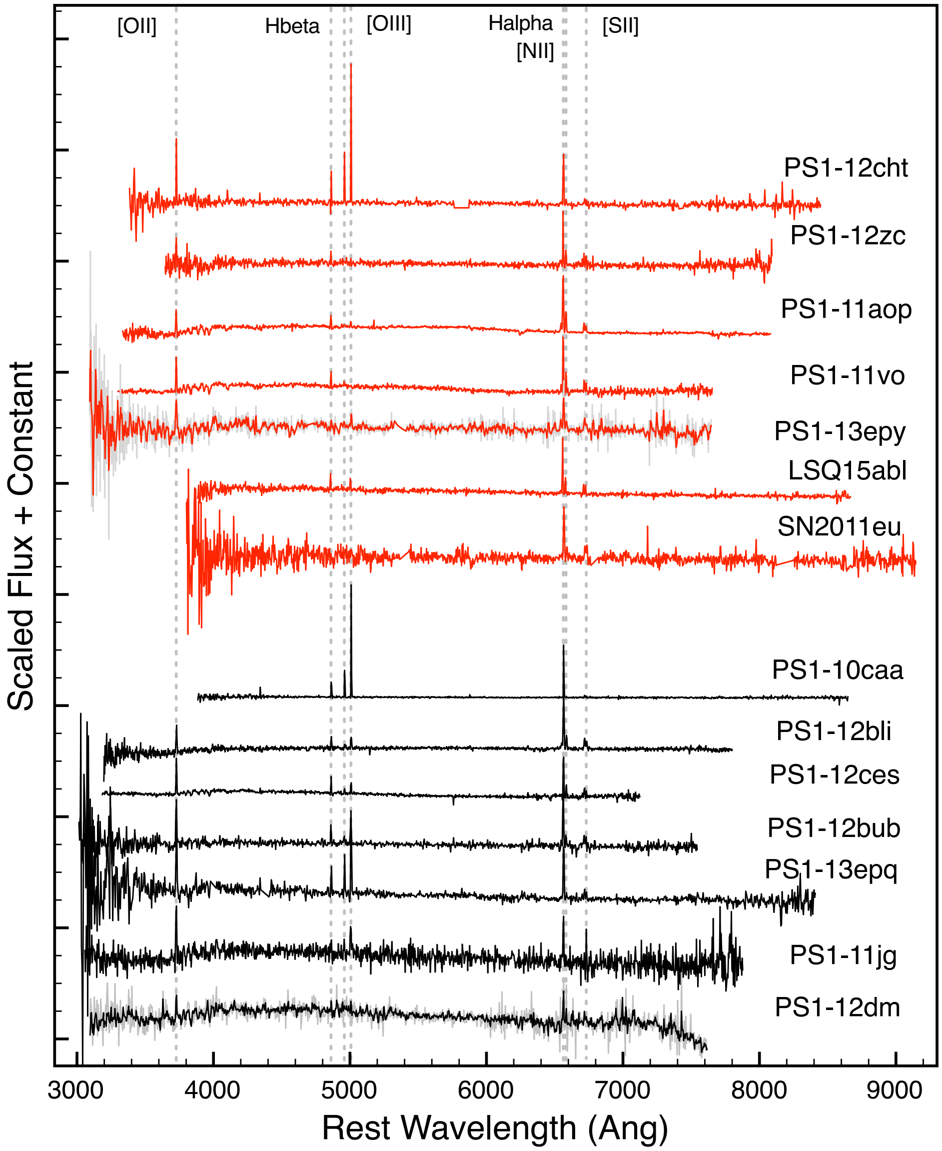

Figure 7.6.—: Host galaxy spectra for a subset of our spectroscopic sample which includes host galaxies of luminous interacting transients (red) and standard luminosity Type IIn SN (black).

We supplement our sample with the metallicities of eight luminous Type IIn host galaxies from the literature: the sample of six events from Leloudas et al. (2015a, SN 2006tf, SN 2008am, SN 1999bd, PTF10heh, PTF10qaf, and PTF11dsf), SN 2003ma (Rest et al. 2011) and SN 2010jl (Stoll et al. 2011), all of which were also measured on the PP04N2 metallicity scale, allowing for a direct comparison. The median metallicity for this full sample of 15 luminous Type IIn hosts is $\langle 12+\mathrm{Log(O/H)_{N2}} \rangle = 8.54 \approx 0.7\mathrm{Z}_{\odot}$. We plot its cumulative distribution in Figure 7.7.

Our sample of 7 luminous Type IIn host galaxies and those examined by Leloudas et al. (2015a) span a similar range PP04N2 measured metallicities. However, the PS1-MDS sample is weighted towards the higher metallicity end of this range. The cumulative distribution of the combined sample is consistent the host galaxy metallicities of the PS1-MDS standard luminosity Type IIn SN ($p = 0.85$), as well as with the distribution of explosion site metallicities for Type IIn SN found by Taddia et al. (2015, $p = 0.93$; see Figure 7.7). Thus, based on the current sample, we do not find evidence that luminous Type IIn SN explode in lower metallicity environments than standard luminosity Type IIn SN.

While our definition of a “luminous” transient is less strict that some other studies, four of our highest metallicity galaxies were the hosts of PS1-11vo, PS1-12zc, PS1-11aop, and LSQ15abl, all of which reached peak magnitudes <-20.5 mag. In addition, while some previous examples of luminous SN in massive, metal-rich, galaxies exploded at large offsets (e.g. PTF10qaf Leloudas et al. 2015a) with lower explosion site metallicities, PS1-11vo, PS1-11aop and LSQ15abl all exploded in the inner regions of their hosts (see Chapter 8). Thus, our conclusion that luminous interacting transients also explode in moderately massive galaxies at roughly solar metallicity is robust.

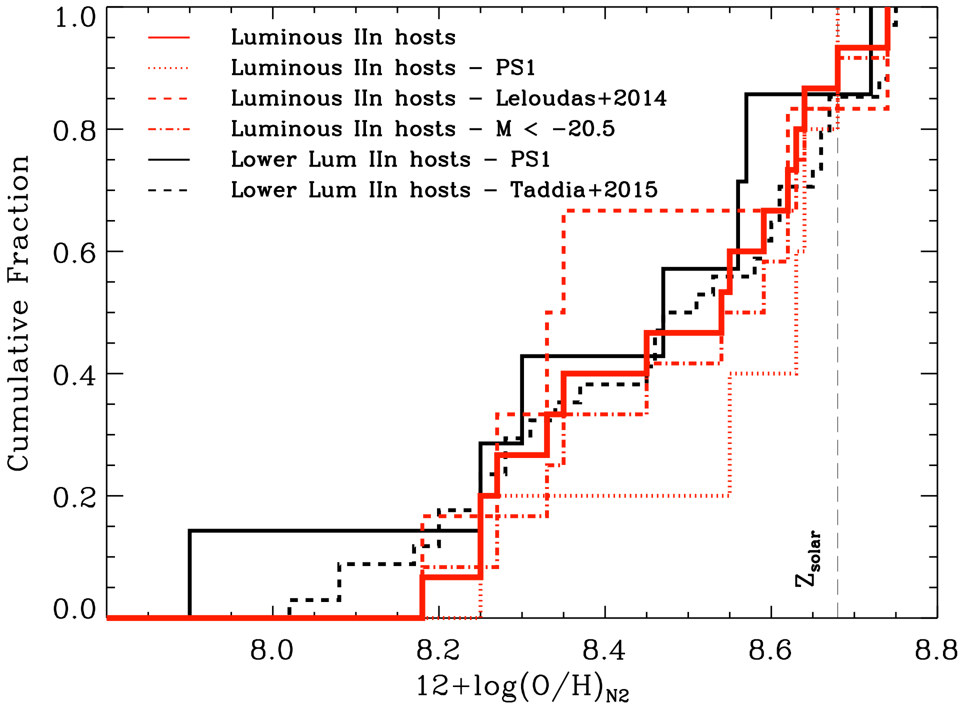

Figure 7.7.—: Cumulative distributions of PP04N2 metallicity values for Type IIn SN. Luminous Type IIn SN are shown in red. The full sample of 15 luminous Type IIn SN is plotted as a solid line, the luminous Type IIn SN from the PS1-MDS as a dotted line, the luminous Type IIn SN sample from Leloudas et al. (2015a) as a dashed line, and all events which pass a stricter transient luminosity cutoff of M<-20.5 mag as a dashed dotted line. Standard luminosity Type IIn SN are shown in black. The PS1-MDS sample presented here is plotted as a solid line and the explosion site metallicities from Taddia et al. (2015) as a dashed line. The full sample of luminous Type IIn SN is consistent with being drawn from the same distribution as the standard luminosity Type IIn SN ($p = 0.93$) and have a median value of $\langle 12+\mathrm{Log(O/H)}_{\mathrm{N2}}\rangle = 8.54 \approx 0.7\mathrm{Z}_{\odot}$.

In Figure 7.8 we plot the cumulative distribution for luminous Type IIn SN versus other classes of SN. We plot metallicities for Type IIP SN discovered by PTF from Stoll et al. (2013, blue), the Type Ib/c SN and Type Ic-BL SN discovered by untargeted surveys from Sanders et al. (2012, cyan and green, respectively), and the SLSN-I from Leloudas et al. (2015a, black). All metallicities were measured via the PP04N2 diagnostic. Luminous Type IIn SN appear at slightly lower metallicities that the Type IIP and Type Ibc samples ($p = 0.18$ and $p = 0.65$, respectively) and are offset to higher metallicities than either Type Ic-BL or SLSN-I. This distinction is *statistically significant* for SLSN-I ($p = 0.04$).

Indeed, based on their initial sample of six objects, Leloudas et al. (2015a) found evidence that the host galaxies of luminous Type IIn SN were higher metallicity than either SLSN-I or LGRBs. We have now doubled the number of luminous Type IIn SN with host galaxy metallicities available. Our results not only confirm this initial trend, but push the distribution for luminous Type IIn SN to even higher metallicities, further demonstrating that the environments that host luminous interacting transients are physically distinct from those of SLSN-I and LGRBs.

In Figure 7.9 we plot a mass-metallicity diagram, which further highlights this distinction. The SLSN-I sample of Lunnan et al. (2014) is plotted as green squares, the LGRB sample from Levesque (2010) as black circles and the luminous Type IIn SN as stars. Grey contours represent the sample of 53,000 SDSS star-forming galaxies from Tremonti et al. (2004). Metallicities for the SLSN-I and LGRB samples were measured via the R_{23} diagnostic and we have plotted Figure 7.9 in the system of Kobulnicky & Kewley (2004). Leloudas et al. (2015a) also present metallicities in the KK04 calibration, and these are plotted directly (orange stars).

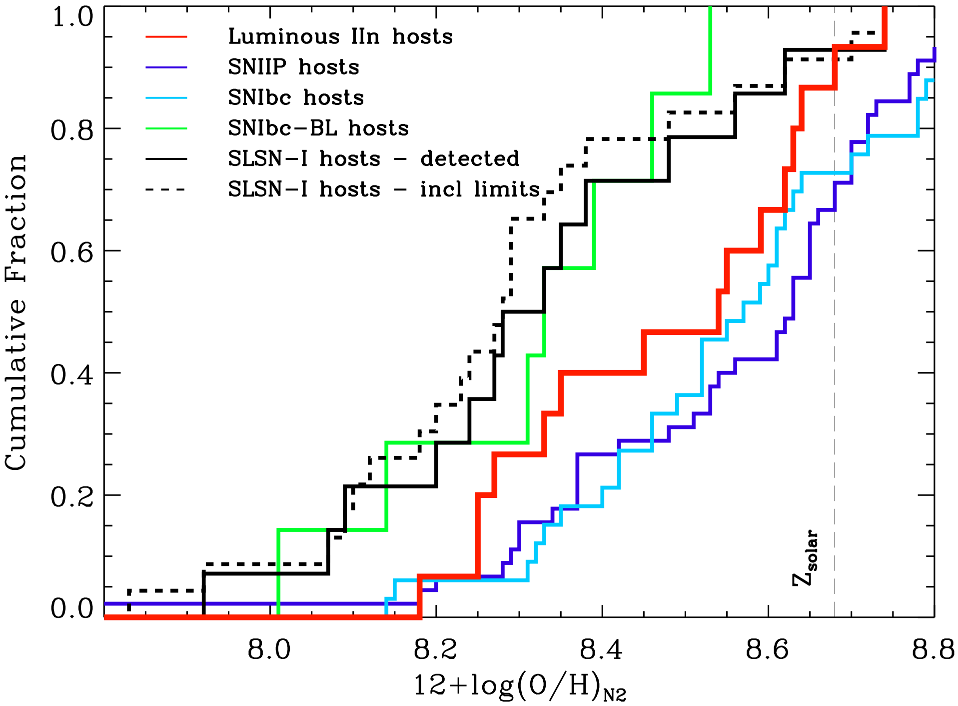

Figure 7.8.—: Cumulative distributions of PP04N2 metallicity values for Luminous Type IIn SN in comparison to other transients. Also shown are the explosion site metallicities for Type IIP SN discovered by PTF from Stoll et al. (2013, blue), the Type Ib/c SN and Type Ibc-BL SN discovered by untargeted surveys from Sanders et al. (2012, cyan and green, respectively), and the SLSN-I from Leloudas et al. (2015a, black). All metallicities were measured via the PP04N2 diagnostic. For 40% of the SLSN-I in the sample of Leloudas et al. (2015a) only upper limits could be placed on the metallicity using the PP04N2 diagnostic. The solid black line includes only detected measurements, while the dashed line incorporates information from the upper limits. Luminous Type IIn SN appear at slightly lower metallicities that the Type IIP and Type Ibc samples (p =0.18 and p =0.65, respectively) and are offset to higher metallicities than either Type Ic-BL or SLSN-I. This is statistically significant for SLSN-I (p =0.04).

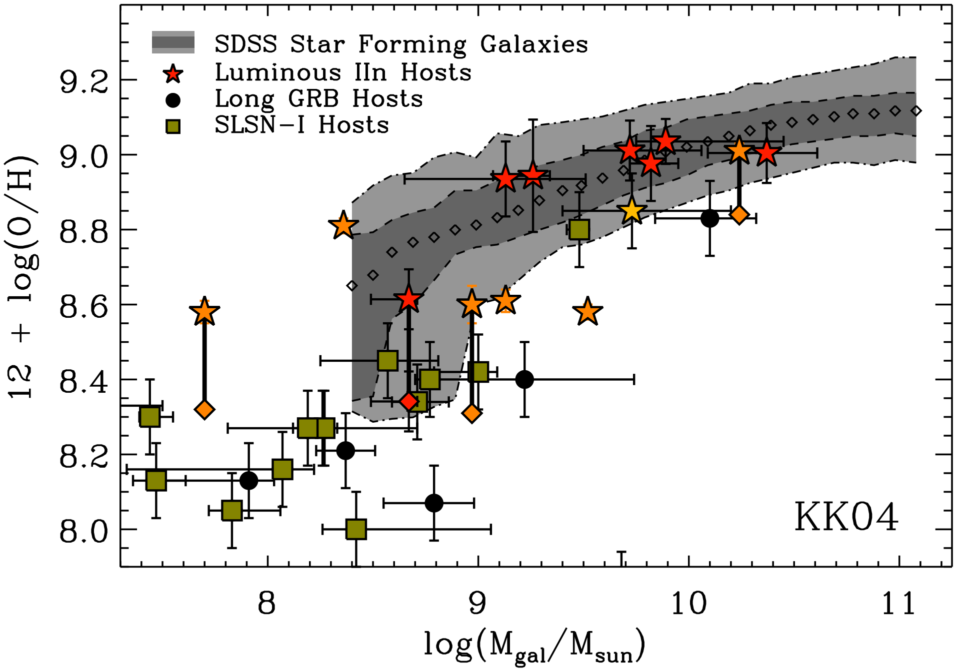

Figure 7.9.—: Mass metallicity diagram. Grey contours represent SDSS star forming galaxies from Tremonti et al. (2004). LGRB host galaxies are shown as black circles, SLSN-I host galaxies as green squares, and luminous interacting transients as stars. The sample of luminous transients from Leloudas et al. (2015a) is plotted in orange, events analyzed in this work in red, and SN 2003ma (Rest et al. 2011) in yellow. Luminous interacting transients are found in more massive, metal-rich galaxies on average than either SLSN-I or LGRBs. See text for further details.

For the transients in our spectroscopic sample and SN 2003ma (red and yellow symbols, respectively), we have converted PP04N2 metallicities to the the KK04 system using the conversions of Kewley & Ellison (2008). These events may therefore contain a small systematic offset from their true values on this metallicity scale. A full analysis of our entire spectroscopic sample across multiple metallicity calibrations—allowing for a direct comparison with the distributions of SLSN-I and LGRBs—will be completed in future work. However, the distinction between the luminous Type IIn SN host and SLSN-I/LGRB hosts is clear, with a significant number of luminous Type IIn SN hosts appearing at higher masses and metallicities.

7.5 Global Host Properties: Summary

In this Chapter we have presented a preliminary analysis of the global host galaxy properties of luminous interacting transients in comparison to both standard luminosity Type IIn SN and other classes of luminous transients. We have examined the absolute magnitudes, masses, and metallicities of the largest sample of luminous Type IIn SN compiled to date, including 13 luminous SN discovered as part of the PS1-MDS. The host galaxies of luminous interacting transients span a wide range in all three properties, with median values of $\langle \mathrm{M_B} \rangle = -18.5$ mag, $\langle \mathrm{M_{gal}} \rangle = 10^9$ $\mathrm{M_\odot}$, and $\langle 12 + \mathrm{Log(O/H)_{N2}} \rangle = 8.54$. Although there are indications of slight differences between discovery surveys, and a possible dearth of Type IIn with peak luminosities below $\sim 6\times10^{42}$ erg $\mathrm{s^{-1}}$ exploding in dwarf galaxies, we do not find any statistically distinguishable trends between the host galaxies of luminous interacting SN and the hosts of "standard luminosity" Type IIn SN. However, *the host galaxies of luminous interacting transients are robustly distinguished* *from those of hydrogen-poor super-luminous SN, in being more luminous, massive, and metal-rich.* This finding appears to be independent of the luminosity cutoff considered for interacting transients, and is *accentuated* when considering the low redshift sample. While a fraction luminous Type IIn SN do occur in faint dwarf galaxies with low metallicities, the physical conditions present in these galaxies are not required to produce all luminous and interacting transients.

In future work, this analysis will be expanded to include estimates of the star formations rates and stellar population ages of the interacting transient host galaxies, as well as quantitative estimates for the CSM density and explosion properties of the the transients considered. Particular questions we wish to address include:

1. Does the distribution of host galaxies observed for various classes of interacting transients match the expectation if they trace star formation, or is there an excess of explosions in low mass galaxies as has been found for LGRBs? (e.g. Perley et al. 2013; Stanek et al. 2006)
2. Is there a robust distinction between the distribution of host galaxies properties for Type IIn at low peak luminosities? How do these trends depend on quantitative estimates of their explosion and mass-loss properties?

Acknowledgments

The Pan-STARRS1 Surveys (PS1) have been made possible through contributions of the Institute for Astronomy, the University of Hawaii, the Pan-STARRS Project Office, the Max-Planck Society and its participating institutes, the Max Planck Institute for Astronomy, Heidelberg and the Max Planck Institute for Extraterrestrial Physics, Garching, The Johns Hopkins University, Durham University, the University of Edinburgh, Queen's University Belfast, the Harvard-Smithsonian Center for Astrophysics, the Las Cumbres Observatory Global Telescope Network Incorporated, the National Central University of Taiwan, the Space Telescope Science Institute, the National Aeronautics and Space Administration under Grant No. NNX08AR22G issued through the Planetary Science Division of the NASA Science Mission Directorate, the National Science Foundation under Grant No. AST-1238877, the University of Maryland, and Eotvos Lorand University (ELTE). This work includes data gathered with the 6.5 m Magellan Telescopes located at Las Campanas Observatory, Chile. Some observations reported here were obtained at the MMT observatory, a joint facility of the Smithsonian Institution and the University of Arizona.

Chapter 8

Luminous Interacting Transients IV: Sub-galactic Environments

M. R. Drout, E. Berger and the Pan-STARRS1-MDS Transient Group

In Preparation

Abstract

We present the first statistical analysis of the location of luminous interacting transients within their host galaxies. While luminous Type IIn SN are observed at a wide range of host-transient offsets, we find that a significant fraction explode within the central regions of their hosts ($\langle \mathrm{R} \rangle = 1.43$ kpc; $\langle \mathrm{R}/\mathrm{R}_{\mathrm{gal},50} \rangle = 0.42$). This central concentration is in excess of that predicted by an exponential disk profile and is also in stark contrast to standard luminosity Type IIn SN, for which a central *deficit* is observed. We conclude that the physical conditions of star formation in the bright inner regions of galaxies (including Milky Way-like and S0 galaxies) are conducive for the formation of luminous Type IIn SN progenitors. Possible relevant factors include stellar interactions or IMF variations in dense nuclear stars clusters or circumnuclear rings.

8.1 Introduction

In this Chapter, we now turn to the question of where luminous interacting transients explode *within* the light distributions of their host galaxies. While this work represents the first statistical study of the sub-galactic environments of luminous interacting transients, such methods have been widely used to shed light on the progenitors of other classes of astronomical transients. For example, LGRBs have been shown to explode preferentially on the brightest star-forming regions of their hosts. This is notable in comparison to core-collapse SN, which uniformly trace the light of their host galaxies (Fruchter et al. 2006; Svensson et al. 2010), and to SLSN-I, which also correlate with the UV light of their hosts (Lunnan et al. 2015b). In contrast, short-duration gamma-ray bursts (SGRBs) are distinctive in *not* tracing the light from their host galaxies, providing evidence for a compact object merger interpretation (Fong & Berger 2013).

In studies of low-redshift SN, both Type Ia and Type II SN have been shown to uniformly trace the light from their host galaxies, while Type Ic SN are also concentrated on the brightest regions of their hosts—in a similar manner as LGRBs (Kelly et al. 2008). As described in Chapter 5, the locations of standard luminosity Type IIn SN are notable in *not* strongly correlating the tracers of active stars formation in their host galaxies (Anderson et al. 2012; Habergham et al. 2014). Numerous studies have also noted a *lack* of both Type II and Type IIn SN in the central regions of their host galaxies, which is offset by a central excess of Type Ic SN (Prieto et al. 2008; Anderson & James 2009; Kelly & Kirshner 2012b). This contrast is often interpreted as a metallicity effect (e.g. Anderson et al. 2012).

Our main goal is to understand where luminous interacting transients occur within their hosts and to contrast those results with (a) standard luminosity Type IIn SN and (b) other classes of transients. The full sample of luminous and standard luminosity Type IIn SN considered here is described in Section 8.2. Throughout this chapter, we compare the empirical distribution functions found for our samples of interacting transients, as well as other classes of SN, using the Kolmogorov-Smirnov (KS) goodness-of-fit test. The main comparison samples considered are the low redshift SN samples of Kelly et al. (2008); Prieto et al. (2008); Kelly & Kirshner (2012b), the LGRB sample from Blanchard et al. (2016), the SLSN-I sample from Lunnan et al. (2015b), and the SGRB sample from Fong & Berger (2013).

8.2 Sample

In order to investigate the sub-galactic environments of luminous interacting transients, we have constructed a sample of 64 Type IIn SN. This includes 30 standard luminosity Type IIn SN, 22 luminous Type IIn SN, and 12 events which were explicitly classified as Type IIn/Ia-CSM. In order for an event to be included in our sample, we required two conditions to be met: 1) we were able to obtain deep template images of the explosion environment, with sufficient angular resolution and signal-to-noise to resolve the host galaxy, *and* 2) light curve information was available for the transient which could be used to characterize its explosion properties. The main sources for our sample are the PS1-MDS Type IIn SN—17 of which have both resolved imaging and sufficient constraints on their light curve peaks for inclusion—the PTF sample of Ofek et al. (2014a), the Type IIn/Ia-CSM sample compiled by Silverman et al. (2013), and other Type IIn SN from the literature.

In Table 8.1 we list the full sample of 64 transients considered. As we note in the table, some of the standard-luminosity Type IIn SN in our sample were also included in various literature studies of SN environments (Kelly & Kirshner 2012b; Anderson & James 2009; Anderson et al. 2012; Habergham et al. 2014). In all cases, we have carried out an independent analysis to ensure that the same physical quantities were measured in a consistent manner for our entire sample. In Figure 8.1, we plot redshift versus peak transient luminosity for all of the SN considered. Events discovered by the PS1-MDS are shaded in red. Events classified as Type IIn/Ia-CSM are plotted as squares, while events considered luminous by the definition outlined in Chapter 5 are plotted as stars, and standard-luminosity Type IIn SN are plotted as circles.

Table 8.1. Type IIn Sample

Name	Redshift	Discovery	(Un)Targeted[a]	$L_{\rm peak}$ (erg s^{-1})	LC Reference	Prev. Host Studies[b]
"Luminous" SNIIn						
PS11ad	0.422	PS1-MDS	U	6.21e+43	···	···
PS11kj	0.400	PS1-MDS	U	5.15e+43	···	···
PS11vo	0.116	PS1-MDS	U	5.02e+43	···	···
PS11aop	0.128	PS1-MDS	U	5.42e+43	···	···
PS12zc	0.167	PS1-MDS	U	5.33e+43	···	···
PS12car	0.680	PS1-MDS	U	7.50e+43	···	···
PS12cht	0.148	PS1-MDS	U	3.71e+43	···	···
PS13byi	0.682	PS1-MDS	U	7.32e+43	···	···
PS13epy	0.294	PS1-MDS	U	3.09e+43	···	···
SN1999bd	0.151	SCP	U	1.10e+44	Richards et al. (1999)	
SN2003ma	0.289	SuperMACHO	U	7.00e+43	Rest et al. (2011)	
SN2006tf	0.074	ROTSE	U	6.30e+43	Smith et al. (2008)	
SN2006gy	0.019	ROTSE	U	1.70e+44	Smith et al. (2007)	KK12
SN2008am	0.230	ROTSE	U	3.00e+44	Chatzopoulos et al. (2011)	
SN2010jl	0.011	POSS	T	3.80e+43	Fransson et al. (2014)	KK12,H14
SN2011cp	0.380	CRTS	U	9.90e+43	Drake et al. (2011a)	
SN2011eu	0.110	CRTS	U	5.70e+43	Graham et al. (2011)	
CSS100217	0.147	CRTS	U	1.00e+45	Drake et al. (2011b)	
CSS121015	0.287	CRTS	U	3.20e+44	Benetti et al. (2014)	
PS15blq	0.125	PSST	U	6.50e+43	Huber et al. (2015a)	
PS15ces	0.134	PSST	U	3.90e+43	Foley et al. (2015)	
LSQ15abl	0.087	LSQ	U	5.50e+43	Prajs et al. (2015)	
"SNIIn/Ia-CSM"						
PS11jf	0.282	PS1-MDS	U	2.52e+43	···	···
SN1997cy	0.064	MSACSS	(U)	1.83e+43	Turatto et al. (2000)	
SN1999E	0.026	R. Antezana	T	1.18e+43	Rigon et al. (2003)	
SN2002ic	0.066	NEAT	U	2.91e+43	Wood-Vasey et al. (2004)	
SN2005gj	0.062	SDSS	U	2.45e+43	Aldering et al. (2006)	
SN2008J	0.016	LOSS	T	1.01e+43	Taddia et al. (2012)	H14
SN2008cg	0.036	CRTS	U	≈1.1e+43	Silverman et al. (2013)	
SN2011jb	0.083	CRTS	U	≈2.7e+43	Silverman et al. (2013)	
SN2012ca	0.019	BOSS	T	1.90e+43	Inserra et al. (2016)	
SN2013dn	0.060	CRTS	U	3.6e+43	Fox et al. (2015)	
CSS120327	0.091	CRTS	U	3.20e+43	Silverman et al. (2013)	
PTF11kx	0.047	PTF	U	8.90e+42	Dilday et al. (2012)	
"Normal" SNIIn						
PS10caa	0.092	PS1-MDS	U	9.40e+41	···	···
PS12dm	0.201	PS1-MDS	U	1.35e+43	···	···
PS12bli	0.189	PS1-MDS	U	1.34e+43	···	···
PS12ces	0.193	PS1-MDS	U	9.24e+42	···	···
PS13hi	0.040	PS1-MDS	U	2.55e+42	···	···
PS13adh	0.137	PS1-MDS	U	1.05e+43	···	···
PS13epq	0.261	PS1-MDS	U	1.22e+43	···	···
SN1988Z	0.023	AAO	T	4.4e+42	Turatto et al. (1993)	
SN1994W	0.004	G. Cortini	T	1.0e+43	Sollerman et al. (1998)	KK08,KK12,H14
SN1994Y	0.009	W. Wren	T	6.30e+42	Ho et al. (2001)	KK08,KK12,H14
SN1995G	0.016	R. Evans	T	5.08e+42	Pastorello et al. (2002)	KK12
SN1998S	0.003	BAOSS	T	2.00e+43	Fassia et al. (2000)	KK12
SN2005cl	0.026	LOSS	T	1.08e+43	Kiewe et al. (2012)	KK08

Table 8.1—Continued

Name	Redshift	Discovery	(Un)Targeted[a]	L_{peak} (erg s^{-1})	LC Reference	Prev. Host Studies[b]
SN2005cp	0.022	LOSS	T	4.24e+42	Kiewe et al. (2012)	KK12
SN2005db	0.015	L. Monard	T	2.42e+42	Kiewe et al. (2012)	KK12,H14
SN2005ip	0.007	T. Boles	T	2.31e+42	Stritzinger et al. (2012)	KK12,H14
SN2005kj	0.017	SNF/NEAT	U	5.97e+42	Taddia et al. (2013)	
SN2006aa	0.021	LOSS	T	2.68e+42	Taddia et al. (2013)	KK12
SN2006bo	0.015	T. Boles	T	1.38e+42	Taddia et al. (2013)	KK12
SN2006jd	0.019	LOSS	T	1.81e+42	Stritzinger et al. (2012)	KK12
SN2006qq	0.029	LOSS	T	5.09e+42	Taddia et al. (2013)	
SN2007pk	0.017	LOSS	T	1.70e+43	Pritchard et al. (2012)	KK12
SN2008fq	0.011	LOSS	T	1.16e+43	Taddia et al. (2013)	
SN2009ip	0.006	CHASE	T	1.64e+43	Margutti et al. (2014b)	
SN2009kn	0.016	POSS	T	3.31e+42	Kankare et al. (2012)	
SN2011ht	0.004	T. Boles	T	3.50e+42	Roming et al. (2012)	
PTF10tyd	0.063	PTF	U	5.30e+42	Ofek et al. (2014a)	
PTF12cxj	0.036	PTF	U	2.60e+42	Ofek et al. (2014a)	
PTF12ksy	0.031	PTF	U	5.20e+42	Ofek et al. (2014a)	
iPTF13agz	0.057	PTF	U	3.90e+42	Ofek et al. (2014a)	

[a] U = event was discovered in an untargeted survey; T = event was discovered in a targeted survey.

[b] KK08 = Kelly et al. (2008); KK12 = Kelly & Kirshner (2012b); H14 = Habergham et al. (2014)

Note. — SN Surveys: CRTS = Catalina Real-Time Transient Survey (Drake et al. 2009); PTF = Palomar Transient Factory (Law et al. 2009); PS1-MDS = PanSTARRS1 Medium Deep Survey (Kaiser et al. 2010); PSST = PanSTARRS Survey for Transients (Huber et al. 2015b); ROTSE = Robotic Optical Transient Search Experiment (Akerlof et al. 2003); SCP = Supernova Cosmology Project; POSS = Puckett Observatory Supernova Search (Newton & Puckett 2010); LSQ = La Silla Quest Survey (Hadjiyska et al. 2011); SuperMACHO = SuperMACHO Project microlensing survey; NSF/NEAT = "Nearby SN Factory" collaboration as part of the JPL Near-Earth Asteroid Tracking component of the Palomar Consortium; CHASE = Chilean Automatic SN Search; BAOSS Beijing Astronomical Observatory SN Search (Li et al. 1998); AAO = Asiago Astronomy Observatory; MSACSS = Mount Stromlo Abell Cluster SN Search (Reiss et al. 1998); BOSS = Backyard Observatory SN Search

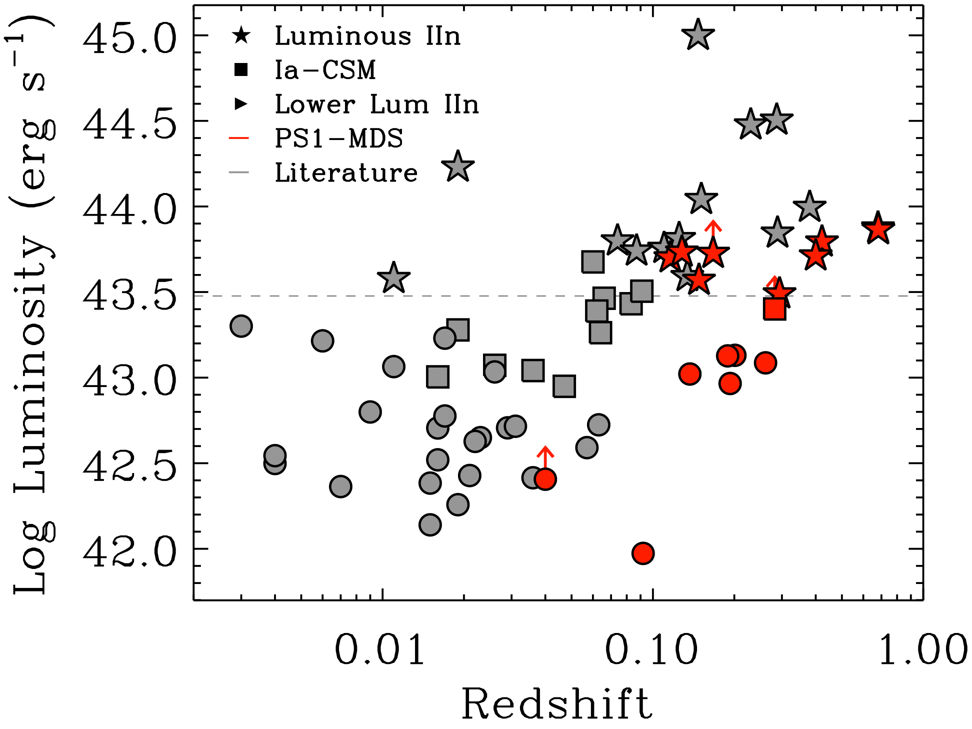

Figure 8.1.—: Redshift versus transient peak luminosity for the full sample of interacting transients whose sub-galactic environments are analyzed in this work. SN discovered by the PS1-MDS are plotted in red and those from the literature in grey. Transients which are considered luminous are plotted as stars, events classified as Type IIn/Ia-CSM are plotted as squares and all other Type IIn SN are plotted as circles.

8.3 Observations and Data Reduction

8.3.1 Host Galaxy Images

We use ground-based data from a number of telescopes/instruments to obtain deep, resolved imaging of the host galaxies of the transients in our sample. For interacting transients discovered in the PS1-MDS, we use templates of their host environments that were made by stacking pre-explosion survey images. As discussed in Chapter 7, the construction of these PS1-MDS "deep stacks" follows Rest et al. (2014), in that 30–80 high-quality nightly stacks are combined, weighted by the product of the inverse variance and the inverse area of the PSF. The typical depth achieved in the templates is $\sim$24.5 mag in $griz_{\rm PS1}$. For the events discovered in the PS1-MDS, we assess the location of the transients within their host galaxy light distribution in all of (observed-frame) $griz_{\rm PS1}$.

For non-PS1 discovered events, we focus on rest-frame g-band imaging of their host galaxies (4000 Å $\lesssim \lambda_{\rm eff} \lesssim$ 4600 Å). For 17 nearby events in our sample, high-quality SDSS imaging of their host galaxies is available. In these cases we download the "corrected frame" fits images from the DR10 online skyserver. For use, we require that an SDSS frame was observed >6 months prior or >3 years post-discovery in order to avoid contaminating SN flux. For four SN, we use stacks from the PS1 3π survey which were constructed from an average of 20 single night frames, all obtained pre-explosion. Finally, for four additional events, we download individual frames from the Palomar Transient Factory DR2 archives which were either obtained prior to explosion or >4 years post-explosion.

Finally, for 20 events, which were either located outside the SDSS/PS1 footprint or lacked high S/N SDSS/PS1 detections, we obtained deep rest-frame g-band imaging with IMACS on Magellan-Baade or LDSS-3 on Magellan-Clay. A majority of these are luminous transients located at moderate redshift. Images were bias/flat-field corrected and stacked using standard tasks in IRAF. Observations were taken a minimum of 2 years post-explosion, with a median age of $\gtrsim$6 years post-explosion. In Table 8.2 we summarize the source of host galaxy imaging for all non-PS1 events.

8.3.2 Transient Images

Pinpointing the location of a transient within its host galaxy to sub-arcsecond precision generally requires an image with the transient visible, which can be used to preform relative astrometry. For objects discovered in the PS1-MDS, we used all detections of the transient (typically 50−200) during the duration of the survey in order to determine its centroid to higher precision, as described below.

For non-PS1 targets (whose explosion epochs span back to the 1990s) we acquired transient images from a wide array of sources. Most images were either supplied by the Carnegie Supernova Project (CSP) or were publicly available in the European Southern Observatory (ESO) or Palomar Transient Factory DR2 archives. We also utilized data from the PS1 3π survey, the Fred Lawrence Whipple Observatory (FLWO), Palomar-QUEST, and Keck Observatories. FITS images for some events were also provided by amateur astronomers Joseph Brimacombe, Stan Howerton, and Odd Trondal. In total, transient images were obtained for 33 of the 45 non-PS1 transients in our sample, including all but 3 events with peak luminosities above 3×10^{43} erg s^{-1}. In Table 8.2 we summarize the instrument and filter used to obtain each of these images.

Table 8.2. Sub-Galactic Environment Literature Sample Observations

		Host Image				SN Image	
Event	Redshift	Telescope	Filter	Exp Time (s)	Obs Date (UT)	Telescope	Filter
“Luminous” SNIIn							
SN1999bd	0.151	Magellan/IMACS	g	3x200	2015 Feb 19	GEODSS/NEAT	unf.
SN2006tf	0.074	Magellan/IMACS	g	2x300	2015 Apr 23	Keck/LRIS	g
SN2006gy	0.01919	SDSS/2.5m	g	53.9	2003 Jan 29	FLWO/1.2m	i
SN2008am	0.230	Magellan/IMACS	g	200	2015 Jan 17	···	···
SN2010jl	0.01069	SDSS/2.5m	g	53.9	2002 Dec 14	NTT/EFOSC	R
SN2011cp	0.38	Magellan/IMACS	g	2x420	2015 Dec 15	···	···
SN2011eu	0.110	Magellan/LDSS3	g	240	2015 July 17	J. Brimacombe	Clear
CSS121015	0.286	Magellan/IMACS	r	3x300	2015 Sept 09	NTT/EFOSC	V
PS15blq	0.125	PS1 (3π stack)	g	···	···	PS1 (3π warp)	···
PS15ces	0.134	PS1 (3π stack)	g	···	···	Magellan/IMACS	r
LSQ15abl	0.087	PS1 (3π stack)	g	···	···	Magellan/IMACS	r
SNIIn/SNIa-CSM							
SN1997cy	0.0642	Magellan/IMACS	g	3x180	2015 Jan 15	NTT/EMMI	i
SN1999E	0.0258	Magellan/IMACS	g	2x60	2015 May 15	NTT/SOFI	J
SN2002ic	0.0660	Magellan/IMACS	g	2x120	2015 Sept 09	LCO-40	V
SN2005gj	0.0616	Magellan/IMACS	g	3x200	2015 Jan 16	LCO-40	V
SN2008J	0.0159	Magellan/IMACS	g	2x60	2015 Sept 09	LCO-40	V
SN2008cg	0.0362	Magellan/IMACS	g	2x180	2015 May 17	S. Howerton	Clear
SN2011jb	0.0826	Magellan/IMACS	g	2x240	2015 May 16	J. Brimacombe	Clear
SN2012ca	0.019	···	···	···	···	NTT/EFOSC	r
SN2013dn	0.0600	Magellan/LDSS3	g	3x60	2015 July 17	NTT/EFOSC	V
CSS120327	0.0908	Magellan/IMACS	g	2x240	2015 May 15	···	···
PTF11kx	0.0466	SDSS/2.5m	g	53.9	2000 Apr 25	P48/PTF/MOSAIC	R
“Normal” SNIIn							
SN1988Z	0.02282	SDSS/2.5m	g	53.9	2005 Jun 01	NTT/SUSI	r
SN1994W	0.00412	SDSS/2.5m	g	53.9	2001 May 23	···	···
SN1994Y	0.001544	P48/PTF/MOSAIC	g	3x60	2009 Mar 20	···	···
SN1995G	0.01627	SDSS/2.5m	g	53.9	2007 Feb 07	NTT/EMMI	i
SN1998S	0.00299	SDSS/2.5m	g	53.9	2002 Dec 13	···	···
SN2005cl	0.02588	SDSS/2.5m	g	53.9	2000 Sept 03	···	···
SN2005cp	0.02216	SDSS/2.5m	g	53.9	2008 Oct 02	···	···
SN2005db	0.01513	SDSS/2.5m	g	53.9	2008 Oct 01	···	···
SN2005ip	0.00714	SDSS/2.5m	g	53.9	2003 Jan 28	LCO-40	V
SN2005kj	0.01685	Magellan/IMACS	g	4x30	2015 Jan 15	LCO-40	V
SN2006aa	0.02067	SDSS/2.5m	g	53.9	2005 May 10	LCO-40	V
SN2006bo	0.01535	SDSS/2.5m	g	53.9	2000 Sept 30	LCO-40	V
SN2006jd	0.01856	SDSS/2.5m	g	53.9	1999 Mar 22	LCO-40	V
SN2006qq	0.02905	Magellan/IMACS	g	4x45	2015 Jan 15	LCO-40	V
SN2007pk	0.01665	P48/PTF/MOSAIC	g	3x60	2012 Oct 09	···	···
SN2008fq	0.01061	Magellan/IMACS	g	30	2015 Apl 23	NTT/EFOSC	V
SN2009ip	0.00594	Magellan/IMACS	g	2x180	2015 May 15	Magellan/IMACS	g
SN2009kn	0.01580	Magellan/IMACS	g	2x60	2015 May 16	NTT/EFOSC	R
SN2011ht	0.003646	P48/PTF/MOSAIC	g	3x60	2011 Jan 1,2	···	···
PTF10tyd	0.063	SDSS/2.5m	g	53.9	2004 Sept 15	P48/PTF/MOSAIC	R
PTF12cxj	0.036	SDSS/2.5m	g	53.9	2003 Mar 06	P48/PTF/MOSAIC	R
PTF12ksy	0.031	PS1 3π (stack)	g	1x60	2012 Oct 08	P48/PTF/MOSAIC	R
iPTF13agz	0.057	SDSS/2.5m	g	53.9	2004 May 22	···	···

8.4 Astrometry and SN centroids

To accurately determine the centroid of the PS1-MDS transients within the PS1-MDS templates, we made use of the astrometry framework within the PS1-MDS `photpipe` pipeline, which is described in detail elsewhere (Rest et al. 2014). The SN centroid and associated error are first determined in each individual difference image. These measurements are then combined to calculate a weighted, 3σ clipped, SN centroid. Through this process we achieve typical centroid uncertainties of 10–30 mas, depending on the number of SN detections for each event and their S/N ratios. The centroid accuracy, $\sigma_{\rm SN}$, for all of the PS1 interacting transients is listed in Table 8.3. The PS1 templates have a pixel scale of $0.''258$, and on average we pin-point the location where the SN exploded to within $\sim$1/10th of a pixel.

We also performed relative astrometry on the non-PS1 transients for which we obtained archival SN images. We use SExtractor to create a catalogs of overlapping sources between the SN and host images and the IRAF task `ccmap` to create an astrometric tie. The ($1\ \sigma$) uncertainties for these astrometric ties, $\sigma_{\rm tie}$, are typically $50-200$ mas, depending on the number of matched sources and the pixel scale/FWMH in the SN images. We then use SExtractor to determine the position of the SN in the frame of the host galaxy image. For each event, we use a single SN image and estimate the uncertainty in the centroid as $\frac{\rm FWHM}{2({\rm S/N})}$. Both $\sigma_{\rm tie}$ and $\sigma_{\rm SN}$ for these events listed in Table 8.3, and we add them in quadrature to compute our final uncertainty in the position of the SN within our host image. For literature objects currently considered in the sample, we have not performed image subtraction before computing the SN centroid. However, for inclusion in the sample we require that either the resolution is high enough (for low-redshift transients) or the SN outshines its host by >2.5 mag (for moderate-redshift luminous SN), such that the host galaxy does not significantly influence the computed centroid.

When no archival SN image was available, we rely on absolute astrometry and the SN positions listed in online circulars. For SDSS and PS1 3π host images, we use the astrometric solution present in the corrected frames/stacks, while for Magellan host images we create matched source catalogs and tie them to either the SDSS (when possible) or DSS astrometric system. The SDSS astrometric solution has sub-pixel accuracy (Kelly & Kirshner 2012b), but many of the SN positions listed in the ATELs rely on a wide array of catalogs with various astrometric precision. As a result, we adopt a systematic uncertainty in the SN positions of 1.0" for all of these objects.

In addition, we consider three special cases. For the luminous Type IIn SN 2003ma, Rest et al. (2011) provide a precise offset from the underlying host of $0.064 \pm 0.012'' = 460 \pm 85$ pc based on centroids in the SuperMACHO difference images. We list this offset in Table 8.3 and use it in our statistical analysis, below. In addition, the luminous transient CSS100217 exploded in the very central region of a Seyfert 1 galaxy. Drake et al. (2011b) argue for a luminous Type IIn interpretation of this event as opposed either an extreme AGN flare or tidal disruption event, and they place a limit on its offset from the galaxy core of <150 pc. While we do not consider this event in the statistical analysis below (because its nature is less certain), we list the limit on its offset in Table 8.3. Finally, for SN 2008am, we perform relative astrometry on our host image with the offsets to 2 nearby stars reported by Yuan et al. (2008).

In Figures 8.2 and 8.3, we show our the host galaxy images for all non-PS1

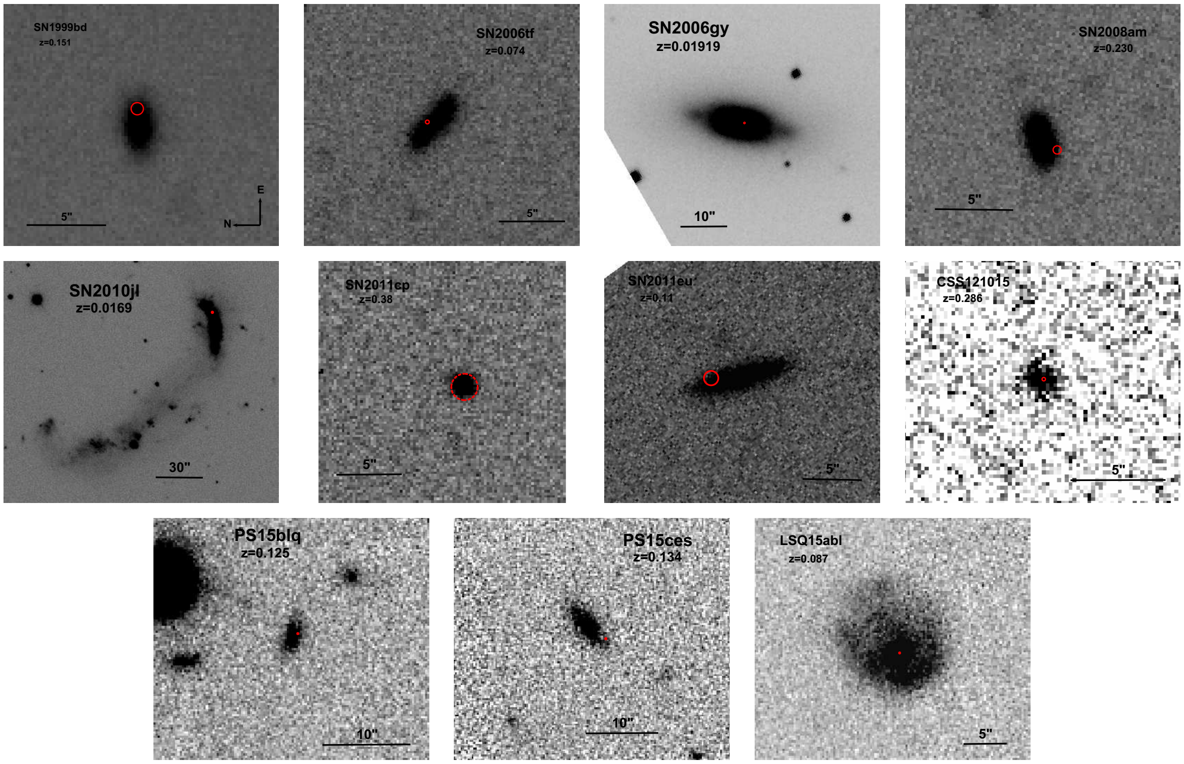

Figure 8.2.—: Host galaxy images of non-PS1-MDS discovered luminous Type IIn SN considered in this analysis. Red circles mark the transient location and error.

discovered luminous Type IIn and Type IIn/Ia-CSM transients considered in this analysis, respectively. Host galaxy images for all PS1-MDS Type IIn SN were shown in Chapter 7 (Figure 7.1).

8.5 Galaxy Sizes and Positions

We use SExtractor to measure the positions and effective radii of the host galaxies in our sample. To determine which pixels are part of the galaxy we set a S/N threshold of 1 (DETECT_THRESH = 1) for consistency with the samples SLSN-I, LGRBs, and SN of Lunnan et al. (2014), Svensson et al. (2010) and Kelly & Kirshner (2012b), respectively.

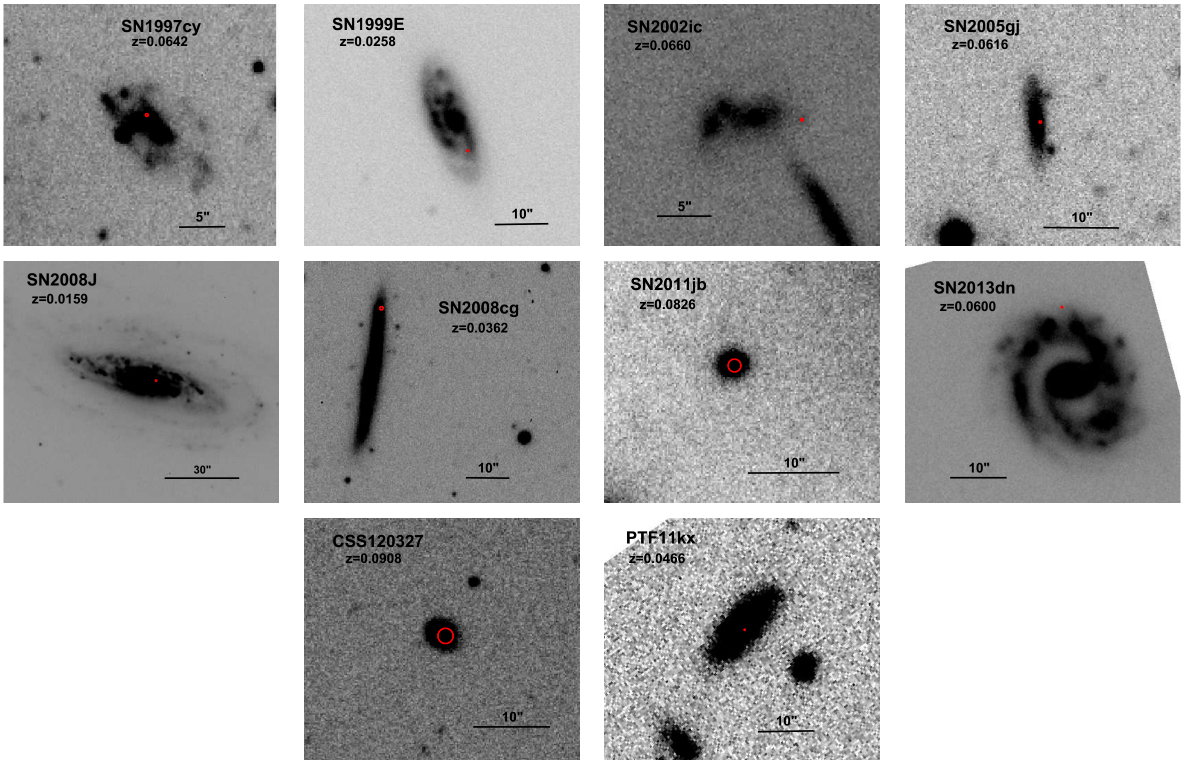

Figure 8.3.—: Host galaxy images of non-PS1-MDS Type IIn/Ia-CSM SN considered in this analysis. Red circles designate the transient location and error.

The position (and associated error) are then determined as the flux-weighted centroid of the galaxy. The error on this location is listed in Table 8.3 ($\sigma_{\rm gal}$). The effective size of the galaxy is then computed with the FLUX_RADIUS parameter, which calculates the radius which contains a certain fraction of the total light of the galaxy. In Table 8.3 we list both the half-light and 80% radii (r_{50} and r_{80}) for our sample.

In Figure 8.4 we plot the cumulative distribution of r_{80} values for the galaxies considered in this analysis. In the left panel, we compare the host galaxies of the standard luminosity Type IIn SN, luminous Type IIn SN, and Type IIn/Ia-CSM SN included in our sample. The samples for all three classes of interacting transients probe a similar range of galaxies sizes. For reference, in the right panel we compare the sizes

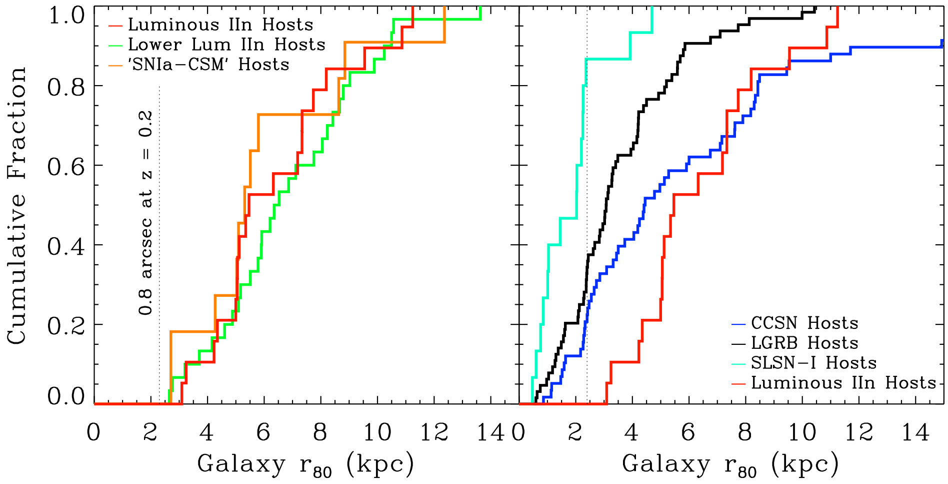

Figure 8.4.—: *Left:* Cumulative distribution of host galaxy sizes for the samples of luminous (red), Type IIn/Ia-CSM (orange) and standard luminosity (green) Type IIn SN. *Right:* Cumulative distribution of the host galaxy sizes for our sample of luminous Type IIn SN (red) in comparison to SLSN-I (Lunnan et al. 2014, teal), LGRBs (Blanchard et al. 2016, black), the GOODS CCSN (Svensson et al. 2010, blue).

of the host galaxies for the luminous Type IIn SN in our sample to the hosts of the SLSN-I from Lunnan et al. (2014), the LGRBs from Blanchard et al. (2016), and the GOODS-CCSN from Svensson et al. (2010). Although our sample is shifted to larger sizes, we caution that each of these comparison distributions were derived from HST imaging, while our data is ground-based. A FWHM resolution of ∼0.8” corresponds to ∼ 2 kpc at z∼0.2 (the median redshift of our luminous IIn sample). As we have only consider resolved host galaxies in this analysis, this plot mainly emphasizes a finding from Chapter 7: that a significant number of luminous interacting transients explode in galaxies significantly larger than *any* observed hosts for SLSN-I.

Table 8.3. Astrometric Results, Sizes, Offsets, and Fractional Flux

Event	Filter	$\lambda_{\rm eff}$ Å	$\sigma_{\rm SN}$ (")	$\sigma_{\rm gal}$ (")	$\sigma_{\rm tie}$ (")	r_{50} (kpc)	r_{80} (kpc)	Offset (")	Offset (kpc)	Offset (r_{50} norm)	Fractional Flux	Error Ratio
"Luminous" SNIIn												
PS11ad	g	3429.5	0.011	0.062	···	4.074	6.344	0.133	0.735	0.180	0.839	0.00021
···	r	4360.1	0.011	0.051	···	4.098	7.335	0.086	0.474	0.116	0.979	0.00021
···	i	5288.9	0.011	0.036	···	3.861	6.635	0.065	0.358	0.093	0.978	0.00023
···	z	6093.7	0.011	0.021	···	3.848	6.761	0.027	0.151	0.039	1.000	0.00024
PS11kj	g	3483.4	0.012	0.068	···	5.270	8.051	1.110	5.937	1.127	0.252	0.00016
···	r	4428.6	0.012	0.026	···	4.891	7.735	1.143	6.113	1.250	0.410	0.00018
···	i	5372.0	0.012	0.060	···	5.047	8.256	1.230	6.575	1.303	0.352	0.00017
···	z	6189.5	0.012	0.040	···	5.351	8.679	1.144	6.117	1.143	0.521	0.00015
PS11vo	g	4369.8	0.011	0.058	···	3.169	5.057	0.545	1.133	0.358	0.938	0.00005
···	r	5555.6	0.011	0.041	···	3.063	4.964	0.566	1.177	0.384	0.935	0.00005
···	i	6739.1	0.011	0.023	···	2.923	4.787	0.529	1.100	0.376	0.928	0.00006
···	z	7764.6	0.011	0.029	···	2.930	4.817	0.542	1.127	0.385	0.918	0.00006
PS11aop	g	4323.3	0.009	0.011	···	2.636	5.119	0.351	0.794	0.301	0.883	0.00006
···	r	5496.5	0.009	0.017	···	2.556	4.889	0.353	0.799	0.313	0.866	0.00006
···	i	6667.4	0.009	0.028	···	2.534	4.952	0.343	0.777	0.307	0.853	0.00006
···	z	7682.0	0.009	0.019	···	2.674	5.304	0.319	0.722	0.270	0.847	0.00006
PS12zc	g	4178.8	0.017	0.051	···	7.042	11.244	4.057	11.475	1.630	0.384	0.00005
···	r	5312.9	0.017	0.056	···	6.882	11.244	4.101	11.600	1.686	0.363	0.00005
···	i	6444.6	0.017	0.052	···	6.561	10.786	4.062	11.489	1.751	0.286	0.00006
···	z	7425.3	0.017	0.029	···	6.878	11.588	4.076	11.528	1.676	0.268	0.00005
PS12car	g	2902.8	0.046	0.068	···	6.170	8.821	1.879	13.274	2.151	0.190	0.00281
···	r	3690.5	0.046	0.050	···	6.864	10.664	2.025	14.302	2.084	0.119	0.00227
···	i	4476.7	0.046	0.043	···	6.834	10.865	2.039	14.405	2.108	0.026	0.00229
···	z	5157.9	0.046	0.067	···	6.878	11.192	1.095	7.735	1.125	0.080	0.00226
PS12cht	g	4248.0	0.017	0.085	···	1.963	3.244	0.285	0.730	0.372	0.785	0.00051
···	r	5400.8	0.017	0.063	···	1.943	3.454	0.270	0.690	0.355	0.845	0.00052
···	i	6551.2	0.017	0.058	···	1.754	3.147	0.306	0.782	0.446	0.832	0.00064
···	z	7548.2	0.017	0.059	···	1.854	3.258	0.360	0.923	0.498	0.776	0.00057
PS13byi	g	2899.3	0.022	0.069	···	4.832	7.037	0.920	6.504	1.346	0.265	0.00107
···	r	3686.1	0.022	0.047	···	5.734	9.192	0.826	5.839	1.018	0.449	0.00076
···	i	4471.3	0.022	0.050	···	5.059	8.192	0.768	5.430	1.073	0.352	0.00097
···	z	5151.8	0.022	0.022	···	4.938	7.780	0.738	5.217	1.057	0.419	0.00102
PS13epy	r	4791.4	0.050	0.035	···	3.978	7.337	1.038	4.529	1.138	0.257	0.00295
···	i	5812.1	0.050	0.040	···	3.551	6.139	0.958	4.180	1.177	0.473	0.00370

Table 8.3—Continued

Event	Filter	$\lambda_{\rm eff}$ Å	$\sigma_{\rm SN}$ (”)	$\sigma_{\rm gal}$ (”)	$\sigma_{\rm tie}$ (”)	r_{50} (kpc)	r_{80} (kpc)	Offset (”)	Offset (kpc)	Offset (r_{50} norm)	Fractional Flux	Error Ratio
···	z	6696.5	0.050	0.050	···	3.619	6.100	0.974	4.247	1.173	0.443	0.00356
SN1999bd	g	4097.9	0.268	0.035	0.280	2.741	4.348	1.066	2.767	1.009	0.612	0.13471
SN2003ma[a]	···	···	0.012	···	···	···	···	0.064	0.460	···	···	···
SN2006tf	g	4391.7	0.006	0.027	0.132	1.980	3.093	0.378	0.525	0.265	0.709	0.00858
SN2006gy	g	4627.9	0.005	0.072	0.058	2.106	4.229	0.939	0.339	0.161	0.948	0.00010
SN2008am	g	3834.7	0.150	0.023	0.210	3.408	5.347	1.180	4.285	1.257	0.243	0.07561
SN2010jl	g	4666.8	0.003	···	0.097	···	···	···	···	···	0.802	···
SN2011cp	g	3417.9	1.000	0.036	0.087	3.484	5.464	0.246	1.274	0.366	···	2.22584
SN2011eu	g	4249.3	0.515	0.043	0.339	3.746	6.322	2.419	4.885	1.304	0.317	0.11047
CSS100217[b]	···	···	···	···	···	···	···	<0.15	<0.381	···	1.000	···
CSS121015	r	4794.0	0.008	0.030	0.091	3.271	4.997	0.198	0.849	0.260	0.913	0.01434
PS15blq	g	4334.8	0.050	0.023	···	3.146	5.049	0.590	1.308	0.416	0.644	0.00124
PS15ces	g	4300.4	0.028	0.029	0.094	4.078	7.181	3.111	7.320	1.795	0.044	0.00320
LSQ15abl	g	4486.4	0.003	0.028	0.061	6.602	9.547	0.043	0.069	0.010	0.997	0.00022
“SNIIn/SNIa-CSM”												
PS11jf	r	4836.3	0.011	0.090	···	3.601	5.511	0.490	2.076	0.576	0.968	0.00017
···	i	5866.5	0.011	0.085	···	4.021	6.524	0.504	2.135	0.531	0.973	0.00013
···	z	6759.2	0.011	0.090	···	3.304	5.063	0.440	1.861	0.563	0.956	0.00020
SN1997cy	g	4433.0	0.006	0.044	0.152	3.260	5.311	1.257	1.531	0.470	0.668	0.00323
SN1999E	g	4597.2	0.107	0.048	0.113	2.458	4.269	6.298	3.224	1.311	0.478	0.00105
SN2002ic	g	4424.7	0.011	0.046	0.117	3.285	5.029	4.293	5.363	1.633	0.316	0.00200
SN2005gj	g	4441.3	0.005	0.016	0.150	2.993	5.094	0.505	0.594	0.198	0.864	0.00348
SN2008J	g	4642.4	0.005	0.028	0.099	4.591	8.632	4.963	1.585	0.345	0.791	0.00005
SN2008cg	g	4552.8	0.251	0.032	0.290	4.991	8.849	16.002	11.351	2.274	0.570	0.00297
SN2011jb	g	4355.2	1.000	0.011	0.250	1.519	2.706	0.430	0.660	0.434	···	1.08265
SN2012ca	g	4628.7	0.001	0.058	···	···	···	9.138	3.675	···	···	···
SN2013dn	g	4449.7	0.023	0.021	0.090	8.064	12.365	13.146	15.337	1.902	0.078	0.00018
CSS120327	g	4323.3	1.000	0.027	0.240	1.631	2.706	0.564	0.941	0.577	···	1.10889
PTF11kx	g	4504.9	0.025	0.037	0.104	3.640	5.797	6.442	5.819	1.599	0.516	0.00070
“Normal” SNIIn												
PS10caa	g	4465.8	0.047	0.037	···	1.506	2.651	2.298	3.891	2.584	0.090	0.00274
···	r	5677.7	0.047	0.056	···	1.638	2.939	2.372	4.016	2.452	0.089	0.00232
···	i	6887.2	0.047	0.035	···	1.455	2.595	2.296	3.887	2.672	0.044	0.00294
···	z	7935.3	0.047	0.031	···	1.861	3.524	2.239	3.790	2.037	0.009	0.00180
PS12dm	g	4060.5	0.014	0.037	···	5.617	9.024	1.946	6.387	1.137	0.359	0.00007

Table 8.3—Continued

Event	Filter	$\lambda_{\rm eff}$	$\sigma_{\rm SN}$	$\sigma_{\rm gal}$	$\sigma_{\rm tie}$	r_{50}	r_{80}	Offset			Fractional Flux	Error Ratio
		Å	(")	(")	(")	(kpc)	(kpc)	(")	(kpc)	(r_{50} norm)		
···	r	5162.4	0.014	0.046	···	5.263	8.783	1.982	6.506	1.236	0.326	0.00008
···	i	6262.1	0.014	0.039	···	4.996	8.481	1.890	6.204	1.242	0.311	0.00008
PS12bli	g	4101.5	0.018	0.073	···	5.111	8.664	2.357	7.370	1.442	0.355	0.00013
···	r	5214.6	0.018	0.024	···	5.166	9.065	2.181	6.818	1.320	0.398	0.00012
···	i	6325.3	0.018	0.053	···	4.789	8.442	2.126	6.647	1.388	0.369	0.00014
PS12ces	g	4087.8	0.029	0.010	···	3.323	5.510	1.181	3.755	1.130	0.514	0.00077
···	r	5197.1	0.029	0.010	···	3.364	5.561	1.151	3.658	1.087	0.530	0.00075
···	i	6304.1	0.029	0.008	···	3.211	5.394	1.153	3.664	1.141	0.497	0.00082
···	z	7263.5	0.029	0.010	···	3.245	5.450	1.179	3.747	1.155	0.505	0.00081
PS13hi	g	4689.1	0.019	0.039	···	3.410	5.912	6.134	4.793	1.405	0.583	0.00002
···	r	5961.6	0.019	0.029	···	3.389	6.013	6.065	4.739	1.399	0.582	0.00002
···	i	7231.5	0.019	0.030	···	3.284	5.922	6.098	4.765	1.451	0.554	0.00002
···	z	8332.0	0.019	0.040	···	3.215	5.826	6.077	4.748	1.477	0.542	0.00002
PS13adh	g	4289.1	0.023	0.110	···	1.849	2.762	0.323	0.775	0.419	0.704	0.00086
···	r	5453.0	0.023	0.052	···	2.024	3.367	0.323	0.774	0.382	0.845	0.00072
···	i	6614.6	0.023	0.036	···	1.868	3.236	0.274	0.657	0.352	0.939	0.00084
···	z	7621.2	0.023	0.090	···	1.896	3.053	0.284	0.680	0.359	0.697	0.00082
PS13epq	g	3867.3	0.052	0.029	···	3.076	4.712	0.489	1.957	0.636	0.829	0.00458
···	r	4916.8	0.052	0.017	···	3.126	5.094	0.536	2.146	0.686	0.761	0.00444
···	i	5964.2	0.052	0.051	···	2.940	4.924	0.610	2.443	0.831	0.751	0.00502
···	z	6871.8	0.052	0.068	···	2.737	4.323	0.449	1.796	0.656	0.813	0.00579
SN1988Z	g	4610.6	1.000	0.077	···	5.115	8.052	10.214	4.748	0.928	0.488	0.00826
SN1994W	g	4697.9	1.000	0.061	···	2.129	4.603	20.763	2.326	1.093	0.423	0.00277
SN1994Y	g	4676.9	1.000	0.034	···	9.274	15.123	36.604	6.564	0.708	0.578	0.00037
SN1995G	g	4642.4	1.000	0.065	···	2.581	4.881	16.672	5.134	1.989	0.361	0.01424
SN1998S	g	4702.4	1.000	0.073	···	3.189	6.350	48.176	4.133	1.296	0.483	0.00072
SN2005cl	g	4597.2	1.000	0.063	···	8.740	13.634	22.094	11.063	1.266	0.282	0.00328
SN2005cp	g	4615.2	1.000	0.046	···	3.899	6.863	6.530	2.706	0.694	0.873	0.01129
SN2005db	g	4647.0	1.000	0.072	···	4.894	8.791	17.962	5.155	1.053	0.483	0.00344
SN2005ip	g	4683.9	0.003	0.036	0.070	2.436	4.157	14.340	2.296	0.943	0.338	0.00002
SN2005kj	g	4637.8	0.003	0.128	0.160	3.418	5.897	5.441	1.862	0.545	0.475	0.00026
SN2006aa	g	4619.7	0.038	0.124	0.071	6.281	10.498	13.637	5.864	0.934	0.681	0.00003
SN2006bo	g	4647.0	0.010	0.131	0.070	4.011	6.526	18.567	5.824	1.452	0.062	0.00003
SN2006jd	g	4628.7	0.013	0.103	0.078	3.593	5.782	21.954	8.597	2.392	0.462	0.00007
SN2006qq	g	4583.7	0.018	0.046	0.160	4.163	7.754	8.468	4.587	1.102	0.584	0.00044

Table 8.3—Continued

Event	Filter	$\lambda_{\rm eff}$	$\sigma_{\rm SN}$	$\sigma_{\rm gal}$	$\sigma_{\rm tie}$	r_{50}	r_{80}	Offset			Fractional Flux	Error Ratio
		Å	(”)	(”)	(”)	(kpc)	(kpc)	(”)	(kpc)	(r_{50} norm)		
SN2007pk	g	4637.8	1.000	0.212	···	4.352	7.114	7.939	2.491	0.572	0.842	0.00520
SN2008fq	g	4665.4	1.000	0.030	···	6.602	9.885	7.497	1.687	0.255	0.784	0.00116
SN2009ip	g	4688.6	0.060	0.027	···	1.974	3.202	44.023	5.442	2.757	0.188	0.00001
SN2009kn	g	4642.4	1.000	0.020	···	3.894	6.206	22.971	7.339	1.885	0.266	0.00673
SN2011ht	g	4697.9	1.000	0.210	···	3.227	5.167	20.394	2.002	0.621	0.600	0.00093
PTF10tyd	g	4437.2	0.142	0.067	0.072	6.924	10.568	10.092	12.076	1.744	0.137	0.00076
PTF12cxj	g	4552.8	0.200	0.069	0.104	5.222	8.424	8.703	6.145	1.177	0.274	0.00093
PTF12ksy	g	4574.9	0.053	0.024	0.072	5.849	10.240	16.468	10.080	1.723	0.453	0.00009
iPTF13agz	g	4462.4	1.000	0.066	···	4.077	8.229	2.011	2.192	0.538	0.737	0.07147

[a] SN 2003ma was discovered behind the LMC by the SuperMACHO microlensing survey. We take the precise offset provided in Rest et al. (2011). The $\sigma_{\rm SN}$ value quotes for SN 2003ma is the error in the transient-host offset provided in Rest et al. (2011).

[b] The Seyfert host galaxy of CSS100217 is unresolved in SDSS. We take the limit on the offset provided in Drake et al. (2011b).

8.6 Transient-Host Offsets

Using these SN centroids, galaxy positions, and galaxy radii, we compute the projected angular separation between the transient location and the galaxy core (R), the projected physical separation (R_{kpc}), and the r_{50} host-normalized offset (R_{norm}). All three values are listed in Table 8.3. The total error on the offset measurement is taken to be the quadrature sum of σ_{tie}, σ_{gal}, and σ_{SN}. For the nearby (z=0.01) irregular host galaxy of the luminous SN 2010jl, we were unable to arrive at a SExtractor solution for the entire host galaxy, prohibiting a robust determinations of the galaxy center. Therefore, we have not computed a transient-host offset for this event, but note that it exploded near the center of of the bright northern portion of the galaxy (see Figure 8.2).

8.6.1 Projected Physical Offsets

In the left panel of Figure 8.5 we plot the cumulative distributions of the projected physical offsets for the three classes of interacting transients in our sample. The distribution for the luminous Type IIn SN does not include the luminous transient CSS100217, which exploded in the inner 150pc of its Seyfert host galaxy. Our final sample of events with computed host-transient offsets consists of 20 luminous Type IIn SN, 12 Type IIn/Ia-CSM SN, and 30 standard luminosity Type IIn SN. To match the literature sample, for the transients discovered in the PS1-MDS we plot data based on the observed band whose effective pivot wavelength is closest to rest frame g−band.

On average, both the luminous Type IIn and Type IIn/Ia-CSM SN occur at smaller projected physical offsets than standard luminosity Type IIn. The three samples have

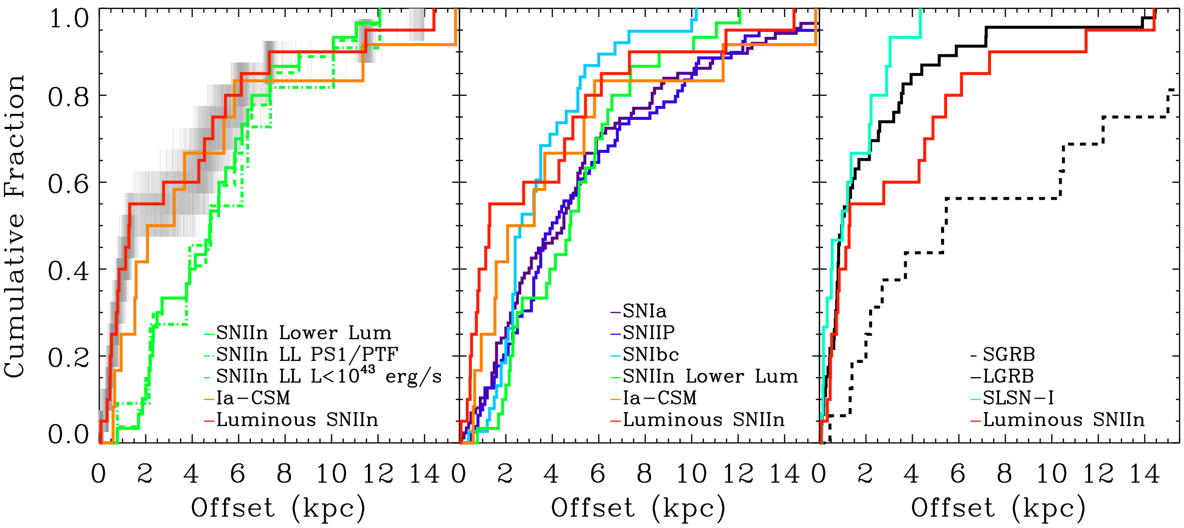

Figure 8.5.—: Cumulative distributions of projected physical offsets. *Left:* Luminous Type IIn SN (red), Type IIn/Ia-CSM (orange) and standard luminosity Type IIn SN (green). Grey shaded regions show the results of a Monte Carlo error analysis for the cumulative distribution of the luminous Type IIn SN (see text). *Middle:* Same as left, but also shown are Type Ia (purple), Type IIP (blue), and Type Ibc (cyan) from Prieto et al. (2008) *Right:* Luminous Type IIn SN (red), SLSN-I (teal), LGRBs (black) and SGRBs (Fong & Berger 2013, dashed black).

median values of 1.3 kpc, 3.2 kpc, and 4.8 kpc, respectively. 55% of the luminous Type IIn SN in our sample occur within the inner 2 kpc of their host galaxies, while only ∼5% of the standard luminosity Type IIn SN are observed in these regions. As described above, lack of standard luminosity Type IIn SN, in the central regions of their host galaxies has been observed in previous studies (Anderson & James 2009; Anderson et al. 2012; Kelly & Kirshner 2012b; Habergham et al. 2014), and we now demonstrate that this trend does *not* also apply to luminous members of this spectroscopic class.

In the left panel of Figure 8.5 we also show (dashed green lines) the cumulative distributions of two sub-samples of our standard luminosity Type IIn SN: events with peak luminosities explicitly below 10^{43} erg s^{-1} (to examine the influence of our adopted luminosity cutoff) and events discovered by the PS1 and PTF surveys only (to examine any biases due to discovery by targeted versus untargeted surveys). All three distributions of standard luminosity Type IIn SN are highly consistent with one another ($p > 0.98$). A K$-$S test between the luminous Type IIn SN and the Type IIn/Ia-CSM yields a $p-$value of 0.43, while a K$-$S test between the luminous Type IIn SN and the standard luminosity Type IIn SN yields a p-value of 1.8×10^{-3}, indicating that these were drawn from distinct populations.

The total errors on our offset measurements (σ_{R}) for the PS1-MDS transients and the (low-redshift) standard luminosity Type IIn SN are small compared to the offsets themselves. However, our samples also include a small number of luminous Type IIn SN and Type IIn/Ia-CSM events from the literature for which only absolute astrometric positions were available, resulting in larger values of $\sigma_{\mathrm{R}}/\mathrm{R}$. In order to examine the effect that these uncertainties have on our conclusions, we carry a Monte Carlo analysis. We compute multiple realizations of the cumulative distribution function for both our luminous Type IIn SN and IIn/Ia-CSM samples. The offset value for each event is drawn from a probability distribution described by its measurement and error. Transient-host offsets are a positive definite quantity and can be described by a Rice distribution (see Blanchard et al. 2016). The results of this Monte Carlo analysis for the luminous Type IIn SN are shown as a grey 2D histogram in the left panel of Figure 8.5, with darker regions corresponding to higher probability. In 1000 realizations, the KS test p-value for the luminous and standard luminosity Type IIn SN was always below 0.05, with a *maximum* value of 6.7×10^{-3}. This indicates that our conclusion that they are statistically distinct populations does not result from the small number of events in our sample with higher offset uncertainties.

In the middle panel of Figure 8.5 we compare our samples of interacting transients to the projected physical offsets of Type Ia SN, Type II SN and Type Ibc SN from Prieto et al. (2008). KS-tests between the luminous Type IIn SN and the Type II and Ibc SN yield p-values of 4.2×10^{-3} and 3.6×10^{-3}, respectively (and remain below 0.05 in all iterations of our Monte Carlo analysis). KS-tests between the Type IIn/Ia-CSM and Type Ia SN and between the standard luminosity Type IIn and Type II SN yield $p-$values of 0.54 and 0.72, respectively.

Finally, in the right panel of Figure 8.5 we compare our sample of luminous Type IIn SN to the SLSN-I sample from Lunnan et al. (2015b), the LGRB sample from Blanchard et al. (2016) and the SGRB sample from Fong & Berger (2013). Luminous Type IIn SN, SLSN-I and LGRBs all have similar median offset values of $\sim$1 kpc, but their distributions separate beyond this point. However, we note that the galaxy sizes probed by each of these samples are different (see Figure 8.4).

8.6.2 Host-Normalized Offsets

In order to account for the intrinsic size variations between different galaxies, we next examine the host-normalized offset ($R_{\rm norm}$). In Figure 8.6, we plot cumulative distribution functions of $R_{\rm norm}$ for our sample of interacting transients along with comparison samples from the literature—similar to Figure 8.5.

In the left panel of Figure 8.6 we see that the luminous Type IIn SN and Type IIn/Ia-CSM events are significantly more centrally concentrated than the standard luminosity Type IIn SN, even when galaxy size is taken into account. The median host-normalized offsets are 0.42, 0.58, and 1.2, respectively. KS-tests between the

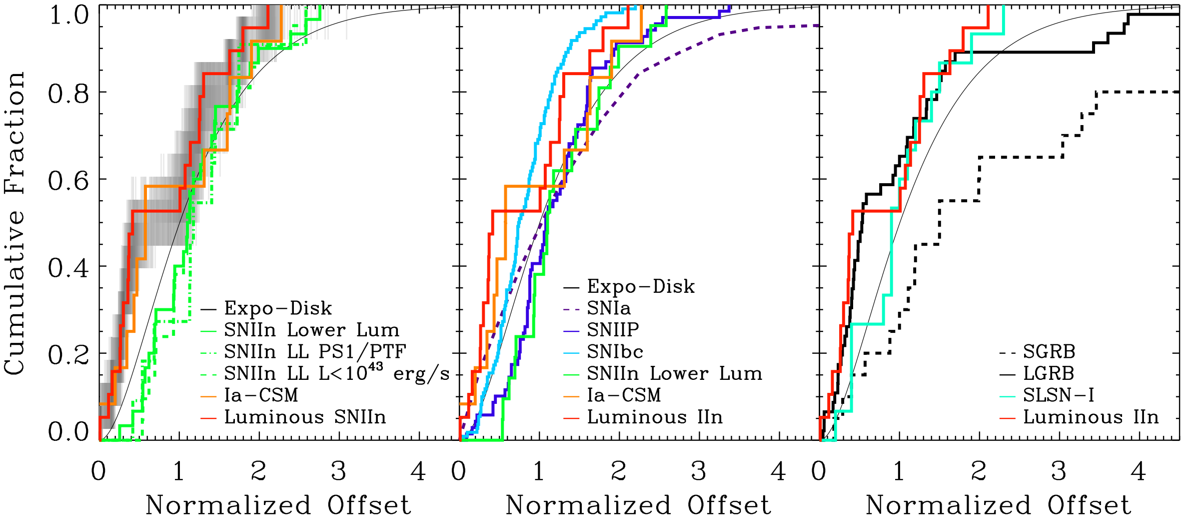

Figure 8.6.—: Same as Figure 8.5 but host-transient offsets have been normalized by the galaxy half-light radius. Middle panels now shows the Type Ibc SN (cyan) and Type II SN (blue) samples of Kelly & Kirshner (2012b) and the Type Ia SN from Galbany et al. (2012). All panels also show the cumulative distribution of an exponential disk profile (smooth black line).

luminous Type IIn SN and the Type IIn/Ia-CSM events and standard luminosity Type IIn SN yield *p*-values of 0.55 and 4.6×10^{-3}, respectively (and in the latter case remain below 0.05 in all iterations of our Monte Carlo analysis). Intriguingly, both the current samples of luminous Type IIn SN and IIn/Ia-CSM events show an apparent gap in host-normalized offsets between 0.5 and 1.0 effective radii. Larger samples will be necessary to confirm this observation.

In the middle and right panels of Figure 8.6, we compare our samples of interacting transients to the normalized offset distributions of Type Ibc and Type II SN from Kelly & Kirshner (2012b) Type Ia SN from Galbany et al. (2012), and the same samples of LGRBs, SGRBs, and SLSN-I described above. Our independent analysis recovers the result found in previous studies even when only PS1/PTF discovered events are considered: that standard luminosity Type IIn SN and Type II SN appear to explode in similar locations in their host galaxies. While Type Ibc SN are also centrally concentrated in their hosts in comparison to Type II SN, we find a nominal KS test *p*-value of 1.6×10^{-2} between our sample of luminous events and the Type Ibc sample from Kelly & Kirshner (2012b). This difference is driven by the high fraction of luminous Type IIn SN with $\mathrm{R_{norm}} < 0.5$ in comparison to Type Ibc SN (∼50% versus ∼22%). In approximately 50% of our Monte Carlo trials this *p*-value rises above 0.05. However, if we perform a quality cut on our sample by removing the one luminous Type IIn SN (SN 2011cp) with $\sigma_{\mathrm{Rnorm}} > \mathrm{R_{norm}}$, then this fraction falls to ∼20%. Finally, we find that the luminous Type IIn SN and LGRBs show very similar normalized offsets, with the exception of a set of LGRBs at very high offsets (although see Blanchard et al. 2016 for a discussion of these events).

In each panel of Figure 8.6 we also plot (smooth black lines) the distribution function that is predicted if a class of transients explodes at locations which trace an exponential disk profile (the expected surface brightness profile for star-forming disk galaxies). We find that the luminous Type IIn SN also show a large excess in comparison to the exponential disk profile at small offsets ($\mathrm{R_{norm}} < 0.5$), with a KS test *p*-value between the two distributions of 7.0×10^{-3}. This value exceeds 0.05 in only 5.5% of Monte Carlo trials when we perform the quality cut on our sample described above (∼20% of cases when SN 2011cp in included). A similar excess at small offsets compared to an exponential disk profile was observed by Blanchard et al. (2016) for LGRBs.

In Figure 8.7 we further examine this comparison by plotting the *ratio* of the cumulative distributions for four populations (luminous Type IIn SN, LGRBs, Type Ibc SN, and standard luminosity Type IIn SN) to the the cumulative distribution of the exponential disk profile. This highlights the large excess of both luminous Type IIn SN and LGRBs in the central regions of their hosts, before they settle onto the exponential disk profile between normalized offsets of 0.5 and 1.0. In contrast, the Type Ibc SN follow the exponential disk distribution out to a normalized offset of ∼0.5 and then show and excess beyond that point. Standard luminosity Type IIn SN show a strong deficit of events at small radii.

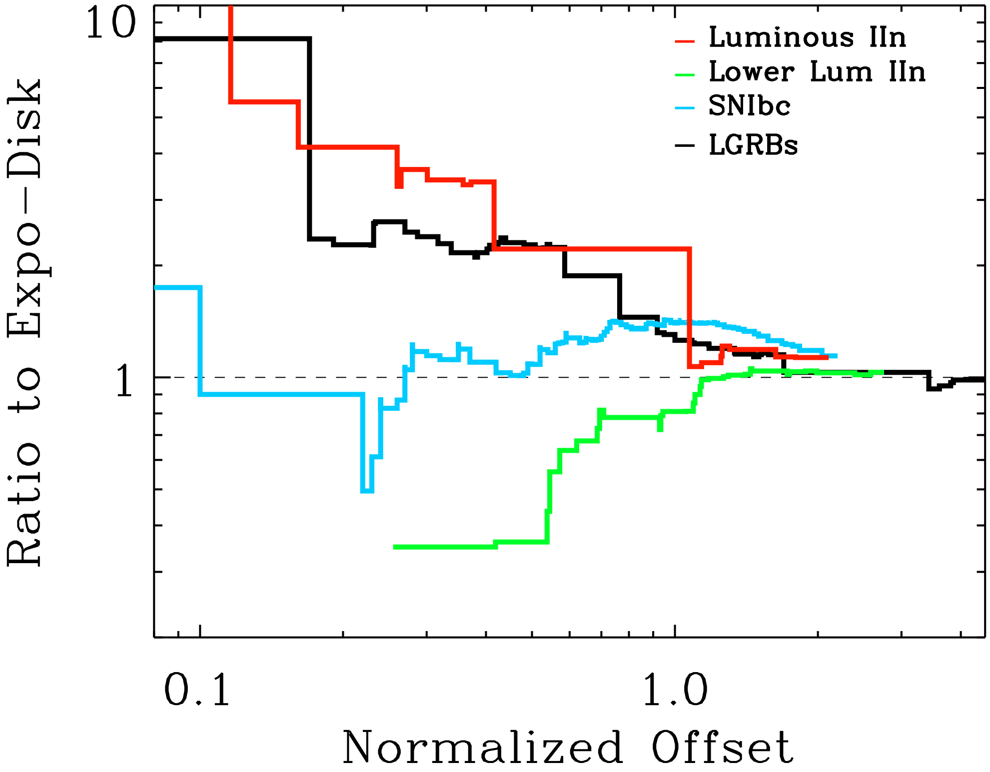

Figure 8.7.—: Ratio of the cumulative distribution of Luminous Type IIn SN (red), LGRBs (black), Type Ibc SN (cyan) and standard luminosity Type IIn SN (green) to the exponential disk profile. Both Luminous Type IIn SN and LGRBs show a large excess inside a $R_{\mathrm{norm}} = 0.5$, Type Ibc SN show an excess beyond $R_{\mathrm{norm}} = 0.5$, and standard luminosity Type IIn SN show a central deficit.

8.6.3 Host-galaxy Offset versus Transient Luminosity

In the sections above we found that luminous interacting transients are more readily observed in the inner portions of their galaxies than standard luminosity Type IIn SN. In Figure 8.8 we plot the peak luminosity of the transients in our sample versus their projected physical (right panel) and host-normalized (left panel) offsets. Symbols and colors have the same meaning as Figure 8.1. There does not appear to be a strong linear correlation between transient luminosity and host offset. Pearson correlation coefficients for each panel are only -0.22 and -0.18, respectively. While a significant number of luminous transients explode in the inner regions of their host galaxies, they also explode at high offsets. This is true independent of the cutoff which we impose in our definition a "luminous" transient. Even at the highest luminosities ($L_{\rm bol,p} > 10^{44}$ erg s^{-1}; $M_{\rm p} < -22$ mag) events are observed at both large and small offset. This plot also highlights (a) the apparent lack of luminous Type IIn SN between 0.5 and 1.0 effective radii and (b) the dearth of Type IIn SN with $L_{\rm bol,p} < 10^{43}$ erg s^{-1} in the inner $\sim$ 2 kpc (or inner $0.5 \times r_{50}$) of their host galaxies. Possible physical explanations for these trends are discussed in Section 8.8, below.

8.7 Fractional Flux Measurements

In addition to simple host-transient offsets, we also investigate how the brightness at the SN location compares to the overall surface brightness distribution of the host galaxy. Such methods offer a useful means to examine if SN locations correlate with sites of active star formation (as traced by Hα or UV light) as well as in cases of irregular

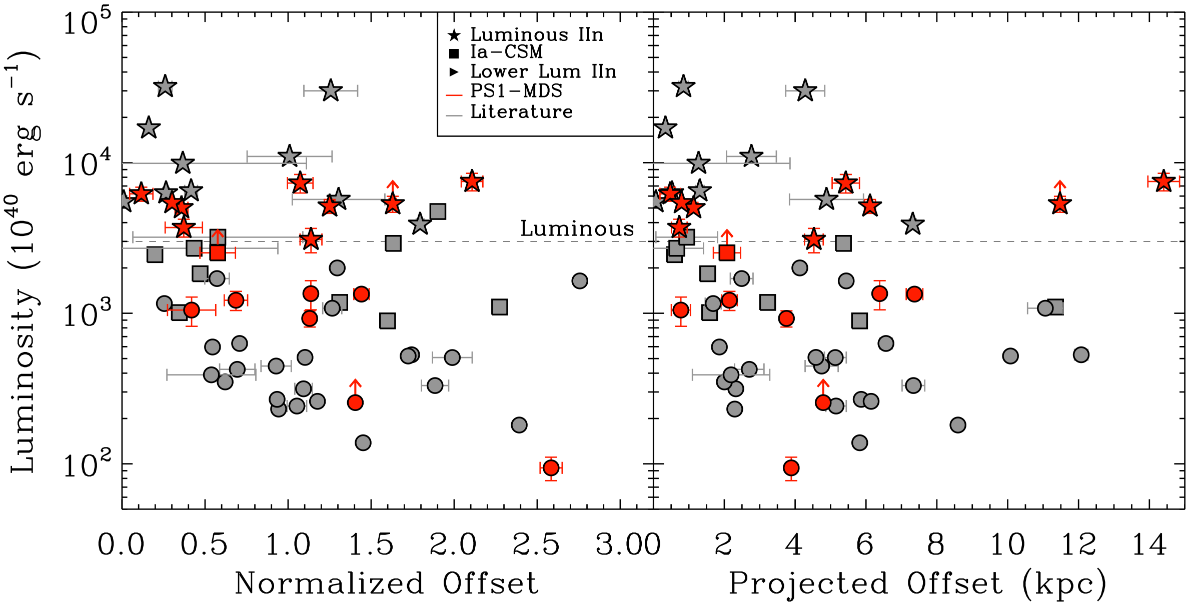

Figure 8.8.—: Host-normalized (left) and physical (right) offsets versus peak transient luminosity. Symbols have the same meaning as in Figure 8.1. There is a deficit of standard luminosity Type IIn SN which not observed for luminous events, but no strong correlation between offset and luminosity is observed.

galaxies where the concept of a "galaxy center" is not well-defined. As described in the introduction to this work, these methods have been successfully applied to a wide array of transients in the literature.

Here we utilize the method outlined by Fruchter et al. (2006) and calculate the fraction of the host galaxy flux which is contained in pixels fainter than or equal to the flux at the location of the transient. Using SExtractor, we first extract the pixels of the host galaxy, defined as concurrent pixels $>1\sigma$ above the sky background. We then calculate the flux at the SN position. For cases where the error circle of the SN position is contained within a single pixel (as is the case for all PS1-MDS-discovered SN) we simply take the flux at the transient location as the flux within that pixel. For events where the error circle encompasses multiple pixels, we take an area-weighted mean of the flux within those pixels. We then compute the "fractional flux" as total flux in galaxy pixels fainter than or equal to the flux at the SN location. Thus, a fractional flux measurement of 1.0 implies that the SN exploded on the brightest pixel in the host galaxy, while a fractional flux measurement of 0.0 implies that the SN exploded outside the region of the galaxy which is $>1\sigma$ above the background. The resulting fractional flux measurements for our sample of interacting transients is listed in Table 8.3.

In a detailed error analysis, Blanchard et al. (2016) found that fractional flux measurements can be significantly biased if the ratio of the area contained with SN error circle to the total galaxy area is high. As a result, we have not computed fractional flux values for three events in our sample (a single luminous Type IIn event, and two IIn/Ia-CSM events) where this ratio (listed for all events in Table 8.3) is larger than 0.15. With this cut, our sample of interacting transients with fractional flux measurements consists of 19 luminous Type IIn SN, 9 Type IIn/Ia-CSM SN, and 30 standard luminosity Type IIn SN.

In Figure 8.9 we plot the cumulative distributions of the g-band fractional flux measurements for various subsets of our sample (left panel), compared to low redshift Type Ic, Type II and Type Ia SN (Kelly et al. 2008, middle panel) and to LGRBs, SLSN-I, high redshift CCSN, and SGRBs (Blanchard et al. 2016; Lunnan et al. 2015b; Svensson et al. 2010; Fong & Berger 2013, respectively; right panel). The one-to-one relation shown in each panel represents the expectation if a population of transients uniformly traces the light in their hosts.

The standard luminosity Type IIn and luminous Type IIn SN initially follow similar distributions. However, the luminous events then deviate to the right portion of the plot,

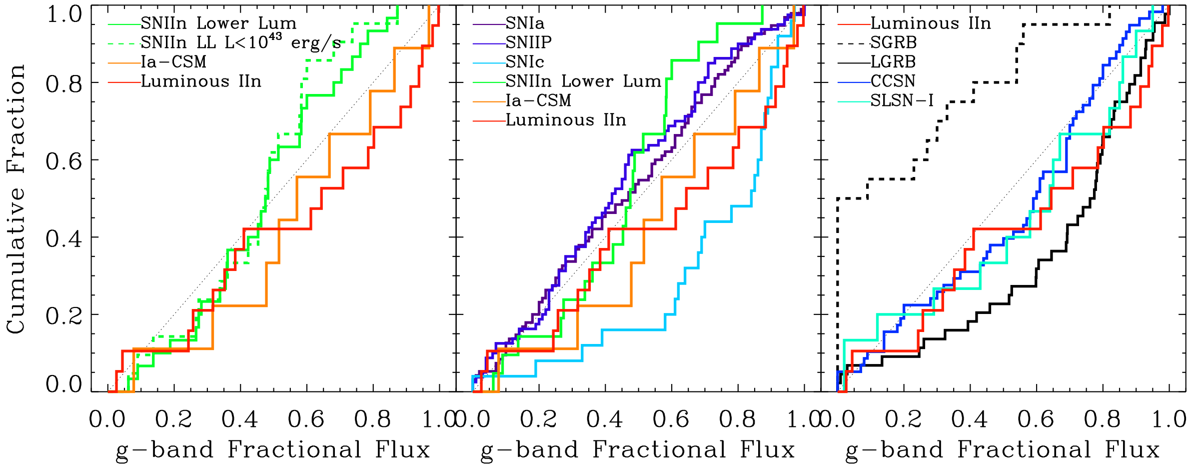

Figure 8.9.—: Cumulative distribution of the fraction of galaxy flux contained in pixels fainter than the SN location. *Left:* Luminous Type IIn SN (red), Type IIn/Ia-CSM (orange), and standard luminosity Type IIn SN (green). *Middle:* Same as left, but also showing Type Ic (cyan) Type IIP (blue) and Type Ia (purple) from Kelly et al. (2008). *Right:* Luminous Type IIn SN (red) in comparison to LGRBs (Blanchard et al. 2016, black), SLSN-I (Lunnan et al. 2015b, teal), high-redshift CCSN (Svensson et al. 2010, blue), and SGRBs (Fong & Berger 2013, dashed black).

indicating that they more closely trace the brighter regions of their hosts. A KS-test between their distributions yields a p-value of 0.03. The luminous Type IIn SN show a similar distribution to the Type IIn/Ia-CSM SN and SLSN-I (p = 0.93 and 0.86, respectively) while both LGRBs and Type Ic SN are shifted to even higher fractional flux values (although, p = 0.38 and 0.39, respectively).

In literature studies of fractional flux measurements, a common supposition made when a class of transients closely trace the brightest regions of their hosts is that these bright regions correspond to the largest star forming regions where the most massive stars can form (e.g Fruchter et al. 2006; Kelly et al. 2008). And, indeed, in the case of LGRB hosts, which are primarily dwarf galaxies with high specific star-formation rates, detailed studies of local examples have revealed that bright clumps are predominately massive

O−star and WR clusters (Hadfield & Crowther 2006). However, this interpretation is more complex for the luminous Type IIn SN host galaxies presented here.

In Figure 8.10 we plot fractional flux versus host normalized offset for all of the interacting transients in our sample. A clear correlation between the two parameters is seen, with a Pearson correlation coefficient of −0.8. Thus, the location of luminous Type IIn SN in Figure 8.9 mainly reflects the result that a significant number of luminous Type IIn SN explode in the (bright) central regions of their host galaxies. Notably, (Blanchard et al. 2016) come to a similar conclusion for LGRBs. They find that LGRBs located at offsets greater than $0.5\mathrm{R}_{\mathrm{norm}}$ uniformly trace their host galaxy light (similar manner Type II SN) and that the location of LGRBs in the far right portion of the fractional flux diagram is driven primarily by GRBs which explode in the bright *central* regions of their host galaxies.

However, while the luminosity in these bright central knots of LGRB host galaxies is likely dominated by young star formation—and a subset of luminous Type IIn host galaxies *are* dwarf galaxies similar to LGRB hosts—our sample also includes a number of Milky Way-like/S0 galaxies. In Figure 8.11 we plot our host−normalized offsets versus host galaxy M_{B} for the galaxies which were also studied in Chapter 7. Of the luminous transients in our sample that exploded at small offsets, half are located in galaxies with $\mathrm{M}_{\mathrm{B}} \approx -20$ mag. An examination of these galaxies (e.g. PS1-11vo, PS1-11aop, LSQ15abl, SN2006gy; see Figure 8.12) reveal color gradients and signatures of older stellar populations—in addition to active star formation—in their central regions. Thus, the high fractional flux values measured for these objects mainly emphasizes that some aspect of the stellar populations present in the central regions is conducive for the formation of luminous Type IIn SN progenitors.

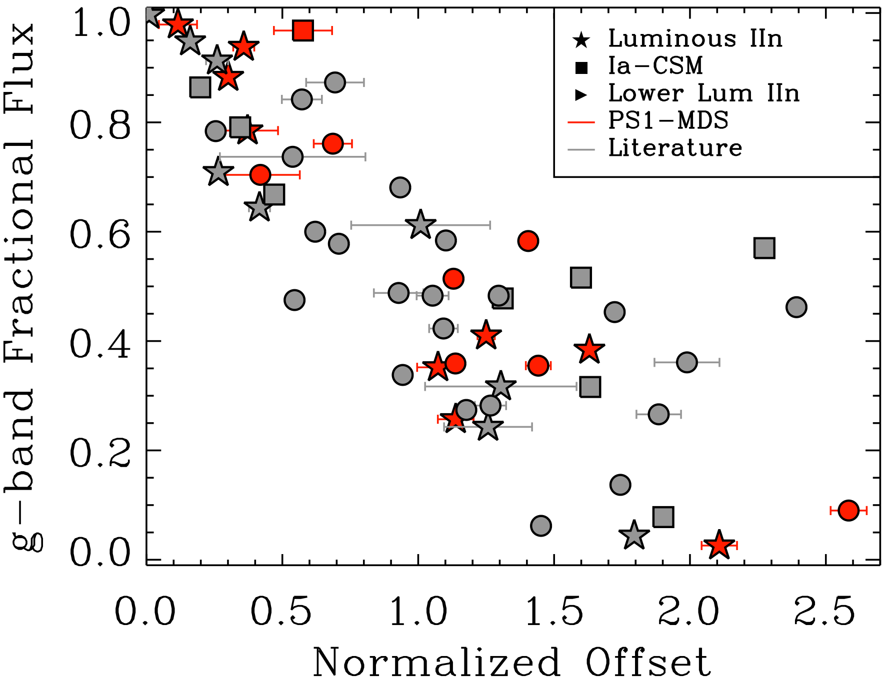

Figure 8.10.—: Fraction of galaxy flux in pixels fainter than SN location versus normalized host galaxy offset. A clear correlation is observed. The shift of Luminous Type IIn SN to higher fractional flux values in comparison to standard luminosity Type IIn SN (Figure 8.9) is entirely driven by the population of luminous events located at small normalized offsets.

Finally, we note that many of our events in our luminous Type IIn SN and Type IIn/Ia-CSM samples occur at higher redshift than the standard luminosity Type IIn SN taken from the literature. By setting a common signal-to-noise ratio of one when defining galaxy pixels for all events in our sample, we may be including faint surface brightness regions of local galaxies, which would below our detection limit for higher-redshift events. However, such an effect would only *accentuate* the observed difference between luminous and standard luminosity Type IIn SN.

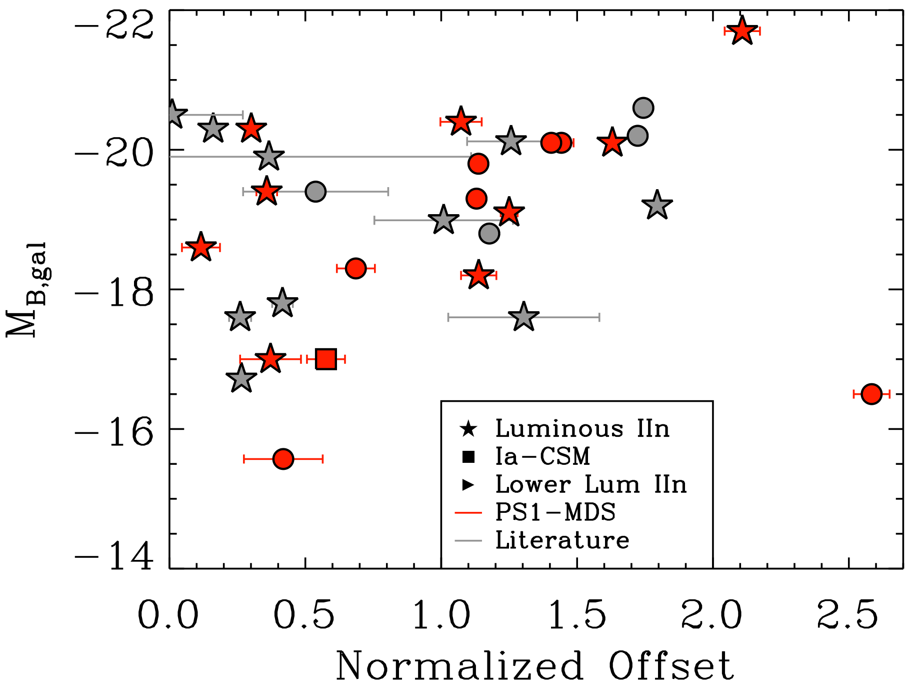

Figure 8.11.—: Host-normalized offset versus galaxy M_B from Chapter 7.

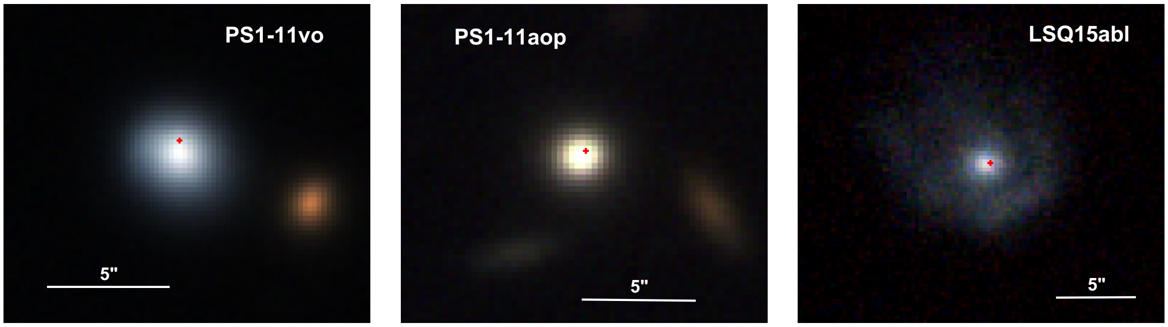

Figure 8.12.—: Color images of PS1-11vo, PS1-11aop, and LSQ15abl host galaxies constructed from giz_{P1}-band images. The explosion sites of the transients within the central regions of their giant hosts ($M_B \sim -20$ mag) are marked with red crosses.

8.8 Sub-galactic Environments: Summary and Discussion

We have performed the first statistical analysis of the locations of luminous interacting transients within their host galaxies. In our sample, we find that while luminous Type IIn SN explode at a wide range of host-transient offsets, a significant fraction occur in the central regions of their hosts—50% explode within half an effective radius of their galaxies' centers. This is in explicit contrast to Type IIP SN and standard-luminosity Type IIn SN, both of which have been found to to display a dearth of events in the central portions of their galaxies (Anderson & James 2009; Anderson et al. 2012; Kelly & Kirshner 2012b; Habergham et al. 2014). Our independent analysis of standard-luminosity Type IIn SN also observes a central deficit, even when our sample is restricted to events discovered by untargeted surveys that perform image subtraction (PS1/PTF). The central concentration of luminous Type IIn events is in excess of an exponential disk profile. A similar distribution is also observed for interacting transients explicitly classified as Type IIn/Ia-CSM due to underlying broad features in their spectra.

Though our sample represents an extensive collection of the events where suitable data is available, we cannot rule out the presence of systematic biases in detection efficiency, particularly due to the differing survey and follow-up schemes employed in the underlying reports. This is especially true for the standard-luminosity Type IIn SN in our sample, as many are low-redshift events taken from a mixture of targeted and untargeted surveys (see Table 8.1). However, at the core of this analysis is the sample drawn from the PS1-MDS. This sample is unbiased in the sense that the events were identified in a single, untargeted, survey. We note that the same trends described above (central excess of luminous Type IIn SN, central deficit of lower luminosity Type IIn SN) are observed in the 16 events from the PS1-MDS survey *only*, albeit at lower statistical significance due to the smaller sample size.

In interpreting these results it is interesting to consider both the observed contrast between luminous and standard luminosity transients, as well as the central concentration of luminous events. First, the differing spatial distributions of standard-luminosity and luminous Type IIn SN could arise from either a true physical difference between the location where their progenitor star systems form within their host galaxies, or from an observational bias. In particular, surveys could be 'missing' faint Type IIn SN in the bright central regions of their host galaxies, due to increased noise and/or extinction. This possibility was recently considered in detail by Habergham et al. (2014) for another sample of low-redshift Type IIn SN. They concluded that such biases were likely not responsible for the observed central deficit, based in part on the fact that other classes of transients with comparable peak magnitudes (e.g. Type Ibc) *were* discovered in the central regions. We have not yet performed a rigorous analysis of our detection efficiency as a function of galactic offset for the PS1-MDS sample. However, even if surveys are missing low-luminosity transients at small offsets due to the effects of increased noise and extinction, this cannot explain the observed central *concentration* of luminous Type IIn SN, as there should be no such bias prohibiting the detection of luminous events at larger offsets.

Another important consideration when interpreting the distinction between the location of these events is whether luminous and standard luminosity Type IIn SN explode in similar or different *types* of galaxies. This topic was considered in Chapter 7 where we found no statistically distinguishable trends between the host galaxies of luminous and standard luminosity Type IIn SN. However, the literature sample of standard luminosity Type IIn SN which we use to supplement the PS1-MDS in *this* chapter consists of events drawn from a mixture of targeted and untargeted surveys, resulting in possible oversampling of moderately large spiral galaxies. However, as shown in Figure 8.11 the central concentration exhibited by the luminous Type IIn SN is not driven *exclusively* by SN which explode in dwarf galaxies. There is *also* a central concentration amongst luminous events which explode in galaxies with $M_B \sim -20$ mag.

Thus, if we assert that our sample is representative, then the observed central concentration of luminous transients implies that the physical conditions for star formation in the bright central regions of galaxies—*including Milky Way-like and S0 galaxies*—is conducive for the formation of luminous Type IIn progenitors. Gal-Yam (2012) noted that the luminous Type IIn SN 2006gy and CSS200217—which at the time were the only luminous SN not found in dwarf galaxies—both exploded in the central regions of their giant hosts, and posited that some physical condition in these environments might mimic those found in dwarf star-forming galaxies. One possibility is that young and dense stellar clusters occur in *both* of these environments (van den Heuvel & Portegies Zwart 2013). Thus, some byproduct of star formation/evolution in dense environments—such as binary fractions (Hut et al. 1992), dynamical interactions (van den Heuvel & Portegies Zwart 2013), IMF variations (e.g Kelly et al. 2014), or other—could facilitate the production of luminous Type IIn SN. Possible binary effects are particularly intriguing as the "prototypical" LBV η Car—one of the only known stars with a dense CSM of $\sim$10 $M_\odot$—is located in an eccentric binary, and it is still debated what influence this binarity has had on its evolution (e.g Smith 2014). Finally, we note that while a central concentration is observed, this tenancy is not exclusive: luminous

Type IIn SN are also found at a wide range of host-transient offsets. Thus, any proposed model (*if* all luminous Type IIn SN due to the similar phenomena/progenitors) must also operate in these environments. Future studies will examine how the preliminary results presented here depend on both the global host galaxy properties and the explosion/CSM parameters of the transient events.

Acknowledgments

The Pan-STARRS1 Surveys (PS1) have been made possible through contributions of the Institute for Astronomy, the University of Hawaii, the Pan-STARRS Project Office, the Max-Planck Society and its participating institutes, the Max Planck Institute for Astronomy, Heidelberg and the Max Planck Institute for Extraterrestrial Physics, Garching, The Johns Hopkins University, Durham University, the University of Edinburgh, Queen's University Belfast, the Harvard-Smithsonian Center for Astrophysics, the Las Cumbres Observatory Global Telescope Network Incorporated, the National Central University of Taiwan, the Space Telescope Science Institute, the National Aeronautics and Space Administration under Grant No. NNX08AR22G issued through the Planetary Science Division of the NASA Science Mission Directorate, the National Science Foundation under Grant No. AST-1238877, the University of Maryland, and Eotvos Lorand University (ELTE). This work includes data gathered with the 6.5 m Magellan Telescopes located at Las Campanas Observatory, Chile.

References

Abadie, J., Abbott, B. P., Abbott, R., et al. 2010, Classical and Quantum Gravity, 27, 173001

Ahn, C. P., Alexandroff, R., Allende Prieto, C., et al. 2012, ApJS, 203, 21

Akerlof, C. W., Kehoe, R. L., McKay, T. A., et al. 2003, PASP, 115, 132

Aldering, G., Antilogus, P., Bailey, S., et al. 2006, ApJ, 650, 510

Allington-Smith, J., Breare, M., Ellis, R., et al. 1994, PASP, 106, 983

Anderson, J. P., Habergham, S. M., James, P. A., & Hamuy, M. 2012, MNRAS, 424, 1372

Anderson, J. P., & James, P. A. 2009, MNRAS, 399, 559

Andrews, J. E., Sugerman, B. E. K., Clayton, G. C., et al. 2011, ApJ, 731, 47

Arcavi, I., Gal-Yam, A., Yaron, O., et al. 2011, ApJ, 742, L18

Arcavi, I., Gal-Yam, A., Cenko, S. B., et al. 2012, ApJ, 756, L30

Arnett, W. D. 1982, ApJ, 253, 785

Asplund, M., Grevesse, N., & Sauval, A. J. 2005, in Astronomical Society of the Pacific Conference Series, Vol. 336, Cosmic Abundances as Records of Stellar Evolution and Nucleosynthesis, ed. T. G. Barnes, III & F. N. Bash, 25

Baade, W., & Zwicky, F. 1934, Proceedings of the National Academy of Science, 20, 254

Balberg, S., & Loeb, A. 2011, MNRAS, 414, 1715

Barbon, R., Benetti, S., Cappellaro, E., et al. 1995, A&AS, 110, 513

Barnes, J., & Kasen, D. 2013, ApJ, 775, 18

Begelman, M. C., & Sarazin, C. L. 1986, ApJ, 302, L59

Ben-Ami, S., Gal-Yam, A., Filippenko, A. V., et al. 2012, ApJ, 760, L33

Benetti, S., Cappellaro, E., Turatto, M., et al. 2006, ApJ, 653, L129

Benetti, S., Turatto, M., Valenti, S., et al. 2011, MNRAS, 411, 2726

Benetti, S., Nicholl, M., Cappellaro, E., et al. 2014, MNRAS, 441, 289

Berger, E. 2010, ApJ, 722, 1946

Berger, E., Kulkarni, S. R., & Chevalier, R. A. 2002, ApJ, 577, L5

Berger, E., Leibler, C. N., Chornock, R., et al. 2013, ApJ, 779, 18

Bersten, M. C., Tanaka, M., Tominaga, N., Benvenuto, O. G., & Nomoto, K. 2013, ApJ, 767, 143

Bersten, M. C., Benvenuto, O. G., Nomoto, K., et al. 2012, ApJ, 757, 31

Bethe, H. A., & Wilson, J. R. 1985, ApJ, 295, 14

Bildsten, L., Shen, K. J., Weinberg, N. N., & Nelemans, G. 2007, ApJ, 662, L95

Blanchard, P. K., Berger, E., & Fong, W.-f. 2016, ApJ, 817, 144

Blondin, S., Matheson, T., Kirshner, R. P., et al. 2012, AJ, 143, 126

Bloom, J. S., Kulkarni, S. R., & Djorgovski, S. G. 2002, AJ, 123, 1111

Bongard, S., Baron, E., Smadja, G., Branch, D., & Hauschildt, P. H. 2008, ApJ, 687, 456

Botticella, M. T., Riello, M., Cappellaro, E., et al. 2008, A&A, 479, 49

Botticella, M. T., Pastorello, a., Smartt, S. J., et al. 2009, MNRAS, 398, 1041

Bowen, D. V., Roth, K. C., Meyer, D. M., & Blades, J. C. 2000, ApJ, 536, 225

Brammer, G. B., van Dokkum, P. G., & Coppi, P. 2008, ApJ, 686, 1503

Branch, D., Jeffery, D. J., Young, T. R., & Baron, E. 2006, PASP, 118, 791

Branch, D., Benetti, S., Kasen, D., et al. 2002, ApJ, 566, 1005

Branch, D., Benetti, S., Kasen, D., et al. 2002, ApJ, 566, 1005

Breeveld, A. A., Landsman, W., Holland, S. T., et al. 2011, in American Institute of Physics Conference Series, Vol. 1358, American Institute of Physics Conference Series, ed. J. E. McEnery, J. L. Racusin, & N. Gehrels, 373–376

Brown, P. J., Holland, S. T., Immler, S., et al. 2009, AJ, 137, 4517

Burrows, A., Dessart, L., Livne, E., Ott, C. D., & Murphy, J. 2007, ApJ, 664, 416

Burrows, D. N., Hill, J. E., Nousek, J. A., et al. 2005, Space Sci. Rev., 120, 165

Campana, S., Mangano, V., Blustin, A. J., et al. 2006, Nature, 442, 1008

Campbell, H., Fraser, M., Blagorodnova, N., et al. 2014, The Astronomer's Telegram, 5912

Cao, Y., Kasliwal, M. M., Arcavi, I., et al. 2013, ApJ, 775, L7

Cao, Y., Kulkarni, S. R., Howell, D. A., et al. 2015, Nature, 521, 328

Cappellaro, E., Mazzali, P. A., Benetti, S., et al. 1997, A&A, 328, 203

Cenko, S. B., Fox, D. B., Moon, D.-s., et al. 2006, PASP, 118, 1396

Cenko, S. B., Bloom, J. S., Kulkarni, S. R., et al. 2012, MNRAS, 420, 2684

Chakraborti, S., Yadav, N., Cardamone, C., & Ray, A. 2012, ApJ, 746, L6

Chakraborti, S., Soderberg, A., Chomiuk, L., et al. 2015, ApJ, 805, 187

Chatzopoulos, E., Craig Wheeler, J., & Vinko, J. 2012, ApJ, 746, 121

Chatzopoulos, E., & Wheeler, J. C. 2012, ApJ, 760, 154

Chatzopoulos, E., Wheeler, J. C., Vinko, J., Horvath, Z. L., & Nagy, A. 2013, ApJ, 773, 76

Chatzopoulos, E., Wheeler, J. C., Vinko, J., et al. 2011, ApJ, 729, 143

Chen, J., Wang, X., Ganeshalingam, M., et al. 2014, ApJ, 790, 120

Chevalier, R. A. 1998, ApJ, 499, 810

—. 2012, ApJ, 752, L2

Chevalier, R. A., & Fransson, C. 1994, ApJ, 420, 268

—. 2006, ApJ, 651, 381

Chevalier, R. A., & Irwin, C. M. 2011, ApJ, 729, L6

Chevalier, R. A., & Plait, P. C. 1988, ApJ, 331, L109

Chomiuk, L., Chornock, R., Soderberg, a. M., et al. 2011, ApJ, 743, 114

Chornock, R., Berger, E., Rest, A., et al. 2013, ApJ, 767, 162

Chugai, N., Blinnikov, S., Fassia, A., et al. 2002, MNRAS, 330, 473

Chugai, N. N., & Danziger, I. J. 1994, MNRAS, 268, 173

Clocchiatti, A., & Wheeler, J. C. 1997, ApJ, 491, 375

Cobb, B. E., Bloom, J. S., Perley, D. a., et al. 2010, ApJ, 718, L150

Corsi, a., Ofek, E. O., Gal-Yam, a., et al. 2012, ApJ, 747, L5

Crowther, P. A. 2007, ARA&A, 45, 177

Crowther, P. a. 2012, MNRAS, 1943, 1927

Darbha, S., Metzger, B. D., Quataert, E., et al. 2010, MNRAS, 409, 846

de Jager, C., Nieuwenhuijzen, H., & van der Hucht, K. A. 1988, A&AS, 72, 259

de Vaucouleurs, G., & Corwin, Jr., H. G. 1985, ApJ, 295, 287

Dessart, L., Burrows, A., Ott, C. D., et al. 2006, ApJ, 644, 1063

Dessart, L., Hillier, D. J., Li, C., & Woosley, S. 2012, MNRAS, 424, 2139

Dilday, B., Howell, D. A., Cenko, S. B., et al. 2012, Science, 337, 942

Drake, A. J., Djorgovski, S. G., Mahabal, A., et al. 2009, ApJ, 696, 870

Drake, A. J., Djorgovski, S. G., Prieto, J. L., et al. 2010, ApJ, 718, L127

Drake, A. J., Djorgovski, S. G., Mahabal, A. A., et al. 2011a, The Astronomer's Telegram, 3340

Drake, A. J., Djorgovski, S. G., Mahabal, A., et al. 2011b, ApJ, 735, 106

Dressler, A., Hare, T., Bigelow, B. C., & Osip, D. J. 2006, in Society of Photo-Optical Instrumentation Engineers (SPIE) Conference Series, Vol. 6269, Society of Photo-Optical Instrumentation Engineers (SPIE) Conference Series

Drout, M. R., Soderberg, A. M., Gal-Yam, A., et al. 2011, ApJ, 741, 97

Drout, M. R., Soderberg, A. M., Mazzali, P. A., et al. 2013, ApJ, 774, 58

Drout, M. R., Chornock, R., Soderberg, A. M., et al. 2014, ApJ, 794, 23

Drout, M. R., Milisavljevic, D., Parrent, J., et al. 2016, The Astrophysical Journal, 821, 57

Eldridge, J. J., & Tout, C. A. 2004, MNRAS, 353, 87

Elias-Rosa, N., Van Dyk, S. D., Li, W., et al. 2009, ApJ, 706, 1174

—. 2010, ApJ, 714, L254

Elmhamdi, A., Danziger, I. J., Branch, D., & Leibundgut, B. 2007, in American Institute of Physics Conference Series, Vol. 924, The Multicolored Landscape of Compact Objects and Their Explosive Origins, ed. T. di Salvo, G. L. Israel, L. Piersant, L. Burderi, G. Matt, A. Tornambe, & M. T. Menna, 277–284

Faber, S. M., Phillips, A. C., Kibrick, R. I., et al. 2003, in Society of Photo-Optical Instrumentation Engineers (SPIE) Conference Series, Vol. 4841, Society of Photo-Optical Instrumentation Engineers (SPIE) Conference Series, ed. M. Iye & A. F. M. Moorwood, 1657–1669

Fabricant, D., Cheimets, P., Caldwell, N., & Geary, J. 1998, PASP, 110, 79

Fabricant, D., Fata, R., Roll, J., et al. 2005, PASP, 117, 1411

Fassia, A., Meikle, W. P. S., Vacca, W. D., et al. 2000, MNRAS, 318, 1093

Fesen, R. A. 2001, ApJS, 133, 161

Filippenko, A. V. 1988, AJ, 96, 1941

—. 1989, AJ, 97, 726

Filippenko, A. V. 1997, ARA&A

Filippenko, A. V., Li, W. D., Treffers, R. R., & Modjaz, M. 2001a, in Astronomical Society of the Pacific Conference Series, Vol. 246, IAU Colloq. 183: Small Telescope Astronomy on Global Scales, ed. B. Paczynski, W.-P. Chen, & C. Lemme, 121

Filippenko, A. V., Li, W. D., Treffers, R. R., & Modjaz, M. 2001b, in Astronomical Society of the Pacific Conference Series, Vol. 246, IAU Colloq. 183: Small Telescope Astronomy on Global Scales, ed. B. Paczynski, W.-P. Chen, & C. Lemme, 121

Filippenko, A. V., Richmond, M. W., Branch, D., et al. 1992, AJ, 104, 1543

Filippenko, A. V., Barth, A. J., Matheson, T., et al. 1995, ApJ, 450, L11

Folatelli, G., Contreras, C., Phillips, M. M., et al. 2006, ApJ, 641, 1039

Folatelli, G., Phillips, M. M., Morrell, N., et al. 2012, ApJ, 745, 74

Foley, R. J., Berger, E., Fox, O., et al. 2011, ApJ, 732, 32

Foley, R. J., Brown, P. J., Rest, A., et al. 2010, ApJ, 708, L61

Foley, R. J., Chornock, R., Filippenko, A. V., et al. 2009, AJ, 138, 376

Foley, R. J., Challis, P. J., Chornock, R., et al. 2013, ApJ, 767, 57

Foley, R. J., Hounsell, R., Miller, J. A., et al. 2015, The Astronomer's Telegram, 8151

Fong, W., & Berger, E. 2013, ApJ, 776, 18

Fox, O. D., Silverman, J. M., Filippenko, A. V., et al. 2015, MNRAS, 447, 772

Fransson, C., & Chevalier, R. A. 1989, ApJ, 343, 323

Fransson, C., Chevalier, R. A., Filippenko, A. V., et al. 2002, ApJ, 572, 350

Fransson, C., Ergon, M., Challis, P. J., et al. 2014, ApJ, 797, 118

Fraser, M., Takáts, K., Pastorello, A., et al. 2010, ApJ, 714, L280

Fremling, C., Sollerman, J., Taddia, F., et al. 2014, A&A, 565, A114

Fruchter, A. S., Levan, A. J., Strolger, L., et al. 2006, Nature, 441, 463

Fryer, C. 1999, ApJ, 522, 413

Fryer, C. L., & Kalogera, V. 2001, ApJ, 554, 548

Fryer, C. L., Brown, P. J., Bufano, F., et al. 2009, ApJ, 707, 193

Gal-Yam, A. 2012, Science, 337, 927

Gal-Yam, A., & Leonard, D. C. 2009, Nature, 458, 865

Gal-Yam, A., Leonard, D. C., Fox, D. B., et al. 2007, ApJ, 656, 372

Gal-Yam, A., Arcavi, I., Ofek, E. O., et al. 2014, Nature, 509, 471

Galbany, L., Miquel, R., Östman, L., et al. 2012, ApJ, 755, 125

Gehrels, N., Chincarini, G., Giommi, P., et al. 2004a, ApJ, 611, 1005

—. 2004b, ApJ, 611, 1005

Georgy, C. 2012, A&A, 538, L8

Gerardy, C. L., Fesen, R. A., Nomoto, K., et al. 2002, PASJ, 54, 905

Germany, L. M., Reiss, D. J., Sadler, E. M., Schmidt, B. P., & Stubbs, C. W. 2000, ApJ, 533, 320

Gezari, S., Halpern, J. P., Grupe, D., et al. 2009, ApJ, 690, 1313

Gezari, S., Chornock, R., Rest, A., et al. 2012, Nature, 485, 217

Ginzburg, S., & Balberg, S. 2014, ApJ, 780, 18

Gorbikov, E., Gal-Yam, A., Ofek, E. O., et al. 2014, MNRAS, 443, 671

Graham, J. F., & Fruchter, A. S. 2013, ApJ, 774, 119

Graham, M. J., Drake, A. J., Djorgovski, S. G., et al. 2011, Central Bureau Electronic Telegrams, 2787

Grefenstette, B. W., Harrison, F. A., Boggs, S. E., et al. 2014, Nature, 506, 339

Habergham, S. M., Anderson, J. P., James, P. A., & Lyman, J. D. 2014, MNRAS, 441, 2230

Hachinger, S., Mazzali, P. a., Taubenberger, S., et al. 2012, MNRAS, 422, 70

Hadfield, L. J., & Crowther, P. A. 2006, MNRAS, 368, 1822

Hadjiyska, E., Rabinowitz, D., Baltay, C., et al. 2011, The Astronomer's Telegram, 3812

Hammer, N. J., Janka, H.-T., & Müller, E. 2010, ApJ, 714, 1371

Hamuy, M. 2003, ApJ, 582, 905

Hamuy, M., Phillips, M. M., Suntzeff, N. B., et al. 2003, Nature, 424, 651

Hatano, K., Branch, D., & Deaton, J. 1998, ApJ, 502, 177

Heger, A., Fryer, C. L., Woosley, S. E., Langer, N., & Hartmann, D. H. 2003, ApJ, 591, 288

Hicken, M., Garnavich, P. M., Prieto, J. L., et al. 2007, ApJ, 669, L17

Hicken, M., Challis, P., Kirshner, R. P., et al. 2012, ApJS, 200, 12

Hillebrandt, W., & Niemeyer, J. C. 2000, ARA&A, 38, 191

Hirata, K., Kajita, T., Koshiba, M., Nakahata, M., & Oyama, Y. 1987, Physical Review Letters, 58, 1490

Hirschi, R., Meynet, G., & Maeder, A. 2004, A&A, 425, 649

Ho, L. C., Filippenko, A. V., & Sargent, W. L. W. 1997, ApJS, 112, 315

Ho, W. C. G., Van Dyk, S. D., Peng, C. Y., et al. 2001, PASP, 113, 1349

Hogg, D. W., Baldry, I. K., Blanton, M. R., & Eisenstein, D. J. 2002, ArXiv Astrophysics e-prints, astro-ph/0210394

Hook, I. M., Jørgensen, I., Allington-Smith, J. R., et al. 2004, PASP, 116, 425

Hopkins, P. F., Richards, G. T., & Hernquist, L. 2007, ApJ, 654, 731

Howell, D. A., Sullivan, M., Nugent, P. E., et al. 2006, Nature, 443, 308

Hoyle, F., & Fowler, W. A. 1960, ApJ, 132, 565

Hsiao, E. Y., Burns, C. R., Contreras, C., et al. 2015, A&A, 578, A9

Huber, M., Chambers, K. C., Smith, K. W., et al. 2015a, The Astronomer's Telegram, 8115

Huber, M., Chambers, K. C., Flewelling, H., et al. 2015b, The Astronomer's Telegram, 7153

Humphreys, R. M., & Davidson, K. 1994, PASP, 106, 1025

Hunter, D. J., Valenti, S., Kotak, R., et al. 2009, A&A, 508, 371

Hut, P., McMillan, S., Goodman, J., et al. 1992, PASP, 104, 981

Hwang, U., Laming, J. M., Badenes, C., et al. 2004, ApJ, 615, L117

Iben, Jr., I., Ritossa, C., & Garcia-Berro, E. 1997, ApJ, 489, 772

Inserra, C., Fraser, M., Smartt, S. J., et al. 2016, MNRAS, 459, 2721

Janka, H.-T., Langanke, K., Marek, A., Martínez-Pinedo, G., & Müller, B. 2007, Phys. Rep., 442, 38

Jerkstrand, A., Ergon, M., Smartt, S. J., et al. 2015, A&A, 573, A12

Joggerst, C. C., Woosley, S. E., & Heger, A. 2009, ApJ, 693, 1780

Kaiser, N., Burgett, W., Chambers, K., et al. 2010, in Society of Photo-Optical Instrumentation Engineers (SPIE) Conference Series, Vol. 7733, Society of Photo-Optical Instrumentation Engineers (SPIE) Conference Series

Kalberla, P. M. W., Burton, W. B., Hartmann, D., et al. 2005, A&A, 440, 775

Kamble, A., Soderberg, A. M., Chomiuk, L., et al. 2014, ApJ, 797, 2

Kamble, A., Margutti, R., Soderberg, A. M., et al. 2016, ApJ, 818, 111

Kankare, E., Ergon, M., Bufano, F., et al. 2012, MNRAS, 424, 855

Kasen, D. 2010, ApJ, 708, 1025

Kasen, D., & Bildsten, L. 2010, ApJ, 717, 245

Kashiyama, K., & Quataert, E. 2015, MNRAS, 451, 2656

Kasliwal, M. M., Kulkarni, S. R., Gal-Yam, A., et al. 2010, ApJ, 723, L98

—. 2012, ApJ, 755, 161

Kelly, P. L., Filippenko, A. V., Modjaz, M., & Kocevski, D. 2014, ApJ, 789, 23

Kelly, P. L., & Kirshner, R. P. 2012a, ApJ, 759, 107

—. 2012b, ApJ, 759, 107

Kelly, P. L., Kirshner, R. P., & Pahre, M. 2008, ApJ, 687, 1201

Kennicutt, R. C. 1998, ARA&A, 36, 189

Kewley, L. J., & Dopita, M. A. 2002, ApJS, 142, 35

Kewley, L. J., & Ellison, S. L. 2008, ApJ, 681, 1183

Khandrika, H., & Li, W. 2005, Central Bureau Electronic Telegrams, 232, 1

Kiewe, M., Gal-Yam, A., Arcavi, I., et al. 2012, ApJ, 744, 10

Kifonidis, K., Plewa, T., Scheck, L., Janka, H.-T., & Müller, E. 2006, A&A, 453, 661

Kitaura, F. S., Janka, H.-T., & Hillebrandt, W. 2006, A&A, 450, 345

Kleiser, I. K. W., & Kasen, D. 2014, MNRAS, 438, 318

Kobulnicky, H. A., & Kewley, L. J. 2004, ApJ, 617, 240

Krauss, M. I., Soderberg, A. M., Chomiuk, L., et al. 2012, ApJ, 750, L40

Kriek, M., van Dokkum, P. G., Labbé, I., et al. 2009, ApJ, 700, 221

Laming, J. M., Hwang, U., Radics, B., Lekli, G., & Takács, E. 2006, ApJ, 644, 260

Landolt, A. U. 1992, AJ, 104, 340

Law, N. M., Kulkarni, S. R., Dekany, R. G., et al. 2009, PASP, 121, 1395

Leibundgut, B., Tammann, G. A., Cadonau, R., & Cerrito, D. 1991, A&AS, 89, 537

Leibundgut, B., Kirshner, R. P., Phillips, M. M., et al. 1993, AJ, 105, 301

Leloudas, G., Schulze, S., Krühler, T., et al. 2015a, MNRAS, 449, 917

Leloudas, G., Hsiao, E. Y., Johansson, J., et al. 2015b, A&A, 574, A61

Levesque, E. M. 2010, New Astronomy Reviews, 54, 1

Levesque, E. M., Berger, E., Kewley, L. J., & Bagley, M. M. 2010, AJ, 139, 694

Levesque, E. M., Kewley, L. J., Berger, E., & Zahid, H. J. 2010, AJ, 140, 1557

Levesque, E. M., Massey, P., Plez, B., & Olsen, K. A. G. 2009, AJ, 137, 4744

Levesque, E. M., Soderberg, a. M., Foley, R. J., et al. 2010, ApJ, 709, L26

Li, L.-X. 2007, MNRAS, 375, 240

Li, W., Filippenko, A. V., Chornock, R., & Jha, S. 2003, PASP, 115, 844

Li, W., Leaman, J., Chornock, R., et al. 2011, MNRAS, 412, 1441

Li, W.-D., Li, C., Filippenko, A. V., & Moran, E. C. 1998, IAU Circ., 6829

Liu, Q.-Z., Hu, J.-Y., Hang, H.-R., et al. 2000, A&AS, 144, 219

Liu, Y.-Q., Modjaz, M., Bianco, F. B., & Graur, O. 2015, ArXiv e-prints, arXiv:1510.08049

Lodato, G., & Rossi, E. M. 2011, MNRAS, 410, 359

Lucy, L. 1999, A&A, 220, 211

Lucy, L. B. 1991, ApJ, 383, 308

Lunnan, R., Chornock, R., Berger, E., & Pan-Starrs1 Cfa/Jhu Transient Team. 2015a, in American Astronomical Society Meeting Abstracts, Vol. 225, American Astronomical Society Meeting Abstracts, 104.05

Lunnan, R., Chornock, R., Berger, E., et al. 2013, ApJ, 771, 97

—. 2014, ApJ, 787, 138

—. 2015b, ApJ, 804, 90

Lyman, J. D., Bersier, D., James, P. A., et al. 2016, MNRAS, 457, 328

MacFadyen, A., Woosley, S., & Heger, A. 2001, ApJ, 20, 410

Mackey, J., Mohamed, S., Gvaramadze, V. V., et al. 2014, Nature, 512, 282

Maeda, K., Mazzali, P. A., Deng, J., et al. 2003, ApJ, 593, 931

Maeda, K., Nakamura, T., Nomoto, K., et al. 2002, ApJ, 565, 405

Maeda, K., Tanaka, M., Nomoto, K., et al. 2007, ApJ, 666, 1069

Magnier, E. 2006, in The Advanced Maui Optical and Space Surveillance Technologies Conference

Magnier, E. A., Liu, M., Monet, D. G., & Chambers, K. C. 2008, in IAU Symposium, Vol. 248, IAU Symposium, ed. W. J. Jin, I. Platais, & M. A. C. Perryman, 553–559

Maraston, C. 2005, MNRAS, 362, 799

Marek, A., & Janka, H.-T. 2009, ApJ, 694, 664

Margutti, R., Parrent, J., Kamble, A., et al. 2014a, ApJ, 790, 52

Margutti, R., Soderberg, A. M., Chomiuk, L., et al. 2012, ApJ, 751, 134

Margutti, R., Milisavljevic, D., Soderberg, A. M., et al. 2014b, ApJ, 780, 21

Margutti, R., Guidorzi, C., Lazzati, D., et al. 2015, ApJ, 805, 159

Margutti, R., Kamble, A., Milisavljevic, D., et al. 2016, ArXiv e-prints, arXiv:1601.06806

Marion, G. H., Brown, P. J., Vinkó, J., et al. 2016, ApJ, 820, 92

Marshall, J. R., van Loon, J. T., Matsuura, M., et al. 2004, MNRAS, 355, 1348

Martini, P., Stoll, R., Derwent, M. A., et al. 2011, PASP, 123, 187

Massey, P., Neugent, K. F., Morrell, N., & John Hillier, D. 2015, in IAU Symposium, Vol. 307, IAU Symposium, 64–69

Matheson, T., Filippenko, A. V., Chornock, R., Leonard, D. C., & Li, W. 2000, AJ, 119, 2303

Matheson, T., Kirshner, R. P., Challis, P., et al. 2008, AJ, 135, 1598

Matzner, C. D., & McKee, C. F. 1999, ApJ, 510, 379

Mauerhan, J. C., Smith, N., Silverman, J. M., et al. 2013a, MNRAS, 431, 2599

Mauerhan, J. C., Smith, N., Filippenko, A. V., et al. 2013b, MNRAS, 430, 1801

Maund, J. R., Smartt, S. J., Kudritzki, R. P., Podsiadlowski, P., & Gilmore, G. F. 2004, Nature, 427, 129

Mazzali, P., & Lucy, L. 1993, A&A, 279, 447

Mazzali, P. A. 2000, A&A, 363, 705

Mazzali, P. A., Benetti, S., Stehle, M., et al. 2005a, MNRAS, 357, 200

Mazzali, P. A., Deng, J., Hamuy, M., & Nomoto, K. 2009, ApJ, 703, 1624

Mazzali, P. A., & Lucy, L. B. 1998, MNRAS, 295, 428

Mazzali, P. a., Maurer, I., Valenti, S., Kotak, R., & Hunter, D. 2010, MNRAS, 408, 87

Mazzali, P. a., Sauer, D. N., Pastorello, A., Benetti, S., & Hillebrandt, W. 2008, MNRAS, 386, 1897

Mazzali, P. A., Walker, E. S., Pian, E., et al. 2013, MNRAS, 432, 2463

Mazzali, P. A., Kawabata, K. S., Maeda, K., et al. 2005b, Science, 308, 1284

Mazzali, P. A., Valenti, S., Della Valle, M., et al. 2008, Science, 321, 1185

McGaugh, S. S. 1991, ApJ, 380, 140

Metzger, B. D. 2010, MNRAS, 409, 284

Metzger, B. D. 2012, MNRAS, 419, 827

Metzger, B. D., & Piro, A. L. 2014, MNRAS, 439, 3916

Metzger, B. D., Piro, a. L., & Quataert, E. 2009, MNRAS, 396, 1659

Metzger, B. D., Martínez-Pinedo, G., Darbha, S., et al. 2010, MNRAS, 406, 2650

Milisavljevic, D., & Fesen, R. A. 2013, ApJ, 772, 134

Milisavljevic, D., Margutti, R., Soderberg, A. M., et al. 2013, ApJ, 767, 71

Milisavljevic, D., Fesen, R., Pickering, T., et al. 2013, The Astronomer's Telegram, 5142, 1

Milisavljevic, D., Margutti, R., Parrent, J. T., et al. 2015, ApJ, 799, 51

Millard, J., Branch, D., Baron, E., et al. 1999, ApJ, 527, 746

Miller, J. S., & Stone, R. P. S. 1993, Lick Observatory Technical Reports, Vol. 66 (Santa Cruz, CA: Lick Obs.)

Miville-Deschênes, M.-A., & Lagache, G. 2005, ApJS, 157, 302

Modjaz, M. 2007, PhD thesis, Harvard University

Modjaz, M., Kewley, L., Bloom, J. S., et al. 2011, ApJ, 731, L4

Modjaz, M., Li, W., Filippenko, A. V., et al. 2001, PASP, 113, 308

Modjaz, M., Li, W., Butler, N., et al. 2009a, ApJ, 702, 226

—. 2009b, ApJ, 702, 226

Modjaz, M., Blondin, S., Kirshner, R. P., et al. 2014, AJ, 147, 99

Moriya, T., Tominaga, N., Tanaka, M., et al. 2010, ApJ, 719, 1445

Moriya, T. J., Liu, Z.-W., & Izzard, R. G. 2015, MNRAS, 450, 3264

Mould, J. R., Huchra, J. P., Freedman, W. L., et al. 2000, ApJ, 529, 786

Nakar, E. 2015, ApJ, 807, 172

Nakar, E., & Piro, A. L. 2014, ApJ, 788, 193

Nakar, E., & Sari, R. 2010, ApJ, 725, 904

Neill, J. D., Sullivan, M., Gal-Yam, A., et al. 2011, ApJ, 727, 15

Newton, J., & Puckett, T. 2010, Central Bureau Electronic Telegrams, 2532

Nicholl, M., Smartt, S. J., Jerkstrand, A., et al. 2015, MNRAS, 452, 3869

Nomoto, K. 1987, ApJ, 322, 206

Nomoto, K., & Kondo, Y. 1991, ApJ, 367, L19

Nomoto, K., Thielemann, F., & Yokoi, K. 1984, ApJ, 286, 644

Nomoto, K., Yamaoka, H., Pols, O. R., et al. 1994, Nature, 371, 227

Nugent, P., Kim, A., & Perlmutter, S. 2002, PASP, 114, 803

Nugent, P. E., Sullivan, M., Cenko, S. B., et al. 2011, Nature, 480, 344

Ofek, E. O., Rabinak, I., Neill, J. D., et al. 2010, ApJ, 724, 1396

Ofek, E. O., Sullivan, M., Cenko, S. B., et al. 2013, Nature, 494, 65

Ofek, E. O., Arcavi, I., Tal, D., et al. 2014a, ApJ, 788, 154

Ofek, E. O., Sullivan, M., Shaviv, N. J., et al. 2014b, ApJ, 789, 104

Ofek, E. O., Zoglauer, A., Boggs, S. E., et al. 2014c, ApJ, 781, 42

Olivares, E. F., Greiner, J., Schady, P., et al. 2012, in IAU Symposium, Vol. 279, Death of Massive Stars: Supernovae and Gamma-Ray Bursts, 375–376

Parrent, J., Friesen, B., & Parthasarathy, M. 2014, Ap&SS, 351, 1

Parrent, J. T. 2014, ArXiv e-prints, arXiv:1412.7163

Parrent, J. T., Milisavljevic, D., Soderberg, A. M., & Parthasarathy, M. 2016, ApJ, 820, 75

Parrent, J. T., Thomas, R. C., Fesen, R. a., et al. 2011, ApJ, 732, 30

Pastorello, A., Turatto, M., Benetti, S., et al. 2002, MNRAS, 333, 27

Pastorello, A., Smartt, S. J., Mattila, S., et al. 2007, Nature, 447, 829

Pastorello, a., Kasliwal, M. M., Crockett, R. M., et al. 2008, MNRAS, 389, 955

Pereira, R., Thomas, R. C., Aldering, G., et al. 2013, A&A, 554, A27

Perets, H. B., Badenes, C., Arcavi, I., Simon, J. D., & Gal-yam, A. 2011, ApJ, 730, 89

Perets, H. B., Gal-Yam, A., Mazzali, P. a., et al. 2010, Nature, 465, 322

Perley, D. A., Levan, A. J., Tanvir, N. R., et al. 2013, ApJ, 778, 128

Pettini, M., & Pagel, B. E. J. 2004, MNRAS, 348, L59

Phillips, M. M. 1993, ApJ, 413, L105

Phillips, M. M., Lira, P., Suntzeff, N. B., et al. 1999, AJ, 118, 1766

Phillips, M. M., Li, W., Frieman, J. A., et al. 2007, PASP, 119, 360

Pian, E., Amati, L., Antonelli, L. A., et al. 2000, ApJ, 536, 778

Piro, A. L., & Morozova, V. S. 2014, ApJ, 792, L11

Piro, A. L., & Nakar, E. 2013, ApJ, 769, 67

Podsiadlowski, P., Joss, P. C., & Hsu, J. J. L. 1992, ApJ, 391, 246

Pogge, R. W., Atwood, B., Brewer, D. F., et al. 2010, in Society of Photo-Optical Instrumentation Engineers (SPIE) Conference Series, Vol. 7735, Society of Photo-Optical Instrumentation Engineers (SPIE) Conference Series, 0

Poole, T. S., Breeveld, A. A., Page, M. J., et al. 2008, MNRAS, 383, 627

Poznanski, D., Ganeshalingam, M., Silverman, J. M., & Filippenko, A. V. 2011, MNRAS, 415, L81

Poznanski, D., Prochaska, J. X., & Bloom, J. S. 2012, MNRAS, 426, 1465

Poznanski, D., Chornock, R., Nugent, P. E., et al. 2010, Science, 327, 58

Prajs, S., Cartier, R., Frohmaier, C., et al. 2015, The Astronomer's Telegram, 7412

Prieto, J. L., Stanek, K. Z., & Beacom, J. F. 2008, ApJ, 673, 999

Pritchard, T. A., Roming, P. W. A., Brown, P. J., et al. 2012, ApJ, 750, 128

Quimby, R., Gal-Yam, A., Arcavi, I., et al. 2010, The Astronomer's Telegram, 2634

Quimby, R. M., Yuan, F., Akerlof, C., & Wheeler, J. C. 2013, MNRAS, 431, 912

Quimby, R. M., Yuan, F., Akerlof, C., Wheeler, J. C., & Warren, M. S. 2012, AJ, 144, 177

Quimby, R. M., Cenko, S. B., Yaron, O., et al. 2011a, The Astronomer's Telegram, 3465

Quimby, R. M., Kulkarni, S. R., Kasliwal, M. M., et al. 2011b, Nature, 474, 487

Rabinak, I., & Waxman, E. 2011, ApJ, 728, 63

Reiss, D. J., Germany, L. M., Schmidt, B. P., & Stubbs, C. W. 1998, AJ, 115, 26

Rest, A., Stubbs, C., Becker, A. C., et al. 2005, ApJ, 634, 1103

Rest, A., Foley, R. J., Sinnott, B., et al. 2011, ApJ, 732, 3

Rest, A., Scolnic, D., Foley, R. J., et al. 2014, ApJ, 795, 44

Richards, G., Newberg, H., Kent, S., & Phillips, M. M. 1999, IAU Circ., 7133

Richmond, M. W., van Dyk, S. D., Ho, W., et al. 1996, AJ, 111, 327

Riess, A. G., Filippenko, A. V., Li, W., et al. 1999, AJ, 118, 2675

Rigon, L., Turatto, M., Benetti, S., et al. 2003, MNRAS, 340, 191

Roberts, L. F., Kasen, D., Lee, W. H., & Ramirez-Ruiz, E. 2011, ApJ, 736, L21

Roming, P. W. A., Kennedy, T. E., Mason, K. O., et al. 2005, Space Sci. Rev., 120, 95

Roming, P. W. A., Pritchard, T. A., Brown, P. J., et al. 2009, ApJ, 704, L118

Roming, P. W. A., Pritchard, T. A., Prieto, J. L., et al. 2012, ApJ, 751, 92

Ryder, S. D., Sadler, E. M., Subrahmanyan, R., et al. 2004, MNRAS, 349, 1093

Sahu, D. K., Gurugubelli, U. K., Anupama, G. C., & Nomoto, K. 2011, MNRAS, 413, 2583

Sanders, N. E., Soderberg, a. M., Levesque, E. M., et al. 2012, ApJ, 758, 132

Sauer, D. N., Mazzali, P. a., Deng, J., et al. 2006, MNRAS, 369, 1939

Savaglio, S., Glazebrook, K., & Le Borgne, D. 2009, ApJ, 691, 182

Scalzo, R., Yuan, F., Childress, M., Tucker, B., & Schmidt, B. 2013, The Astronomer's Telegram, 5480

Scalzo, R., Aldering, G., Antilogus, P., et al. 2012, ApJ, 757, 12

Scheck, L., Kifonidis, K., Janka, H.-T., & Müller, E. 2006, A&A, 457, 963

Schlafly, E. F., & Finkbeiner, D. P. 2011, ApJ, 737, 103

Schlegel, D. J., Finkbeiner, D. P., & Davis, M. 1998, ApJ, 500, 525

Schlegel, E. M. 1990, MNRAS, 244, 269

Schmidt, B. P., Kirshner, R. P., Eastman, R. G., et al. 1993, Nature, 364, 600

Schmidt, G. D., Weymann, R. J., & Foltz, C. B. 1989, PASP, 101, 713

Scolnic, D., Rest, A., Riess, A., et al. 2014, ApJ, 795, 45

Shappee, B. J., Prieto, J. L., Grupe, D., et al. 2014, ApJ, 788, 48

Shen, K. J., Kasen, D., Weinberg, N. N., Bildsten, L., & Scannapieco, E. 2010, ApJ, 715, 767

Shiode, J. H., & Quataert, E. 2014, ApJ, 780, 96

Silva, L., Granato, G. L., Bressan, A., & Danese, L. 1998, ApJ, 509, 103

Silverman, J. M., & Filippenko, A. V. 2012, MNRAS, 425, 1917

Silverman, J. M., Foley, R. J., Filippenko, A. V., et al. 2012, MNRAS, 425, 1789

Silverman, J. M., Nugent, P. E., Gal-Yam, A., et al. 2013, ApJS, 207, 3

Sim, S. a., Fink, M., Kromer, M., et al. 2012, MNRAS, 420, 3003

Simcoe, R. A., Burgasser, A. J., Schechter, P. L., et al. 2013, PASP, 125, 270

Smartt, S. J. 2009, ARA&A, 47, 63

Smartt, S. J. 2015, PASA, 32, e016

Smith, J. A., Tucker, D. L., Kent, S., et al. 2002, AJ, 123, 2121

Smith, N. 2014, ARA&A, 52, 487

Smith, N., & Arnett, W. D. 2014, ApJ, 785, 82

Smith, N., Chornock, R., Li, W., et al. 2008, ApJ, 686, 467

Smith, N., Li, W., Filippenko, A. V., & Chornock, R. 2011, MNRAS, 412, 1522

Smith, N., & McCray, R. 2008, ApJL, 17

Smith, N., & Tombleson, R. 2015, MNRAS, 447, 598

Smith, N., Li, W., Foley, R. J., et al. 2007, ApJ, 666, 1116

Smith, N., Miller, A., Li, W., et al. 2010, AJ, 139, 1451

Soderberg, A. M. 2007, in American Institute of Physics Conference Series, Vol. 937, Supernova 1987A: 20 Years After: Supernovae and Gamma-Ray Bursters, ed. S. Immler, K. Weiler, & R. McCray, 492–499

Soderberg, a. M., Brunthaler, a., Nakar, E., Chevalier, R. a., & Bietenholz, M. F. 2010, ApJ, 725, 922

Soderberg, A. M., Chevalier, R. A., Kulkarni, S. R., & Frail, D. A. 2006a, ApJ, 651, 1005

Soderberg, A. M., Kulkarni, S. R., Berger, E., et al. 2005, ApJ, 621, 908

Soderberg, A. M., Nakar, E., Berger, E., & Kulkarni, S. R. 2006b, ApJ, 638, 930

Soderberg, A. M., Kulkarni, S. R., Nakar, E., et al. 2006c, Nature, 442, 1014

Soderberg, a. M., Berger, E., Page, K. L., et al. 2008, Nature, 453, 469

Soderberg, A. M., Chakraborti, S., Pignata, G., et al. 2010, Nature, 463, 513

Sollerman, J., Cumming, R. J., & Lundqvist, P. 1998, ApJ, 493, 933

Speziali, R., Di Paola, A., Giallongo, E., et al. 2008, in Society of Photo-Optical Instrumentation Engineers (SPIE) Conference Series, Vol. 7014, Society of Photo-Optical Instrumentation Engineers (SPIE) Conference Series, 4

Sramek, R. A., Panagia, N., & Weiler, K. W. 1984, ApJ, 285, L59

Stanek, K. Z., Gnedin, O. Y., Beacom, J. F., et al. 2006, ACTAA, 56, 333

Stoll, R., Prieto, J. L., Stanek, K. Z., & Pogge, R. W. 2013, ApJ, 773, 12

Stoll, R., Prieto, J. L., Stanek, K. Z., et al. 2011, ApJ, 730, 34

Stritzinger, M., Taddia, F., Fransson, C., et al. 2012, ApJ, 756, 173

Strubbe, L. E., & Quataert, E. 2009, MNRAS, 400, 2070

Stubbs, C. W., Doherty, P., Cramer, C., et al. 2010, ApJS, 191, 376

Sutherland, P. G., & Wheeler, J. C. 1984, ApJ, 280, 282

Svensson, K. M., Levan, A. J., Tanvir, N. R., Fruchter, A. S., & Strolger, L.-G. 2010, MNRAS, 405, 57

Taddia, F., Stritzinger, M. D., Phillips, M. M., et al. 2012, A&A, 545, L7

Taddia, F., Stritzinger, M. D., Sollerman, J., et al. 2013, A&A, 555, A10

Taddia, F., Sollerman, J., Fremling, C., et al. 2015, A&A, 580, A131

Tanaka, M., Mazzali, P. A., Benetti, S., et al. 2008, ApJ, 677, 448

Tanaka, M., Kawabata, K. S., Maeda, K., et al. 2009, ApJ, 699, 1119

Taubenberger, S., Pastorello, A., Mazzali, P. a., et al. 2006, MNRAS, 371, 1459

Taubenberger, S., Hachinger, S., Pignata, G., et al. 2008, MNRAS, 385, 75

Tauris, T. M., Langer, N., Moriya, T. J., et al. 2013, ApJ, 778, L23

Thomas, R. C., Nugent, P. E., & Meza, J. C. 2011, PASP, 123, 237

Thomas, R. C., Aldering, G., Antilogus, P., et al. 2007, ApJ, 654, L53

Tonry, J., & Onaka, P. 2009, in Advanced Maui Optical and Space Surveillance Technologies Conference

Tonry, J. L., Stubbs, C. W., Lykke, K. R., et al. 2012, ApJ, 750, 99

Tremonti, C. A., Heckman, T. M., Kauffmann, G., et al. 2004, ApJ, 613, 898

Trundle, C., Kotak, R., Vink, J. S., & Meikle, W. P. S. 2008, A&A, 483, L47

Turatto, M., Benetti, S., Cappellaro, E., Astronomico, O., & Osservatorio, V. 2003, in From Twilight to Highlight: The Physics of Supernovae, ed. W. Hillebrandt & B. Leibundgut (Springer-Verlag), 200

Turatto, M., Cappellaro, E., Danziger, I. J., et al. 1993, MNRAS, 262, 128

Turatto, M., Suzuki, T., Mazzali, P. A., et al. 2000, ApJ, 534, L57

Vacca, W. D., Cushing, M. C., & Rayner, J. T. 2003, PASP, 115, 389

Valenti, S., Benetti, S., Cappellaro, E., et al. 2007, MNRAS, 383, 1485

Valenti, S., Elias-Rosa, N., Taubenberger, S., et al. 2008, ApJ, 673, L155

Valenti, S., Pastorello, a., Cappellaro, E., et al. 2009, Nature, 459, 674

Valenti, S., Fraser, M., Benetti, S., et al. 2011, MNRAS, 416, 3138

Valenti, S., Taubenberger, S., Pastorello, A., et al. 2012, ApJ, 749, L28

Valenti, S., Yuan, F., Taubenberger, S., et al. 2014, MNRAS, 437, 1519 van den Heuvel, E. P. J., & Portegies Zwart, S. F. 2013, ApJ, 779, 114

van Dyk, S. D., Sramek, R. A., Weiler, K. W., & Panagia, N. 1993, ApJ, 409, 162

Van Dyk, S. D., Zheng, W., Fox, O. D., et al. 2014, AJ, 147, 37

van Loon, J. T., Cioni, M.-R. L., Zijlstra, A. A., & Loup, C. 2005, A&A, 438, 273

van Marle, A. J., Smith, N., Owocki, S. P., & van Veelen, B. 2010, MNRAS, 407, 2305

van Velzen, S., Farrar, G. R., Gezari, S., et al. 2011, ApJ, 741, 73

Vink, J. S., de Koter, A., & Lamers, H. J. G. L. M. 2001, A&A, 369, 574

Waldman, R., Sauer, D., Livne, E., et al. 2011, ApJ, 738, 21

Wang, B., & Han, Z. 2012, NewAR, 56, 122

Weiler, K. W., Panagia, N., Stockdale, C., et al. 2011, ApJ, 740, 79

Wellons, S., Soderberg, A. M., & Chevalier, R. A. 2012, ApJ, 752, 17

Wheeler, J. C., Harkness, R. P., Clocchiatti, A., et al. 1994, ApJ, 436, L135

Wheeler, J. C., Harkness, R. P., Khokhlov, A. M., & Hoeflich, P. 1995, Phys. Rep., 256, 211

Wheeler, J. C., Johnson, V., & Clocchiatti, A. 2015, MNRAS, 450, 1295

Wheeler, J. C., & Levreault, R. 1985, ApJ, 294, L17

Wheeler, J. C., Barker, E., Benjamin, R., et al. 1993, ApJ, 417, L71

Willmer, C. N. A., Faber, S. M., Koo, D. C., et al. 2006, The Astrophysical Journal, 647, 853

Wong, D. S., Park, S., Shimasaki, K., & Filippenko, A. V. 2005, Central Bureau Electronic Telegrams, 235, 1

Wood-Vasey, W. M., Wang, L., & Aldering, G. 2004, ApJ, 616, 339

Woosley, S. 1986, ARA&A, 24, 205

Woosley, S., & Bloom, J. 2006, ARA&A, 44, 507

Woosley, S., & Weaver, T. 1995, ApJSS, 101, 181

Woosley, S. E., Blinnikov, S., & Heger, A. 2007, Nature, 450, 390

Woosley, S. E., Eastman, R. G., Weaver, T. A., & Pinto, P. A. 1994, ApJ, 429, 300

Woosley, S. E., & Heger, A. 2002, RMP, 74, 1015

Woosley, S. E., Taam, R. E., & Weaver, T. A. 1986, ApJ, 301, 601

Woosley, S. E., & Weaver, T. A. 1980, ApJ, 238, 1017

Yoon, S.-C., Podsiadlowski, P., & Rosswog, S. 2007, MNRAS, 380, 933

Yoon, S.-C., Woosley, S. E., & Langer, N. 2010, ApJ, 725, 940

Yu, Y.-W., Zhang, B., & Gao, H. 2013, ApJ, 776, L40

Yuan, F., Quimby, R., Rykoff, E., et al. 2008, Central Bureau Electronic Telegrams, 1262

Yun, M. S., & Carilli, C. L. 2002, ApJ, 568, 88

Zaritsky, D., Kennicutt, Jr., R. C., & Huchra, J. P. 1994, ApJ, 420, 87